ION BERNSTEIN WAVE EXPERIMENTS ON THE ALCATOR C TOKAMAK

by

JOHN DOUGLAS MOODY

B.A., University of California, Berkeley

(1982)

Submitted to the Department of Physics
in Partial Fulfillment of the
Requirements for the
Degree of

DOCTOR OF PHILOSOPHY

at the

MASSACHUSETTS INSTITUTE OF TECHNOLOGY

15 April 1988

Signature of Author _____
Department of Physics
15 April 1988

Certified by _____
Professor Miklos Porkolab
Thesis Supervisor

Accepted by _____
Professor George F. Koster
Chairman, Departmental Graduate Committee

ION BERNSTEIN WAVE EXPERIMENTS ON THE ALCATOR C TOKAMAK

by

John Douglas Moody

Submitted to the Department of Physics
on 15 April 1988, in Partial Fulfillment of the
Requirements for the
Degree of
Doctor of Philosophy

Abstract

Ion Bernstein wave experiments are carried out on the Alcator C tokamak to study wave excitation, propagation, absorption, and plasma heating due to wave power absorption. It is shown that ion Bernstein wave power is coupled into the plasma and follows the expected dispersion relation. The antenna loading is maximized when the hydrogen second harmonic layer is positioned just behind (to the low field side of) the antenna. Plasma heating results at three values of the toroidal magnetic field are presented. Central ion temperature increases of $\Delta T_i/T_i \gtrsim 0.1$ and density increases $\Delta n/n < 1$ are observed during rf power injection of up to 180 kW at a frequency of $183.6 \times 10^6\,\mathrm{s}^{-1}$ for plasmas within the density range $0.6 \times 10^{20}\,\mathrm{m}^{-3} \leq \bar{n}_e \leq 4 \times 10^{20}\,\mathrm{m}^{-3}$ and magnetic fields $2.4 \geq \omega/\Omega_H \geq 1.1$. The density increase is usually accompanied by an improvement in the global particle confinement time relative to the Ohmic value. The ion heating rate is measured to be $\Delta T_i/P_{rf} \simeq 2$–$4.5\,\mathrm{eV/kW}$ at low densities $\sim 1 \times 10^{20}\,\mathrm{m}^{-3}$. At higher densities $\bar{n}_e \geq 1.5 \times 10^{20}\,\mathrm{m}^{-3}$ the ion heating rate dramatically decreases. It is shown that the decrease in the ion heating rate can be explained by the combined effects of wave scattering through the edge turbulence and the decreasing ion energy confinement of these discharges with density. The effect of observed edge turbulence is shown to cause a broadening of the rf power deposition profile with increasing density. It is shown that the inferred value of the Ohmic ion thermal conduction, when compared to the Chang–Hinton neoclassical prediction, exhibits an increasing anomaly with increasing plasma density. This increasing anomaly, which may result from the presence of the ion temperature gradient driven instability, can essentially account for the observed ion heating rate behavior.

Thesis Supervisor: Dr. Miklos Porkolab
Title: Professor of Physics

Acknowledgments

I begin by acknowledging my Lord and my God who has given meaning to all that I am and who has formed me with the ability to carry out this work.

I am grateful for the direction and leadership of my thesis advisor, Professor Miklos Porkolab. Miklos has often served as a role model to me; he is an exceptionally good physicist, both in his experimental and theoretical abilities. Miklos has provided me with encouragement and continual challenges through nearly six years of study at MIT. His frank and direct manner has often stimulated me to a deeper understanding of physics.

Professor Bruno Coppi has also been a respected role model of a very good physicist. He has provided a refreshing view of plasma physics which I benefitted from in several of the courses I had with him. I am also grateful to professor Ron Parker for his encouragement. His questions and insights always led me to a better understanding of my own research.

I am grateful to all of the staff scientists in the Alcator group who have at one time or another helped me in some way; without them, much of this work could not have been done. In particular, Dr. Paul Bonoli provided many suggestions and much advice in modeling the ion Bernstein wave ray trajectories, power deposition, and scattering from edge density fluctuations. He also helped me understand some of the results of the plasma power balance analyses. Dr. Bonoli was always willing to discuss my questions. Dr. Steve Wolfe was very helpful in teaching me to use the ONETWO transport code and in discussing the code results. Dr. Wolfe was always willing to discuss the many questions I had regarding all aspects of the ion Bernstein wave experiments. He would often inquire into my progress with his characteristic "So, how's it goin' John?" Dr. F. Scott McDermott was very helpful in many aspects of the ion Bernstein wave experiments and the initial interpretation of the results. He spent many hours helping set up the 9–inch coaxial cable, conditioning the antenna, performing calibrations, and many other tasks which were vital to the success of the experiment. Dr. Yuichi Takase was primarily responsible for operating the CO_2 laser scattering diagnostic; his work was crucial to the understanding of the ion Bernstein wave propagation, coupling, and power absorption. Dr. Takase was always available and willing to discuss my questions regarding many aspects of the experimental results and interpretation. I am also grateful to Dr. Boyd Blackwell who was a mentor to me during my first three years of graduate school. He too, was always available and willing to discuss my many

questions. Dr. Catherine Fiore was responsible for operating the ion temperature diagnostic and for interpreting the results. I am grateful for her help with this essential measurement.

I am grateful to many of the engineers and technicians who helped in designing and constructing the antenna, installing it in the tokamak, and operating the experiment. Thank you for your help Frank Silva, Dave Griffin, Bob Childs, Matt Besen, Ces Holtjer, Paul Telesmanic, and many others.

Many thanks go to my fellow graduate students Frank Camacho, Tom Shepard, Roger Richardson, Jeff Colborn, and visiting scientist Roberto Zanino. These people all provided friendship and stimulation during my studies at MIT.

I also thank many of my friends and roommates who have supported me through this work. Thanks John Erickson, Don Wardius, Michael Kou, Gary Paul, Richard Temple, Jeff Collier, Michael Reskahlla, and Robert Rosinsky.

I thank my wife Terri who has provided much love and encouragement and has exercised great patience throughout the course of this work. She was always willing to provide grammatical assistance in the writing of this thesis. Her relaxed, cheerful, and optimistic spirit helped make the completion of this work bearable.

Finally, I thank my family Dr. Fred, Phyllis, David, Paul, and Daniel, whose enthusiastic interest in my life and frequent visits to the east coast have made my time in graduate school enjoyable. They have all been an encouragement to me.

To my parents,
Dr. Fred and Phyllis Moody,
And to my wife,
Terri.

Table of Contents

CHAPTER 1

Introduction

1.1: Plasma Physics

1.1.1: Introduction

Plasma physics can be defined as the study of the behavior of *interacting charged particles in large numbers*. The key words are *interacting* and *large numbers*. There must be a large enough number of particles so that the cumulative effect of overlapping long range electric and magnetic forces is a factor in determining the statistical properties of the particles; yet, not so many particles that the near neighbor forces dominate the dynamics. Plasma physics is sometimes described as an extreme form of the many body problem. Throughout the study of plasmas, the subtleties in its statistical mechanics and kinetic theory have offered considerable challenges to physicists and mathematicians and some fundamental questions have in fact not yet been completely resolved.

The plasma state is sometimes described as the fourth state of matter, a term which was coined by W. Crookes[1] in 1879. Although somewhat imprecise, this term follows

from the idea that on constant addition of heat, a solid will usually transform to a liquid, then to a gas, then the gas will ionize and become a plasma. This same concept had perhaps its earliest beginnings with the ancient philosophers who conceived of the universe as composed of four *elements*: earth, water, air, and fire. Quite obviously they must have had in mind the four states of matter represented by these elements rather than the basic substances of chemistry.

The spectacular growth of plasma research during the last three decades has been caused not so much by interest in the field *per se* but rather by its exceptionally large range of overlap with other branches of science and by its many applications in modern technology. The best known and probably most challenging application of plasma physics is controlled fusion. Some of the less publicized although clearly very important uses of plasma physics include the direct conversion of thermal into electrical energy, for instance in the thermionic plasma diode; new developments of intense x–ray and neutron bursts; and the acceleration of charged particles in collective fields.

1.1.2: Thermonuclear Fusion

Thermonuclear fusion refers to the process where the nuclei of two atoms become so close to each other that they combine to form a third, heavier nucleus. In this reaction, some of the mass from the initial nuclei is converted into a quantity of energy far greater than the energy initially required to bring about the fusion reaction. Ordinary atoms very rarely undergo fusion because the electron cloud surrounding each atom keeps the individual nuclei too far away from each other. Fusion can occur, however, in a plasma when the *fuel* atoms are heated to such an high temperature that they become ionized, that is, the electrons are no longer bound to the nuclei. The nuclei in a plasma are free to move about independently of the electrons and interact with each other through binary collisions where the dominant force is the Lorentz force. This force is repulsive due to the like charges of the nuclei and tends to keep them well separated. Under certain situations however, the nuclei can come so close together that the nuclear force, which is attractive, overcomes the repulsive Lorentz force and the nuclei then fuse together.

Thermonuclear plasma fusion power production relies on the idea that it is possible to create a system in which a plasma is undergoing so many fusion events that useful power, substantially greater than the system operating power, can be extracted. The sort of plasma which is ideal for fusion power production must have both a high fusion rate and the ability to sustain this high fusion rate. These two criteria can be expressed in terms of the plasma density, temperature, and energy confinement time.

For example, a plasma which consists of a number density of n_i incident nuclei and n_t target nuclei in a Maxwellian velocity distribution at temperature T has a fusion

reaction rate given by

$$R = n_i n_t \overline{u\sigma(u)}. \tag{1.1.1}$$

Here, $u = |\mathbf{v}_i - \mathbf{v}_t|$ is the relative speed of the interacting particles, $\sigma(u)$ is the cross section† for a fusion collision, and the bar indicates averaging over the particle velocity distribution. If the incident and target nuclei are the same, the product $n_i n_t$ in Eq. 1.1.1 is replaced by $1/2n_i^2$[2]. The value of $\overline{u\sigma(u)}$ has been measured for various types of fusion reactions[3]as a function of temperature, and depending on the reacting ions, typically achieves its maximum value for a temperature greater than 10 keV. For a deuterium–tritium fusion reaction, $\overline{u\sigma(u)}$ reaches a maximum value of $9 \times 10^{-16}\,\mathrm{cm^3\,s^{-1}}$ at a temperature of 80 keV. Simple consideration of Eq. 1.1.1 thus indicate that a high reaction rate is possible for a high density plasma with a temperature not far from the value corresponding to the maximum of $\overline{u\sigma(u)}$.

Sustaining a high fusion rate in a plasma relies on the balance of input power and power loss. Power enters the plasma through fusion reactions, Ohmic heating, and any additional auxiliary power inputs; power loss results from radiation, transport, instabilities, and certain anomalous processes. In order for the power loss to be less than or equal to the input power, the product of the plasma density, n, and the energy confinement time, τ_E, must exceed a critical value. This product is known as the *Lawson Product*[2] and has a critical value which is dependent on the plasma temperature and reacting ions. For a deuterium–tritium reaction, the minimum critical value of $n\tau_E$ is $6 \times 10^{19}\,\mathrm{m^{-3}}$–s This is the value for a *breakeven* condition. A fusion device must exceed the Lawson *n–tau* value by a considerable amount to be a useful source of power.

The hope of controlled fusion is to create sources of energy that are literally inexhaustible, sources which will supply beyond our needs, even at an increased rate of demand, for centuries to come. Two fundamentally different approaches to controlled fusion are presently being researched. These are inertial confinement and magnetic confinement. There are two methods of magnetic confinement; closed configurations and open configurations depending on whether the magnetic field closes upon itself or not. The most successful of either of these magnetic configurations to date is the tokamak (from the Russian acronym for this kind of machine, the concept for it was originally developed by physicists in the USSR[4]). This device uses magnetic field lines in the shape of a torus to confine the plasma particles and Ohmically heats the plasma by

---

† Recall that the *differential scattering cross section* is given by the total number of particles crossing the area that subtends a solid angle $d\Omega$ at the target, divided by the incident flux. The *total cross section* is obtained by integrating the differential cross section over $d\Omega$.

inducing a large toroidal current to flow through it. The Alcator C tokamak, previously at the *Massachusetts Institute of Technology*, is one such tokamak experiment designed to study a high density plasma in a large magnetic field. The various experiments and studies conducted on Alcator C and many other tokamaks throughout the world will hopefully provide insight into the physics and engineering aspects of building a working fusion reactor

1.2: Motivation for this Thesis

It has been thought for some time that heating a tokamak plasma solely via an induced toroidal plasma current is not sufficient to bring the plasma to ignition temperatures. Although this limitation is not certain, its possibility has inspired much research into auxiliary methods of heating the plasma. Some of these methods include neutralized ion beam injection, relativistic electron beams, and rf † (radio frequency) waves ranging in frequency from Alfvén waves to waves near the electron cyclotron frequency. One particular wave heating method in the ion cyclotron range of frequencies which has received much attention lately and looks very promising utilizes the directly launched ion Bernstein wave.

Plasma heating via the ion Bernstein wave is an attractive heating scheme because it is possible to use a waveguide launching structure which can easily be accommodated between the toroidal field coils in a tokamak. In addition, power sources in the ion cyclotron range of frequencies are relatively inexpensive and efficient. Also, ion Bernstein waves can heat at high harmonics allowing a waveguide launching structure to be kept small in size. Finally, ion Bernstein waves heat the bulk ions and are accessible to the plasma for a wide range of parallel wave numbers[5].

At this time it is still too early to say for sure whether ion Bernstein wave heating is a good possibility for auxiliary heating of fusion type devices. More details of the wave heating mechanisms, parametric processes, and coupling in high density, high temperature, and large magnetic field plasmas must still be understood. At the time of this writing, two new ion Bernstein wave experiments are presently in their early stages. These are planned for the PBX tokamak at the Princeton Plasma Physics Laboratory and the D–III–D tokamak at the General Atomic Company in San Diego. Hopefully, the results of these experiments will improve the understanding of ion Bernstein waves as a possible auxiliary heating scheme.

---

† The abbreviation rf will henceforth be used to indicate oscillations in the radio frequency range of frequencies.

1.3: Scope of this Thesis

Ion Bernstein wave experiments were conducted on the Alcator C tokamak during the year of 1986. The purpose of the experiments was mainly to study the characteristics of ion Bernstein waves as an auxiliary heating scheme in a high density, high magnetic field plasma. In addition to this, ion Bernstein wave propagation, coupling, and wave power absorption physics were studied. The experiments were performed near the end of the Alcator C program at MIT and unfortunately, many interesting results which appeared during the 1986 experiments could not be studied in greater detail.

This thesis presents the experimental study of ion Bernstein waves in the Alcator C tokamak and attempts to explain through detailed analyses the causes for the experimentally observed results. In particular, the behavior of the antenna–plasma coupling, wave propagation and power absorption, and the plasma response to ion Bernstein wave power injection are analyzed within the context of current plasma theories.

The antenna–plasma coupling was studied by measuring the antenna radiation resistance as a function of plasma density, magnetic field, and rf power. The radiation resistance exhibited a maximum when the hydrogen second harmonic layer was located just behind (toward the low field side of) the antenna. The radiation resistance increased with line–averaged density up to a density of $\bar{n}_e \simeq 2.6 \times 10^{20}\,\mathrm{m}^{-3}$, above this density the radiation resistance decreased. A weak dependence on rf power was observed in the radiation resistance. When the rf power was increased by a factor of three (50 kW to 150 kW) the radiation resistance decreased slightly by about 20%. These measurements are compared with the results of an antenna–plasma coupling model developed by M. Brambilla. This model, which is based entirely upon linear plasma wave theory, predicts the observed dependence of the radiation resistance on magnetic field over a narrow range of fields. The density dependence of the radiation resistance may be reproduced by the model. The discrepancy outside of the narrow field range may result from certain parametric processes which can occur near the antenna surface where the electric field energy density is large compared to the plasma thermal energy density. The physics contained in the model is described and the similarities and differences between the predicted and measured values are discussed.

Ion Bernstein wave propagation and absorption was studied in the plasma using a CO_2 laser scattering diagnostic system. Dr. Y. Takase was responsible for operating this important diagnostic during the ion Bernstein wave experiments. The correct dispersion relation was verified by mapping out the perpendicular wave vector as a function of the minor radial position. The scattered signal showed a nearly linear dependence on the rf power coupled into the antenna system. Power absorption was investigated

across the $\omega/\Omega_H = 1.5$ ($\omega/\Omega_D = 3$) layer for two different magnetic field regimes. The CO_2 scattered signal showed a large attenuation across this layer suggesting ion Bernstein wave power absorption. At the higher field, broad and downshifted frequency spectra were observed by the scattering system indicating the possibility of nonlinear processes (parametric decay for example) in addition to wave power absorption.

Central ion temperature increases of $\Delta T_i/T_{i0} \gtrsim 0.1$ and density increases of $\Delta n/n < 1$ were observed during rf power injection of up to 180 kW for plasmas within the density range of $0.6 \times 10^{20}\,\mathrm{m}^{-3} \leq \bar{n}_e \leq 4 \times 10^{20}\,\mathrm{m}^{-3}$ and magnetic fields within the range $4.8\,\mathrm{T} \leq B_0 \leq 11\,\mathrm{T}$. Although the greatest ion heating was observed at a central magnetic field of 9.3 T, heating occurred over a broad range of magnetic fields $2.4 \geq \omega/\Omega_{cH(0)} \geq 1.1$ ($\omega/2\pi = f_0 = 183.6 \times 10^6\,\mathrm{s}^{-1}$) and did not show a strong dependence on having a particular ion cyclotron resonance located near the plasma center. The density increase was usually accompanied by an improvement in the global particle confinement time relative to the Ohmic value and the ion temperature increase appeared to show rf power thresholds which were dependent on the magnetic field and agreed with the theoretical predictions within experimental error. Near densities of $\bar{n}_e \lesssim 1 \times 10^{20}\,\mathrm{m}^{-3}$ rf power injection typically produced an ion heating rate of $\Delta T_i/P_{rf} \sim 2$–$4.5\,\mathrm{eV/kW}$. At higher densities, $\bar{n}_e > 1.5 \times 10^{20}\,\mathrm{m}^{-3}$, the heating rate decreased to 0.5 eV/kW.

Several density dependent mechanisms are considered which may explain the decrease of the ion heating rate. For example, wave power attenuation due to edge collisions which becomes worse at higher densities can be shown to have a negligible effect on the wave power. The nonlinear power threshold increases with density but cannot account for the heating rate decrease at the low magnetic field. CO_2 laser scattering results show that low–frequency edge plasma turbulence increases with density. This suggests that turbulence may scatter the ion Bernstein wave power and broaden its radial power deposition profile. It is shown by ray tracing and power absorption modeling that a normalized scattering amplitude of $\hat{n}_e \equiv \tilde{n}_e/n_e = 0.3$ is sufficient to broaden the power deposition from being centrally peaked to nearly uniform over the poloidal cross–section. Unfortunately, accurate measurements of $\hat{n}_e$ are not available for the ion Bernstein wave data. Another effect which may contribute to the decrease in the ion heating rate is that the global energy confinement time in these discharges, which is increasing linearly with density at low densities, begins to saturate at higher densities. This saturation is caused by increased coupling between the ions and electrons and an increasing anomaly in the ion thermal conduction compared to the Chang–Hinton neoclassical prediction. The mechanism causing the increasing anomaly may be due to increased ion thermal transport caused by ion temperature gradient driven instabilities. It is shown that the increasing ion thermal conduction anomaly causes the ion energy confinement to degrade with increasing density contributing to the observed decrease in the ion heating rate.

1.4: Thesis Outline

The first part of this thesis is intended to outline the general characteristics of ion Bernstein waves for both the reader who is entirely unfamiliar with this particular plasma oscillation as well as one who is quite familiar with plasma waves in general. Properties of the wave ranging from its dispersion in homogeneous plasma to ray tracing and power deposition in a weakly inhomogeneous plasma are described in Chapter 2. The remaining chapters and their subjects are as follows. The third chapter describes the MIT Alcator C tokamak, the ion Bernstein wave antenna system, and additional equipment and diagnostics important in the ion Bernstein wave experiments. Chapter 4 presents the experimental results. The heart of the experimental analyses and interpretation is given in Chapter 5. Finally, Chapter 6 reviews the results, presents the conclusions, and offers suggestions for future work.

REFERENCES

1. W. CROOKES, *Phil. Trans.*, **1**, 135, (1879).

2. J. D. LAWSON, *Proc. Phys. Soc. (London)*, B70, 6, (1957).

3. S. L. GREENE, Lawrence Radiation Laboratory Report UCRL–70522, 1967.

4. I. E. TAMM AND A. D. SAKHAROV, in *Plasma Physics and the Problem of Controlled Thermonuclear Reactions, Vol. I*, edited by M. A. Leontovich, (Pergamon Press, New York, 1961).

5. M. ONO, Ion Bernstein Wave Heating, Theory and Experiment, in Proc. Course and Workshop on Applications of rf Waves to Tokamak Plasmas, Varenna, 1985, p. 197.

CHAPTER 2

Description of Ion Bernstein Modes

2.1: Introduction

The study of ion Bernstein modes originated out of the early work on electrostatic modes in a magnetized plasma which is discussed in detail by E. P. Gross[1](1951), V. A. Bailey[2](1951), G. V. Gordeyev[3](1952), I. B. Bernstein[4](1958), and H. K. Sen[5](1952). Bernstein (1958) first obtained the dispersion relation for ion Bernstein waves and showed that there are two types of waves depending on the departure from exact perpendicular propagation across the magnetic field. One type, known as a pure ion Bernstein wave, propagates almost perpendicularly to the magnetic field so that the electrons are nearly stationary. The other type called a neutralized ion Bernstein wave, propagates at an angle to the magnetic field which is close to perpendicular; however, the electrons are not stationary but move along the magnetic field lines so as to be in Boltzmann equilibrium with the wave potential. This wave is also referred to as an

electrostatic ion cyclotron wave. These two domains of wave propagation are separated by a region where the waves are electron Landau damped. Neutralized ion Bernstein waves have been observed by E. R. Ault and H. Ikezi[6], J. P. M. Schmitt[7], and Y. Ohnuma, S. Miyake, T. Sato, and T. Watari[8]. Pure ion Bernstein waves were first observed by J. P. M. Schmitt[9]in a potassium Q–machine plasma column. Schmitt excited the waves with a long wire carefully positioned along the magnetic field line in the center of the plasma column. S. Puri[10]first suggested using directly launched ion Bernstein waves to heat a tokamak plasma. Experimental study of directly launched ion Bernstein waves was first done by Skiff *et al.*[11, 12, 13] on the Princeton ACT–I torus. Plasma ion heating using directly launched ion Bernstein waves was first done by Ono *et al.*[14]on the JIPPT–II–U tokamak in Japan and then similar heating experiments were performed on the PLT[15]and ALCATOR C[16] tokamaks. The experiments on JIPPT–II–U showed ion heating at odd half–integral harmonics of the ion cyclotron frequency. Two theories of nonlinear plasma heating by ion Bernstein waves have been suggested by Abe[17]and Porkolab[18]to explain this result.

A general intuitive understanding of ion Bernstein mode characteristics can be obtained by considering small amplitude wave perturbations near the ion cyclotron frequency in an infinite, homogeneous, fully ionized, finite temperature, and magnetized plasma. A simplified plasma of this sort provides a way to examine these modes in a detailed way without introducing the complications of an inhomogeneous plasma. The intuition developed in this simplified theory can then be useful in generalizing the theory of ion Bernstein modes to inhomogeneous plasma.

The ion Bernstein mode is essentially a sound–like mode which propagates at frequencies between the harmonics of the ion cyclotron frequency. Consequently, the mode can only exist in a finite temperature plasma where the charged particles circulate about the magnetic lines of force on orbits with finite gyro–radii. These orbits cause the particles to behave not as point charges, but rather as charges smeared out over the particle's gyro–orbit. Finite temperature allows the particle to sample a region of the plasma rather than a single point. The results are that the particle experiences an average of the electromagnetic plasma fields over one gyro–orbit and the particle may come into resonance with the plasma fields under certain conditions. Although present in any finite temperature plasma, these effects are especially important for the ion Bernstein mode because the mode's wavelength perpendicular to the lines of force is of the same order of magnitude as the ion gyro–orbit radius. As a result, an ion can experience significantly different electromagnetic fields at different points in its gyro–orbit; this difference is strongly dependent on the ratio of the wave frequency to the particle's gyro–frequency.

The outline of this chapter is as follows. Section two outlines the governing equations for waves in a plasma. Section three describes the linearization of the governing equations and outlines the procedure for deriving the wave equation in an homogeneous plasma. The dielectric tensor is also given in detail in section three. Section four discusses the characteristics of the three ICRF modes by analyzing a simplified wave equation. Section five discusses in particular, the ion Bernstein wave characteristics. Section six gives a brief review of the recent models which describe ICRF wave propagation in an inhomogeneous plasma; special attention is given to the Brambilla model. Section seven describes ion Bernstein wave ray propagation and damping. Finally, section eight gives a review of nonlinear plasma wave effects on the ion Bernstein wave and discusses nonlinear wave absorption processes important for the ion Bernstein wave.

2.2: Electromagnetic Wave Propagation in a Plasma

Wave propagation in a plasma is described by the following Vlasov–Maxwell equations:

$$\nabla \cdot \mathbf{E} = 4\pi\rho \tag{2.2.1}$$

$$\nabla \cdot \mathbf{B} = 0 \tag{2.2.2}$$

$$\nabla \times \mathbf{E} = -\frac{1}{c}\frac{\partial \mathbf{B}}{\partial t} \tag{2.2.3}$$

$$\nabla \times \mathbf{B} = \frac{1}{c}\frac{\partial \mathbf{E}}{\partial t} + \frac{4\pi}{c}\mathbf{J} \tag{2.2.4}$$

$$\frac{\partial f_\alpha}{\partial t} + \mathbf{v}\cdot\nabla f_\alpha + \frac{1}{m_\alpha}\left[\mathbf{F} + q_\alpha(\mathbf{E} + \frac{1}{c}\mathbf{v}\times\mathbf{B})\right]\cdot\frac{\partial f_\alpha}{\partial \mathbf{v}} = 0. \tag{2.2.5}$$

The subscript α refers to the particle species, m_α is the mass, and q_α is the charge. Equations 2.2.1–4 are the standard Maxwell equations that describe electromagnetic phenomena. Equation 2.2.5 is the collisionless Boltzmann equation or Vlasov equation which describes the motion of the single particle distribution function $f_\alpha(\mathbf{r},\mathbf{v},t)$ in phase space and offers a precise description of the plasma in the fluid limit. A probabilistic interpretation of f_α is as follows: The probability of finding a particle within the phase space volume $\Delta^3 r\Delta^3 v$ centered around the phase space point $(\mathbf{r},\mathbf{v})$ is $P(\mathbf{r},\mathbf{v},t,\Delta^3 r,\Delta^3 v) = f_\alpha(\mathbf{r},\mathbf{v},t)\Delta^3 r\Delta^3 v/N$ where N is the total number of particles in the system. The quantity $\mathbf{F}$ in Eq. 2.2.5 contains all nonelectromagnetic forces (which satisfy $\nabla_{\mathbf{v}}\cdot\mathbf{F} = 0$) such as gravity and will be neglected here.

The local particle space density is obtained by integrating f_α over $\mathbf{v}$

$$\int d^3v\, f_\alpha(\mathbf{r},\mathbf{v},t) = n_\alpha(\mathbf{r},t). \tag{2.2.6}$$

The total charge and current densities are obtained from f_α through the following constitutive relations

$$\rho(\mathbf{r},t) = \rho_{\mathbf{ext}} + \sum_\alpha q_\alpha \int d^3v\, f_\alpha(\mathbf{r},\mathbf{v},t) \tag{2.2.7}$$

$$\mathbf{J}(\mathbf{r},t) = \mathbf{J}_{\mathbf{ext}} + \sum_\alpha q_\alpha \int d^3v\, \mathbf{v}\, f_\alpha(\mathbf{r},\mathbf{v},t) \tag{2.2.8}$$

where $\rho_{\mathbf{ext}}$ and $\mathbf{J}_{\mathbf{ext}}$ are the externally imposed charge and current density. The Maxwell equations determine the fields $\mathbf{E}$ and $\mathbf{B}$ which then determine the single particle distribution function f_α through the Vlasov equation. The distribution function f_α determines the charge and current densities, which are sources of the electromagnetic fields, closing the system of equations.

Particle collisions enter the Boltzmann equation through the term $(\frac{\partial f_\alpha}{\partial t})_{\mathrm{coll}}$ which may be added to the right side of Eq. 2.2.5. The time required for a region of plasma particles of volume l_{mfp}^3 (where l_{mfp} is the collisional mean free path) to equilibrate is denoted as τ. This time is typically of the same order as the collision time between two particles of type α, $\tau \simeq 1/\nu_\alpha$ where ν_α is the collision frequency. Collisions may be neglected in describing plasma modes provided that the typical mode wavelength $\lambda << l_{mfp}$ and the mode frequency $f_0 = \omega_0/2\pi >> \nu_\alpha$.

2.3: Linear Plasma Wave Theory

2.3.1: Introduction

The system of equations (Eqs. 2.2.1–5) is implicitly nonlinear due to the product of $\mathbf{E}$ and $\mathbf{B}$ with f_α in Eq. 2.2.5. A solution can be obtained for small amplitude linear modes by assuming perturbations of electromagnetic field and plasma quantities about a zero order equilibrium solution. An appropriate perturbation parameter, ϵ, is the ratio of the perturbed wave energy density to the plasma thermal energy density. A

small value of ϵ indicates that the equilibrium plasma parameters and particle orbits are not affected much by the presence of the wave.

A quantity Q can thus be expanded in ϵ as

$$\mathrm{Q}(\mathbf{r},\mathbf{v},t) = \mathrm{Q}^{(0)}(\mathbf{r},\mathbf{v},t) + \epsilon \mathrm{Q}^{(1)}(\mathbf{r},\mathbf{v},t) + \epsilon^2 \mathrm{Q}^{(2)}(\mathbf{r},\mathbf{v},t) + \cdots \qquad (2.3.1).$$

First order quantities describe wave propagation, damping, and growth of a small amplitude wave. Second and higher order quantities describe nonlinear effects such as wave–wave coupling and wave–wave–particle coupling. These higher order nonlinear phenomena are discussed in more detail in section 8 of this chapter.

2.3.2: First Order Wave Equation

The zeroth order Vlasov equation is written as,

$$\frac{\mathrm{D}f_\alpha^{(0)}}{\mathrm{D}t} = \left[\frac{\partial}{\partial t} + \mathbf{v}\cdot\nabla + \frac{q_\alpha}{m_\alpha c}(\mathbf{v}\times\mathbf{B}_0)\cdot\nabla_v\right] f_\alpha^{(0)} = 0 \qquad (2.3.2)$$

where $\frac{\mathrm{D}}{\mathrm{D}t}$ is the operator in braces and indicates differentiation along the unperturbed single particle phase space trajectory. The solution for $f_\alpha^{(0)}$ is an arbitrary function of the constants of motion for a single charged particle moving in a background magnetic field $\mathbf{B}_0$. Collisions are usually important in determining the form of the zeroth order distribution function. This is because there is no short time scale $1/\omega$ introduced by the wave frequency at this order which would ordinarily justify ignoring collisions.

Equating terms from Eq. 2.2.5 which are proportional to ϵ gives

$$\frac{\mathrm{D}f_\alpha^{(1)}}{\mathrm{D}t} = -\frac{q_\alpha}{m_\alpha}(\mathbf{E}^{(1)} + \frac{1}{c}\mathbf{v}\times\mathbf{B}^{(1)})\cdot\frac{\partial f_\alpha^{(0)}}{\partial \mathbf{v}} \qquad (2.3.3).$$

The solution for $f_\alpha^{(1)}$ is obtained by integrating Eq. 2.3.3 along the unperturbed particle orbits[19]. The result for $f_\alpha^{(1)}$ is expressed in terms of this integral as

$$f_\alpha^{(1)}(\mathbf{r},\mathbf{v},t) = -\frac{q_\alpha}{m_\alpha}\int_{-\infty}^{t} dt' \left[\mathbf{E}^{(1)}(\mathbf{x}',t') + \frac{1}{c}\mathbf{v}'\times\mathbf{B}^{(1)}(\mathbf{x}',t')\right]\cdot\frac{\partial f_\alpha^{(0)}}{\partial \mathbf{v}} \qquad (2.3.4).$$

The details of evaluating this type of integral are given in Ref 19. Once $f^{(1)}(\mathbf{r},\mathbf{v},t)$ is known, the perturbed current density is obtained through the relation

$$\mathbf{J}^{(1)} = \sum_\alpha q_\alpha \int d^3v\, \mathbf{v} f_\alpha^{(1)}(\mathbf{r},\mathbf{v},t) \qquad (2.3.5).$$

This current is the self–consistent source of the perturbed electric field in the first order wave equation[19] obtained from Eqs. 2.2.1–4

$$\nabla \times \nabla \times \mathbf{E}^{(1)} + \frac{1}{c^2}\frac{\partial^2}{\partial t^2}\mathbf{E}^{(1)} = -\frac{4\pi}{c^2}\frac{\partial}{\partial t}\left[\mathbf{J}^{(1)} + \mathbf{J}^{(1)}_{\mathrm{ext}}\right] \qquad (2.3.6).$$

The wave equation together with the equation for the perturbed current completely describe linear waves in a fluid plasma. These equations, in general, are quite difficult to solve; however, a completely analytical solution can be obtained by assuming that the plasma is homogeneous and that the zeroth order distribution function is a Maxwellian. These assumptions are not far from being realistic and they provide a starting point for understanding the complex nature of this wave equation.

2.3.3: The Wave Equation in an Homogeneous Plasma

The plasma is assumed to be homogeneous with only a zeroth order static magnetic field oriented in the $\hat{z}$ direction with a negligible zeroth order electric field and current, $\mathbf{B}_0 = B_0\,\hat{z}$, $\mathbf{J}_0 = 0$, $\mathbf{E}_0 = 0$. As a result, there are only two constants of the particle motion and $f_\alpha^{(0)}$ is a function of the particle velocity parallel to the background magnetic field $v_\parallel$ and the energy perpendicular to the field $v_\perp^2$. Collisions are important in determining the analytic form of $f_\alpha^{(0)}$ and when included, the most general solution for $f_\alpha^{(0)}$ is a Maxwellian distribution of velocities. Often, in rf heating and neutral beam heating experiments, a two temperature Maxwellian velocity distribution is observed

$$f_\alpha^{(0)}(v_\perp^2, v_\parallel) = n_\alpha \frac{1}{(\pi v_{t\alpha\perp}^2)} e^{-v_\perp^2/v_{t\alpha\perp}^2} \frac{1}{(\pi v_{t\alpha\parallel}^2)^{1/2}} e^{-v_\parallel^2/v_{t\alpha\parallel}^2} \qquad (2.3.7)$$

where $v_{t\alpha\perp}^2 = 2\mathrm{T}_{\alpha\perp}/m_\alpha$ and $v_{t\alpha\parallel}^2 = 2\mathrm{T}_{\alpha\parallel}/m_\alpha$ are the thermal speeds of the plasma particle perpendicular and parallel to the background magnetic field and n_α is the particle number density. A two temperature distribution function is more general and does not introduce much additional complication into the analysis.

In addition to assuming that the plasma is homogeneous in space it is also assumed to be stationary in time. This means that a nonlocal physical quantity (a quantity such as the electric field which depends on long range particle fields in addition to local fields), is not explicitly dependent on its space–time position $(\mathbf{x}, t)$ but is only dependent on the separation between its space–time position and that of other plasma particles $(\mathbf{x}', t')$. This allows Fourier decomposition in space and Laplace decomposition in time of the electromagnetic and plasma quantities. A quantity Q(r,t) and its transform

$\tilde{Q}(\omega,k)$ are related through the following equations[20] as

$$Q(r,t) = \frac{1}{(2\pi)^2}\int d\omega \int d^3k\, \tilde{Q}(\omega,k)e^{i(k\cdot r-\omega t)} \tag{2.3.8}$$

$$\tilde{Q}(\omega,k) = \frac{1}{(2\pi)^2}\int dt \int d^3x\, Q(r,t)e^{-i(k\cdot r-\omega t)}. \tag{2.3.9}$$

Applying this transformation to the wave equation gives

$$k \times k \times \tilde{E}^{(1)} + \frac{\omega^2}{c^2}\left[\tilde{E}^{(1)} + \frac{4\pi i}{\omega}\tilde{J}^{(1)}\right] = -\frac{4\pi i\omega}{c^2}\tilde{J}^{(1)}_{ext}. \tag{2.3.10}$$

It is possible to express $\tilde{J}^{(1)}$ in terms of $\tilde{E}^{(1)}$ through Eq. 2.3.5 and therefore Eq. 2.3.10 can be solved for $\tilde{E}^{(1)}$. From this point onward, all quantities will be considered transformed quantities, unless specifically stated, and they will be represented without a tilde ($\tilde{}$).

2.3.4: Dielectric Tensor

Equation 2.3.10 expresses three algebraic equations for the three transformed electric field components. The second term on the left side of Eq. 2.3.10, the term which contains the displacement and particle currents, can be rewritten as a 3×3 matrix multiplying the electric field which is represented as a column vector. This matrix is defined as the dielectric tensor K_{ij} and is defined here as[19]

$$K_{ij}E^{(1)}_j \equiv E^{(1)}_i + \frac{4\pi i}{\omega}J^{(1)}_i \tag{2.3.11}$$

To obtain an explicit form for K_{ij}, the coordinate axis is first positioned so that $\hat{z}$ is along the equilibrium magnetic field and k lies in the x–z plane. The vector k is now expressed as $k = k_\perp\hat{x} + k_\parallel\hat{z}$ where $\perp$ and $\parallel$ refer to the orientation with respect to the magnetic field. The tensor K_{ij} is obtained by performing the integrals in Eqs. 2.3.4–5 and can be represented in matrix form[21] as

$$K = I + \sum_\alpha \sum_{n=-\infty}^{\infty} \int_0^\infty 2v_\perp dv_\perp \int_{-\infty}^{+\infty} dv_\parallel$$

$$\times \begin{pmatrix} \frac{n^2\Omega_\alpha^3}{k_\perp^2} J_n^2 P_{n\alpha} & i\frac{n\Omega_\alpha^2}{k_\perp} v_\perp J_n J_n' P_{n\alpha} & \frac{n\Omega_\alpha^2}{k_\perp^2} v_\parallel J_n^2 Q_{n\alpha} \\ -i\frac{n\Omega_\alpha^2}{k_\perp} v_\perp J_n J_n' P_{n\alpha} & \Omega_\alpha [v_\perp J_n]^2 P_{n\alpha} & -i\Omega_\alpha v_\perp v_\parallel J_n J_n' Q_{n\alpha} \\ \frac{n\Omega_\alpha^2}{k_\perp} v_\parallel J_n^2 P_{n\alpha} & i\Omega_\alpha v_\perp v_\parallel J_n J_n' P_{n\alpha} & \Omega_\alpha v_\parallel^2 J_n^2 Q_{n\alpha} \end{pmatrix} \tag{2.3.12}$$

where,

$$P_{n\alpha} = 2\pi \left(\frac{\omega_{p\alpha}^2}{\omega\Omega_\alpha}\right) \frac{\frac{\partial f_\alpha^{(0)}}{\partial v_\perp^2} + \frac{k_\parallel v_\parallel}{\omega}\left(\frac{\partial}{\partial v_\parallel^2} - \frac{\partial}{\partial v_\perp^2}\right) f_\alpha^{(0)}}{\omega - n\Omega_\alpha - k_\parallel v_\parallel} \tag{2.3.13}$$

$$Q_{n\alpha} = 2\pi \left(\frac{\omega_{p\alpha}^2}{\omega\Omega_\alpha}\right) \frac{\frac{\partial f_\alpha^{(0)}}{\partial v_\perp^2} - \frac{n\Omega_\alpha}{\omega}\left(\frac{\partial}{\partial v_\parallel^2} - \frac{\partial}{\partial v_\perp^2}\right) f_\alpha^{(0)}}{\omega - n\Omega_\alpha - k_\parallel v_\parallel} \tag{2.3.14}$$

I is the unit matrix, $\omega/2\pi = f$ is the wave frequency, J_n is the Bessel function of order n with argument $k_\perp v_\perp/\Omega_\alpha$, and J_n' is the derivative of J_n with respect to its argument. The wave equation can now be written as[19]

$$\mathrm{G}_{ij}\mathrm{E}_j^{(1)} = -\frac{4\pi i\omega}{c^2}\mathrm{J}_{j(\mathrm{ext})} \tag{2.3.15}$$

where G_{ij} is represented in matrix form as

$$\mathbf{G} = \begin{pmatrix} K_{xx} - n_\parallel^2 & K_{xy} & K_{xz} + n_\perp n_\parallel \\ K_{yx} & K_{yy} - n^2 & K_{yz} \\ K_{zx} + n_\perp n_\parallel & K_{zy} & K_{zz} - n_\perp^2 \end{pmatrix} \tag{2.3.16}$$

and $n_\parallel \equiv \frac{ck_\parallel}{\omega}$ and $n_\perp \equiv \frac{ck_\perp}{\omega}$ are the parallel and perpendicular indices of refraction.

In the absence of external driving currents, Eq. 2.3.15 becomes

$$\mathrm{G}_{ij}\mathrm{E}_j^{(1)} = 0 \tag{2.3.17}$$

and nontrivial solutions for $\mathbf{E}^{(1)}$ exist only if

$$\det\left[\mathbf{G}(\omega, \mathbf{k})\right] = 0. \tag{2.3.18}$$

Equation 2.3.18 describes the possible normal modes of plasma oscillation, $\omega(\mathbf{k})$, with $\mathbf{k}$ being complex, denoting spatial growth or damping of the mode. Once $\omega(\mathbf{k})$ is known, one can solve for the eigenvectors of Eq. 2.3.17; these represent the electric field polarization of each mode.

The elements of the tensor **K** can be easily obtained for an isotropic ($T_\perp = T_\parallel$) Maxwellian zero order distribution function and are given here as follows

$$K_{xx} = 1 + \sum_\alpha \sum_{n=-\infty}^{\infty} \frac{\omega_{p\alpha}^2}{\omega^2} \frac{n^2}{b_\alpha} I_n e^{-b_\alpha} \zeta_{0\alpha} Z(\zeta_{n\alpha}) \tag{2.3.19}$$

$$K_{xy} = -i \sum_\alpha \sum_{n=-\infty}^{\infty} n \frac{\omega_{p\alpha}^2}{\omega^2} \left[I_n - I_n' \right] e^{-b_\alpha} \zeta_{0\alpha} Z(\zeta_{n\alpha}) \tag{2.3.20}$$

$$K_{xz} = -\sum_\alpha \sum_{n=-\infty}^{\infty} n \frac{\omega_{p\alpha}^2}{\omega^2} I_n e^{-b_\alpha} \zeta_{0\alpha} Z'(\zeta_{n\alpha}) \frac{\Omega_\alpha}{k_\perp v_{t\alpha}} \tag{2.3.21}$$

$$K_{yy} = K_{xx} + \sum_\alpha \sum_{n=-\infty}^{\infty} \frac{\omega_{p\alpha}^2}{\omega^2} 2b_\alpha \left[I_n - I_n' \right] e^{-b_\alpha} \zeta_{0\alpha} Z(\zeta_{n\alpha}) \tag{2.3.22}$$

$$K_{yz} = -i \sum_\alpha \sum_{n=-\infty}^{\infty} \frac{\omega_{p\alpha}^2}{\omega^2} \left[I_n - I_n' \right] e^{-b_\alpha} \zeta_{0\alpha} Z'(\zeta_{n\alpha}) \frac{k_\perp v_{t\alpha}}{2\Omega_\alpha} \tag{2.3.23}$$

$$K_{zz} = 1 - \sum_\alpha \sum_{n=-\infty}^{\infty} \frac{\omega_{p\alpha}^2}{\omega^2} I_n e^{-b_\alpha} \zeta_{0\alpha} \zeta_{n\alpha} Z'(\zeta_{n\alpha}) \tag{2.3.24}$$

with, $K_{yx} = -K_{xy}$, $K_{xz} = K_{zx}$, and $K_{zy} = -K_{yz}$. In the above relations, the plasma frequency is defined as

$$\omega_{p\alpha}^2 = \frac{4\pi n_\alpha q_\alpha^2}{m_\alpha}, \tag{2.3.25}$$

I_n is the modified Bessel function of order n with argument $b_\alpha = k_\perp^2 \rho_\alpha^2$ where ρ_α is the particle Larmor radius

$$\rho_\alpha = \frac{1}{\sqrt{2}} \frac{v_{t\alpha}}{\Omega_\alpha}. \tag{2.3.26}$$

The cyclotron frequency if defined as $\Omega_\alpha = q_\alpha B/(m_\alpha c)$. The plasma dispersion function of Fried and Conte[22]is written as $Z(\zeta_{n\alpha})$ and has the argument

$$\zeta_{n\alpha} = \frac{\omega - n\Omega_\alpha}{k_\parallel v_{t\alpha}}. \tag{2.3.27}$$

Derivatives of functions are denoted with a prime such as I_n' or $Z'(\zeta_{n\alpha})$; these derivatives are taken with respect to the argument of the function.

2.4: The Three ICRF Modes in a Warm Plasma

2.4.1: Introduction

The term ICRF, which represents Ion Cyclotron Range of Frequencies, is used to refer to the electromagnetic frequency range near the ion cyclotron frequency or its first few harmonics. The following discussion will direct the study of Eq. 2.3.18 to the three modes in the ICRF (fast mode, slow mode, and ion Bernstein mode) for an homogeneous, isotropic Maxwellian, and magnetized plasma.

2.4.2: Approximations to the Wave Equation

Equation 2.3.18 represents an analytical, yet still somewhat complicated form of the dispersion relation. Analysis of the dispersion relation is facilitated by first making several approximations. These approximations greatly aid the analysis of the dispersion relation while still retaining the basic physics of the three plasma modes.

Equation 2.3.18 is first expanded to only a few terms in two parameters. The first parameter, b_α, is small when the plasma is considered to be warm so that a charged particle's Larmor radius is small compared to the perpendicular wavelength of a plasma wave. This allows the modified Bessel function to be expanded for small argument[23]

$$I_0(b_\alpha)e^{-b_\alpha} = 1 - b_\alpha + \frac{3}{4}b_\alpha^2 + \cdots + O(b_\alpha^3), \tag{2.4.1}$$

$$I_1(b_\alpha)e^{-b_\alpha} = \frac{1}{2}b_\alpha - \frac{1}{2}b_\alpha^2 + \cdots + O(b_\alpha^3), \tag{2.4.2}$$

$$I_2(b_\alpha)e^{-b_\alpha} = \frac{1}{8}b_\alpha^2 + \cdots + O(b_\alpha^3), \tag{2.4.3}$$

$$\vdots$$

$$I_n(b_\alpha)e^{-b_\alpha} = e^{-b_\alpha}\sum_{k=0}^{\infty}\left(\frac{b_\alpha}{2}\right)^{2k+n}\frac{1}{k!(n+k)!}. \tag{2.4.4}$$

The second expansion parameter is $k_\parallel v_{te}/\omega$ which, when small, indicates that the wave parallel phase velocity is much greater than the electron thermal velocity. This condition assures that the electrons cannot move quickly enough along the lines of force to short out the parallel electric field ($E_\parallel$) of the plasma wave. This limit is known as the cold plasma or fluid limit as opposed to the isothermal limit ($k_\parallel v_{te}/\omega >> 1$). This

description is also true for the ions; however, fluid ions do not affect the wave character as significantly as the electrons. As a result, the plasma dispersion function $Z(\zeta_{n\alpha})$ can be expanded in the asymptotic limit for real argument $\zeta_{n\alpha}$ as

$$Z(\zeta_{n\alpha}) = -\frac{1}{\zeta_{n\alpha}}\left[1+\frac{1}{2\zeta_{n\alpha}^2}+\frac{3}{4\zeta_{n\alpha}^4}+\frac{15}{8\zeta_{n\alpha}^6}+\cdots\right]+i\sqrt{\pi}e^{-\zeta_{n\alpha}^2} \qquad (2.4.5).$$

According to the above limits, the dielectric elements are approximated as

$$K_{xx} \simeq S-\sum_\alpha\left\{\frac{3\omega_{p\alpha}^2\Omega_\alpha^2}{(\omega^2-\Omega_\alpha^2)(\omega^2-4\Omega_\alpha^2)}b_\alpha - i\left[(1-b_\alpha)\mathrm{L}_{1\alpha}^+ + b_\alpha \mathrm{L}_{2\alpha}^+\right]\right\} \qquad (2.4.6)$$

$$K_{xy} \simeq -iD - i\sum_\alpha\left\{\frac{6\omega_{p\alpha}^2\Omega_\alpha^3}{\omega(\omega^2-\Omega_\alpha^2)(\omega^2-4\Omega_\alpha^2)b_\alpha}b_\alpha - i\left[(1-2b_\alpha)\mathrm{L}_{1\alpha}^- + b_\alpha \mathrm{L}_{2\alpha}^-\right]\right\} \qquad (2.4.7)$$

$$K_{xz} \simeq -\sum_\alpha\left\{\frac{2\omega_{p\alpha}^2\Omega_\alpha^2}{(\omega^2-\Omega_\alpha^2)^2}\frac{k_\parallel}{k_\perp}b_\alpha + i\frac{\Omega_\alpha}{k_\perp v_{t\alpha}}b_\alpha \mathrm{L}_{1\alpha}'^-\right\} \qquad (2.4.8)$$

$$K_{yy} \simeq S-\sum_\alpha\left\{\frac{\omega_{p\alpha}^2\Omega_\alpha^2(\omega^2+8\Omega_\alpha^2)}{\omega^2(\omega^2-\Omega_\alpha^2)(\omega^2-4\Omega_\alpha^2)}b_\alpha - i\left[2b_\alpha \mathrm{L}_{0\alpha} + (1+b_\alpha)\mathrm{L}_{1\alpha}^+ + b_\alpha \mathrm{L}_{2\alpha}^+\right]\right\} \qquad (2.4.9)$$

$$K_{yz} \simeq -i\sum_\alpha\left\{\frac{k_\parallel}{k_\perp}\frac{\Omega_\alpha}{\omega}\frac{\omega_{p\alpha}^2(\Omega_\alpha^2-3\omega^2)}{\omega^2(\omega^2-\Omega_\alpha^2)^2}b_\alpha + i\frac{k_\perp v_{t\alpha}}{2\Omega_\alpha}\left[\frac{1}{2}(2-3b_\alpha)\mathrm{L}_{0\alpha}' - (1-3b_\alpha)\mathrm{L}_{1\alpha}'^+\right]\right\} \qquad (2.4.10)$$

$$K_{zz} \simeq P-\sum_\alpha\left\{\frac{\omega_{p\alpha}^2\Omega_\alpha^2}{\omega^2(\omega^2-\Omega_\alpha^2)}b_\alpha + i\frac{1}{2}\left\{\mathrm{L}_{0\alpha}' + b_\alpha\left[-\mathrm{L}_{0\alpha}' + \mathrm{L}_{1\alpha}'^+\right]\right\}\right\} \qquad (2.4.11)$$

where S, D, and P are the Stix[19] parameters defined here as

$$S = 1 - \sum_{\alpha} \frac{\omega_{p\alpha}^2}{\omega^2 - \Omega_{\alpha}^2} \tag{2.4.12}$$

$$D = \sum_{\alpha} \frac{\omega_{p\alpha}^2}{\omega^2 - \Omega_{\alpha}^2} \frac{\Omega_{\alpha}}{\omega} \tag{2.4.13}$$

$$P = 1 - \sum_{\alpha} \frac{\omega_{p\alpha}^2}{\omega^2} \tag{2.4.14}$$

and the Landau damping parameters are defined as

$$\mathrm{L}_{m\alpha}^{\pm} = \frac{\omega_{p\alpha}^2}{\omega^2} \zeta_{0\alpha} \frac{\sqrt{\pi}}{2} \left[e^{-\zeta_{m\alpha}^2} \pm e^{-\zeta_{-m\alpha}^2} \right] \tag{2.4.15}$$

$$\mathrm{L}_{m\alpha}^{\prime\pm} = -\frac{\omega_{p\alpha}^2}{\omega^2} \zeta_{0\alpha} \sqrt{\pi} \left[\zeta_{m\alpha} e^{-\zeta_{m\alpha}^2} \pm \zeta_{-m\alpha} e^{-\zeta_{-m\alpha}^2} \right]. \tag{2.4.16}$$

For the case of $m = 0$, the above expressions are still applicable provided the $\pm$ is replaced with a $+$. It is pointed out that since the sum over cyclotron harmonics is only carried out to the second harmonic in Eqs. 2.4.6–11, the basic physics is retained provided $|\omega| \lesssim 2\Omega_i$.

It is next useful to assume that the plasma ion kinetic pressure is small compared to the total magnetic pressure (*i.e.*, low beta approximation)

$$\beta_i \equiv \frac{8\pi n_i T_i}{B^2} << 1 \tag{2.4.17}.$$

The effect of K_{xz} and K_{yz} is small in this case and both of these elements can be neglected. In addition, the finite β_i terms (terms proportional to b_α) in all of the dielectric elements except K_{xx} can be neglected. This can be justified since the finite β_i term in K_{xx} is essential for the existence of the ion Bernstein mode, whereas the finite β_i terms in the other dielectric elements only produce order β_i corrections in the already existing fast and slow plasma modes.

2.4.3: Ion Cyclotron Dispersion Relation

The dispersion relation, Eq. 2.3.17, with the above approximations now takes the following form[24]

$$\mathrm{T} n_{\perp}^6 + \mathrm{A} n_{\perp}^4 - \mathrm{B} n_{\perp}^2 + \mathrm{C} = 0 \tag{2.4.18}$$

where

$$\mathrm{T} = \sum_{\alpha=\mathrm{ion}} \frac{1}{2}\frac{\omega^2}{\Omega_\alpha^2}\frac{v_{t\alpha}^2}{c^2}\left\{\frac{3\omega_{p\alpha}^2\Omega_\alpha^2}{(\omega^2-\Omega_\alpha^2)(4\Omega_\alpha^2-\omega^2)} + i\left[\mathrm{L}_{1\alpha}^+ - \mathrm{L}_{2\alpha}^+\right]\right\} \tag{2.4.19}$$

$$\mathrm{A} = S^{(h)} - \mathrm{T}(S^{(h)} + P^{(h)} - n_\parallel^2) \tag{2.4.20}$$

$$\mathrm{B} = (S^{(h)} - n_\parallel^2)(S^{(h)} + P^{(h)} - \mathrm{T}P^{(h)}) - D^{(h)2} \tag{2.4.21}$$

$$\mathrm{C} = P^{(h)}\left\{(S^{(h)} - n_\parallel^2)^2 - D^{(h)2}\right\} \tag{2.4.22}$$

and

$$S^{(h)} = S + i\sum_{\alpha=\mathrm{ion}} \mathrm{L}_{1\alpha}^+ \tag{2.4.23}$$

$$D^{(h)} = D - i\sum_{\alpha=\mathrm{ion}} \mathrm{L}_{1\alpha}^- \tag{2.4.24}$$

$$P^{(h)} = P - i\sum_{\alpha}\frac{1}{2}\mathrm{L}_{0\alpha}'. \tag{2.4.25}$$

Note that the sum over α is carried out for the ion species only except for $P^{(h)}$ which includes Landau damping from the electrons. Equation 2.4.18 is written as a cubic in $n_\perp^2$ since the parallel wave number $k_\parallel$ ($n_\parallel$) is generally specified as a boundary condition which is determined by the antenna structure, while the dispersion relation determines $n_\perp^2$. Beyond this point the superscript $^{(h)}$ will be dropped from the Stix parameters and the Landau damping term will be assumed to be included.

Equation 2.4.18 describes three plasma modes. Each mode consists of one electric field polarization (eigenvector) associated with two equal but oppositely directed perpendicular wave vectors (the equation is unchanged for $n_\perp \rightleftharpoons -n_\perp$). For example, the electric field for the mode M is written as

$$\mathbf{E}_M(x,z,t) = \begin{pmatrix} E_x \\ E_y \\ E_z \end{pmatrix}_M \left[e^{ik_\perp x} + Ce^{-ik_\perp x}\right] e^{i(k_\parallel z - \omega t)} \tag{2.4.26}$$

where $(E_x, E_y, E_z)_M$ is the eigenvector of the mode and C is an arbitrary complex constant. In a cold plasma where T is identically zero Eq. 2.4.18 describes the well known fast wave and slow wave modes. These are the electromagnetic modes one obtains in an anisotropic dielectric medium, the anisotropy arising from the D. C. magnetic field. When the plasma has finite temperature, T (Eq. 2.4.19) is nonvanishing and a third sound–like mode results which is the ion Bernstein mode. This mode is described as sound–like since most of the wave energy is in the sloshing motion of the

ions and only a small fraction of the energy is in the electric and magnetic fields. This will be shown later in section 2.5

In a high density plasma where $\left(\frac{\omega_{pi}}{\Omega_i}\right)^2 >> 1$ the three modes are well separated in $n_\perp^2$ and the solutions to Eq. 2.4.18 can be approximated as

$$n_\perp^2|_F \simeq \frac{\mathrm{C}}{\mathrm{B}} \tag{2.4.27}$$

$$n_\perp^2|_S \simeq \frac{\mathrm{B}}{\mathrm{A}} \tag{2.4.28}$$

$$n_\perp^2|_B \simeq -\frac{\mathrm{A}}{\mathrm{T}} - \frac{\mathrm{B}}{\mathrm{A}}. \tag{2.4.29}$$

Here, the subscripts F, S, and B represent the fast, slow, and ion Bernstein wave modes. In general, $P >> S, D$, and, assuming that $S - n_\parallel^2 \neq 0$, Eqs. 2.4.27–29 can be simplified further to

$$n_\perp^2|_F \simeq S - n_\parallel^2 - \frac{D^2}{S - n_\parallel^2} \tag{2.4.30}$$

$$n_\perp^2|_S \simeq \frac{(S - n_\parallel^2)P}{S} \tag{2.4.31}$$

$$n_\perp^2|_B \simeq -\frac{S}{T} + \frac{P}{S}n_\parallel^2 + \frac{1}{S}\left[D^2 + TS\left(S - n_\parallel^2\right)\right]. \tag{2.4.32}$$

2.4.4: Electric Field Polarization

The electric field polarization of the modes can be approximated from the above dispersion relations as

$$\mathbf{E}_F \simeq E_{yF}\begin{pmatrix} i\frac{D}{S-n_\parallel^2} \\ 1 \\ i\frac{n_\perp n_\parallel D}{P(S-n_\parallel^2)} \end{pmatrix};\ \mathbf{E}_S \simeq E_{yS}\begin{pmatrix} -i\frac{P(S-n_\parallel^2)}{DS} \\ 1 \\ i\frac{n_\perp(S-n_\parallel^2)}{Dn_\parallel} \end{pmatrix};\ \mathbf{E}_B \simeq E_{yB}\begin{pmatrix} i\frac{S}{TD} \\ 1 \\ -i\frac{n_\perp n_\parallel}{D} \end{pmatrix}. \tag{2.4.33}$$

The fast wave electric field is elliptically polarized in the x–y plane and has a small component in the $\hat{\mathbf{z}}$ direction. This mode is partly longitudinal and partly transverse as

$$|\hat{\mathbf{n}} \cdot \mathbf{E}|_F \sim |\hat{\mathbf{n}} \times \mathbf{E}|_F. \tag{2.4.34}$$

where $\hat{\mathbf{n}}$ is the unit vector in the direction of $\mathbf{n} \equiv \frac{c}{\omega}\mathbf{k}$. The value of $n_\perp^2$ for the slow wave is large and negative for $\omega \gtrsim \Omega_i$, thus the wave is evanescent (cut–off) in the $\perp$ direction. The electric field has a large E_x component, a somewhat smaller E_z component and a very small E_y component. This mode is also partly longitudinal and partly transverse as can be seen from

$$|\hat{\mathbf{n}} \cdot \mathbf{E}|_S \sim |\hat{\mathbf{n}} \times \mathbf{E}|_S. \tag{2.4.35}$$

The ion Bernstein wave has a large and positive value of $n_\perp^2$ indicating that the wave has a slow phase velocity (compared with the velocity of light c) across the magnetic field. The wave electric field has its largest component in the $\hat{\mathbf{x}}$ direction, a somewhat smaller component in the $\hat{\mathbf{z}}$ direction and a very small electric field along the $\hat{\mathbf{y}}$ direction. The wave is almost entirely longitudinal as can be seen from

$$|\hat{\mathbf{n}} \cdot \mathbf{E}|_B >> |\hat{\mathbf{n}} \times \mathbf{E}|_B. \tag{2.4.36}$$

The wave field and wave vector are nearly parallel and can be simply related as

$$\mathbf{E} \simeq -i\mathbf{k}\phi = -\nabla\phi \tag{2.4.37}$$

which shows that this mode is electrostatic in nature.

The above is only a brief description of the characteristics of the three basic ICRF modes in a warm plasma. The next section focuses on the ion Bernstein wave and discusses its characteristics in greater detail.

2.5: Ion Bernstein Waves

2.5.1: Introduction

As was indicated earlier, the ion Bernstein wave is primarily electrostatic in nature so that

$$|\mathbf{B}^{(1)}| = |\mathbf{n} \times \mathbf{E}^{(1)}| << |\mathbf{E}^{(1)}|. \tag{2.5.1}$$

and the wave magnetic field energy is smaller than the wave electric field energy by a factor of the plasma β_i. Using the electrostatic character of the ion Bernstein wave a simplified dispersion relation can be derived starting from the Vlasov–Maxwell equations. The details of this derivation are given in Ref. 19. Detailed characteristics of the ion Bernstein mode are obtained by studying this dispersion relation numerically and analytically. The remainder of this section will describe the characteristics of the ion Bernstein mode by studying the behavior of the electrostatic dispersion relation.

2.5.2: Electrostatic Dispersion Relation

For an isotropic Maxwellian distribution of velocities the electrostatic dispersion relation can be written as[19]

$$\epsilon(\mathbf{k},\omega) = 1 + \sum_{\alpha} \frac{2\omega_{p\alpha}^2}{k^2 v_{t\alpha}^2} \left[1 + \frac{\omega}{k_{\parallel} v_{t\alpha}} \sum_{n=-\infty}^{\infty} \mathrm{I}_n(b_\alpha) e^{-b_\alpha} Z(\zeta_{n\alpha}) \right] = 0 \qquad (2.5.2)$$

where

$$b_\alpha = \frac{k_\perp^2 v_{t\alpha}^2}{2\Omega_\alpha} \qquad (2.5.3)$$

and the other terms are defined in section 2.3. Equation 2.5.2 is the dispersion relation of magnetized warm electrostatic plasma modes and gives a relation between the frequency ω and wave number $\mathbf{k}$ of the wave. When the frequency ω is near the ion cyclotron frequency, $\epsilon(\mathbf{k},\omega)$ describes electrostatic ion Bernstein modes.

Equation 2.5.2 can be rewritten exactly[19] as

$$\epsilon(\mathbf{k},\omega) = \frac{1}{k^2} \left\{ k_\parallel^2 K_{zz} + k_\perp^2 K_{xx} + 2k_\parallel k_\perp K_{xz} \right\} \qquad (2.5.4)$$

where expressions for K_{zz}, K_{xz}, and K_{xx} have already been given. In terms of S, P, and T, which were given in section 2.4, ϵ is approximated as

$$\epsilon(k_\parallel, k_\perp, \omega) = \frac{1}{k^2} \left\{ k_\parallel^2 P + k_\perp^2 \left(S + n_\perp^2 T \right) \right\} \qquad (2.5.5)$$

where the terms from K_{xz} have been neglected. Setting this to zero (for normal modes) and solving for $n_\perp^2$ gives

$$n_\perp^2 \simeq -\frac{S}{T} + \frac{P}{S} n_\parallel^2. \qquad (2.5.6)$$

This is almost exactly the same result as that obtained from the fully electromagnetic dispersion relation (Eq. 2.4.32). It is expected that both results agree for small $k_\perp \rho_i$ since this is equivalent to $\beta_i \ll 1$ and electromagnetic effects are negligible in this regime. Once again, this dispersion relation is only valid for $|\omega| \lesssim 2\Omega_i$.

2.5.3: Wave Propagation and Wave Damping

Figure 2.1 shows a plot of $\omega/\Omega_{\mathrm{H}}$ vs. $k_\perp \rho_{\mathrm{H}}$ for the electrostatic ion Bernstein wave in a hydrogen plasma. The figure shows that the ion Bernstein wave propagates between integral harmonic bands of the hydrogen ion cyclotron frequency. At the higher

frequency end of each band the mode is cut–off ($k_\perp = 0$) and at the lower frequency end of each band the mode experiences a resonance ($k_\perp \to \infty$) with the hydrogen ions. It is assumed that the applied frequency $f_0 = \omega/2\pi$ is real and any wave damping or growth arises from an imaginary part in $k_\perp$ so that the wave damps or grows spatially. In a collisionless plasma, a finite value of $k_\parallel$ is necessary for $k_\perp$ to acquire a nonzero imaginary part. The effect of increasing $k_\parallel$ is shown in Fig. 2.2 . Each sub–figure shows the ion Bernstein wave dispersion relation in a hydrogen plasma with 1% deuterium ($n_D/n_{(H+D)} = 0.01$). The value of $k_\parallel$ is zero for the first sub–figure and its value is increased in steps until $\omega/k_\parallel v_{te} = 1.5$. Figure 2.3 shows the corresponding value of the perpendicular group velocity $\partial\omega/\partial k_\perp$. As the wave approaches (toward decreasing ω/Ω_H) the location of an hydrogen harmonic, it's perpendicular group velocity decreases. As a result, the wave energy density increases and wave power may be absorbed, transmitted, reflected, or converted to another plasma wave through some linear or nonlinear process. In the region between the dispersion curve ($\epsilon = 0$) and the upper cyclotron harmonic in each band, ϵ is positive. Between the $\epsilon = 0$ curve and the lower harmonic, ϵ is negative. As the value of $k_\parallel$ is increased (and electron shielding becomes important) the entire dispersion curve shifts upward toward the region of $\epsilon > 0$.

Figure 2.4 shows a comparison between the electrostatic and electromagnetic ion Bernstein wave dispersion relations as a function of β_i. The difference is most apparent when β_i exceeds about 0.25 and is seen most significantly in the value of $\mathrm{Im}(k_\perp)$. Above $\beta_i \simeq 0.25$, the electrostatic approximation overestimates the electron Landau damping due to the neglect of important electromagnetic terms in the dispersion relation.

In a low density ($\omega_{pi}^2/\Omega_i^2 \ll 1$), low temperature plasma, the ion Bernstein wave becomes an electron plasma wave[25] with the dispersion relation

$$n_\perp^2 = n_\parallel^2 \frac{\omega_{pe}^2}{\omega^2}. \tag{2.5.7}$$

This dispersion relation is shown graphically in Fig. 2.5 . Near an ion cyclotron harmonic where finite Larmor radius effects are most important, the dispersion curve is unaffected. This shows that the electron plasma wave is insensitive to finite temperature effects.

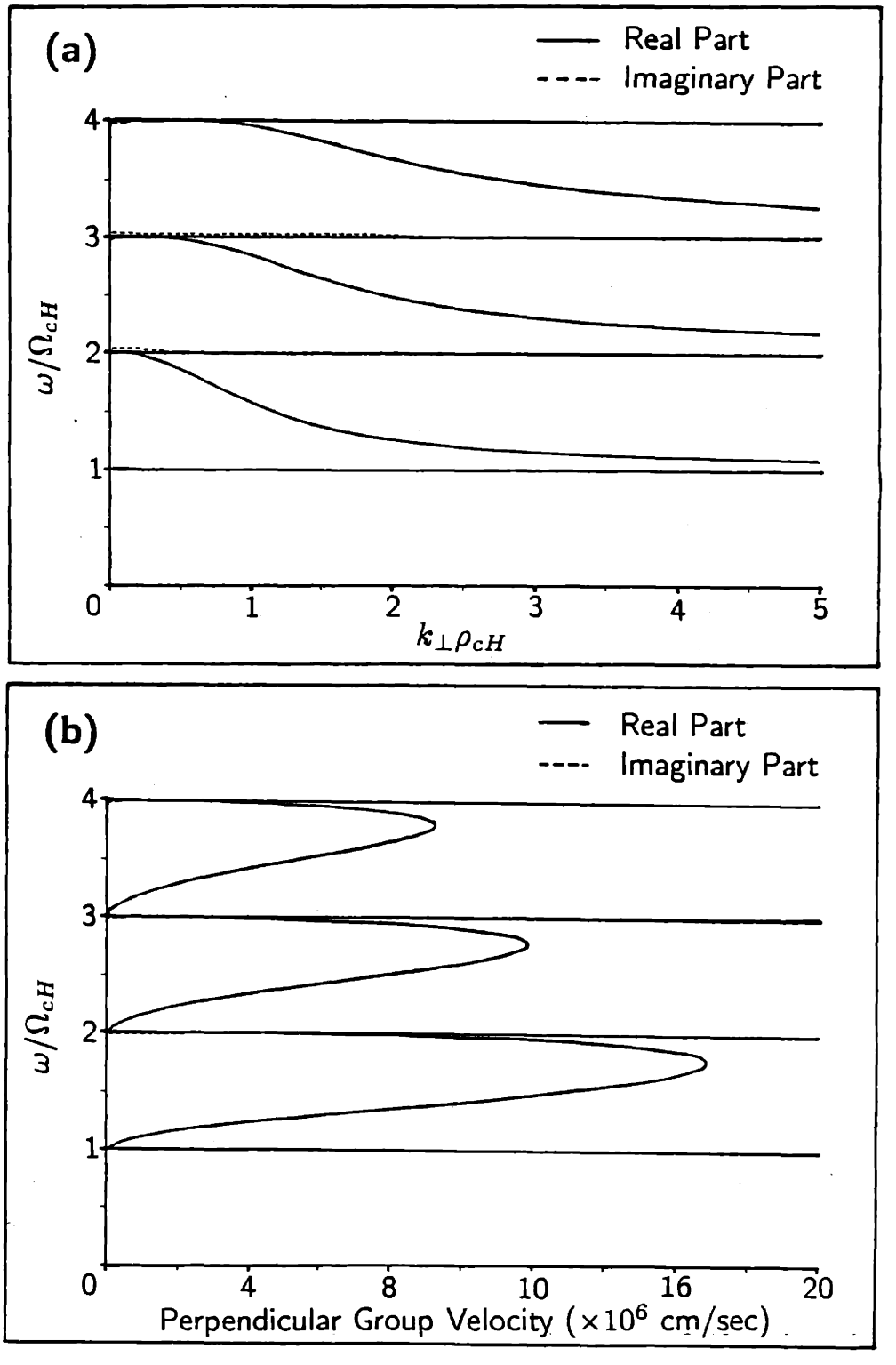

Figure 2.1 —(a) Dispersion relation of the ion Bernstein wave in a hydrogen plasma. (b) Perpendicular group velocity of the ion Bernstein wave. Plasma parameters: $n_e = 2 \times 10^{20}\,\mathrm{m}^{-3}$, $T_H = 900\,\mathrm{eV}$, $T_e = 1600\,\mathrm{eV}$, $f = 183.6 \times 10^6\,\mathrm{s}^{-1}$, $k_\parallel = 0.1\,\mathrm{cm}^{-1}$.

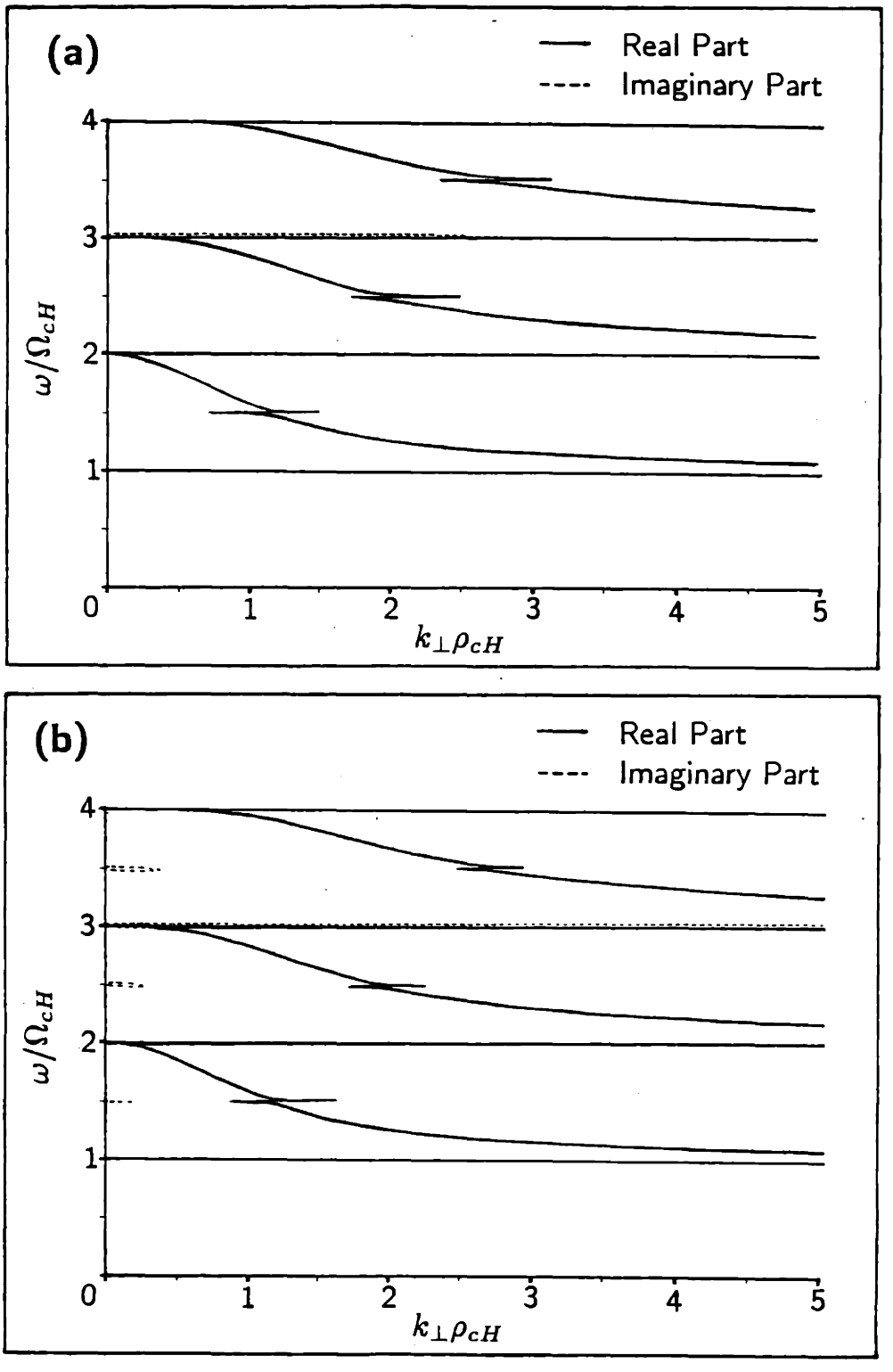

Figure 2.2 —The effect of increasing $k_\parallel$ on the ion Bernstein wave dispersion relation. (a) $k_\parallel = 0$. (b) $k_\parallel = 0.08$. (c) $k_\parallel = 0.16$. (d) $k_\parallel = 0.32$. Plasma parameters: $n_e = 2 \times 10^{20}\,\mathrm{m}^{-3}$, $T_H = 900\,\mathrm{eV}$, $T_e = 1600\,\mathrm{eV}$, $f = 183.6 \times 10^6\,\mathrm{s}^{-1}$, $n_D/n_{H+D} = 0.01$.

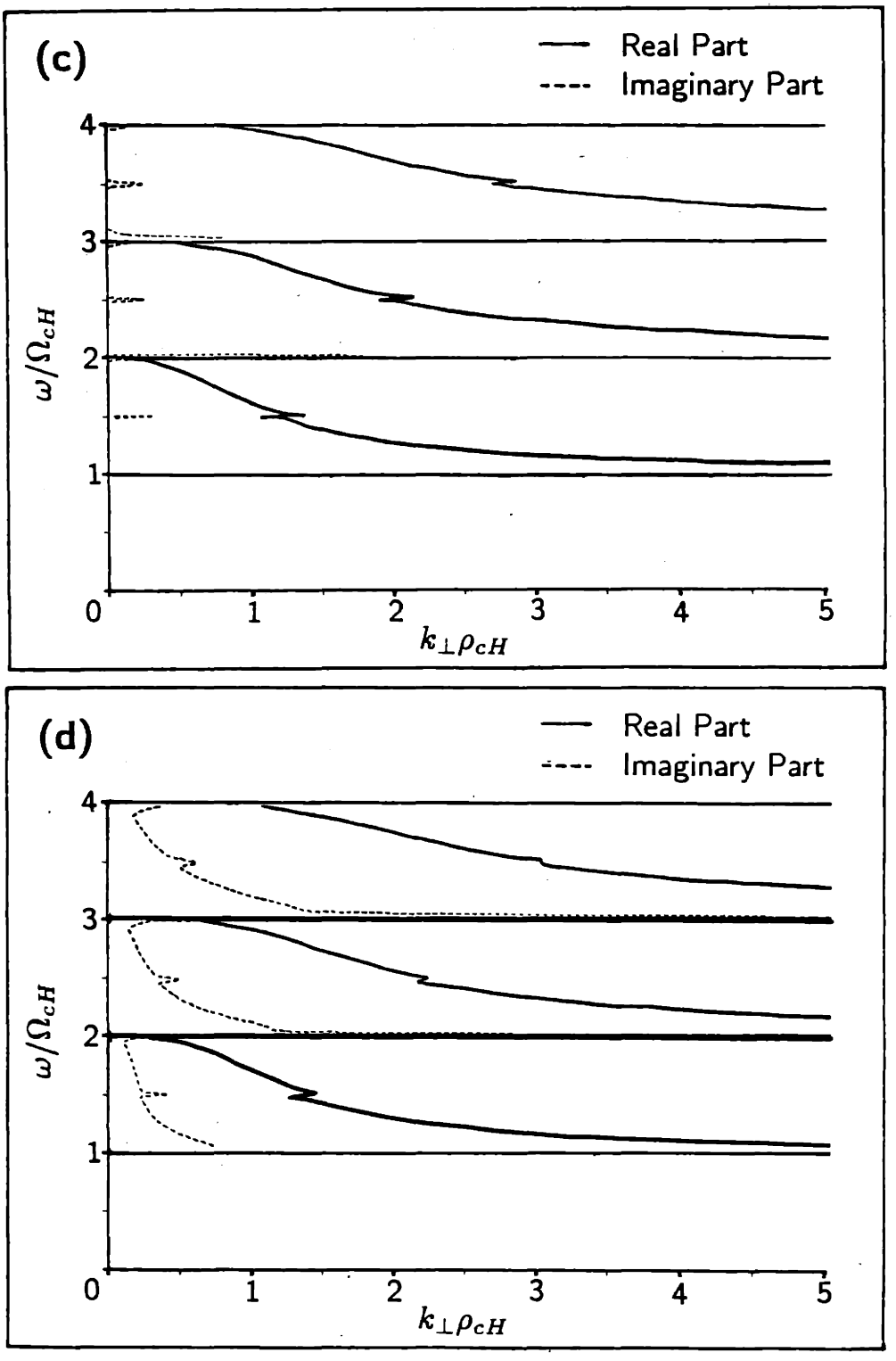
(c)
Real Part
Imaginary Part
ω/Ω_{cH}
$k_\perp \rho_{cH}$
0
1
2
3
4
5
(d)
Real Part
Imaginary Part
ω/Ω_{cH}
$k_\perp \rho_{cH}$
0
1
2
3
4
5

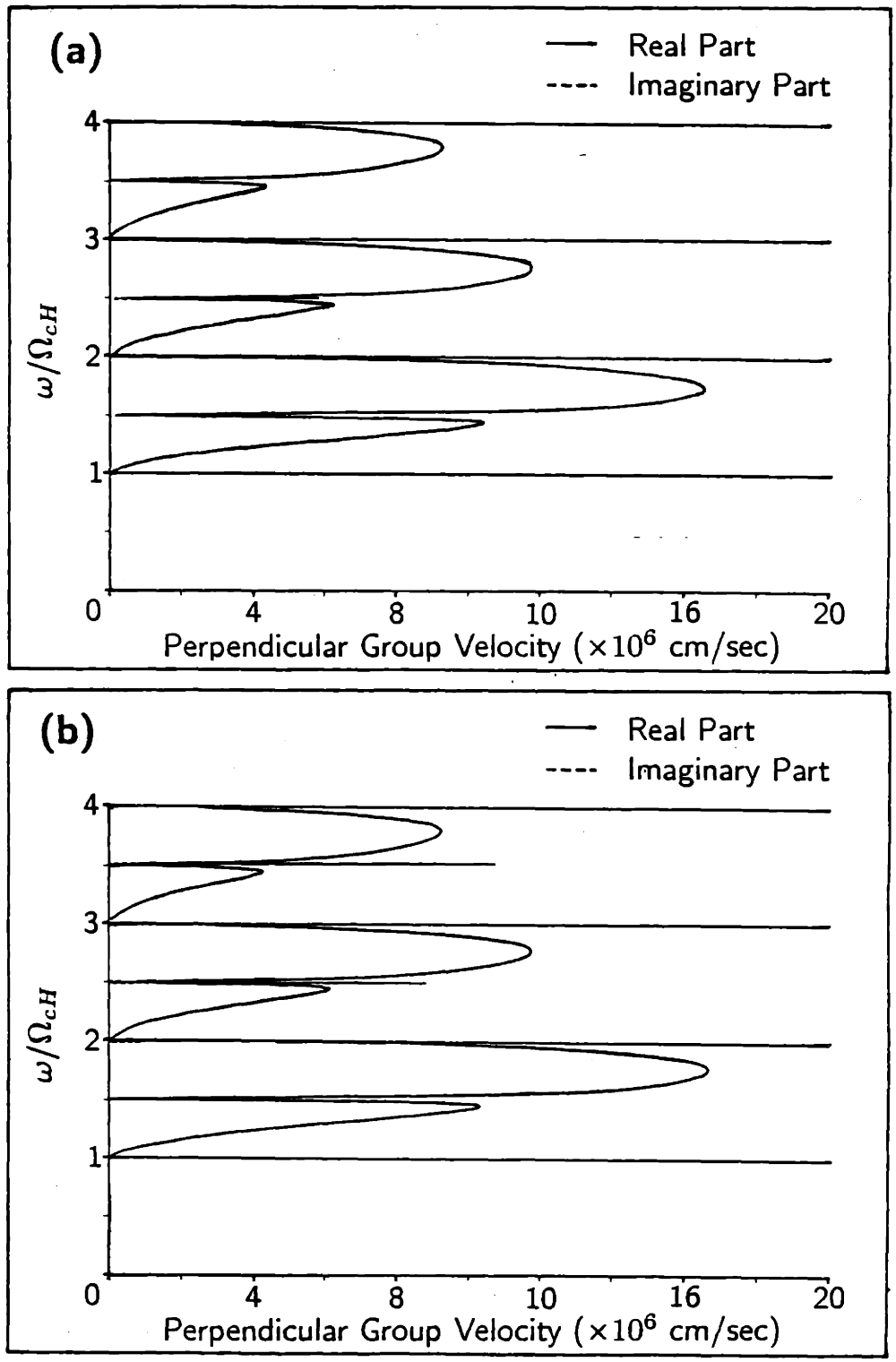

Figure 2.3 —The effect of increasing $k_{\|}$ on the ion Bernstein wave perpendicular group velocity. Plasma parameters are the same as in Fig. 2.2 . (a) $k_{\|} = 0$. (b) $k_{\|} = 0.08$. (c) $k_{\|} = 0.16$. (d) $k_{\|} = 0.32$.

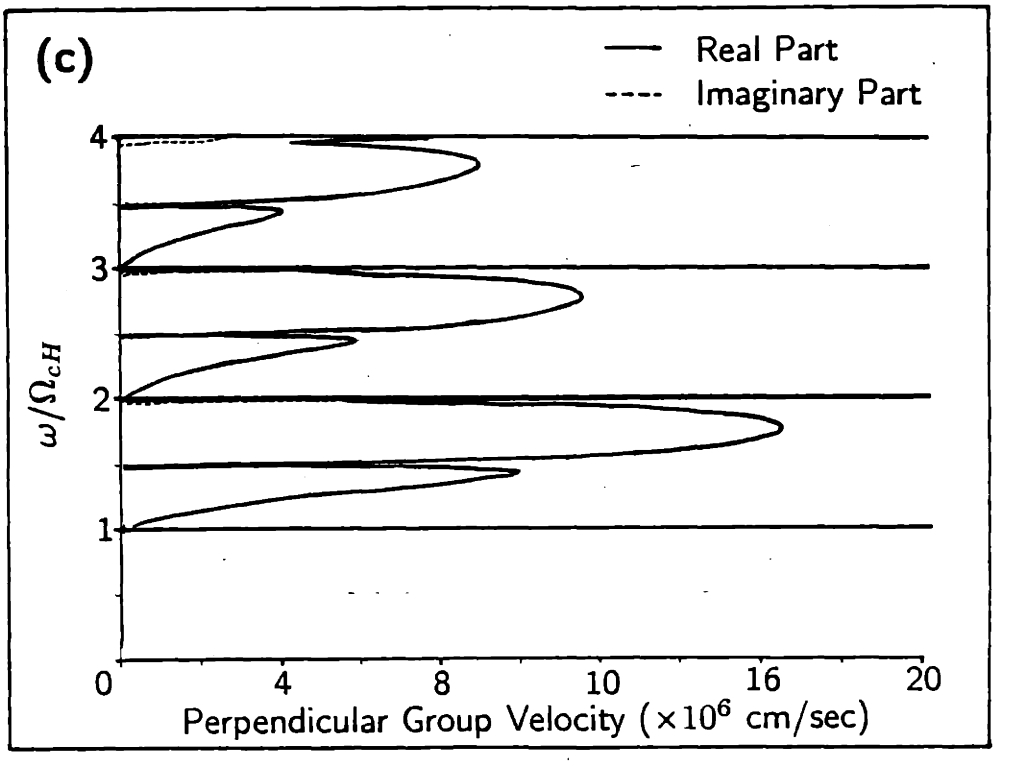
(c)
Real Part
Imaginary Part
4
3
2
1
ω/Ω_{cH}
0
4
8
10
16
20
Perpendicular Group Velocity ($\times 10^6$ cm/sec)

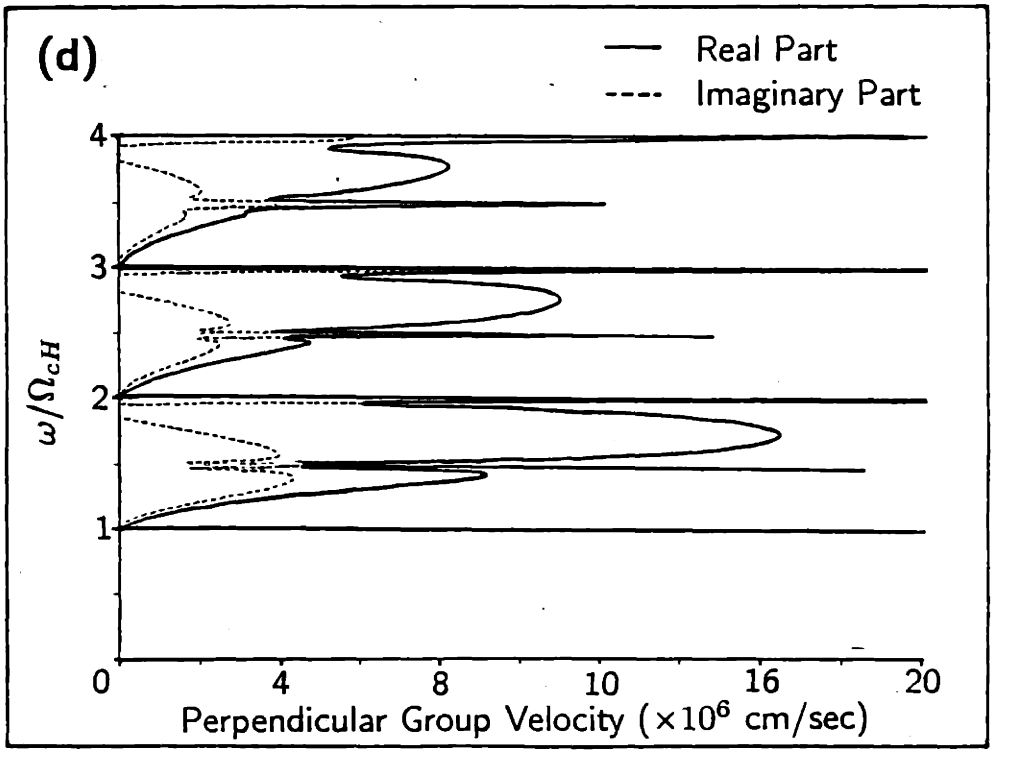
(d)
Real Part
Imaginary Part
4
3
2
1
ω/Ω_{cH}
0
4
8
10
16
20
Perpendicular Group Velocity ($\times 10^6$ cm/sec)

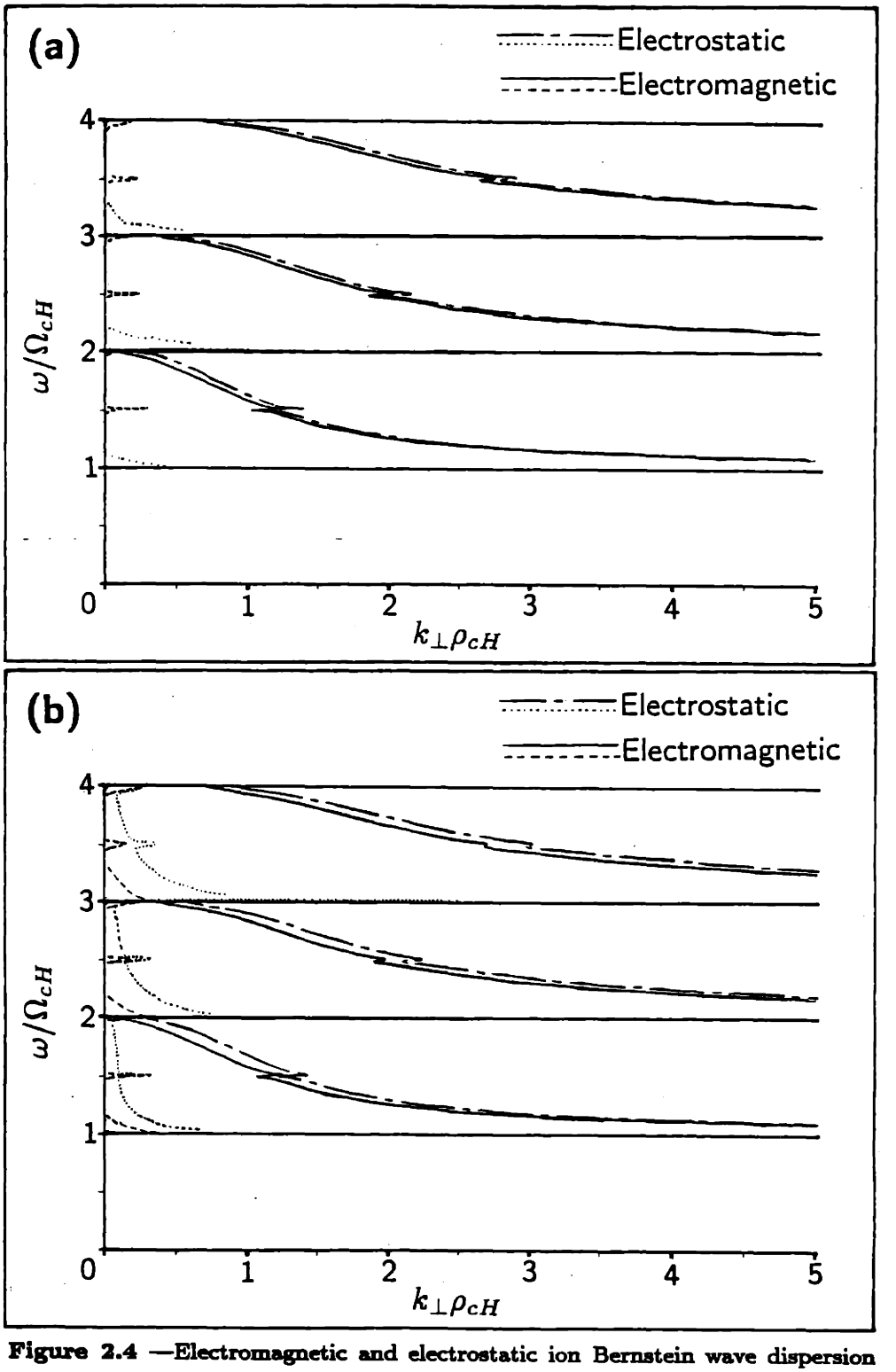

Figure 2.4 —Electromagnetic and electrostatic ion Bernstein wave dispersion relation for several values of β_H. (a) $\beta_H = 0.25$, $T_{H,D} = 900\,eV$, $T_e = 1800\,eV$. (b) $\beta_H = 0.5$, $T_{H,D} = 1800\,eV$, $T_e = 3600\,eV$. (c) $\beta_H = 0.75$, $T_{H,D} = 2700\,eV$, $T_e = 5400\,eV$. (d) $\beta_H = 1$, $T_{H,D} = 3600\,eV$, $T_e = 7200\,eV$. Plasma parameters: $n_e = 7 \times 10^{19}\,m^{-3}$, $f = 30.5 \times 10^6\,s^{-1}$, $k_\parallel = 0.03\,cm^{-1}$.

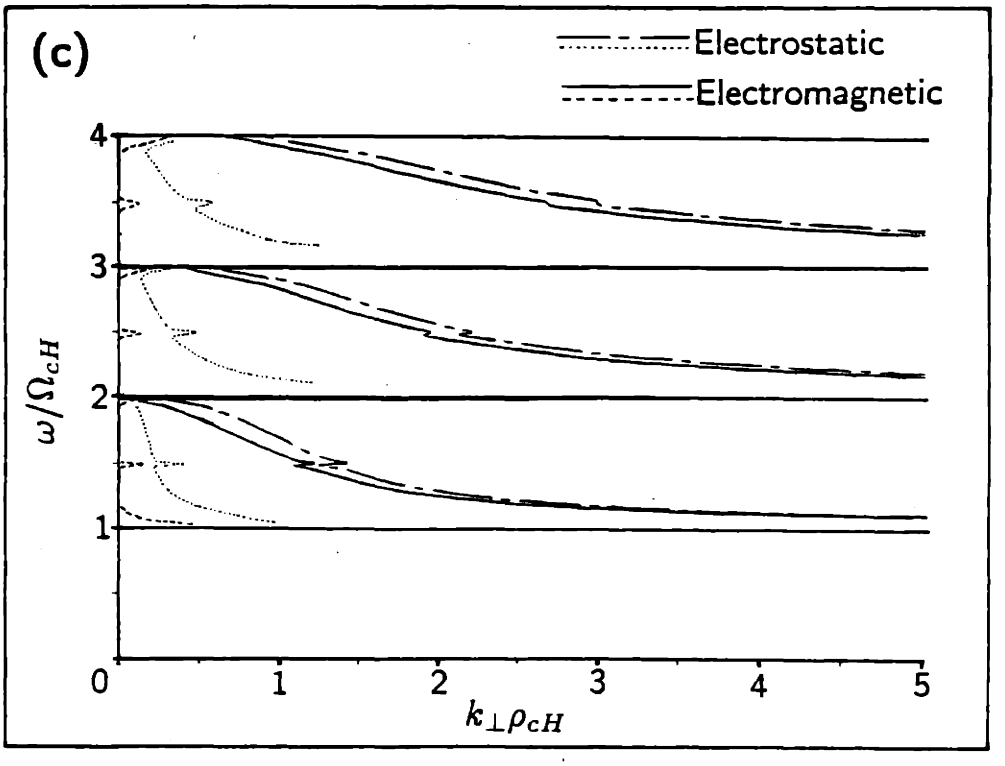
(c)
Electrostatic
Electromagnetic
ω/Ω_{cH}
$k_\perp \rho_{cH}$
0
1
2
3
4
5

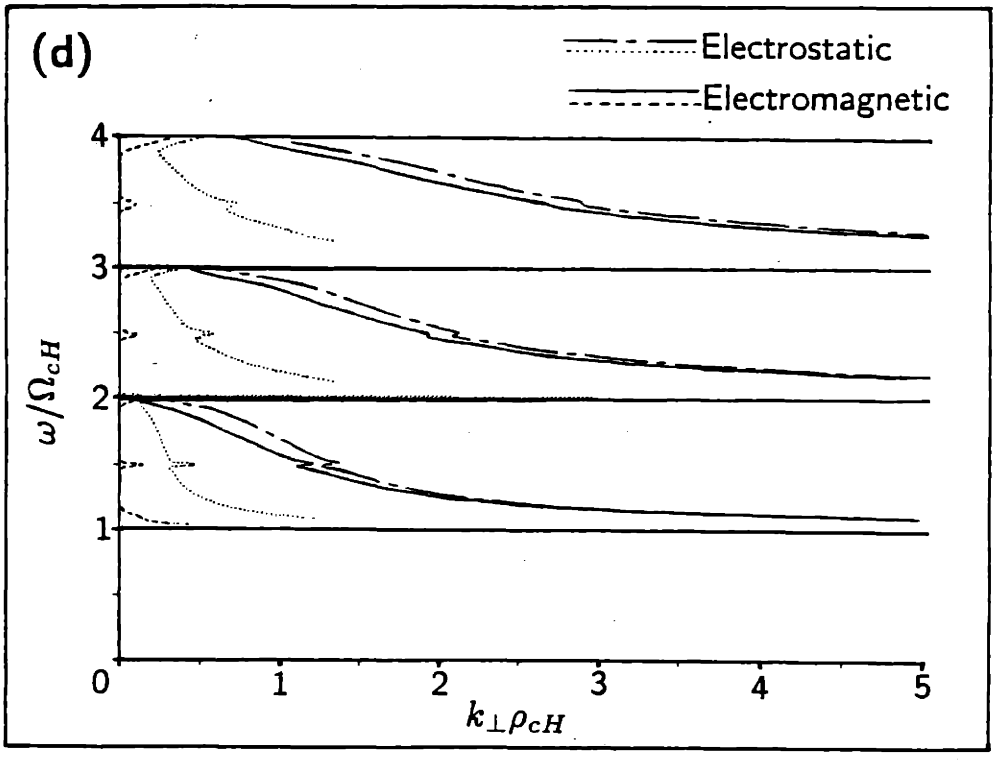
(d)
Electrostatic
Electromagnetic
ω/Ω_{cH}
$k_\perp \rho_{cH}$
0
1
2
3
4
5

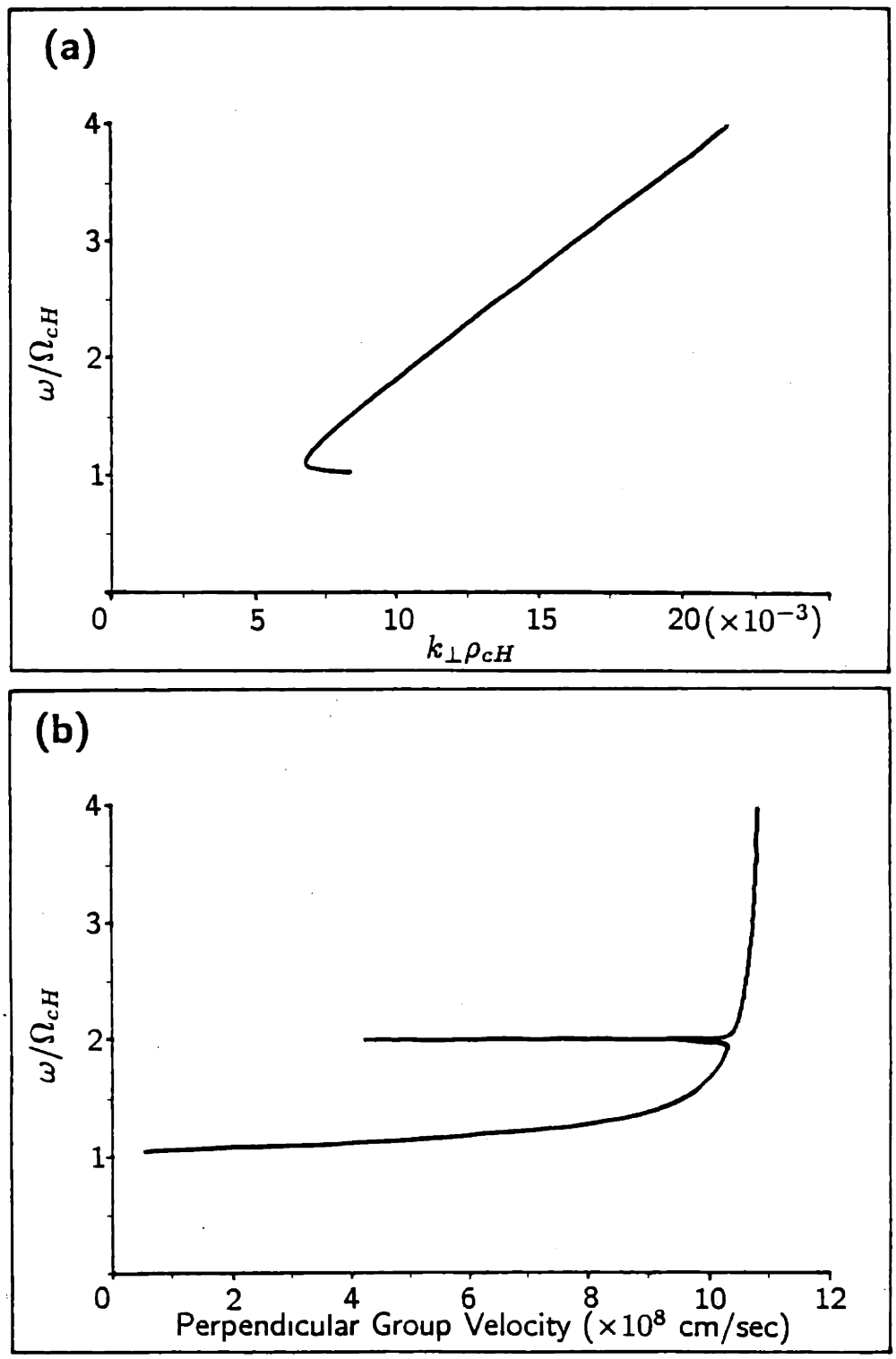

Figure 2.5 —(a) The electron plasma wave dispersion relation and (b) perpendicular group velocity in a pure hydrogen plasma. Plasma parameters: $T_H = 40\,\text{eV}$, $T_e = 40\,\text{eV}$, $n_e = 4 \times 10^{16}\,\text{m}^{-3}$, $f = 183.6 \times 10^6\,\text{s}^{-1}$, $k_\parallel = 0.1\,\text{cm}^{-1}$.

In a high density plasma where $\omega_{pi}/\Omega_i >> 1$ the ion Bernstein dispersion relation is approximated for a single ion species plasma as [26]

$$n_\perp^2 = \frac{1}{T_i}\left[\frac{m_i c^2}{3}\frac{4\Omega_i^2 - \omega^2}{\omega^2}\right] + n_\parallel^2 G(\omega, B) \tag{2.5.8}$$

and $n_\perp^2$ is a linear function of the inverse ion temperature. The function G is only dependent on the frequency ω and the magnetic field B. Typically, the first term on the right of Eq. 2.5.8 is much larger than the second (the second term is ignored in Ref. 26). This result allows the ion Bernstein wave to be used as a temperature diagnostic[26, 27] by relating the measured value of $n_\perp$ to the local ion temperature. If the magnetic field is held constant, changes in T_i can be measured.

If the magnetic field is reduced to zero the ion Bernstein wave becomes a Bohm and Gross wave[28] with the dispersion relation

$$\epsilon(\omega, \mathbf{k}) = 1 - \sum_\alpha \frac{\omega_{p\alpha}^2}{\omega^2}\left[1 + \frac{3}{2}\frac{k^2 v_{t\alpha}^2}{\omega^2}\right]. \tag{2.5.9}$$

This is a similar limit obtained when the frequency ω becomes large compared to the electron cyclotron frequency but not large compared to the electron plasma frequency.

All of the approximations made to the ion Bernstein wave dispersion relation (Eq. 2.5.2) so far assume that both the ions and electrons are in the fluid limit (see subsection 2.4.2). The electrostatic ion cyclotron wave dispersion relation (also called the neutralized ion Bernstein wave) can be obtained by assuming the fluid limit for the ions ($k_\parallel v_{ti}/\omega << 1$) and the isothermal limit ($\omega/k_\parallel v_{te} << 1$) for the electrons. The dispersion relation in this case is written as

$$\epsilon(\omega, \mathbf{k}) = \frac{\omega_{pi}^2}{\omega^2}\left\{-1 + \frac{1}{k^2}\left[\frac{\omega^2}{C_s^2} - k_\perp^2 \frac{\Omega_i^2}{\omega^2 - \Omega_i^2}\right]\right\} \tag{2.5.10}$$

where $C_s^2 = Z_i^2 T_e/m_i$ is the plasma sound speed and Z_i is the atomic charge of the ion species. This mode is only weakly electron and ion Landau damped. This can be understood by noticing that the Landau damping term in Eq. 2.5.2 is proportional to $\zeta_{0\alpha}\exp[-\zeta_{0\alpha}^2]$. This term is linearly small in $\zeta_{0\alpha}$ for $\zeta_{0\alpha} << 1$ and exponentially small in $\zeta_{0\alpha}^2$ for $\zeta_{0\alpha} >> 1$. Thus, for the electron and ion limits assumed, the Landau damping is negligible. It is pointed out that for values of $\zeta_{0\alpha}$ between either the isothermal or fluid limits, $\zeta_{0\alpha}\exp[-\zeta_{0\alpha}^2]$ may no longer be small and Landau damping can become strong.

2.5.4: Linear Wave Damping

Linear ion cyclotron damping and electron Landau damping of ion Bernstein waves is most clearly explained by considering the damping process in an inhomogeneous magnetic field as is the case in a tokamak. In such a geometry, the radial dependence of the magnetic field causes the damping region to be radially localized and separated from undamped regions nearby (such as the wave launching region).

The ion Bernstein mode within an inhomogeneous plasma is properly described with a complicated integral equation. The plasma is inhomogeneous and Fourier and Laplace transforms are not useful in the direction of the inhomogeneity. In spite of this mathematical difficulty, a good approximation to the complete solution can be obtained. The ion Bernstein wave has a perpendicular wave length $\lambda_\perp$ which is typically much smaller than the scale lengths of tokamak plasma parameters, especially within the central plasma, and this justifies application of the WKB approximation[29] to the electric field. Note that the WKB approximation is different than the weakly inhomogeneous approximation which is discussed in the next section. The physical essence of the WKB approximation is that the fractional change in the wave vector $\mathbf{k}$ (due to changes in plasma parameters) over a distance of about one wavelength is small. This is expressed mathematically as

$$\frac{1}{k_j(x_i)} \frac{\partial}{\partial x_i} \ln[k_j(x_i)] \ll 1 \tag{2.5.11}$$

where $i, j = x, y,$ or z. Using the WKB approximation, the spatial dependence of the electric field can be written as

$$\mathbf{E}(x,z) = \mathbf{E}(x_0)\sqrt{\frac{k_\perp(x_0)}{k_\perp(x)}}\, e^{-ik_\parallel z}\, e^{-i\int_{x_0}^{x} k_\perp(x')\,dx'} \tag{2.5.12}$$

where $k_\perp(x)$ is obtained from the local dispersion relation $\epsilon(k_\perp, k_\parallel, \omega, x)$ and all plasma quantities are evaluated at the position x. The WKB approximation given in Eq. 2.5.11 leads to no reflection of power as the ion Bernstein wave propagates through the plasma. A good estimate of local power absorption (for one spectral component) can be made over a region extending from position x_0 to x using this approximation. This is done by calculating the total power in one spectral component as a function of x which is given approximately by

$$P_{\mathbf{k},\omega}(x) \simeq S_{\mathbf{k},\omega}(x)\, A = \frac{\omega}{8\pi} \left|E_{\perp \mathbf{k},\omega}(x)\right|^2 \frac{\partial \epsilon(x)}{\partial k_\perp} A \tag{2.5.13}$$

where $S_{\mathbf{k},\omega}(x)$ is the ion Bernstein wave energy flux and A is the effective area of a wave phase front. Within the WKB approximation, the strongest spatial dependence in Eq. 2.5.13 comes from the term $|E_\perp|^2$ and has the form $\exp[\mathrm{Im}\, k_\perp(x)]$. The spectral power as a function of x can thus be written from Eq. 2.5.13 as

$$P_{\mathbf{k},\omega}(x) = P(x_0)\, e^{-2\int_{x_0}^{x} dx\, \mathrm{Im}[k_\perp(x)]}. \tag{2.5.14}$$

From this, the power transmitted and absorbed is easily obtained. Fig. 2.6 (a) is a plot of $k_\perp^{2/5}$ for the ion Bernstein wave, fast wave, and slow wave as a function of the toroidal major radius for a plasma with 1% deuterium. The value of $k_\perp^2$ is obtained by solving the electromagnetic dispersion relation for an homogeneous plasma at many spatial locations radially across the plasma. The dotted lines correspond to $(\mathrm{Im}\, k_\perp^2)^{1/5}$ and represent spatial damping. Fig. 2.6 (b) is a plot of $P(x)/P(x_0)$ corresponding to Fig. 2.6 (a). This is obtained by evaluating Eq. 2.5.14 for the value of $\mathrm{Im}[k_\perp(x)]$ for the ion Bernstein wave shown in Fig. 2.6 (a). Linear power absorption of ion Bernstein waves due to ion cyclotron damping is very strong even at large ion cyclotron harmonics. Figure 2.7 shows the effect of increasing the deuterium concentration on the ion Bernstein wave ion cyclotron absorption.

Electron Landau damping can be approximated the same way as for ion cyclotron damping (Eq. 2.5.14). Landau damping is typically not as localized as the narrow ion cyclotron absorption region. A more careful and detailed look at power absorption will be given in section 2.7 where ray tracing and the associated change in $k_\parallel$ due to toroidal effects can be incorporated in evaluating the power absorption.

2.5.5: Wave Energy

The energy in the ion Bernstein wave is mainly in the kinetic motion of the ions as they slosh back and forth in the wave potential. This is why the mode is sometimes described as a sound-like mode. This can be seen by examining the terms in the full expression for the $\mathbf{k}$ and ω spectral component of the energy flux of a wave in a dispersive medium[19]

$$\mathbf{S}_{\mathbf{k},\omega} = \frac{c}{8\pi}\mathbf{E}^*_{\mathbf{k},\omega} \times \mathbf{B}_{\mathbf{k},\omega} - \frac{\omega}{8\pi}\mathbf{E}^*_{\mathbf{k},\omega} \cdot \frac{\partial \epsilon(\mathbf{k},\omega)}{\partial \mathbf{k}} \cdot \mathbf{E}_{\mathbf{k},\omega}. \tag{2.5.15}$$

The first term in Eq. 2.5.15 represents wave electromagnetic flux or Poynting flux; the second term represents wave energy in particle motion. A comparison of the magnitude

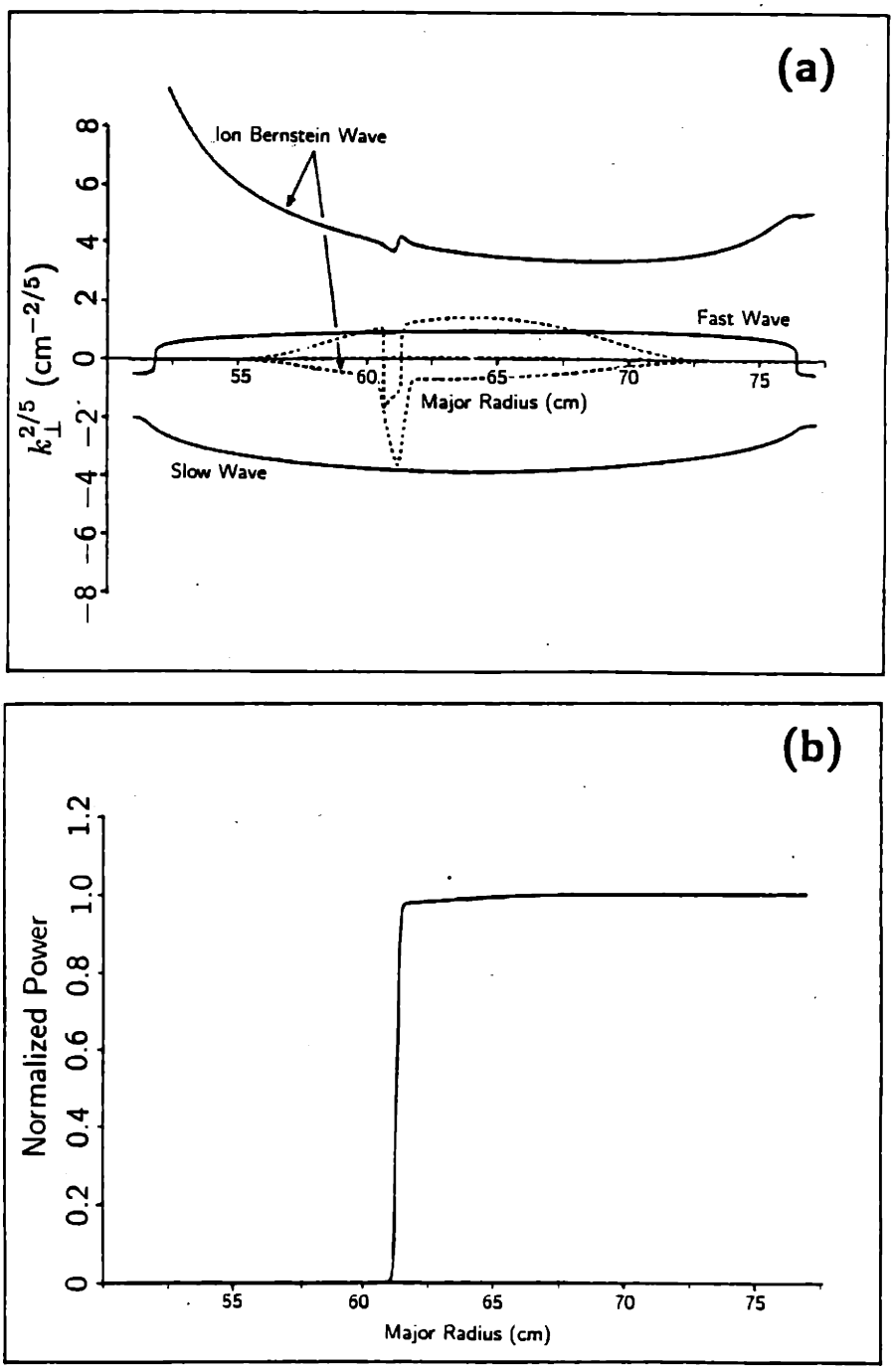

Figure 2.6 —(a) Dispersion relation of ICRF modes in a tokamak plasma. The imaginary part of $k_\perp^{5/2}$ (dotted lines) indicates linear wave damping. (b) Normalized power evaluated from the WKB approximation. Power absorption is due both to electron Landau damping and ion cyclotron damping. Plasma parameters: plasma current = 250 kA, $B_0 = 7.6\,\mathrm{T}$, $f = 183.6 \times 10^6\,\mathrm{s}^{-1}$, $k_\parallel = 0.16\,\mathrm{cm}^{-1}$, $n_{e0} = 2 \times 10^{20}\,\mathrm{m}^{-3}$ (parabolic radial profile), $T_{i0} = 900\,\mathrm{eV}$, $T_{e0} = 1600\,\mathrm{eV}$ (both T_i and T_e have parabolic radial profiles).

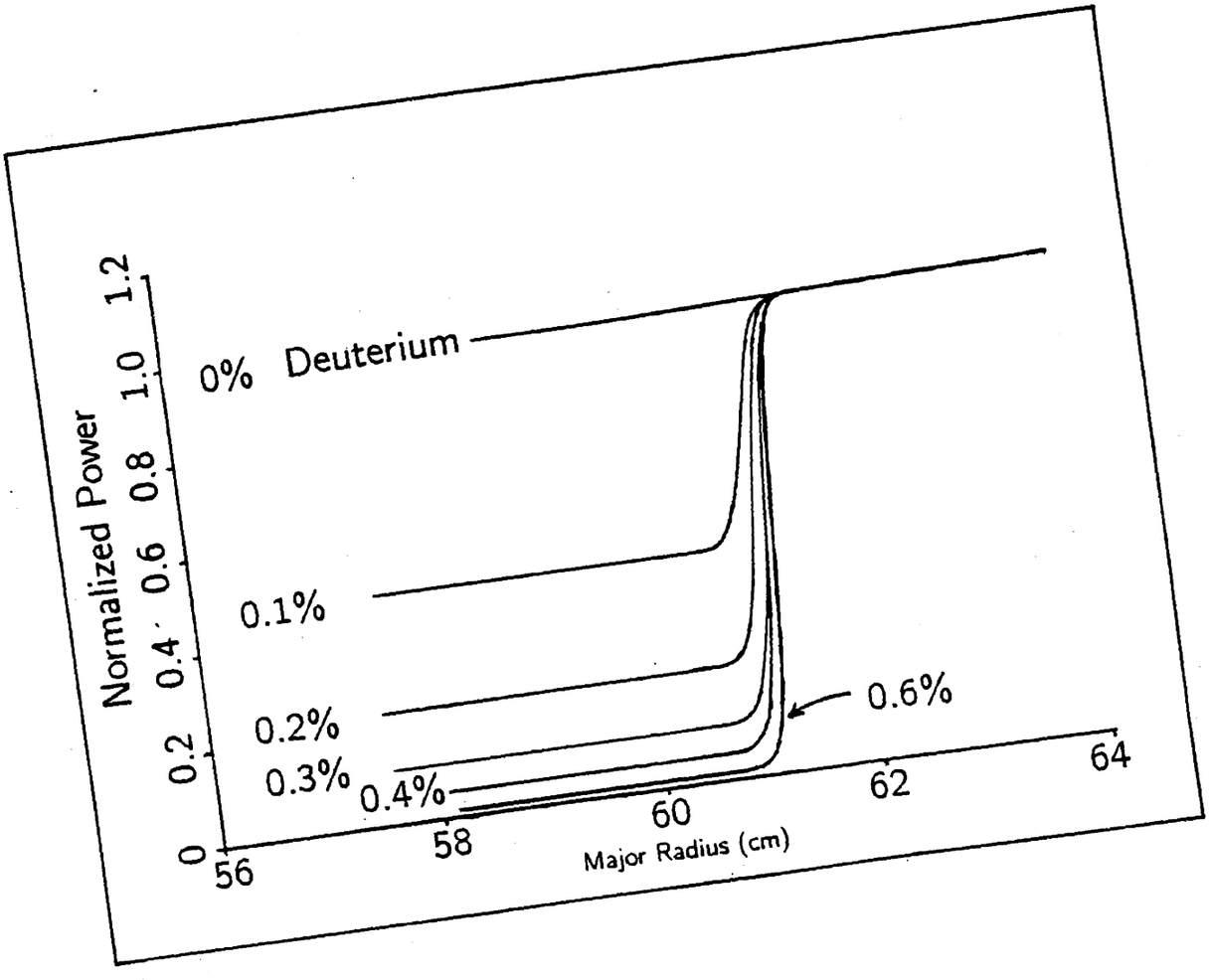

Figure 2.7 —Linear absorption of ion Bernstein wave power in a tokamak plasma for various deuterium concentrations. Plasma parameters are the same as in Fig. 2.6 .

of these two terms for the ion Bernstein wave can be made as follows. Using the Faraday law and the approximation to the ion Bernstein wave polarization from Eq. 2.4.32, the electromagnetic term can be written as

$$\mathbf{E}^*_{\mathbf{k},\omega} \times \mathbf{B}_{\mathbf{k},\omega} = 2|E_y|^2 \frac{n_\perp^2}{D^2} n_\parallel \mathbf{n}. \tag{2.5.16}$$

Using the approximation to K_{xx} (Eq. 2.4.6), the plasma term can be written as

$$\mathbf{E}^*_{\mathbf{k},\omega} \cdot \frac{\partial \epsilon(\mathbf{k},\omega)}{\partial \mathbf{k}} \cdot \mathbf{E}_{\mathbf{k},\omega} = -2n_\perp \frac{c}{\omega} |E_y|^2 \frac{S n_\perp^2}{D^2} \hat{x}. \tag{2.5.17}$$

An approximate expression for $\mathbf{S}_{\mathbf{k},\omega}$ for the ion Bernstein wave is now

$$\mathbf{S}_{\mathbf{k},\omega} \simeq 2\frac{c}{8\pi} |E_y|^2 \frac{n_\perp^2}{D^2} n_\perp \left[n_\parallel^2 + S \right] \hat{x}. \tag{2.5.18}$$

The ratio of electromagnetic energy to plasma kinetic energy is approximately $n_\parallel^2/S$. Typically, this ratio is small compared to unity and the kinetic term dominates over the electromagnetic term.

Another characteristic of the ion Bernstein wave is that it is a backward wave in the direction perpendicular to the background magnetic field. This means that the perpendicular phase velocity and group velocity are antiparallel. This is easy to see graphically by examining a plot of the dispersion relation such as in Fig. 2.1 . The perpendicular phase velocity of a wave described by a point on the $\epsilon = 0$ curve (ω is chosen not to be close to a cyclotron harmonic) is proportional to the slope of a line connecting that point and the origin. Analytically, this is written as

$$\hat{x} \cdot \mathbf{v}_{ph} = \frac{\omega}{k_\perp} \hat{x}. \tag{2.5.19}$$

The perpendicular group velocity is proportional to the slope of a line which is tangent to the $\epsilon = 0$ curve and runs through the point corresponding to the wave. Analytically, this is approximated from Eq. 2.4.32 as

$$\begin{aligned} \hat{x} \cdot \mathbf{v}_g &= \frac{\partial \omega}{\partial k_\perp} \\ &\simeq \frac{2\omega}{k_\perp} \left[2 + \frac{\omega}{S}\frac{\partial S}{\partial \omega} - \frac{\omega}{T}\frac{\partial T}{\partial \omega} \right]^{-1} \qquad (2.5.20) \\ &\simeq -\frac{\omega}{k_\perp} \left[\frac{4\Omega_i^2}{\omega^2} - 1 \right] \qquad (2.5.21). \end{aligned}$$

The term inside the square braces is positive definite for $\omega < 2\Omega_i$ therefore it is clear that $\mathbf{v}_{ph\perp} \cdot \mathbf{v}_{g\perp} < 0$ indicating that the wave is indeed backward.

It is often convenient, when considering a wave packet trajectory, to calculate the ratio of the perpendicular and parallel group velocities and to define this ratio to be the tangent of an angle θ, thus

$$\tan\theta = \frac{v_{g\perp}}{v_{g\parallel}}. \tag{2.5.22}$$

This can be approximated as

$$\tan\theta \simeq -\frac{S}{P}\frac{k_\perp}{k_\parallel}. \tag{2.5.23}$$

It is easy to see that the propagation angle is a function of $k_\parallel$ (unlike lower hybrid waves).

2.5.6: Inhomogeneous Plasma

A self–consistent analysis of wave propagation and damping in an inhomogeneous plasma is very important in understanding and interpreting plasma heating and confinement experiments which use radio frequency power. The analysis should include the excitation of plasma modes by an antenna structure, the propagation of these modes through an inhomogeneous and dispersive medium, and the resulting power deposition due to Landau damping, cyclotron damping, or collisional damping. Such analysis predicts quantitatively the antenna–plasma coupling and the radial power deposition. Antenna coupling information is useful for designing an antenna which preferentially excites one mode and couples power to the plasma efficiently. The information regarding power deposition is essential for studying the time evolution of particle distributions as well as the evolution of the macroscopic plasma parameters such as the temperature.

As stated earlier, the correct description of modes in an inhomogeneous plasma is given by a complicated integral equation. However, assuming that the plasma is weakly inhomogeneous allows one to develop a tractable model for this problem. Physically, the meaning of weakly inhomogeneous is that the fractional change in the magnitude $|Q|$ of a plasma quantity Q over one Larmor radius is small compared to unity. Mathematically, this condition is expressed as

$$\rho_i \left| \frac{\nabla|Q|}{|Q|} \right| = \frac{\rho_i}{l_s} \ll 1 \tag{2.5.24}$$

where ρ_i is the Larmor radius of the ion and l_s is the scale length of the inhomogeneity. This permits the dielectric tensor (as well as the Vlasov equation) to be expanded in a

Taylor series with the expansion parameter $k_\perp \rho_i$. In the case of ion Bernstein waves, the electric field is usually the quantity which exhibits the largest fractional change over one Larmor radius. The reader is referred to references 13, 24, 30, 31, 32, 33, 34, and references therin, for further details of applying this approximation to the problem of waves in an inhomogeneous plasma. The weakly inhomogeneous approximation is usually not as strict as the WKB approximation except in regions where $k_\perp \rho_i$ is close to unity.

The general characteristics of ion Bernstein waves in a weakly inhomogeneous plasma are nearly the same as in an homogeneous plasma because the wavelength of the wave is very short compared to the typical scale length of a plasma inhomogeneity. For example, the mode is still sound–like, is primarily longitudinal, and is damped linearly at cyclotron harmonics. One new feature that the inhomogeneous plasma modification describes is the mode conversion of the ion Bernstein wave to a fast wave and vice–versa. The inhomogeneous plasma model also gives a more quantitative result to the coupling, propagation, and linear absorption problem.

The remaining part of this section will briefly outline some of the current models used to describe inhomogeneous plasmas and will mention some of the features of these models.

2.5.7: Weakly Inhomogeneous Plasma Models

Sy *et al.*[24] suggest a completely analytical model which describes the problem of a current sheet in a vacuum exciting waves in a slab plasma. The only inhomogeneous region in this model is the transition from vacuum to plasma which is treated as a step discontinuity. Coupling to the fast, slow, and ion Bernstein modes is calculated. The dielectric tensor element K_{xx} retains the only finite Larmor radius effect. The main physics involved in this model lies in formulating one additional boundary condition required at the vacuum–plasma interface. There are three outward propagating modes in the plasma which must match onto two modes in the vacuum, thus five boundary conditions are required. Four of these conditions come from the usual continuity of the tangential electromagnetic field quantities. The details of the fifth boundary condition (the x derivative of E_x at the vacuum–plasma interface) are not clearly explained. According to the authors, however, it can be derived by integrating the wave equation across the vacuum–plasma boundary. This apparently involves the assumption of a certain value for the dielectric tensor on the vacuum–plasma boundary. Enforcing mathematical consistency to the resulting equation produces the required boundary condition. This additional boundary condition seems to reflect more of the particular choice of boundary discontinuity than of the actual physics of the problem. The inconsistency of this model is that the additional boundary condition is derived from a wave

equation which assumes a weakly inhomogeneous plasma; yet, the boundary condition is derived at a severe discontinuity. In spite of this inconsistency, the model predicts general characteristics of antenna loading which agree qualitatively with experiment. This result suggests that this simple analytical model may contain much of the essential physics of the antenna–plasma coupling problem. However, the model is not reliable and may only give correct results within a limited regime of plasma parameters.

Fukuyama, Itoh, and Itoh[30,31] have formulated a generalization of the Sy *et al.* model. In their model, the plasma is stratified into many homogeneous slabs with discontinuous plasma parameters from one slab to the next. The wave boundary conditions between slabs can also be obtained, according to the authors, by integrating the wave equation across a slab boundary. This is a similar but more general approach as was taken in the Sy *et al.* model. Although this model may be an improvement to the single slab plasma in the Sy *et al.* model, the boundary conditions between slabs are derived from a wave equation which assumes a weakly inhomogeneous plasma and this again is inconsistent with the severe discontinuity between slabs. This model also predicts antenna loading and plasma electric fields which have the general characteristics of the experimentally observed values.

Skiff[13] describes a model for waves in an inhomogeneous plasma which consists of a self–adjoint wave equation. The self–adjoint property is imposed to uniquely determine the procedure for expanding the dielectric in terms of the operator $\rho_i \frac{\partial}{\partial x}$. The plasma spatial dependence is arbitrary except that all profiles must be continuous and must satisfy the weakly inhomogeneous criterion. Boundary conditions are obtained from the Maxwell equations except where these conditions would predict unobserved behavior. In this case, modified boundary conditions are used which predict the observed behavior. The solution for the electric field spatial dependence is obtained by numerically integrating the wave equation through the inhomogeneity and imposing the boundary conditions. As a result of the self–adjoint property of the wave equation this model does not include wave damping . The lack of wave damping is not severe and generally can be approximated rather well by imposing an outward radiation condition on any wave power which reaches the absorption region. The Skiff model shows quite good agreement with the measured loading from an ion Bernstein wave antenna in the ACT–I torus at Princeton (see Ref. 13).

2.6: Description of the Brambilla Coupling Model

2.6.1: Introduction

Brambilla[35] has developed a coupling model and a computer code implementing the model which quite successfully calculates the antenna plasma loading for the ion Bernstein wave experiments on Alcator C. Because of its availability and reliability, the Brambilla code was used to model and study the antenna–plasma coupling characteristics of the Alcator C ion Bernstein wave antenna. It is not necessary to describe the Brambilla model in great detail here since this is done in Ref. 35. The following discussion however, will outline some of the important physical features of the model and will mention some of the numerical procedures used in the computer code.

2.6.2: Physical Features of the Coupling Model

The toroidal geometry is approximated by a slab model where the coordinates (x, y, z) correspond to the radial, poloidal, and toroidal directions, respectively. Curvature and shear of the magnetic field lines are neglected. The plasma parameters are assumed to vary only in the x direction and the static magnetic field is in the z direction. The wave field is decomposed along y and z (ignorable coordinates) as a double Fourier sum. The toroidal and poloidal wavenumbers $n_z = ck_z/\omega$ and $n_y = ck_y/\omega$ are discretized as in the equivalent toroidal problem:

$$n_z = \frac{c}{\omega R_T} n_\phi \tag{2.6.1}$$

$$n_y = \frac{c}{\omega a} m_\theta \tag{2.6.2}$$

where n_ϕ and m_θ are integers and R_T and a are the major and minor radius of the plasma, respectively. Figure 2.8 shows the antenna and plasma geometry used in the model. The spatial profiles in the main plasma region and scrape–off region can be arbitrarily specified. The direction of antenna current and Faraday shield are also arbitrary. The current in the antenna is assumed known† and the vacuum solution (the solution within the region between the plasma and the antenna back plane) is expressed in terms of the plasma surface impedance matrix. This matrix expresses the linear relation between the electric and magnetic field components at the plasma

† Because the current is assumed known, the field solution is obtained in a non–selfconsistent manner.

surface. Thus,

$$E_y(0) = Z_{11}B_z(0) + Z_{12}B_y(0) \tag{2.6.3}$$

$$E_z(0) = Z_{21}B_z(0) + Z_{22}B_y(0) \tag{2.6.4}$$

All quantities in Eqs. 2.6.3 and 2.6.4 are functions of n_z and n_y and (0) indicates evaluation at the plasma–vacuum interface. The surface impedance matrix elements Z_{ij} contain all of the physics of wave propagation through the inhomogeneous plasma and are obtained by solving the wave equation in the plasma.

The wave equation used in the Brambilla model includes electron Landau damping, ion cyclotron damping, and a form of collisional damping. The equation, which is formally sixth order in $\partial/\partial x$, is solved twice (with two linearly independent initial conditions) to give two independent solutions. A linear combination of these solutions is then constructed to satisfy the boundary condition far away from the antenna (radiation condition or reflecting wall). The method of solving the wave equation uses a finite element discretization with cubic Hermite interpolating functions. Numerically, this method can be more accurate than a multistep method (for example, a Runge–Kutta method). An additional advantage of this method is that the energy equation is automatically satisfied to a high accuracy. The details of this method are given by Brambilla in Ref. 36.

The model predicts the fraction of power coupled into both the ion Bernstein wave and the fast wave; the slow wave is cut–off for the cases of interest. The power which is electron Landau damped, collisionally damped, or ion cyclotron damped is also calculated. Typically, the fraction of power coupled into the fast wave is not more than 10–20% and depends on the magnetic field at the antenna. On one hand, for the case of optimal ion Bernstein wave coupling ($\omega/\Omega_i \simeq 1.95$) the fast wave power fraction is small ($< 20\%$). On the other hand, for the case of poor coupling ($\omega/\Omega_i \gtrsim 2.1$) the fast wave power fraction can reach values as high as 90%. More details of the coupling measurements and interpretation of the code results will be given later in Chapter 5.

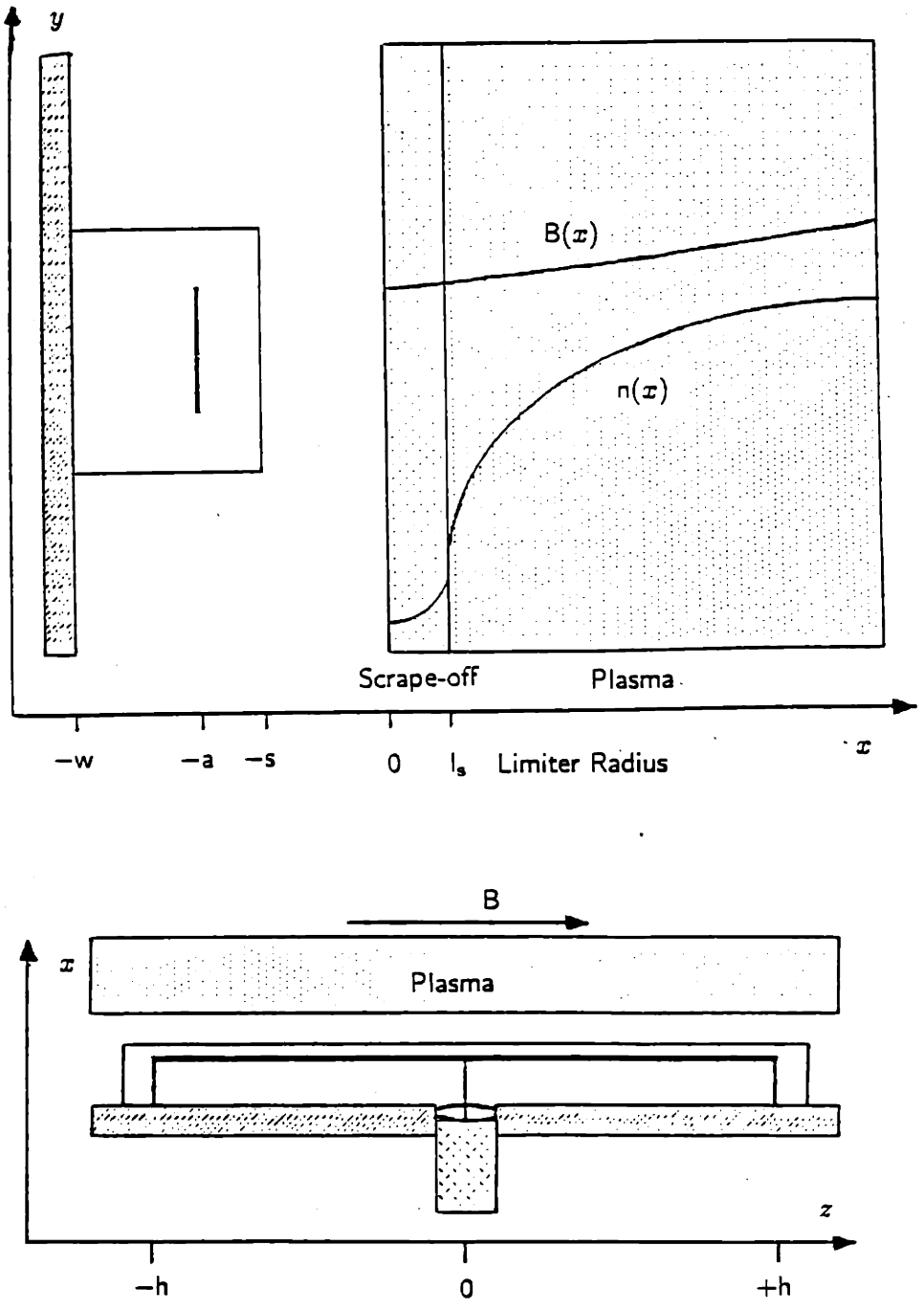

Figure 2.8 —Antenna–plasma geometry used in the Brambilla model. From M. Brambilla (Ref. 36).

2.7: Ray Propagation and Damping

2.7.1: Introduction

The ideal way to obtain the power deposition profile of radio frequency power absorption in a toroidal plasma is to solve for the exact electromagnetic fields within the entire torus. Power deposition is then easily calculated from the energy equation[37]

$$\frac{\partial W}{\partial t} + \nabla \cdot \mathbf{S} = -\mathbf{J} \cdot \mathbf{E}. \tag{2.7.1}$$

The term on the right is the total power density absorbed by the plasma, W is the instantaneous stored energy in the electric and magnetic field, and $\mathbf{S}$ is the Poynting vector.

Solving the Maxwell equations in a hot, inhomogeneous, magnetized, and toroidal plasma is a complicated problem and only simplifications to the full problem have been solved. In the case of ion Bernstein wave heating, the wavelength is relatively short in the perpendicular direction (direction across the magnetic field) thus, ray tracing techniques, which rely on the validity of the WKB approximation, can be used to predict power flow and absorption in the bulk plasma. The following section is a discussion of the model used to calculate ion Bernstein wave ray tracing and power absorption in Alcator C.

2.7.2: Theory of Ray Tracing

The theory of ray tracing and power absorption has been discussed previously by several authors [19, 38, 39]. Numerous authors [40, 41, 42, 43, 44] have studied wave properties in a plasma using ray tracing codes which numerically implement the theory. The following discussion will review some of the important results of toroidal ray tracing, making use of the formalism of the previous authors and noting specific application to Alcator C where possible.

Figure 2.9 shows the geometry in which the ray tracing equations are expressed. A point in the plasma is specified by the three coordinates ρ, θ, and ϕ. At this same location, the ion Bernstein wave vector $\mathbf{k}$ is expressed in terms of the conjugate momentum coordinates k_ρ, m, and n where

$$k_\rho = \mathbf{k} \cdot \hat{\rho}; \qquad m = \rho \mathbf{k} \cdot \hat{\theta}; \qquad n = R\mathbf{k} \cdot \hat{\phi} \tag{2.7.2}$$

and $R = R_0 + \rho\cos\theta$ (see Fig. 2.9). The wave vector can now be written as

$$\mathbf{k} = k_\rho\hat{\rho} + \frac{m}{\rho}\hat{\theta} + \frac{n}{R}\hat{\phi}. \tag{2.7.3}$$

The WKB approximation allows the dispersion relation to be expressed in the homogeneous form and evaluated with the local values of the plasma parameters. In the same spirit of this approximation, a coordinate system is constructed at each point along the ray so that the local magnetic field direction is along the $\hat{z}$ (or parallel $\|$) direction. The $\hat{x}$ axis is then positioned along the component of the wave vector perpendicular to $\hat{z}$ (this defines the perpendicular $\perp$ direction). The components of the wave vector $\mathbf{k}$ are then given as

$$\mathbf{k}_\|(k_\rho, m, n) = \frac{\mathbf{k}\cdot\mathbf{B}}{B^2}\mathbf{B} \tag{2.7.4}$$

$$\mathbf{k}_\perp(k_\rho, m, n) = \mathbf{k} - \mathbf{k}_\| \tag{2.7.5}$$

and all points along the ray trajectory satisfy

$$D(\rho, \theta, \phi, k_\perp, k_\|, \omega) = 0 \tag{2.7.6}$$

where D represents the dielectric function or dispersion relation. It has been shown previously[38] that the function D has the property of a Hamiltonian describing the trajectory of the ray in ρ, θ, and ϕ space with momenta k_ρ, m, and n. The equations of motion for the ray are

$$\frac{\partial D}{\partial \rho}\Big/\frac{\partial D}{\partial \omega} = \frac{\partial k_\rho}{\partial t} \tag{2.7.7}$$

$$\frac{\partial D}{\partial \theta}\Big/\frac{\partial D}{\partial \omega} = \frac{\partial m}{\partial t} \tag{2.7.8}$$

$$\frac{\partial D}{\partial \phi}\Big/\frac{\partial D}{\partial \omega} = \frac{\partial n}{\partial t} \tag{2.7.9}$$

$$\frac{\partial D}{\partial k_\rho}\Big/\frac{\partial D}{\partial \omega} = -\frac{\partial \rho}{\partial t} \tag{2.7.10}$$

$$\frac{\partial D}{\partial m}\Big/\frac{\partial D}{\partial \omega} = -\frac{\partial \theta}{\partial t} \tag{2.7.11}$$

$$\frac{\partial D}{\partial n}\Big/\frac{\partial D}{\partial \omega} = -\frac{\partial \phi}{\partial t} \tag{2.7.12}$$

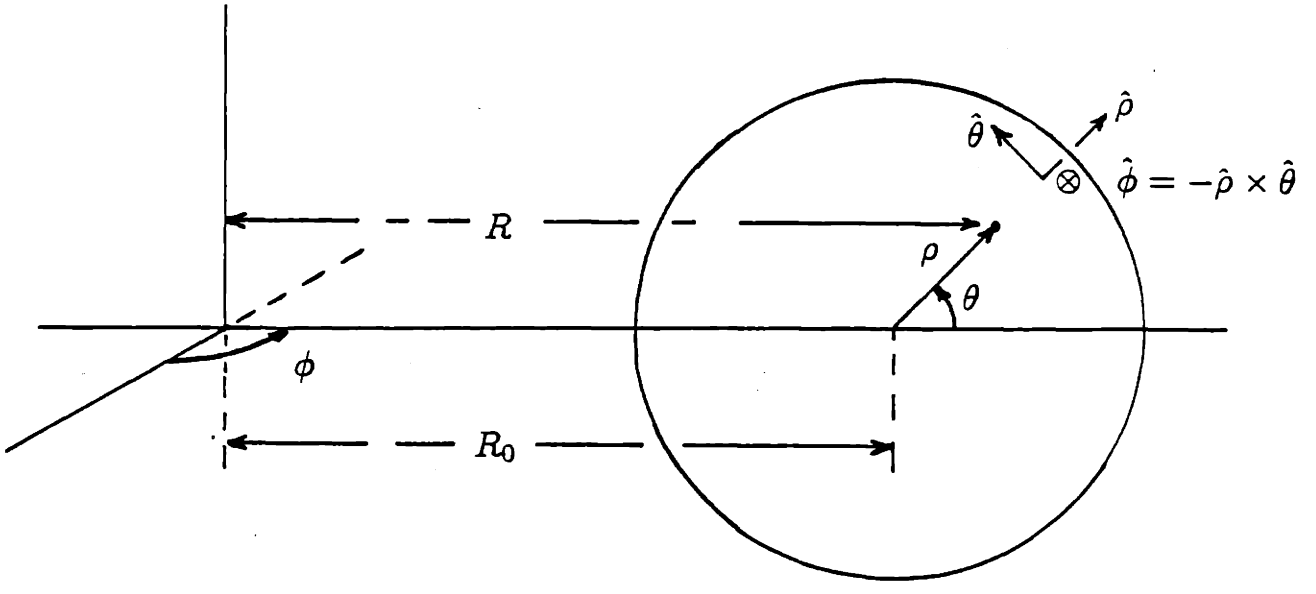

Figure 2.9 —Tokamak geometry used for ray tracing.

It is now assumed that the plasma has no explicit dependence on ϕ (neglect toroidal field ripple) and that there is no radial component of the magnetic field (neglect equilibrium Shafranov shift and assume concentric circular flux surfaces). As a result, the toroidal momentum n is a constant of the motion and the magnetic field can be written as

$$\mathbf{B} = B_\phi \hat{\phi} + B_\theta \hat{\theta}. \tag{2.7.13}$$

The explicit expressions for $k_\parallel$ and $k_\perp$ are now

$$\begin{aligned} k_\parallel &= (k_\theta B_\theta + k_\phi B_\phi)\big/|B| \\ &= \frac{1}{|B|}\left[\frac{mB_\theta}{\rho} + \frac{nB_\phi}{R}\right] \end{aligned} \tag{2.7.14}$$

$$k_\perp = \left[k_\rho^2 + \left(\frac{m}{\rho}\right)^2 + \left(\frac{n}{R}\right)^2 - k_\parallel^2\right]^{1/2}. \tag{2.7.15}$$

Using these equations, the k_ρ, m, and n derivative operators in Eqs. 2.7.7–12 can be cast into the following form

$$\frac{\partial}{\partial k_\rho} = 2k_\rho \frac{\partial}{\partial k_\perp} \tag{2.7.16}$$

$$\frac{\partial}{\partial m} = \frac{2}{\rho}\left(\frac{m}{\rho}\right)\frac{\partial}{\partial k_\perp} + \frac{1}{\rho}\frac{B_\theta}{|B|}\frac{\partial}{\partial k_\parallel} \tag{2.7.17}$$

$$\frac{\partial}{\partial n} = \frac{2}{R}\left(\frac{n}{R}\right)\frac{\partial}{\partial k_\perp} + \frac{1}{R}\frac{B_\phi}{|B|}\frac{\partial}{\partial k_\parallel}. \tag{2.7.18}$$

This form is preferable since D is expressed as a function of $k_\perp$ and $k_\parallel$ and now the momentum derivatives are also expressed in terms of $k_\perp$ and $k_\parallel$. The next step is to carry out all the necessary derivatives of the dispersion relation and obtain analytic forms of the ray equations. The equations used for Alcator C ion Bernstein wave ray tracing were derived assuming an isotropic Maxwellian distribution function with an MHD equilibrium having no Shafranov shift and concentric circular flux surfaces.

The solution to the ray equations is generally best obtained by numerical methods. The equations are numerically integrated forward in time after specifying the initial conditions. The six ray equations are first order ordinary equations and in principle, it is necessary to specify the six starting values of the ray position and momentum. Since the initial conditions must also satisfy the dispersion relation, only five initial conditions can be freely chosen. Usually, these are the three space coordinates and two

components of **k**. The launching structure typically determines k_θ and k_ϕ; k_ρ is then calculated by solving $D = 0$.

The ray equations are integrated numerically using the algorithm described in Ref. 45. This is a variable order and completely variable step size version of the Adams formulas[45, 46] in a predictor corrector combination. The accuracy of the integration can be estimated by calculating the variation of $D(\mathbf{x}, \mathbf{k}, \omega)$ from zero, normalized to the largest term in $D(\mathbf{x}, \mathbf{k}_0, \omega_0)$ (where $\mathbf{k}_0$ and ω_0 satisfy the dispersion relation exactly). Typically, this variation is found to be $\lesssim 10^{-3}$. Figure 2.10 shows the toroidal and poloidal projection of the ray trajectories of a bundle of ion Bernstein wave rays which are launched from the low field side of the tokamak. To understand the spatial trajectory of a single ray, it is helpful to write out the velocity components of the ray. These are as follows:

$$v_\rho = -2k_\rho v_{g\perp}; \qquad v_\theta = -\frac{B_\theta}{|B|}v_{g\|} - 2k_\theta v_{g\perp}; \qquad v_\phi = -\frac{B_\phi}{|B|}v_{g\|} - 2k_\phi v_{g\perp} \quad (2.7.19)$$

where $v_{g\perp}$ and $v_{g\|}$ are the perpendicular and parallel group velocities, respectively. At the plasma edge where the density and temperature are low, the parallel group velocity dominates over the perpendicular velocity so it is easy to see that the ray begins to propagate along the magnetic field line. The ratio of v_ϕ to v_θ is just B_ϕ/B_θ. The parallel group velocity is a function of $k_\|$ and in exceptional cases, for $k_\|$ very small, the ray may propagate radially. As the ray propagates along the field line, the magnetic field increases and the poloidal mode number m changes in a way which decreases the magnitude of $k_\|$. When m achieves a value of $-nq$ where q is the local toroidal safety factor

$$q = \frac{\rho B_\phi}{R B_\theta} \quad (2.7.20)$$

$k_\|$=0 and the group velocity in the $\|$ direction becomes zero. As a result, the ray reflects toroidally; m continues to change, $k_\|$ reverses sign, and the ray begins to propagate toroidally in the reverse direction. The change in θ momentum m is driven by the θ derivative of D. Since the only θ dependence in D is of the form $\rho\cos\theta$, the rate of change of m can be simply expressed as

$$\frac{\partial m}{\partial t} \propto \frac{\partial D}{\partial(\rho\cos\theta)}\rho\sin\theta. \quad (2.7.21)$$

and m is stationary when the ray crosses the $\theta = 0$ plane. At $\theta = 0$, m achieves its largest magnitude and then begins to decrease bringing $k_\|$ toward zero for another

toroidal reflection. Roughly speaking, the ion Bernstein wave ray bounces back and forth toroidally as it propagates radially into the plasma.

It is a bit worrisome that $k_{\|}$ becomes zero at the toroidal bounce points. This means that the parallel wavelength increases to ∞ and the WKB approximation may not be valid here. In theory, this is true and ray tracing is not completely valid for the ion Bernstein wave. An exact wave solution is required to estimate how far beyond the WKB bounce point the ray might tunnel† . The edge region presents another location where ion Bernstein wave ray tracing is not entirely justified. Here the scale length of the plasma parameters is small and the WKB method is not a good approximation. This difficulty is overcome in the Brambilla code by treating the edge region with a full wave analysis. The full wave solution gives the relative magnitude of the spectral components of the wave entering the plasma. The ray tracing method can then be used to accurately propagate these spectral components into the inner plasma.

2.7.3: Linear Power Absorption

Following the discussion of Brambilla[47] the toroidally averaged power transport equation is given as

$$\frac{dP_\tau(k_z)}{dt} = -\frac{d\sigma}{dt}\frac{\mathbf{e}^*_{\mathbf{k},\omega}\cdot\epsilon^A(\mathbf{k},\omega)\cdot\mathbf{e}_{\mathbf{k},\omega}}{\frac{cK}{\omega}(\nu\cdot\mathbf{T}_{\mathbf{k},\omega})}P_\tau(k_z) \tag{2.7.22}$$

Here, ϵ^A is the antihermitian part of the dielectric tensor

$$\epsilon^A \equiv \frac{1}{2}\left[\epsilon - \epsilon^\dagger\right] \tag{2.7.23}$$

$\mathbf{e}_{\mathbf{k},\omega}$ is the unit electric field polarization vector, $K = (k_\rho^2 + k_\theta^2)^{1/2}$, and $\mathbf{T}_{\mathbf{k},\omega}$, ν, and $d\sigma/dt$ are defined as

$$\mathbf{T}_{\mathbf{k},\omega} \equiv \frac{c}{\omega}\left[\mathbf{k} - \mathbf{e}^*_{\mathbf{k},\omega}(\mathbf{k}\cdot\mathbf{e}_{\mathbf{k},\omega})\right] - \frac{\omega}{c}\mathbf{e}^*_{\mathbf{k},\omega}\cdot\frac{\partial\epsilon^H}{\partial\mathbf{k}}\cdot\mathbf{e}_{\mathbf{k},\omega} \tag{2.7.24}$$

$$\nu \equiv \left(k_\rho\,\hat{\rho} + \frac{m_\theta}{\rho}\,\hat{\theta}\right) \Big/ \left[k_\rho^2 + \left(\frac{m_\theta}{\rho}\right)^2\right] \tag{2.7.25}$$

† The scale length of the plasma parameters along the parallel direction is on the order of the tokamak major radius (for q on the order of unity) and tunneling may be small in this case. If this is true, ray tracing (and the WKB approximation) may still be approximately valid even at the toroidal bounce points.

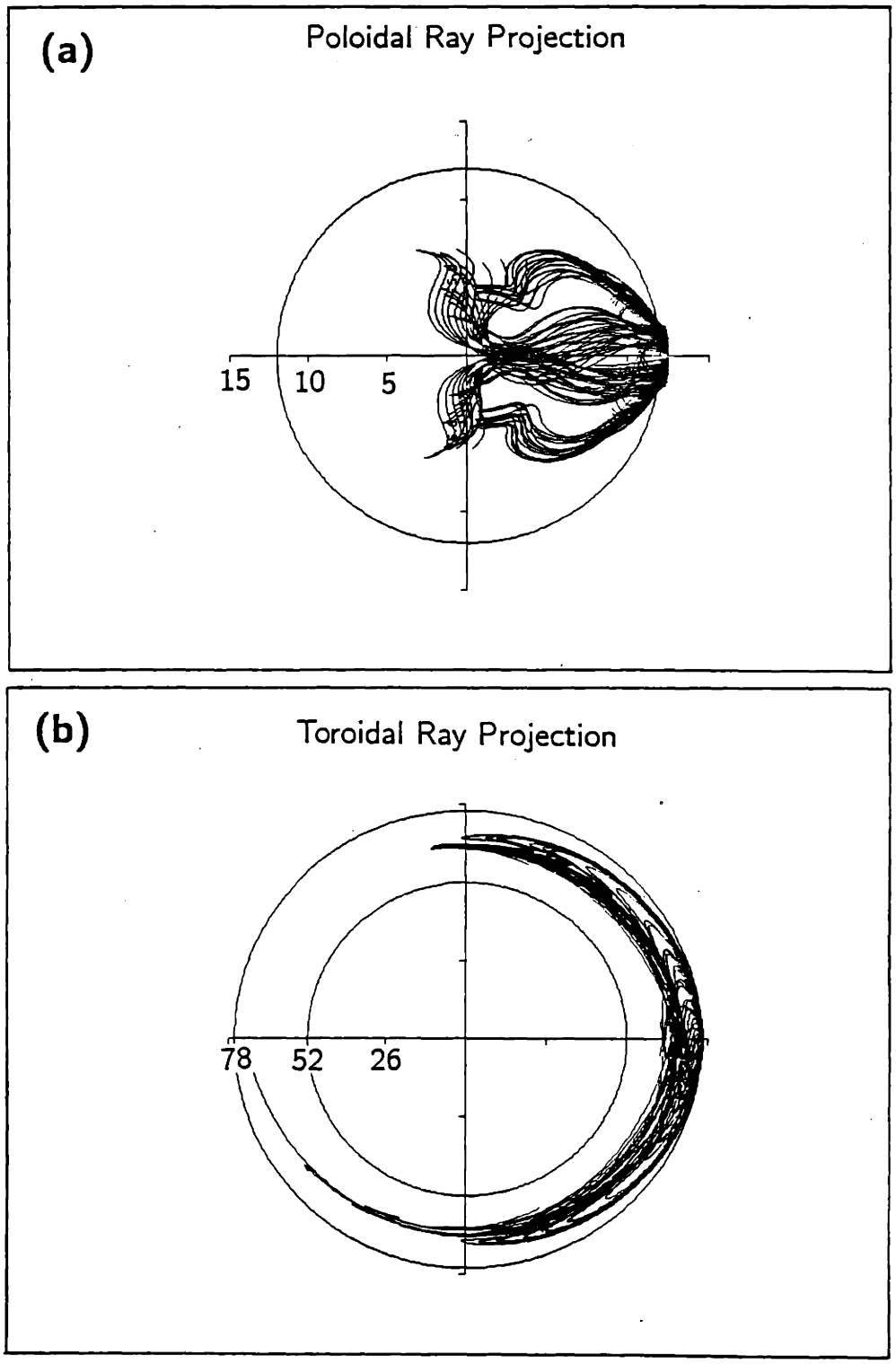

Figure 2.10 —Ion Bernstein wave ray trajectories. (a) Poloidal projection. (b) Toroidal projection. The numbers indicate the major or minor radial locations in centimeters. Plasma parameters: $B_0 = 7.6\,\mathrm{T}$, $n_0 = 2.25 \times 10^{20}\,\mathrm{m}^{-3}$, $T_\mathrm{H} = 900\,\mathrm{eV}$, $T_e = 1600\,\mathrm{eV}$, plasma current $= 250\,\mathrm{kA}$.

$$\frac{d\sigma}{dt} \equiv -\left(k_\rho \frac{\partial H}{\partial k_\rho} + m_\theta \frac{\partial H}{\partial m_\theta}\right) \Big/ \frac{\partial H}{\partial \omega} \tag{2.7.26}$$

and

$$H \equiv \mathbf{e}^*_{\mathbf{k},\omega} \cdot \epsilon^H \cdot \mathbf{e}_{\mathbf{k},\omega} \tag{2.7.27}$$

where ϵ^H is the hermitian part of the dielectric tensor

$$\epsilon^H \equiv \frac{1}{2}\left[\epsilon + \epsilon^\dagger\right]. \tag{2.7.28}$$

The numerator in Eq. 2.7.22 is proportional to the local damping decrement and the denominator is proportional to the projection of the direction of power flow onto the normal to the phase front. This calculates the effective surface area across which the power flows.

It was shown earlier (subsection 2.5.4) that for the ion Bernstein wave, power absorption can be estimated by a simple WKB model. A more accurate power absorption calculation can be obtained by solving the power transport equation (Eq. 2.7.22) with the ray equations. This procedure allows the value of $k_\parallel$ to change as the ray propagates into the plasma center. The local value of $k_\parallel$ can then be used to calculate the damping of the wave power along the ray trajectory. Usually, the radial width of significant power absorption is small (for ion cyclotron absorption) and $k_\parallel$ doesn't change much within this region. However, the ray equations are necessary to determine the value of $k_\parallel$ at the time the ray reaches the absorption layer and this value can be significantly different than the initial $k_\parallel$. The complete absorption calculation is done as follows. A coupling model is first used to determine the power coupled into the plasma as a function of k_ϕ and k_θ. This result is referred to as the k_ϕ, k_θ power spectrum. Then the power spectrum is discretized and a large number of rays are selected so that each ray represents the average k_ϕ, k_θ, and power associated with a discrete portion of the spectrum. Finally, the ray trajectories as well as the power deposition is calculated. A check on the accuracy can be made by increasing the number of rays which are traced and checking the constancy of the power deposition.

The power deposited in the plasma is now known as a function of radius. It is not important to keep information regarding the poloidal and toroidal dependence of absorbed power since it is assumed that the transport of energy in these coordinates is fast compared to transport of energy in the radial direction. Thus, the energy can be averaged poloidally and toroidally. The important physics lies in the radial power deposition and its effect on radial energy and particle transport.

Now that ion Bernstein wave power deposition can be calculated, it is important to consider the potentially detrimental effect of impurities on ion Bernstein wave power

absorption. The plasma generally has very low concentrations $n_{imp}/n_e < 0.01$ of carbon, oxygen, molybdenum, iron, cobalt and other non–hydrogen elements generally referred to as impurities. It is possible that a particular cyclotron harmonic of one of the ionization states of an impurity will be resonant with the ion Bernstein wave power somewhere between the antenna and the region of intended power absorption. This situation is detrimental if impurity power absorption occurs in the outer radial portion of the plasma. In this case, any power absorbed by the impurity is essentially lost (*i.e.*, it is not important to the main plasma power balance). Impurity power absorption can occur for the following condition

$$\left.\frac{\omega}{\Omega_H}\right|_2 < \frac{Z_I}{A_I} m < \left.\frac{\omega}{\Omega_H}\right|_1 \tag{2.7.29}$$

where $\left.\frac{\omega}{\Omega_H}\right|_{1,2}$ is the value of $\frac{\omega}{\Omega_H}$ at the launch point (1) or the intended absorption point (2) (it is assumed that $R_1 > R_2$); Z_I is the impurity charge and depends on the ionization state; A_I is the impurity atomic mass number; and m is an integer which indicates the resonant cyclotron harmonic of the impurity. Figure 2.11 is a summary of the ion Bernstein wave power absorbed in one pass due to linear impurity absorption. The magnetic field geometry is shown in Fig. 4.9 (b). Each impurity is assumed to have an unusually high spatially uniform concentration of $n_{imp}/n_e = 0.01$. This concentration is an higher upper bound. It is clear from the figure that all of the impurities absorb only a very small fraction of the total power and therefore neither influence the total power balance nor affect the ion Bernstein wave propagation. The point corresponding to $4N^{+6}$ is an extreme case due to the small value of $k_{||}$ (the power spectrum contains very little power at this small value of $k_{||}$). Some impurities not shown in the figure such as molybdenum and other ionization states of iron and chromium have fractional power absorption less than 10^{-5}. As was mentioned earlier, a small part of the power coupled into the plasma with the ion Bernstein wave antenna is in the form of the fast wave. Due to warm plasma effects the fast wave can also be absorbed on the impurities. A calculation of this absorbed power shows that it is negligible compared to the power which is absorbed from the ion Bernstein wave. This result can be understood by recalling that fast wave harmonic absorption at harmonic m †, unlike ion Bernstein

† The ion cyclotron harmonic is defined here as the number m where $m = \omega/\Omega_i$. Therefore $\omega = \Omega_i$ denotes the first harmonic or fundamental ion cyclotron resonance. The alternative definition, not used here, defines $\omega = 2\Omega_i$ as the first ion cyclotron harmonic.

wave absorption, is proportional to $(k_\perp \rho_i)^{2(m-1)}$ (where $k_\perp \rho_i << 1$)[48] and absorption on impurities usually occurs at high harmonics $m \gtrsim 3$.

The conclusions reached at this point concerning ray propagation and power absorption are as follows. Ion Bernstein wave ray trajectories begin by following the magnetic field lines at the plasma edge while slowly moving radially into the plasma. The magnitude of $k_\parallel$ decreases initially and may oscillate around the value of zero. Each time the value of $k_\parallel$ becomes zero the ray reaches a toroidal bounce point where it reflects toroidally. As the ray bounces toroidally it propagates into the plasma center. Linear power absorption is accurately evaluated by calculating the local value of $k_\parallel$ in the absorption region. This calculation is done by solving the ray equations together with the power transport equation. Linear absorption due to impurities is negligible and power absorption due to low harmonics of hydrogen or deuterium is very strong.

2.8: Nonlinear Power Absorption

2.8.1: Introduction

The linear theory of plasma waves is obtained by assuming that the ratio of wave energy density to plasma kinetic energy density is small. When this condition is violated, higher order terms in the perturbation expansion of the Maxwell–Vlasov equations become important. Keeping these higher order terms in the wave theory gives rise to various nonlinear plasma wave effects. One obvious region where nonlinear effects might be important in a tokamak for ion Bernstein waves as well as other waves is at the plasma edge near the coupling structure. Here, the energy density of the antenna fields is high and the plasma thermal energy density is low. Another potential region of nonlinear effects, particularly for the ion Bernstein wave, is near an harmonic of a plasma ion species. Here, if the ion species has a large enough concentration, the ion Bernstein wave group velocity decreases significantly as ω/Ω_i approaches (from larger values of ω/Ω_i) the harmonic number. This causes the wave power to pile up, increasing the energy density in the wave. If the wave energy density becomes comparable to the local thermal energy density then nonlinear effects may become significant.

It is possible to obtain a good description of nonlinear plasma effects by constructing a theory which treats the nonlinear terms as a perturbation to the linear theory. This

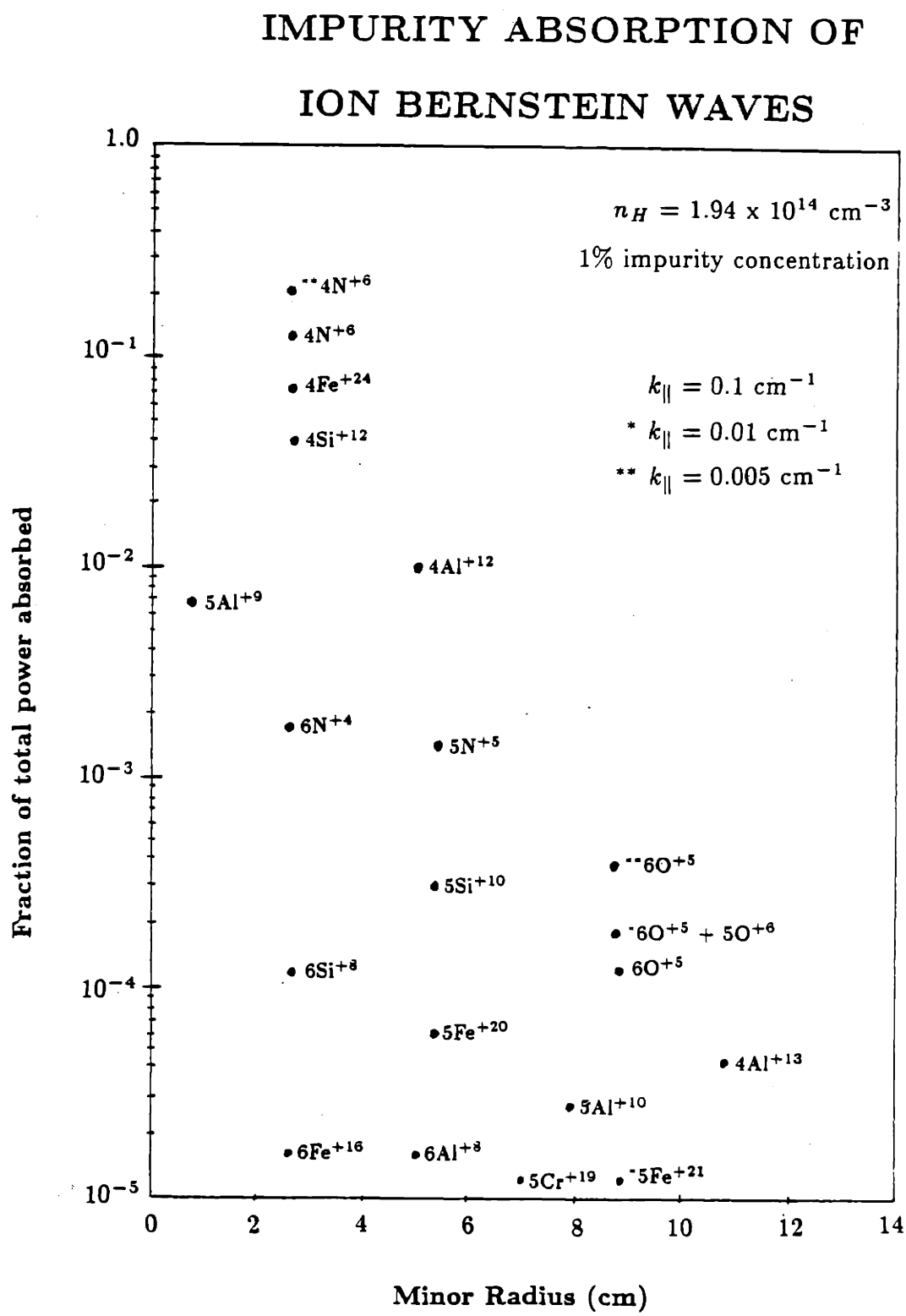

Figure 2.11 —Ion Bernstein wave power absorption in one pass for a variety of plasma impurities.

method rests on the validity of the weak turbulence approximation which is discussed in Ref. 49. This approximation will be assumed throughout this section.

This section reviews some of the important results of nonlinear plasma wave theory and discusses their application to ion Bernstein wave power absorption in a tokamak plasma. The matrix element, which appears in the spatial mode equation and which describes the intensity of the nonlinear interaction is given and some numerical results of integrating the spatial mode equation to calculate power absorption are shown.

2.8.2: Ion Bernstein Wave Nonlinear Effects

Two nonlinear effects of the ion Bernstein wave will be considered here. One is the self–interaction of the wave at an odd half–integral cyclotron harmonic[18] and the other is the decay of the wave into another ion Bernstein wave and a nonresonant quasimode[50]. Both of these interactions have been discussed in the literature [50, 18, 51, 52, 53]. There is also a third nonlinear effect of the ion Bernstein wave which gives rise to power absorption and results from particle trapping. This has been described by Abe[17] and will not be discussed here. References 49, 51, 52, 53, 54, and references therin, are quite useful for the reader who wishes to study the details of these processes.

The goal of most nonlinear plasma wave theories is to obtain a wave kinetic equation which describes the space and time dependence of the electric fields involved in the nonlinear process. Once this equation is obtained, the electric field can in principle be calculated. Using the electric field solution, one can determine the depletion of the incoming wave as it transfers its energy to other waves or plasma particles through the nonlinear process. The following outline of nonlinear plasma wave theory and major results pertinent to the ion Bernstein wave follows the discussion of Rosenbluth, Coppi, and Sudan[54] for nonlinear plasma effects on electrostatic waves.

In the electrostatic approximation, the electric field and wave potential are related by

$$\mathbf{E} = -\nabla\phi \tag{2.8.1}$$

and the energy density of a Fourier wave mode $\mathbf{k}$ can be expressed as

$$U_{\mathbf{k}} = \frac{|\mathbf{E}_{\mathbf{k}}|^2}{8\pi}\omega_R\frac{\partial\epsilon}{\partial\omega_R} \tag{2.8.2}$$

where $|\mathbf{E}_{\mathbf{k}}|$ is the wave electric field amplitude and ϵ is the dielectric function. The corresponding momentum density is given by

$$\mathbf{P_k} = \frac{|\mathbf{E_k}|^2}{8\pi}\mathbf{k}\frac{\partial\epsilon}{\partial\omega_R}. \tag{2.8.3}$$

It is assumed that $\omega = \omega_R + i\gamma$ where $\gamma \ll \omega_R$. It is convenient to define an effective occupation number

$$N_\mathbf{k} = \frac{|\mathbf{E_k}|^2}{8\pi}\left|\frac{\partial\epsilon}{\partial\omega_R}\right| \tag{2.8.4}$$

which is positive definite. Then expressions for energy and momentum density become

$$U_\mathbf{k} = \omega_\mathbf{k} N_\mathbf{k} S_\mathbf{k} \tag{2.8.5}$$

$$\mathbf{P_k} = \mathbf{k} N_\mathbf{k} S_\mathbf{k} \tag{2.8.6}$$

where

$$S_\mathbf{k} = sgn\frac{\partial\epsilon}{\partial\omega_R}. \tag{2.8.7}$$

The weak turbulence approximation[49] is assumed, hence, the energy in the waves considered is small compared to the total energy of the system.

Nonlinear Landau damping is a process where two waves mix to produce a virtual beat wave. Resonant particles then interact with this beat wave through the usual process of cyclotron or Landau damping. The goal in a theory describing this is to calculate the scattering of a wave $\mathbf{k}''$ by a shielded or 'dressed' particle into a wave $\mathbf{k}$. The condition for a particle in a strong magnetic field to be in resonance with waves $\mathbf{k}$ and $\mathbf{k}''$ is

$$\omega'' + \omega - (k''_\parallel + k_\parallel)v_\parallel = m\Omega_i \tag{2.8.8}$$

where Ω_i is the ion cyclotron frequency and m is an integer. Considering the waves and particles to be a statistical system, the principle of microscopic detailed balance can be used to derive a kinetic equation for $N_\mathbf{k}$. The actual derivation of the kinetic equation requires explicit use of the Vlasov equation.

Applying the principle of detailed balance, the rate of change of $N_\mathbf{k}$ is given by summing the rate of creation and destruction of $N_\mathbf{k}$

$$\frac{\partial N_\mathbf{k}}{\partial t} = [\text{Creation Process} + \text{Destruction Process}]. \tag{2.8.9}$$

It can be shown that a stationary state for $N_\mathbf{k}$ ($N_\mathbf{k}$ = constant) is achieved for a Maxwellian distribution of velocities for the particles and a Planck energy distribution for the waves.

In the classical limit, $N_\mathbf{k} \gg 1$ and for $N_\mathbf{k} \ll N_{\mathbf{k}''}$, the wave kinetic equation becomes

$$\frac{\partial N_{\mathbf{k}}}{\partial t} = \left|V_{\mathbf{k},\mathbf{k}''}(E)\right|^2 f(E)\, N_{\mathbf{k}''}. \tag{2.8.10}$$

This describes a wave $\mathbf{k}''$ scattering from a distribution of particles $f(E)$ where the parameter E represents the particle energy, $\mathbf{k}$ is the wave vector of the scattered wave, and $V_{\mathbf{k},\mathbf{k}''}(E)$ is the matrix element which describes the strength of the interaction. The matrix element contains all of the physics of the wave–wave–particle interaction and has been calculated from the Vlasov equation by Rosenbluth and Rostoker[55]. Using their result one finds that the scattering from the particle is the sum of two terms. The bare particle (without shielding) gives the usual Compton scattering term and the shielding cloud gives the other term. These two terms tend to cancel each other in the limit of small $k_\perp \rho_i$; however, the scattering can become significant for $k_\perp \rho_i \gtrsim 1$.

Once the wave–wave–particle scattering is known the next step is to obtain an equation for the spatial dependence of the pump wave $E_{\mathbf{k}''}$ and the scattered wave $E_{\mathbf{k}}$. Porkolab and Chang[52] have obtained these equations for modes with finite $k_\parallel$. More recently Porkolab[18] has given the spatial mode equation for $E_{\mathbf{k}}$ as

$$\frac{\partial E_{\mathbf{k}}}{\partial x} + \alpha_{\mathbf{k}} E_{\mathbf{k}} = \frac{1}{\partial \epsilon / \partial k_\perp} L_{\mathbf{k},\mathbf{k}''} |E_{\mathbf{k}''}|^2 E_{\mathbf{k}} \tag{2.8.11}$$

where $\alpha_{\mathbf{k}}$ is the linear spatial damping rate of the wave in the x direction

$$\alpha_{\mathbf{k}} = \frac{Im(\epsilon)}{\partial \epsilon / \partial k_\perp}. \tag{2.8.12}$$

The quantity $L_{\mathbf{k},\mathbf{k}''}$ is the nonlinear matrix element and is given by

$$L_{\mathbf{k},\mathbf{k}''} = \frac{m\Omega_i}{k'_\parallel v_{ti}} \frac{\omega_{pi}^4}{\Omega_i^4} \frac{-W}{4\sqrt{\pi}} \frac{\exp[-(\omega' - m\Omega_i)^2/(k'_\parallel v_{ti})^2]}{n_0 \kappa T_i} \tag{2.8.13}$$

where W is

$$W = \sum_{s,p=-\infty}^{\infty} \frac{A - BC/D}{[(\frac{\omega}{\Omega_i} - s)^2 - 1][(\frac{\omega}{\Omega_i} - p)^2 - 1]}. \tag{2.8.14}$$

and the energy and momentum of the quasimode or virtual wave which resonates with particles is given by

$$\omega' = \omega \pm \omega''; \qquad \mathbf{k}' = \mathbf{k} \pm \mathbf{k}''. \tag{2.8.15}$$

The quantities A, B, C, and D are given by

$$A = \int_0^\infty d\xi \frac{dg}{d\xi} J_s(z) J_p(z) J_{p-m}(z'') J_{s-m}(z'') \tag{2.8.16}$$

$$B = \int_0^\infty d\xi \frac{dg}{d\xi} J_p(z) J_m(z') J_{p-m}(z'') \tag{2.8.17}$$

$$C = B(p \to s) \tag{2.8.18}$$

$$D = \int_0^\infty d\xi \frac{dg}{d\xi} J_n^2(z') \tag{2.8.19}$$

where

$$g(\xi) = e^{-\frac{1}{2}\xi}; \qquad \xi = 2\frac{v_\perp^2}{v_{ti}^2}; \qquad v_{ti}^2 = \frac{2T_i}{m_i} \tag{2.8.20}$$

and

$$z = \frac{k_\perp v_\perp}{\Omega_i}; \qquad z' = \frac{k'_\perp v'_\perp}{\Omega_i}; \qquad z'' = \frac{k''_\perp v_\perp}{\Omega_i}. \tag{2.8.21}$$

The value of $|W|$ is plotted as a function of $k_\perp \rho_i$ in Fig. 2.12 for three values of m.

2.8.3: Self–Interaction of Ion Bernstein Waves

A wave with frequency $\omega = \frac{m}{2}\Omega_i$ can interact with itself to yield nonlinear Landau damping or instability. Only the case of m–odd is allowed by the dispersion relation. In this case,

$$k' = 2k; \qquad \omega' = 2\omega = m\Omega_i \tag{2.8.22}$$

and $E_{\mathbf{k}''} = -E_{\mathbf{k}}$. Equation 2.8.11 can now be written as

$$\frac{\partial E_{\mathbf{k}}}{\partial x} + \alpha_{\mathbf{k}} E_{\mathbf{k}} + Q(x)|E_{\mathbf{k}}|^2 E_{\mathbf{k}} = 0 \tag{2.8.23}$$

where $Q(x)$ in a radially varying magnetic field has the form

$$Q(x) \equiv Q_0 e^{-\frac{x^2}{\zeta^2}} = \frac{m\Omega_i}{2k_\parallel v_{ti}} \frac{|W|}{4\sqrt{\pi}} \frac{\omega_{pi}^4}{\Omega_i^4} \frac{e^{-\frac{x^2}{\zeta^2}}}{\frac{\partial \epsilon_R}{\partial k_\perp} n_0 \kappa T_i}. \tag{2.8.24}$$

Typically $\alpha_{\mathbf{k}}$ is small ($\alpha_{\mathbf{k}} << 1/\Delta x$ where Δx is the length of the nonlinear interaction region) and Eq. 2.8.23 predicts a threshold value in the pump electric field which is required to produce at least a ~40% reduction in the pump field amplitude after passing through the nonlinear interaction region. Porkolab[52] has obtained an expression for

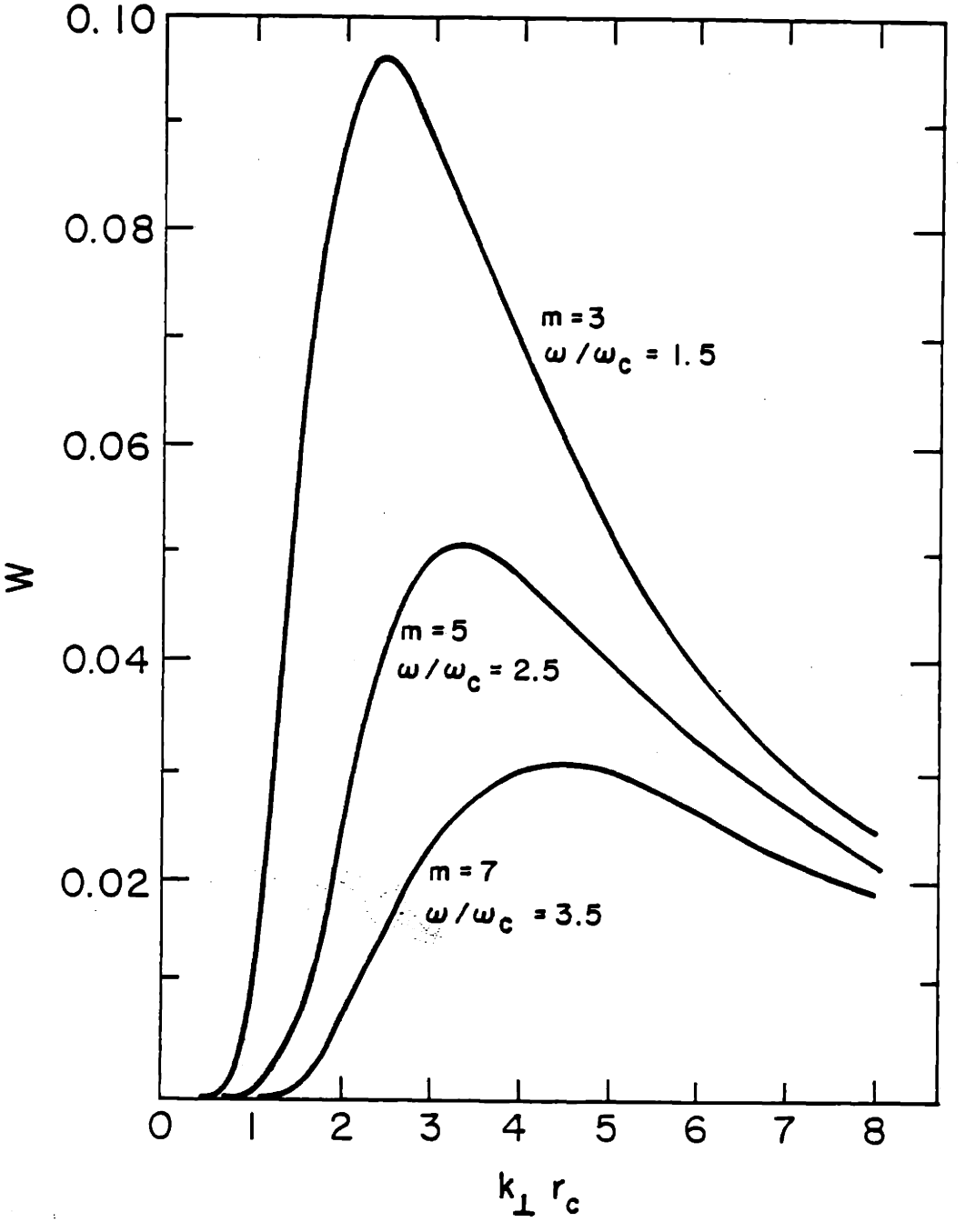

Figure 2.12 —Numerically calculated values of $|W|$ as a function of $k_\perp \rho_i$ for $m = 3, 5,$ and 7.

the threshold power flux necessary in the pump wave to cause at least a $\sim 63\%$ power absorption in the case where $k_\perp$ is slowly changing through the interaction region (the quantity W is nearly constant). Porkolab points out that in the presence of impurities or a minority such that

$$\frac{Z_j}{m_j} = \frac{1}{2}\frac{m}{n} \tag{2.8.25}$$

where Z_j, (m_j) is the charge, (mass) number of the impurity or minority, m is the odd integer describing the self interaction, and n is any positive integer, the ion Bernstein wave dispersion relation can be significantly modified and this can reduce the threshold power. The reason for this is that $\partial\epsilon/\partial k_\perp$ is reduced by the presence of the minority species and W becomes a strong function of position within the interaction region. In this case, the spatial dependence of $E_{\mathbf{k}}$ from Eq. 2.8.23 is best evaluated numerically. Figure 2.13 shows the spatial dependence of the pump wave power for both the cases of no minority and deuterium minority for several initial pump powers. In the numerical calculation, the threshold power is defined as the power necessary to produce a 63% power flow into the nonlinearly absorbing species. The wave power is assumed to spread out over an area $S = 2A$ where A is the antenna surface area ($\sim 100\,\mathrm{cm}^2$). In the case of deuterium minority, the linear cyclotron absorption on deuterium ($\omega = 3\Omega_\mathrm{D}$) competes with the nonlinear absorption at $\omega = 1.5\Omega_\mathrm{H}$. When the nonlinear power threshold is exceeded, the nonlinear absorption depletes a large fraction of the incoming pump power before linear damping begins to occur.

2.8.4: Ion Bernstein Wave Decay

Another nonlinear process related to self–interaction and described by precisely the same physics is the decay of an ion Bernstein wave into another ion Bernstein wave and a quasimode. This process has been described by Porkolab in Ref. 50. The application of this process to ion Bernstein wave heating becomes important when the quasimode is resonant with a particular plasma ion species. For example, an ion Bernstein wave with $\omega/\Omega_\mathrm{H} = 1.6$ might decay into another ion Bernstein wave with $\omega/\Omega_\mathrm{H} = 1.1$ and a quasimode at $\omega/\Omega_\mathrm{H} = 0.5$. If the plasma contains deuterium, the quasimode will be resonant with the deuterium first harmonic. The result is that the deuterium species will absorb power from the pump ion Bernstein wave. The strength of this interaction is determined by the value of $|W|$ given in Eq. 2.8.14.

To study this decay process in a tokamak geometry near $\omega = 1.5\Omega_\mathrm{H}$ the value of $|W|$ was computed numerically for a pump wave with $\omega/\Omega_\mathrm{H} = 1.5 + x$, a decay wave with $\omega/\Omega_\mathrm{H} = 1 + x$, and a quasimode with $\omega/\Omega_\mathrm{H} = 0.5$ for $0 < x < 0.35$. Since the pump

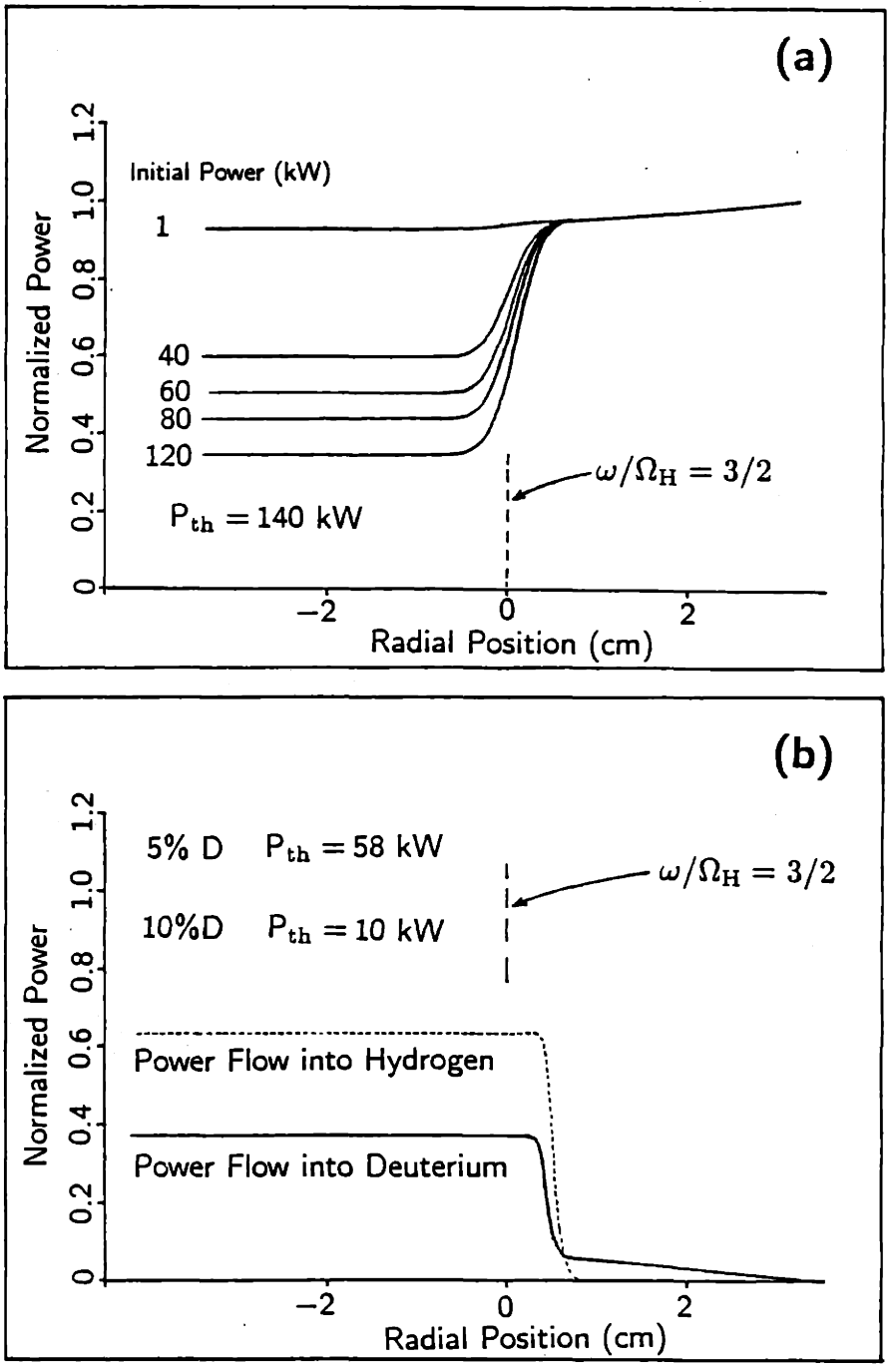

Figure 2.13 —(a) Nonlinear power absorption of ion Bernstein waves in a pure hydrogen plasma at the hydrogen 3/2 harmonic for several initial powers. A small fraction of power is absorbed by electron Landau damping. (b) Power absorbed by hydrogen (nonlinearly) and deuterium (linearly) for 5% and 10% deuterium concentrations. The presence of deuterium reduces the threshold power. Plasma parameters: $n_{e0} = 1.5 \times 10^{20}\,\mathrm{m}^{-3}$, $T_{i0} = 900\,\mathrm{eV}$, $T_{e0} = 1600\,\mathrm{eV}$, $B_0 = 7.6\,\mathrm{T}$, $f = 183.6 \times 10^6\,\mathrm{s}^{-1}$, $k_\parallel = 0.16\,\mathrm{cm}^{-1}$.

depletion occurs from the nonlinear interaction with the deuterium species, the values of $k_\perp \rho_i$ used in evaluating $|W|$ must be given by the values of $k_\perp \rho_D$ corresponding to the values of ω/Ω_H. The result is that the value of $|W|$ increases monotonically and becomes very large (compared to the value of $|W|$ for the self–interaction process) as x approaches zero. An estimate of the threshold power for 63% power absorption by the deuterium species can be made by solving the spatial mode equation for the pump wave (Eq. 2.8.11) simultaneously with the spatial mode equation for the decay wave[52]. The initial value of the decay wave is given by the thermal fluctuation level of this wave in the plasma. The calculated threshold power ($\sim 50\,\mathrm{kW}$) is of a similar magnitude as the threshold power for nonlinear power absorption by self–interaction. Because of the similarity in threshold of the two processes it is possible that as the ion Bernstein wave power propagates from the low field side of the plasma to the high field side, power may be absorbed by the deuterium species through the decay process (at $\omega/\Omega_H \gtrsim 1.5$) before the ion Bernstein wave power reaches the self–interaction region ($\omega/\Omega_H \simeq 1.5$).

Both the nonlinear self–interaction and decay processes can be important in interpreting the experimental results. Since both nonlinear processes are distinguishable, it may be possible to determine how significantly each contributes to the pump power absorption. The analysis of the experimental results in terms of the power absorption mechanisms is discussed in Chapter 4.

2.9: Conclusions

This chapter describes the characteristics of the ion Bernstein wave in a range of plasma parameters. The difference between the electromagnetic and electrostatic wave descriptions is shown to be significant for $\beta_H \gtrsim 0.25$. Ion Bernstein wave energy, dependence on $k_\parallel$, wave damping in the WKB approximation, and characteristics in an inhomogeneous plasma are described. The Brambilla coupling model is outlined. The ion Bernstein wave ray tracing and power absorption model used for Alcator C is also described. Power absorption due to plasma impurities is shown to be negligible. Finally, nonlinear self–interaction and decay of the ion Bernstein wave is shown to be important for Alcator C parameters.

REFERENCES

1. E. P. Gross, *Phys. Rev.*, **82**, 232, (1951).
2. V. A. Bailey, *Phys. Rev.*, **83**, 439, (1951).
3. G. V. Gordeyev, *Zhur. Eksp. i Teoret. Fiz.*, **23**, 660, (1952).
4. I. B. Bernstein, *Phys. Rev.*, **109**, 10, (1958).
5. H. K. Sen, *Phys. Rev*, **88**, 816, (1952).
6. E. R. Ault and H. Ikezi, *Phys. Fluids*, **13**, 2874, (1970).
7. J. P. M. Schmitt, *Phys. Fluids*, **15**, 2057, (1972).
8. Y. Ohnuma, S. Miyake, T. Sato, and T. Watari, *Phys. Rev. Lett.*, **26**, 541, (1970).
9. J. P. M. Schmitt, *Phys. Rev. Lett.*, **31**, 982, (1973).
10. S. Puri, *Phys. Fluids*, **22**, 1716, (1979).
11. F. Skiff, M. Ono, and K. L. Wong, *Phys. Fluids*, **27**, 1051, (1984).
12. F. Skiff, K. L. Wong, and M. Ono, *Phys. Fluids*, **27**, 2205, (1984).
13. F. Skiff, Ph. D. Thesis, *Linear and Nonlinear Excitation of Slow Waves in the Ion Cyclotron Frequency Range*, Princeton University, (1985).
14. M. Ono, T. Watari, R. Ando, *et al.*, *Phys. Rev. Lett.*, **54**, 2339 (1985).
15. M. Ono, P. Beiersdorfer, R. Bell, *et al.*, *Phys. Rev. Lett.*, **60**, 294, (1988).
16. J. D. Moody, M. Porkolab, C. L. Fiore, *et al.*, *Phys. Rev. Lett.*, **60**, 298, (1988).
17. H. Abe, *et al.*, *Phys. Rev. Lett.*, **53**, 1153, (1984).
18. M. Porkolab, *Phys. Rev. Lett.*, **54**, 434, (1985).
19. T. H. Stix, *The Theory of Plasma Waves*, (McGraw–Hill, New York, 1962).
20. P. M. Morse and H. Feshbach, *Methods of Theoretical Physics*, 2 volumes., (McGraw–Hill, New York, 1953), p. 458.
21. K. Miamoto, *Plasma Physics for Nuclear Fusion*, (The MIT Press, Cambridge, MA, 1980), p. 417.
22. B. D. Fried and S. D. Conte, *The Plasma Dispersion Function*, (Academic Press, Inc., New York, 1961).

23. M. ABRAMOWITZ AND I. STEGUN, *Handbook of Mathematical Functions*, (Dover Publications, Inc., New York, 1972), p. 375.

24. W. N.–C. SY, T. AMANO, R. ANDO, A. FUKUYAMA, T. WATARI. *Nucl. Fusion.*, **25**, 795, (1985).

25. L. TONKS AND I. LANGMUIR, *Phys. Rev.*, **33**, 195, (1929).

26. G. A. WURDEN, M. ONO, AND K. L. WONG, *Phys. Rev. A*, **26**, 2297, (1982).

27. H. PARK, P. S. LEE, W. A. PEEBLES, AND N. C. LUHMANN, JR., *Nucl. Fusion*, **25**, 1399, (1985).

28. D. BOHM AND E. P. GROSS, *Phys. Rev.*, **75**, 1864, (1949).

29. C. M. BENDER AND S. A. ORSZAG, *Advanced Mathematical Methods for Scientists and Engineers*, (McGraw–Hill, New York, 1978), Ch. 10.

30. A. FUKUYAMA, K. ITOH, S.–I. ITOH, *Computer Physics Reports*, 4, 137–181, (1986), North Holland Physics Publishing Division.

31. A. FUKUYAMA, S. NISHIYAMA, K. ITOH, AND S.–I. ITOH, *Nucl. Fusion*, **23**, 1005, (1983).

32. K. ITOH, S.–I. ITOH, AND A. FUKUYAMA, *Nucl. Fusion*, **24**, 13, (1984).

33. I. B. BERNSTEIN, *Phys. Fluids*, **18**, 320, (1975).

34. P. L. COLESTOCK AND R. J. KASHUBA, *Nucl. Fusion*, **23**, 763, (1983).

35. M. BRAMBILLA, 7th Topical Conf. on Rf Plasma heating, Kissimmee, FL, (1987).

36. M. BRAMBILLA, Max–Planck Institut für Plasmaphysik Report IPP 5/15, April 1987.

37. J. D. JACKSON, *Classical Electrodynamics*, Second Edition, (John Wiley and Sons, New York, 1975).

38. S. WEINBERG, *Phys. Rev.*, **126**, 1899, (1962).

39. L. B. FELSEN AND N. J. MARCUVITZ, *Radiation and Scattering of Waves*, (Prentice–Hall, Englewood Cliffs, New Jersey, 1972).

40. J. L. KULP, Ph.D. Thesis, Massachusetts Institute of Technology (1978).

41. S. EJIMA, V. S. CHAN, R. LAHAYE, C. MOELLER, P. I. PETERSEN, AND J. C. WESLEY, *Bull. Am. Phys. Soc.*, **22**, 1170, (1977).

42. YU. BARANOV AND V. I. FEDOROV, *Pis'ma Zh. Tekh. Fiz.*, 4, 800, (1978) [*Sov. Phus.–Tech. Phys. Lett.*, 4, 322, (1978)].

43. T. MAEKAWA, Y. TERUMICHI, AND S. TANAKA, *IEEE Trans. Plasma Sci., PS-8*, 64, (1979).

44. P. T. BONOLI AND E. OTT, *Phys. Fluids*, **25**, 359, (1982).

45. L. F. SHAMPINE AND M. K. GORDEN, *Computer Solution of Ordinary Differential Equations*, (Freeman, San Francisco, 1975).

46. S. D. CONTE AND C. DE BOOR, *Elementary Numerical Analysis, An Algorithmic Approach*, (McGraw–Hill, New York, 1980).

47. M. BRAMBILLA AND A. CARDINALI, *Plasma Physics*, **24**, 1187, (1982).

48. M. PORKOLAB, *Fusion*, 2 Vol., Ed. by Edward Teller, (Academic Press, New York, 1981).

49. R. Z. SAGDEEV AND A. A. GALEEV, *Nonlinear Plasma Theory*, (Benjamin, Reading, Massachusetts, 1969), p. 20.

50. M. PORKOLAB AND J. D. MOODY, *Bull. Am. phys. Soc.*, **32**, 1939, (1987). Also to be published.

51. M. PORKOLAB, *Nucl. Fusion*, **18**, 367, (1978).

52. M. PORKOLAB AND R. P. H. CHANG, *Phys. Fluids*, **15**, 283, (1972).

53. R. P. CHANG AND M. PORKOLAB, *Phys. Rev. Lett.*, **25**, 1262, (1970).

54. M. N. ROSENBLUTH, B. COPPI, AND R. N. SUDAN, *Ann. Phys.*, (N.Y.), **55**, 248, (1969).

55. M. N. ROSENBLUTH AND N. ROSTOKER, *Phys. Fluids*, **5**, 776, (1962).

CHAPTER 3

Description of the Experimental Apparatus

3.1: Introduction

This chapter describes the experimental apparatus used in the ion Bernstein wave experiments. The first section describes the Alcator C tokamak and lists some of the important operating paramaters. The second section gives a brief description of the plasma diagnostics involved in the experiment. Finally, section three describes the ion Bernstein wave antenna system. Special focus is given to the electrical design and characteristics of the antenna structure. Ohmic power dissipation is estimated from the measured radiation resistance and the peak voltage in the system is calculated for a given power. A brief discussion of the matching network is also presented.

3.2: The Alcator C Tokamak

The combination of a strong toroidal field and an Ohmic heating plasma current are the basic ingredients of a plasma confinement device known as a tokamak. The Alcator (ALto CAmpo TORus, or high field torus) tokamak concept, initially proposed by Coppi (1970), is an approach to magnetic toroidal confinement which utilizes a very high magnetic field and a high density plasma in a somewhat small and compact device. A large, pulsed, toroidally directed magnetic field and toroidal plasma current are used to confine the plasma particles. The induced plasma current also serves to Ohmically heat the plasma. Figure 3.1 (a) shows the geometry of a tokamak device, Fig. 3.1 (b) shows an artist's rendition of Alcator C, and Table 3.1 lists some of the main operating parameters of the Alcator C tokamak.

Table 3.1

Alcator C Parameters

Major Radius:	$R_0 = 64\,\text{cm}$
Minor Radius:	$a = 16.5\,\text{cm}$
Toroidal Magnetic Field:	$B_\text{T} \leq 13\,\text{Tesla}$
Plasma Current:	$I_p \leq 800\,\text{kA}$
Plasma Density:	$0.3 \times 10^{20} \leq \bar{n}_e \leq 20 \times 10^{20}\,\text{m}^{-3}$
Electron Temperature:	$T_e \leq 3\,\text{keV}$
Ion Temperature:	$T_i \leq 1.5\,\text{keV}$
Energy Confinement Time:	$\tau_E \leq 50\,\text{ms}$
Lawson Product:	$n\tau_\text{E} \leq 6\text{–}8 \times 10^{19}\,\text{m}^{-3}\text{–s}$
Ohmic Heating Input Power:	$P_\text{Oh} \leq 1.5\,\text{MW}$
Duration of Discharge:	$\tau_\text{plasma} \simeq 300\text{–}600\,\text{ms}$

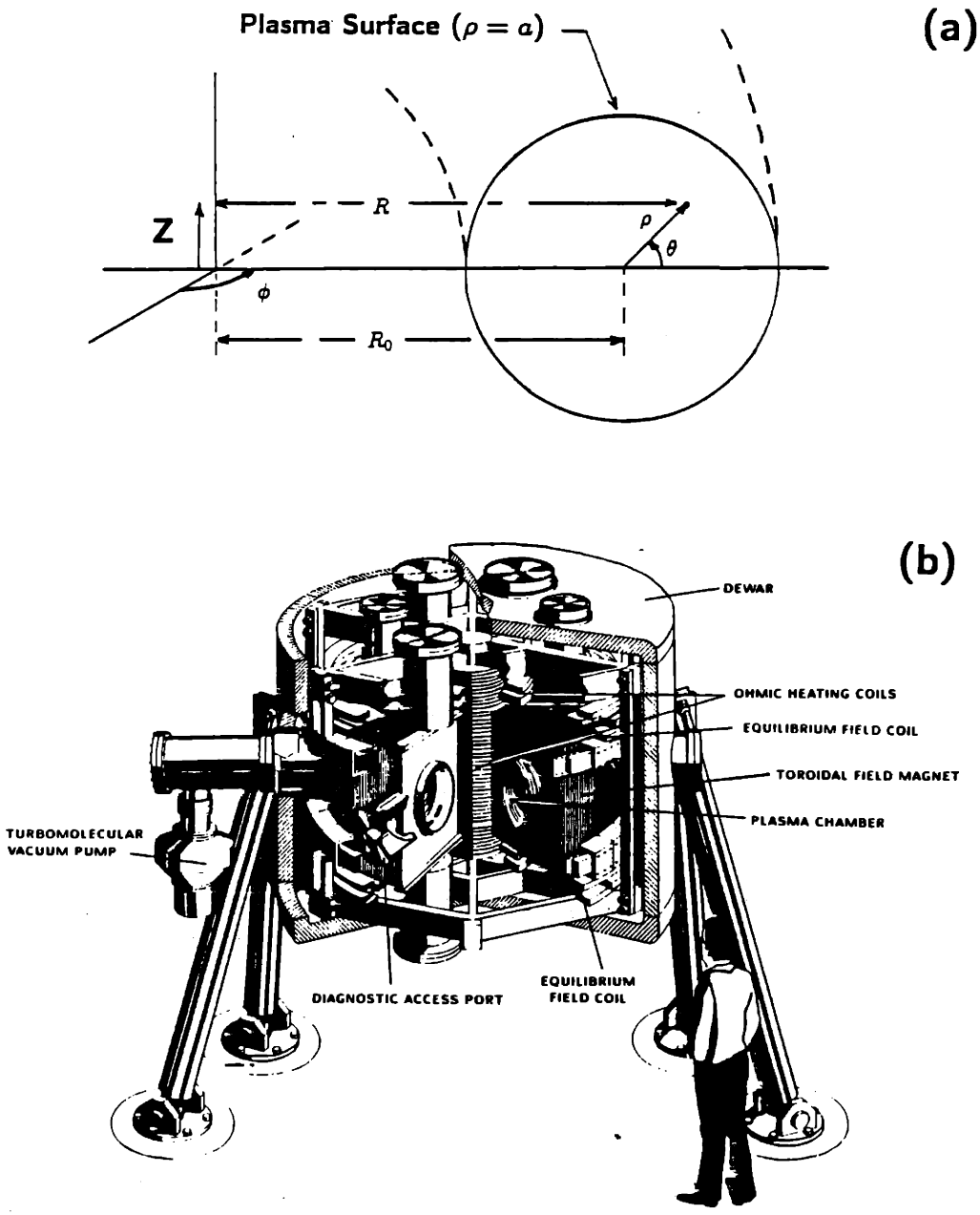

Figure 3.1 —(a) The geometry of a tokamak device. The plasma is confined in the shape of a torus with magnetic fields. The (r, θ) plane is the *poloidal plane*. The coordinate r is the *minor radius*, R is the major radius, θ is the poloidal angle, ϕ is the toroidal angle, and the Z–axis lies along the vertical centerline. On Alcator C, $a = 16.5\,\text{cm}$ and $R_0 = 64\,\text{cm}$. (b) The Alcator C tokamak (cut–away view).

3.3: Plasma Diagnostics

3.3.1: Introduction

An rf plasma heating experiment which is designed to affect global plasma parameters relies heavily on diagnostic measurements which can observe changes in plasma characteristics and properties. A diagnostic is a device which is specially designed to measure one or more particular plasma observables such as the line–averaged density, central ion temperature, visible hydrogen spectral emission, plasma edge potential, and others. A diagnostic serves at least two important functions. First, it provides information which can be used to confirm or modify present models of basic physical processes or extend the regimes of applicability of these models. Second, it provides information about the response of the plasma to experiments which affect the whole plasma. The ion Bernstein wave heating experiment relied heavily on a number of plasma diagnostics. A brief description of these is given in what follows.

3.3.2: Perpendicular Ion Temperature

Perpendicular ion temperature was measured using a charge exchange neutral analyzer[1]. The analyzer provided central plasma ion temperature and ion energy distribution measurements. Located toroidally one port away (60^0) from the antenna, the analyzer viewed the plasma from the low field side of the torus. Radial temperature profiles were obtained on a shot–to–shot basis (requiring about 10–20 shots to determine a profile) by scanning the analyzer viewing angle in the upward direction (direction of the ion grad–B drift); the profiles were assumed to be symmetric about the plasma center. Particle flux from only hydrogen or deuterium could be analyzed during a single shot; however, switching from hydrogen to deuterium could be done on a shot–to–shot basis. The analyzer was calibrated over an energy range of about 0.5 keV to 10 keV. The ion temperature was obtained by making a linear fit to the computed quantity $\log\left[J_i(E_i)/\sqrt{E_i}\right]$ where J_i is the measured ion particle flux and E_i is the ion energy. A typical single measurement error in the ion temperature was about 50 eV; however, repeated measurements on identical discharges could reduce this error. In some cases, the ion flux could be described with two temperatures, one typically somewhat higher than the other. This occurred when a fraction of the plasma ions were hotter than the bulk ions.

3.3.3: Central Electron Temperature and Density

Central electron temperature and density were measured with a Thompson laser scattering system[2]. The laser light was produced from a Nd:YAG laser source operating at a wavelength of 1.06 μm and providing a 1 Joule pulse every 20 milliseconds. The system has operated successfully over a density range of $0.5 \times 10^{20}\,\mathrm{m}^{-3}$ to $7.0 \times 10^{20}\,\mathrm{m}^{-3}$ and a temperature range of 500 eV to 3000 eV. A typical error in the electron temperature is about ± 100 eV, but can become as high as about ± 500 eV. The error in the central density is typically about $0.1 \times 10^{20}\,\mathrm{m}^{-3}$.

3.3.4: Line–Averaged Electron Density

Line–averaged electron density was measured with a phase modulated laser interferometer system[3]. This type of system is insensitive to laser power amplitude variation and gives a resolution which is independent of phase. Laser light is produced from two optically pumped CH_3OH (methyl alcohol) lasers which operate at the 118.8 μm line. Plasma in the density range of $10^{20}\,\mathrm{m}^{-3} \lesssim n_e \lesssim 20 \times 10^{20}\,\mathrm{m}^{-3}$ produces a phase shift of $1.0 \lesssim \phi/2\pi \lesssim 20$ for a plasma radius of 12 cm and a nearly parabolic density profile. The Alcator C system had the capability of measuring the line–averaged density profile at several different radial locations. For the small size plasma ($r = 12$ cm was typical during the ion Bernstein wave experiments) only three density viewing chords passed through the plasma, one in the center, one near the plasma inner edge, and one near the plasma outer edge.

3.3.5: Plasma Impurity Level

The impurity level of the plasma was determined by measuring the visible bremsstrahlung plasma emission[4]. The effective ion charge of the plasma is denoted as Z_{eff} and is defined by

$$Z_{\mathrm{eff}} \equiv \sum_i \frac{n_i Z_i^2}{n_e} \tag{3.3.1}$$

where n_i and n_e are the densities of the ion species and electrons and Z_i is the ion charge number. The instrument measured the line integral brightnesses of the continuum radiation (in the wavelength region near 5360 Å) from up to 20 chords at different radial locations. The value of Z_{eff} was then inferred from the measured radiation.

3.3.6: MHD Activity

Magnetohydrodynamic (MHD) activity was monitored with a soft x–ray diagnostic described in Ref. 5. The device consisted of a detector system which could image the poloidal cross section of the plasma's soft x–ray emissivity. Typically, only the soft x–ray emission from a central chord was monitored during the ion Bernstein wave experiments.

3.3.7: Edge Ion Impurity Temperature

The edge ion impurity temperature ($r/a \sim 0.9$–1.0) was determined by measuring the Doppler broadening of far UV lines from radiation emitted by impurities in the plasma edge[6]. Typically, radiation emitted from OV and OVII was monitored during some of the ion Bernstein wave experiments. Unfortunately, these measurements were not carried out routinely during ion Bernstein wave experimentation.

3.3.8: Edge Plasma Density, Temperature, and Floating Potential

An unshielded double Langmuir probe was constructed to measure the plasma floating potential, electron density, ion temperature, and plasma radial electric field in the scrape–off region. The separation of the probes was about 2–3 mm and the probes could scan a radial distance of 4–5 cm (3–4 temperature scrape–off lengths). Another probe containing both a Langmuir probe and a gridded energy analyzer[7] was used to measure the edge conditions also. This probe, separated by a limiter from the double probe, measured similar plasma edge characteristics as the double probe.

3.3.9: Plasma Radiation Power Loss

Plasma power loss by radiation was monitored with a bolometer array[8]. This array contained 16 detectors and provided a radial profile of plasma emission. Bolometer data is only available for some of the ion Bernstein wave heating experiments.

3.3.10: CO_2 Laser Scattering

A CO_2 laser scattering system was used on Alcator C to measure the density perturbations resulting from both coherent plasma waves and plasma turbulence[9]. Dr. Y. Takase was responsible for operating this diagnostic during the ion Bernstein wave experiments. The experimental and theoretical details of this type of measurement are

discussed in References 10, 11, 12, and references therein. The wavelength of laser light $\lambda = 10.6\,\mu$m was chosen so that refraction, reflection, absorption, and emission by the plasma did not obscure the measurement. The laser frequency was significantly greater than the electron plasma and electron cyclotron frequencies. The scattering of laser light is mainly due to the electron motion since the ion acceleration in the laser electric field is reduced by the electron to ion mass ratio. The scattered power is therefore proportional to the magnitude of the electron density perturbation. The scattering angle is determined by the conservation of wave energy and momentum expressed as

$$\mathbf{k}_0 + \mathbf{k} = \mathbf{k}_s \tag{3.3.2}$$

$$\omega_0 + \omega = \omega_s \tag{3.3.3}$$

where $\mathbf{k}_0$, ω_0 refer to the incident laser radiation and $\mathbf{k}_s$, ω_s refer to the radiation scattered from density perturbations with frequency ω and wave vector $\mathbf{k}$. For scattering from ion Bernstein waves or edge turbulence, $|\mathbf{k}_0| \simeq |\mathbf{k}_s|$ since $\omega \ll \omega_0$ and $\mathbf{k}$ must therefore be nearly perpendicular to $\mathbf{k}_0$. In this case, the scattering angle is quite small $(\cos^{-1}[\hat{\mathbf{k}}_0 \cdot \hat{\mathbf{k}}_s] \lesssim 6°)$.

A schematic of the CO_2 scattering diagnostic set–up to measure density perturbations associated with ion Bernstein waves is shown in Fig. 3.2 . The horizontal location of the scattering volume can be altered by moving the lens–mirror assemblies L2–M2 and L3–M3 horizontally. Similarly, the vertical location can be changed by adjusting the lenses L2 and L3 vertically. The angle ϕ_s, which selects the wave number of the density perturbation to be observed, is determined by the position of M1. Scattering experiments to measure low–frequency density fluctuations require a different experimental set–up which is shown schematically in Fig. 3.3 . In this case, the scattering volume is typically the entire vertical length of the main beam through the plasma. Scattering angles down to $\phi_s \simeq 0$ $(\mathbf{k}_\perp \simeq 0)$ can be studied for this case.

3.4: Ion Bernstein Wave Antenna System

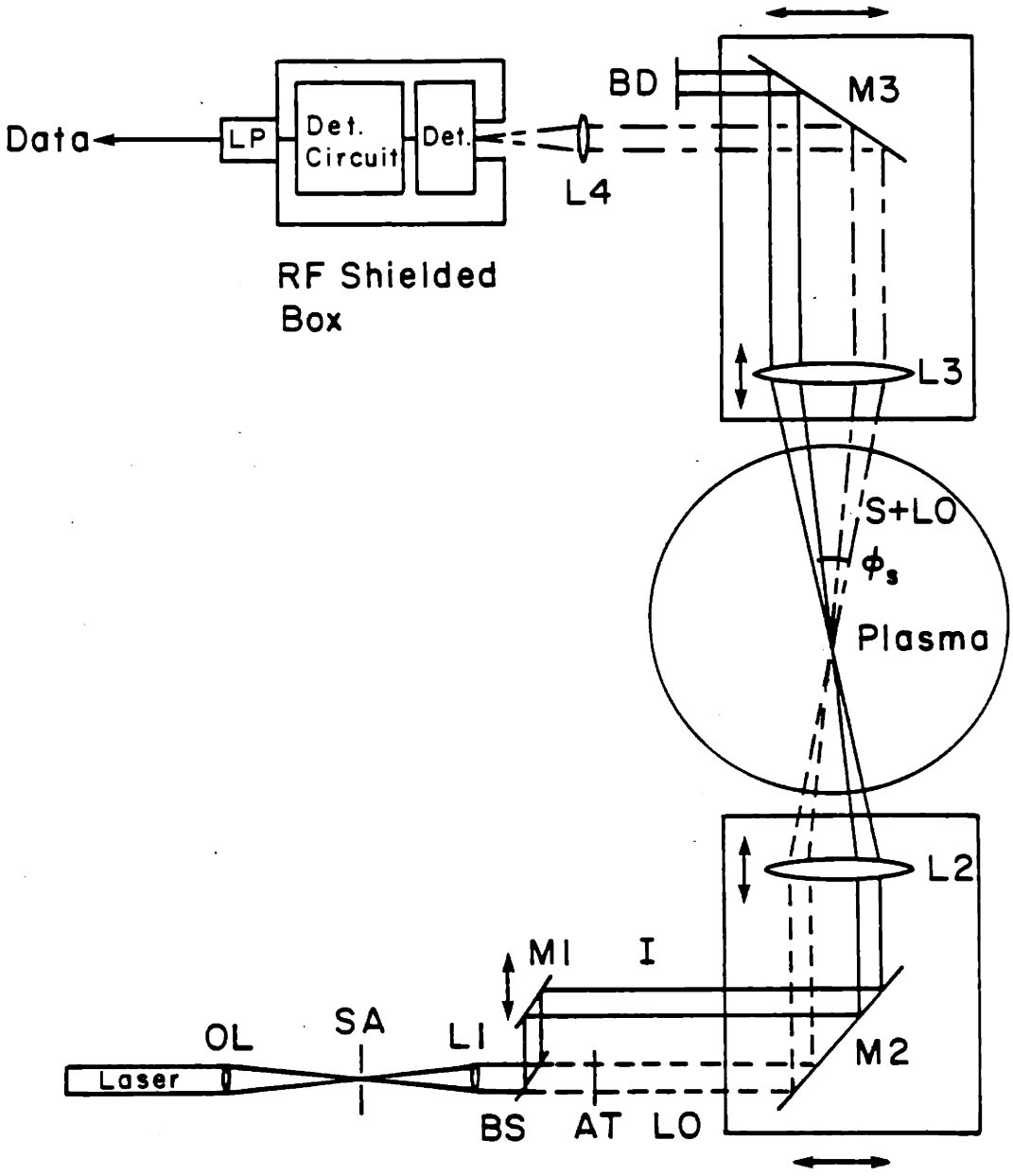

Figure 3.2 —The experimental setup of CO_2 laser scattering experiments from ion Bernstein waves. (from Y. Takase Ref. 9.)

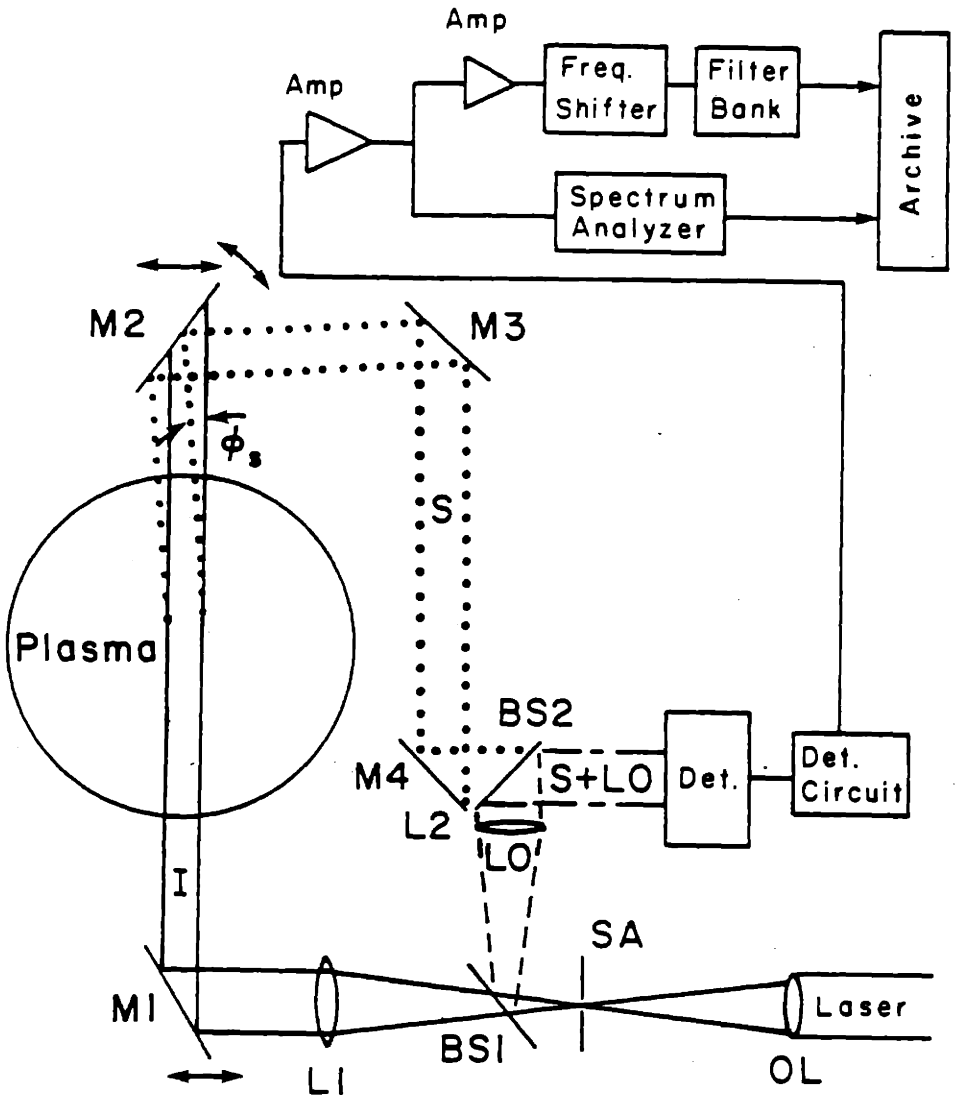

Figure 3.3 —The experimental setup of CO_2 laser scattering experiments from low-frequency fluctuations. (from Y. Takase Ref. 9).

3.4.1: Introduction

The purpose of the Alcator C ion Bernstein wave antenna system is to efficiently carry power from the source to the antenna structure where it can be coupled to the plasma in the form of ion Bernstein wave power. The system can be divided into two major parts:

I. Antenna structure

II. Transmission line and matching network.

Figure 3.4 is a schematic of the entire antenna system. The antenna structure consists of the T–shaped antenna inside of the vacuum chamber. The transmission line and matching network consists of the stub tuner system and transmission line connecting the tuner system and antenna.

Power was supplied to the antenna system from one of three amplifiers. A low power linear amplifier could supply up to 2 kW of continuous rf power in the frequency range of about $2\,\text{MHz} \leq f_0 \leq 200\,\text{MHz}$. For powers up to 80 kW and then up to 450 kW two nonlinear amplifiers with slightly adjustable frequency ($\pm 10\%$) were used. No power above 180 kW was used during the ion Bernstein wave experiments due to voltage breakdown problems and plasma disruptions. The remainder of this section will discuss the details of items I and II.

3.4.2: Antenna Coupling Structure

Ion Bernstein waves were launched from a stainless steel, center fed, T–shaped movable loop antenna with the center conductor aligned along the direction of the edge magnetic field and surrounded by a double layer, molybdenum coated Faraday shield. Figure 3.5 shows a schematic of the antenna. The outer dimensions of the antenna structure are: width 4 cm, length 25 cm, and height 4 cm. The option of a ceramic cup between the inner and outer shield is shown in the schematic; however, all data reported here was obtained without the ceramic cup. This type of antenna has been used previously for slow wave excitation in mirror devices [13, 14], ion Bernstein wave excitation in ACT–I[15], and ion Bernstein wave heating experiments at JIPPT–II–U[16]. Schmitt[17]also used a long wire antenna to excite ion Bernstein waves.

The wave excitation studies on ACT–I[15] confirm that ion Bernstein waves are best excited when the antenna current is close to being parallel to the direction of the background magnetic field (as opposed to being perpendicular as is the case for

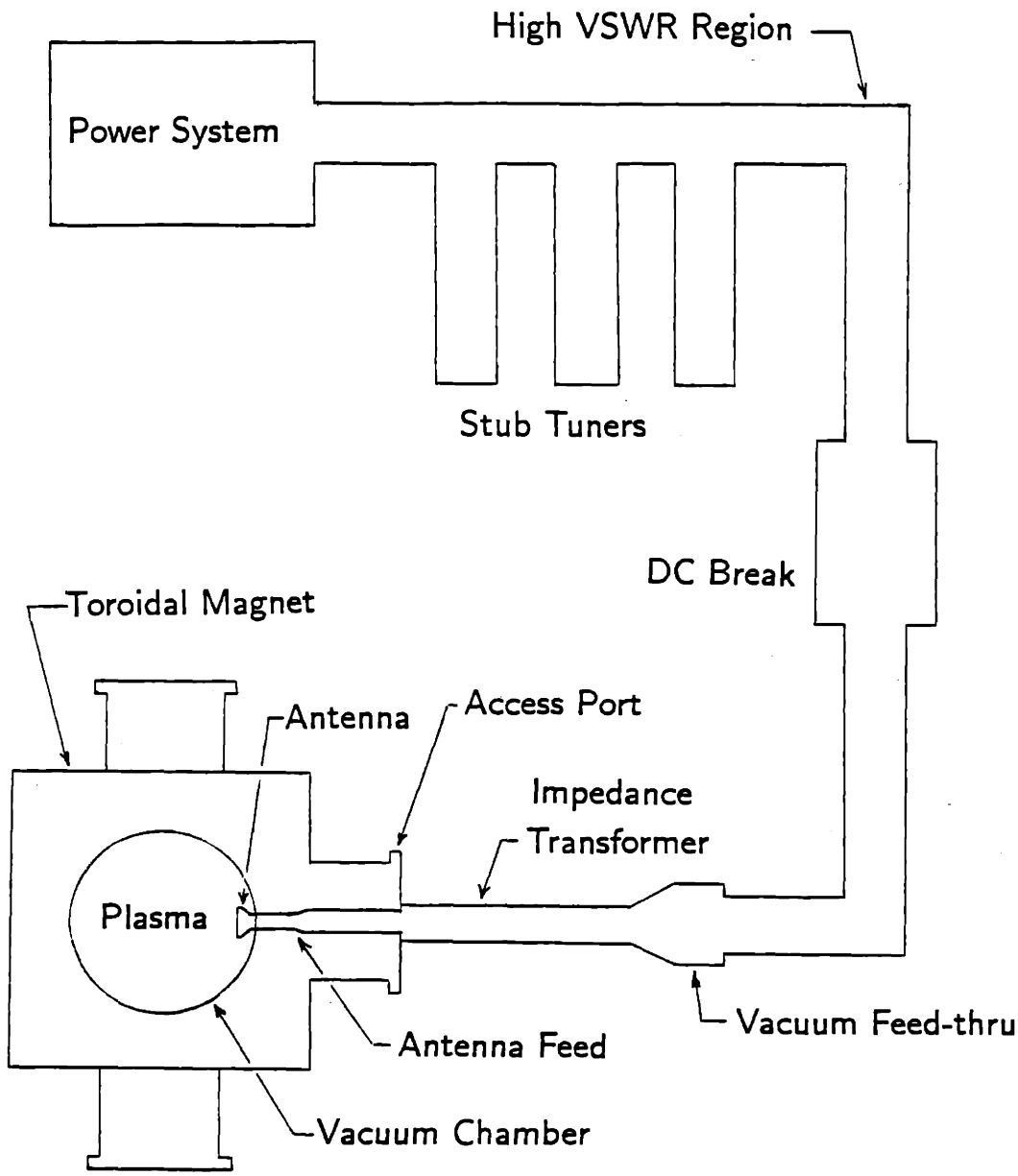

Figure 3.4 —The Alcator C antenna system. Power entering the stub tuners passes through the high VSWR region, through the DC break and into the vacuum break. From the vacuum break, power enters the antenna feed and flows into the antenna.

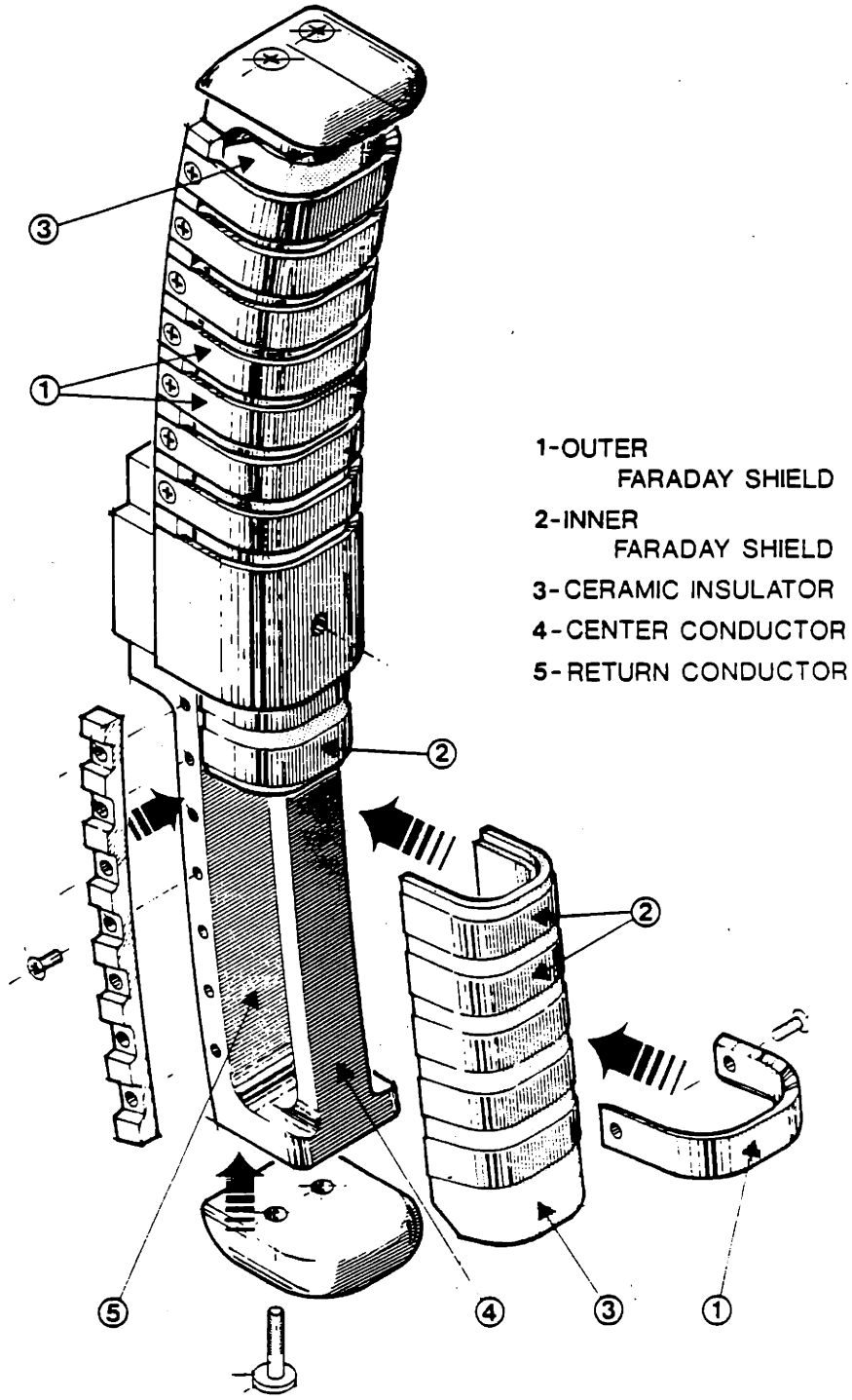

Figure 3.5 —Schematic of the Alcator C ion Bernstein wave antenna.

fast wave launching). This result can be understood intuitively by considering the polarization of the antenna and ion Bernstein wave electric fields. The electric field excited in the plasma by the antenna can be expressed in terms of the scalar and vector potentials whose sources are the charge and current in the antenna. The direction of this electric field is mostly parallel to the antenna center conductor and therefore is also parallel to the background magnetic field. The dispersive property of the plasma acts mainly to reduce the magnitude of the penetrating electric field due to the large value of K_{zz}. The field within the plasma arising from the antenna excitation can be decomposed into a linear combination of the electric fields from all possible plasma oscillations; the oscillations with electric field polarization mainly along the background magnetic field will contribute the most to this linear combination. The ion Bernstein wave at the plasma edge is the only propagating wave with an electric field polarization mainly parallel to the background magnetic field ($E_z/E_x > 1$ for $k_{||} > 0$). Therefore, the dominant term in the linear decomposition will come from the ion Bernstein wave. The slow wave is excited in the vacinity of the antenna due to the antenna reactive fields. The slow wave is evanescent and therefore carries no power; however, it may produce some local power absorption. Most of the power can be shown to couple into the ion Bernstein wave and the remaining power will couple into the fast wave and possibly certain parasitic modes which propagate in the plasma edge region.

There are two dimensions of primary importance in an ion Bernstein wave metal loop coupler. The antenna height which is the distance between the central conductor and return conductor (back plane) and the antenna length. The distance between the central conductor and return conductor determines the magnitude of the antenna current necessary to couple a fixed amount of power into a particular plasma. Current flowing in the return conductor tends to reduce the magnetic field flux from the current flowing in the center conductor. The electric field along the return conductor also tends to reduce the electric field along the center conductor. As a result, to keep the electric and magnetic fields which penetrate into the plasma constant (and thus keep the power which is coupled into the plasma approximately constant) the antenna current and voltage must increase as the the separation between the center and return conductors decreases. A higher voltage and current for a smaller antenna height means more Ohmic loss and more likely a chance of breakdown. Too great of a separation makes the characteristic antenna impedance so large that it is difficult to match to it with a feed transmission line.

The antenna length partly determines the amount of ion Bernstein wave power which is electron Landau damped. The $k_{||}$ power spectrum of the ion Bernstein waves which efficiently couple into the plasma is determined by the antenna geometry (length mainly) and the plasma coupling function[18]. The plasma coupling function acts as a

filter to the antenna Fourier current spectrum† . The general result is that less power is electron Landau damped for a longer antenna assuming that $fl >> \pi v_{te}$ where l is the antenna length, f is the driving frequency, and $v_{te} = (2T_e/m_e)^{1/2}$.

Based on the above simple considerations it can be concluded that a good ion Bernstein wave loop coupler must have a current element aligned along the local magnetic field, a large separation between the central and return conductors, and an antenna length which minimizes the electron Landau damped power. Although these parameters were optimized for the Alcator C antenna, it was primarily the space and engineering constraints which determined the final antenna dimensions.

3.4.3: Electrical Transmission Line Model

The voltage and current characteristics of the antenna are best understood in terms of an electrical transmission line model. Before discussing the specific aspects of the Alcator C ion Bernstein wave antenna it is useful to review some results of standard transmission line theory.

Using the distributed element model for a transmission line shown in Fig. 3.6 the limiting differential equations corresponding to this model for the voltage V and current I are

$$-\frac{\partial V}{\partial x} = L\frac{\partial I}{\partial t} + RI \tag{3.4.1}$$

$$-\frac{\partial I}{\partial x} = C\frac{\partial V}{\partial t} \tag{3.4.2}$$

where L, C, and R are the inductance, capacitance, and resistance per unit length of the transmission line system. These two equations combine to yield a second order partial differential equation for the voltage

$$LC\frac{\partial^2 V}{\partial t^2} - \frac{\partial^2 V}{\partial x^2} + RC\frac{\partial V}{\partial t} = 0. \tag{3.4.3}$$

The power source has a real frequency $f = \omega/2\pi$ so that the time dependence of all quantities can be expressed by the function $\exp[-i\omega t]$. Solving Eqs. 3.4.1 for the voltage and current spatial dependence gives

† The standard treatment of this problem is not self-consistent. The antenna current is assumed known and the antenna–plasma coupling problem is then solved to obtain the $k_{\|}$ power spectrum.

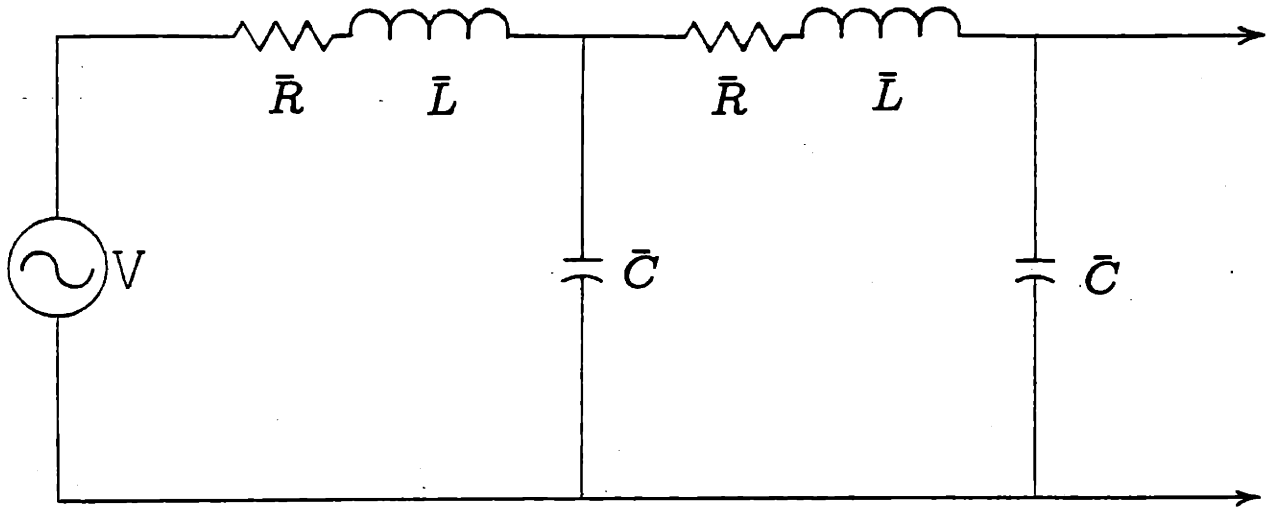

Figure 3.6 —Distributed element model used to derive the transmission line equations.

$$V(x) = V_0 \left[e^{ikx} + \Gamma e^{-ikx} \right] \tag{3.4.4}$$

$$I(x) = \frac{V_0}{Z} \left[e^{ikx} - \Gamma e^{-ikx} \right] \tag{3.4.5}$$

where

$$k = \omega\sqrt{LC} \left[1 + i\frac{R}{L\omega} \right]^{1/2} \tag{3.4.6}$$

$$Z = Z_0 \left[1 + i\frac{R}{L\omega} \right]^{1/2} \tag{3.4.7}$$

$$Z_0 = \sqrt{\frac{L}{C}}. \tag{3.4.8}$$

The quantity Γ is defined as the voltage reflection coefficient and Z is the characteristic impedance of the transmission line. It is pointed out that the analytic expression which is to be used for evaluating a quantity $Q(x,t)$ numerically is

$$Q(x,t) = \mathrm{Re}\left[Q(x) e^{-i\omega t} \right]. \tag{3.4.9}$$

A transmission line may either terminate with a load, expressed as an impedance Z_L, or encounter a transform to another transmission line with characteristic impedance Z_L at the location† $x = 0$. In either case‡ a fraction of power is reflected and a fraction is absorbed (or transmitted) at $x = 0$. The voltage reflection coefficient, which determines the fraction of power reflected, is given by

$$\Gamma = \frac{Z_L - Z}{Z_L + Z} \tag{3.4.10}$$

where

$$Z_L = \frac{V(x=0)}{I(x=0)}. \tag{3.4.11}$$

† The location is completely arbitrary, however it is chosen to be at $x = 0$ since this choice simplifies the resulting expressions.

‡ The remainder of this discussion assumes that the transmission line is terminated in a load. Power dissipated by the load is then written as P_{diss}. This development is equivalent for an impedance transform in which case P_{diss} represents the power transmitted into the transmission line with characteristic impedance Z_L.

The transmission line equations can be combined to give an equation for the temporal and spatial dependence of the power

$$\frac{\partial}{\partial x}P = -\frac{\partial}{\partial t}\left[\frac{1}{2}LI^2 + \frac{1}{2}CV^2\right] - RI^2 \tag{3.4.12}$$

where $P = VI$. The term on the right of Eq. 3.4.12 in square brackets represents the stored magnetic and electric energy; the second term on the right represents Ohmic loss along the transmission line. Assuming quantities of the form of Eq. 3.4.9 and time averaging Eq. 3.4.12 over one period gives

$$\frac{\partial}{\partial x}\bar{P} = -\frac{1}{2}RI^*I \tag{3.4.13}$$

where $\bar{P} = \mathrm{Re}(\frac{1}{2}VI^*)$ is the time averaged power. Assuming that $\Gamma = 0$, Eq. 3.4.13 can be solved to give the spatial dependence of $\bar{P}(x)$ as

$$\bar{P}(x) = P_0 e^{-xR/Z_0}. \tag{3.4.14}$$

(where it is assumed that $R/(k_0 Z_0) \ll 1$). $P_0 = \frac{1}{2}|V_0|^2/Z_0$ is the power which is propagating in the $+x$ direction at $x=0$. An equation for $\bar{P}(x)$ in a coaxial transmission line with inner radius a, outer radius b, and transmission line material of conductivity σ can be obtained by solving the Maxwell equations. This has been done in Ref. 19 and the result is

$$\bar{P}(x) = P_0 e^{-2\gamma x} \tag{3.4.15}$$

where

$$\gamma = \frac{c}{4\pi}\frac{1}{2\sigma\delta}\frac{\frac{1}{a}+\frac{1}{b}}{\ln\frac{b}{a}} \tag{3.4.16}$$

and the skin depth δ is

$$\delta = \frac{c}{\sqrt{4\pi}}\left(\frac{2}{\omega\sigma}\right)^{1/2}. \tag{3.4.17}$$

Equating the two expressions for $\bar{P}(x)$ gives a relation for R in terms of the transmission line material conductivity for a coaxial transmission line as

$$2\gamma = \frac{R}{Z_0}. \tag{3.4.18}$$

If $\Gamma \neq 0$ the solution to Eq. 3.4.13 is slightly more complicated and is written as

$$\bar{P}(x) = P_0 \left[e^{-xR/Z_0} - |\Gamma|^2 e^{xR/Z_0} + \frac{R}{Z_0} \mathrm{Re}\left(i \frac{\Gamma}{k_0} (e^{-2ik_0 x} - 1) \right) \right] \tag{3.4.19}$$

The quantity $\bar{P}(x)$ represents the difference between the power flowing in the $+x$ direction and the reflected power (from the load at $x = 0$) flowing in the $-x$ direction at the position x. Equation 3.4.19 gives the *spatial dependence of the* **dissipated** *power.*

When $R = 0$ and the Ohmic loss is negligible, the power dissipated by the load is given by Eq. 3.4.19 as

$$P_{\mathrm{diss}} = \frac{1}{2} \frac{1}{Z_0} |V_0|^2 \left[1 - |\Gamma|^2 \right] \tag{3.4.20}$$

$$= P_0 \left[1 - |\Gamma|^2 \right]. \tag{3.4.21}$$

where the two terms in square brackets represent the power flow towards the load (P_0) and the power reflected away from the load $P_0|\Gamma|^2$. Since P_0 or P_{diss} is usually a known quantity, Eq. 3.4.21 can be used to determine the value of $|V_0|$. The quantities $V(x)$ and $I(x)$ are now determined to within an arbitrary phase factor.

A measure of the severity of mismatch between the transmission line of characteristic impedance Z and the load of impedance Z_L is indicated by a quantity called the voltage standing wave ratio (VSWR). This is the ratio of the maximum voltage magnitude to the minimum voltage magnitude† and is given by

$$\mathrm{VSWR} = \frac{1 + |\Gamma|}{1 - |\Gamma|}. \tag{3.4.22}$$

A VSWR value of unity means that the transmission line is terminated with a matched load and no power is reflected at the load in this case. In situations where a matching network is placed somewhere between the load and the power source the reflected power is sometimes called the circulating power. The reflected power then circulates back and forth between the load and matching network. An expression for the circulating power can be given in terms of the dissipated power as

$$P_{\mathrm{cir}} = P_{\mathrm{diss}} \frac{|\Gamma|^2}{1 - |\Gamma|^2}. \tag{3.4.23}$$

In terms of the VSWR, the circulating power is written as

$$P_{\mathrm{cir}} = P_{\mathrm{diss}} \frac{(\mathrm{VSWR} - 1)^2}{4\mathrm{VSWR}}. \tag{3.4.24}$$

† This can easily be obtained analytically by calculating the two zeros of $\frac{d}{dx}|V(x)|$.

It is clear from both Eqs. 3.4.23–24 that a severe mismatch ($|\Gamma| \simeq 1$) can establish a very large circulating power. This power can set up large voltages in the transmission line carrying this circulating power. The maximum voltage achieved in the high circulating power region is

$$V_{\max} = \sqrt{2P_{\text{diss}} Z_0 \text{VSWR}} \tag{3.4.25}$$

where $V_{\max}$ is the peak voltage (as opposed to the root mean square value). This voltage is important since the region of high circulating power must be designed to withstand breakdown from this maximum voltage.

3.4.4: Electrical Analysis of the Antenna

Actual values of C, L, and R are necessary in order to apply the preceeding transmission line model to the antenna. Neither C nor L were measured so their values must be estimated. Radiated power from the antenna is included in the transmission line model by an increased value of R. The value of R is chosen so as to give the correct power dissipation due to both the antenna Ohmic loss and any radiated power loss. Its value can be inferred from the measured radiation resistance.

Throughout the antenna electrical analysis the antenna magnetic field is approximated as the magnetic field of a conductor above a finite ground plane (similar to a stripline transmission line). The electric field is approximated as the the electric field of a coaxial transmission line mode. Approximating the fields in this way gives electric and magnetic fields which lie in a cross–sectional plane of the antenna but which are not perpendicular to each other. This means that there must be electric and magnetic field components perpendicular to the cross–sectional plane of the antenna which have been neglected. There are two parameters which roughly indicate the accuracy of this simple approach. The first parameter is $R/(k_0 Z_0)$ where R is determined from both Ohmic and radiation loss. A small value for this parameter indicates that the radiation effects are small and that the antenna fields do not deviate much from the true transmission line fields. The second parameter is $1 - v_\phi/c$ where v_ϕ is the speed of electromagnetic wave propagation along the direction of the antenna central conductor. A small value of this parameter indicates that the neglected electric and magnetic field components (perpendicular to the antenna cross–sectional plane) are small and that the approximate fields are not far from realistic. Both of these parameters are essentially small for the Alcator C antenna and justify the approximations to the antenna electric and magnetic fields.

The quantity C is proportional to the energy density in the electric field. An estimate of C can be made by approximating the antenna electromagnetic mode as a coaxial TEM mode. The electric potential for a TEM mode is obtained by solving the

two dimensional Laplace equation in the cross–section of the antenna. This was done numerically for the antenna geometry using a computer code called JASON[20]. Figure 3.7 shows the potential contours and electric field energy density for the antenna. The capacitance per unit length was computed from this method to be

$$C = \frac{1}{4\pi}(8.0). \tag{3.4.26}$$

The quantity L is proportional to the magnetic field energy density. Its value was estimated by approximating the antenna as a center conductor above a finite back plane, without the Faraday shield. The inductance per unit length is estimated† from Ref. 21 to be

$$L = \frac{4\pi}{c^2}(0.26)\,\mathrm{s^2\text{–}cm^{-2}}. \tag{3.4.27}$$

The characteristic impedance is now calculated to be

$$Z_0 = \sqrt{L/C} = 68\,\mathrm{Ohms}\,(\Omega). \tag{3.4.28}$$

and the phase speed of wave propagation along the antenna is

$$v_\phi = \frac{1}{\sqrt{LC}} = 0.69c. \tag{3.4.29}$$

The value of Z_0 was not measured; however, the value of v_ϕ was measured by determining the spatial dependence of the antenna current with a movable current probe. Measured this way, the phase speed was found to be $v_{\phi\mathrm{meas}} \simeq 0.65\,c$. This measurement has a 10% error associated with it. The estimated value from Eq. 3.4.29 is within the experimental error indicating that the electrical model is quite accurate.

The value of R can be calculated in terms of the measured radiation resistance R_{rad}. To obtain this value, Eq. 3.4.19 is used first to express the dissipated power in one arm of the antenna. This is given approximately by

$$\mathrm{Re}(P_{\mathrm{diss}}) \simeq \frac{1}{2}\frac{1}{Z_0}|V_0|^2\left(\frac{Rl}{Z_0}\right)\left[1+\frac{\sin(k_0 l)}{k_0 l}\right] \tag{3.4.30}$$

where $l = 25\,\mathrm{cm}$, $Z_0 = 68\,\Omega$, $\Gamma = -1$, and it is assumed *a priori* that $Rl/Z_0 << 1$. It is now possible to obtain an equivalent radiation resistance from the above expression.

† The magnetic field energy density can in principle be obtained numerically from JASON since the electric potential and magnetic field in the antenna cross section are proportional. This method was not followed due to the difficulty of numerically expressing the boundary condition far away from the antenna.

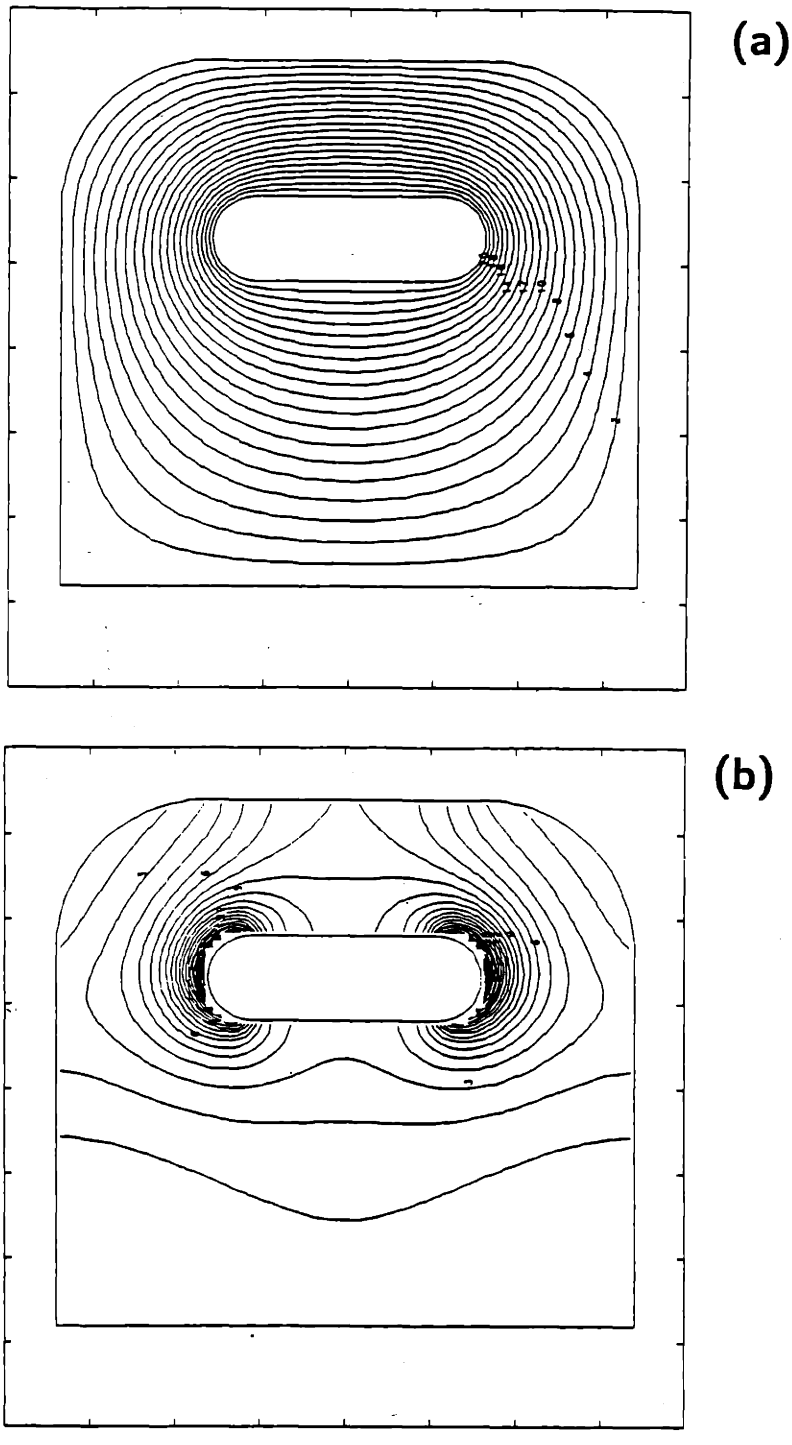

Figure 3.7 —(a) Electric potential contours for the Alcator C ion Bernstein wave antenna. (b) The electric field energy density contours corresponding to (a).

Radiation resistance is defined in terms of the dissipated power as

$$P_{\text{diss}} \equiv \frac{1}{2}|I|^2 R_{\text{rad}} \tag{3.4.31}$$

$$= \frac{1}{2}|I|^2 \left[R_{\text{ant}} + R_{\text{Oh}}\right] \tag{3.4.32}$$

where I is the peak current reached at some point in the antenna, P_{diss} is the total power dissipated, R_{ant} is proportional to the radiated power and R_{Oh} is proportional to the Ohmic power loss. The forward and reflected powers were measured using directional couplers at a location near the matching network. The dissipated power and radiation resistance therefore includes Ohmic power loss in the antenna and along all of the transmission line connecting the matching network and antenna. The fraction of this power which is dissipated by antenna radiation is proportional to R_{ant} and the fraction of power dissipated by Ohmic loss in the antenna and between the antenna and the matching network (where the power is measured) is proportional to R_{Oh}. The value of R_{Oh} is approximately given by the antenna system loading in a vacuum (when no plasma is present). The power radiated by the antenna into the plasma can now be written as

$$P_{\text{ant}} \simeq P_{\text{diss}} \left[1 - \frac{R_{\text{vac}}}{R_{\text{rad}}}\right]. \tag{3.4.33}$$

The peak current occurs at $x = 0$ where $\Gamma = -1$ and has a value given by Eq. 3.4.5 of $I_{\text{max}} \simeq 2V_0/Z_0$. Two antenna arms dissipate twice as much power as is shown by Eq. 3.4.30 and give the contribution to R from only antenna radiated power expressed in terms of R_{rad} as

$$R \simeq 4.3 \times 10^{-2}\,\text{cm}^{-1}\,\left[R_{\text{rad}} - R_{\text{vac}}\right]. \tag{3.4.34}$$

It can now be verified that indeed $Rl/Z_0 \ll 1$ as was assumed.

The part of R which results from Ohmic loss in only the antenna is a small fraction of the total Ohmic loss since the antenna elements are silver plated and the antenna length is small compared to the length of the entire transmission line. Its value, in principle, can be estimated by calculating the Ohmic loss due to the finite conductivity of silver. Since the antenna is not a simple transmission line and the true electromagnetic fields within the antenna are complicated, this calculation will not be done† for the antenna. Rather, the Ohmic loss is better estimated from the measured vacuum radiation resistance. The vacuum radiation resistance results from Ohmic loss in the antenna,

† In fact, if the antenna geometry is approximated as a cylindrical coaxial transmission line and a coaxial electromagnetic mode approximation is made for the antenna fields, the calculated Ohmic loss is within a factor of two of the value estimated from the measured vacuum radiation resistance.

antenna feed, the coaxial cable between the matching network and the antenna, and Ohmic loss in the vacuum chamber. Since the antenna characteristic impedance is $\sim 34\,\Omega$ and the antenna feed characteristic impedance is $\sim 30\,\Omega$ the antenna and feed are essentially matched. In addition, the $30\,\Omega$ feed is matched to the remainder of the transmission line system (at $50\,\Omega$) with a quarter wave impedance transformer. This means that the circulating power is approximately the same in all regions of the antenna system. As a result, the Ohmic power loss per unit length of transmission line is approximately proportional to $(1/a + 1/b)(Z_0\sqrt{\sigma})^{-1}$ (see Eq. 3.4.16) where σ is the conductivity of the transmission line material and a and b are the inner and outer radii of the transmission line respectively. The transmission line system is entirely copper (excluding the antenna and antenna feed) and has a length of approximately 20 meters. The Ohmic loss in the vacuum chamber is difficult to estimate; however, an upper bound on the antenna Ohmic loss R can be estimated by assuming that the vacuum chamber loss is negligible. Therefore, to a very rough approximation, the antenna represents less than 10% of the total Ohmic power loss. The contribution to R from antenna Ohmic loss is therefore

$$R \lesssim 4.3 \times 10^{-3}\,\mathrm{cm}^{-1}\,R_{\mathrm{vac}}. \tag{3.4.35}$$

This gives a total value for the antenna resistance per unit length (for $R_{\mathrm{rad}} \sim 1.5\,\Omega$ and $R_{\mathrm{vac}} \sim 0.3\,\Omega$) of $R \lesssim 5.3 \times 10^{-2}\,\Omega\,\mathrm{cm}^{-1}$.

The antenna electrical characteristics can be summarized at this point as follows. The measured phase speed of electromagnetic waves along the antenna is $0.65\,c$, the characteristic impedance of each half of the antenna is about $68\,\Omega$, and the Ohmic contribution to the antenna loading is very small compared to the radiation loading. For a total dissipated power of 100 kW, the voltage between the antenna center and return conductors reaches a maximum of about 1.3 kV and the maximum current at the antenna end is about 408 Amperes. The electric field along the direction of the antenna center conductor is approximately 1.1 kV/cm for the same power.

3.4.5: Antenna Current Probes

Current probes were placed at each shorted end of the antenna halves. The probes consisted of a coaxial cable filled with a magnesium oxide dielectric with the center conductor rapped into a small loop and electrically connected to the outer conductor. The probe was oriented so as to intercept the magnetic field flux produced by the antenna current. Since each probe was placed at a minimum voltage position on the antenna it was not necessary to correct for any capacitive effects on the probes. The purpose of the probes was to measure the antenna current from which the radiation resistance could be calculated. A typical value for the antenna current was about 400 Amperes for a power of 100 kW.

3.4.6: Antenna Movement

A bellows assembly supported the antenna and allowed it to be moved radially (closer to the plasma) and rotated to change the alignment of the center conductor with respect to the toroidal magnetic field. Moving the antenna radially produced observable and repeatable changes in the radiation resistance and in the hydrogen ion heating rate ($\Delta T_H/P_{rf}$). No significant changes were observed when the antenna was rotated up to 20° from being aligned to the magnetic field.

3.4.7: Faraday Shield

The two purposes of the Faraday shield are to polarize the electric field entering the plasma and to keep plasma particles from entering the antenna interior. One disadvantage of having the Faraday shield present is that the shield reduces the total magnetic flux which couples to the plasma[22]. This can reduce the antenna–plasma coupling and increase the voltage within the antenna. This effect was measured for the Alcator C antenna. It was found that the first shield only reduced the initial flux by about 10% and the first and second shields together reduced the initial flux by about 30%.

3.4.8: Overview of the Transmission Line and Matching Network

Power entered the antenna from a 30 Ω coaxial section of silver plated transmission line. The value of 30 Ω was chosen because it minimizes the voltage between the inner and outer conductors for a given power and because this impedance is nearly matched to the antenna impedance. The feed passed through a gap in the toroidal magnet and connected onto a quarter wave long section of transmission line which transformed the impedance from the 30 Ω antenna feed to the 50 Ω vacuum feed–thru. The feed–thru acted as a vacuum to air transition. After the feed–thru, the 50 Ω transmission line connected to a DC break which electrically insulated the power system and antenna operator controls from the tokamak potential. Finally, the transmission line passed through a matching network which served to electrically match the antenna system to the power system. The remainder of this section will discuss the power flow between the matching network and antenna and present the characteristics of the matching network (see Fig. 3.4).

3.4.9: Power Flow in the High VSWR Region

The region of transmission line between the matching network and antenna contains a large amount of circulating power. This power is attenuated due to the finite conductivity of the transmission line. The Ohmic loss, which amounts to nearly 20% of the incoming power, is proportional to the ratio of R_{vac} to R_{rad} since R_{vac} is proportional to an approximate upper bound on the power Ohmically dissipated by the transmission line. A value of R for the transmission line can be estimated from Eq. 3.4.19 by requiring that 20% of the power is Ohmically dissipated in the line. The result for R is

$$R \simeq 1.4 \times 10^{-4}\,\Omega\,\text{cm}^{-1}. \tag{3.4.36}$$

where the length of the line is 20 meters and the reflection coefficient at the antenna is estimated to be $\Gamma \simeq 0.978$. The value of R can also be calculated from Eqs. 3.4.16 and 3.4.18. The conductivity of copper at 20° is

$$\sigma_{\text{Cu}} = \frac{c^2}{10^{11}}\left(1.7 \times 10^{-8}\right)^{-1}\,\text{sec}^{-1}. \tag{3.4.37}$$

At a frequency of $f = 183.6\,\text{MHz}$ the skin depth is

$$\delta = 4.8 \times 10^{-4}\,\text{cm}. \tag{3.4.38}$$

The value of γ is calculated from this to be

$$\gamma = 1.6 \times 10^{-6}\text{cm}^{-1} \tag{3.4.39}$$

where a and b are measured to be

$$\begin{aligned} a &= 4.84\,\text{cm} \\ b &= 11.2\,\text{cm} \end{aligned} \tag{3.4.40}.$$

The resistance per unit length is calculated from Eq. 3.4.18 as

$$R = 1.6 \times 10^{-4}\,\Omega\,\text{cm}^{-1}. \tag{3.4.41}$$

The two independently evaluated values of R are quite close confirming that most of the Ohmic power loss occurs in the transmission line and only a small amount in the vacuum chamber and antenna structure. It is an easy matter now to estimate the peak voltage in the transmission line system for a total dissipated power of 100 kW. Using Eqs. 3.4.22 and 3.4.25, the maximum voltage, when no plasma is present, is estimated to be 30 kV.

3.4.10: Matching Network

The purpose of the matching network is to transform the antenna system impedance to the impedance of the transmission line coming from the power system (50 Ω). This was done in the ion Bernstein wave antenna system by attaching three stub tuners in parallel with the main transmission line. A stub tuner consists of a transmission line terminated with a movable short. The location of the short in each stub tuner could be adjusted over a distance of about $\lambda/2$ (at a frequency of 180 MHz). Each stub tuner was separated from the other by a section of main transmission line slightly less than $\lambda/8$ in length. The transmitter frequency was adjustable (about $\pm 10\%$), and over this range of frequencies the phase of the antenna load could vary considerably due to the long length of transmission line between the matching system and the antenna. Consequently, it was necessary to use three stubs rather than two. Figure 3.8 shows a scatter plot of the region in the complex Γ plane† accessible to a system of two stub tuners. The scatter plot is obtained by evaluating Γ for a discrete set of tuner settings spanning all possible positions of the tuners. In general, this sort of system cannot access the entire range of $|\Gamma| \leq 1$. There is some redundancy for three stubs, but the entire range of $|\Gamma| \leq 1$ is accessible. During experimental operation, the stub nearest to the power system was generally set to a fixed position and the other stubs were adjusted for tuning.

In principle, it is possible to calculate from the load impedance Z_L the correct stub positions for a match. This can be done by measuring the amplitude and phase of the forward and reflected powers in the high VSWR region near the matching network. From this, the exact value of Z_L can be calculated. Once Z_L is known, the exact stub positions can be obtained numerically.

A system to measure the amplitude and phase of the forward and reflected powers was constructed for the ion Bernstein wave experiments. The system was tested in the lab for several tuner configurations and produced accurate enough results so that the correct tuner positions for a match could be determined. The system failed, however, on the ion Bernstein wave transmission line system due to errors in evaluating the forward and reflected powers and their phases. These errors were due to uncertainties in long cable lengths and power attenuation factors in the cables. It can be justified that small errors in the forward and reflected powers will strongly upset the calculation of the stub positions for a match. This follows by considering the properties of the antenna system as a high Q cavity. The total stored energy in the cavity will exhibit a

† The load impedance Z_L which can be matched to the power system with the particular tuner configuration is related to Γ by Eq. 3.4.10.

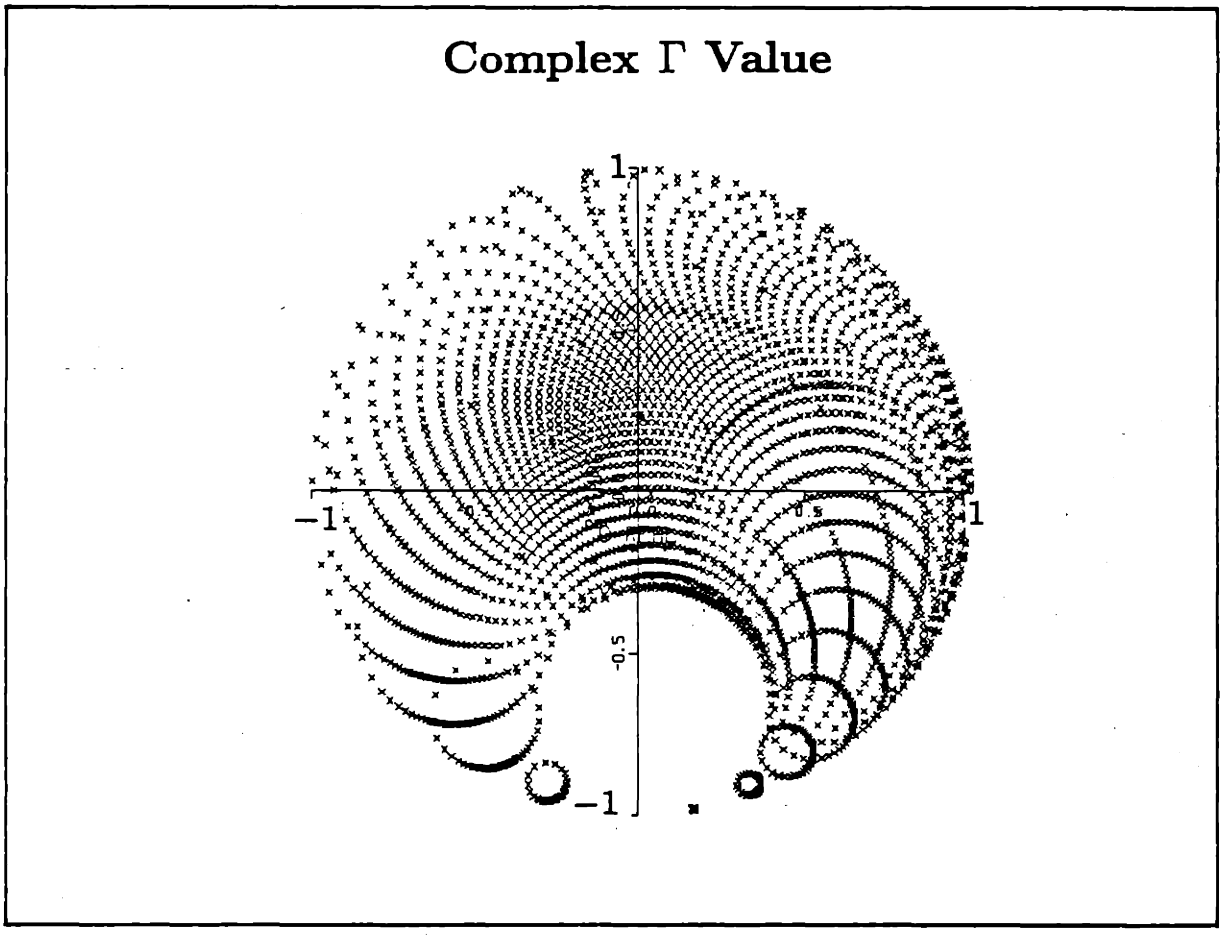

Figure 3.8 —Scatter plot of the accessible complex Γ (reflection coefficient) for a two stub tuner system.

maximum at the correct stub settings. At constant frequency and dissipated power, the stored energy in the cavity is a function of the three stub lengths l_j, where $j = 1, 2, 3$. The width of the stored energy peak expressed in terms of the cavity parameters (l_j) is given approximately by $\Delta l_j \sim (2\pi k_0 Q)^{-1}$ where $k_0 = \omega_0/c$. Thus, the measurements must be accurate enough to give the stub lengths to within Δl_j. A large value of Q therefore requires very accurate measurements to correctly evaluate the stub positions.

3.5: Conclusions

This chapter describes the diagnostics used on Alcator C which were important for the ion Bernstein wave experiments. In addition, the physical and electrical properties of the antenna system have been calculated and the voltage and current inside the antenna structure have been reported. Finally, the properties of the three stub tuner system have been discussed.

REFERENCES

1. S. L. Davis, D. Mueller, and C. J. Keane, *Review of Scientific Instruments*, **54**, 315, (1983).
2. R. Watterson, *et al.*, *Bull. Am. Phys. Soc.*, **30**, 1497, (1985).
3. S. M. Wolfe, K. J. Button, J. Waldman, and D. R. Cohn, *Applied Optics*, **15**, 2645, (1976).
4. M. E. Foord, E. S. Marmar, and J. L. Terry, *Rev. Sci. Instrum.*, **53**, 1407, (1982).
5. J. F. Camacho and R. S. Granetz, *Rev. Sci. Instrum.*, **57**, 417, (1986).
6. R. D. Benjamin, A. Nudelfuden, J. L. Terry, and H. W. Moos, *Rev. Sci. Instr.*, **56**, 870, (1985).
7. A. Wan, MIT Plasma Fusion Center Report PFC/RR–86–13, (1986).
8. M. M. Pickrell, MIT Plasma Fusion Center Report PFC RR/82–30, (1982).
9. Y. Takase, MIT Plasma Fusion Center Report PFC/RR–83–29, (1983).
10. R. L. Watterson, R. E. Slusher, and C. M. Surko, *Phys. Fluids*, **28**, 2857, (1985).
11. R. E. Slusher and C. M. Surko, *Phys. Rev. Lett.*, **37**, 1747, (1976).
12. J. Sheffield, *Plasma Scattering of Electromagnetic Radiation*, (Academic Press, New York, 1975).
13. T. Watari, *et al.*, *Phys. Fluids*, **21**, 2076, (1978).
14. T. Watari, *et al.*, *Nucl. Fusion*, **22**, 1359, (1983).
15. F. Skiff, Ph. D. Thesis, *Linear and Nonlinear Excitation of Slow Waves in the Ion Cyclotron Frequency Range*, Princeton University, (1985).
16. M. Ono, T. Watari, R. Ando, *et al.*, *Phys. Rev. Lett.*, **54**, 2239 (1985).
17. J. P. M. Schmitt, *Phys. Rev. Lett.*, **31**, 982, (1973).
18. M. Ono, Ion Bernstein Wave Heating, Theory and Experiment, in Proc. Course and Workshop on Applications of rf Waves to Tokamak Plasmas, Varenna 1985.
19. J. D. Jackson, *Classical Electrodynamics*, Second Edition, (John Wiley and Sons, New York, 1975).
20. S. J. Sackett, Lawrence Livermore Laboratory Report UCID–17814, (1978).
21. S. Y. Liao, *Microwave Devices and Circuits*, Second Edition, (Prentice Hall, Englewood Cliffs, NJ, 1985).
22. C. M. Fortgang, D. Q. Hwang, *IEEE Transactions on Plasma Science*, **PS–13**, 569, (1985).

CHAPTER 4

Ion Bernstein Wave Experimental Results

4.1: Introduction

Ion Bernstein wave experiments were performed on Alcator C to study wave excitation, propagation, absorption, and plasma heating due to wave power absorption. Since the Alcator C tokamak was designed to mainly study the confinement physics of high density, high temperature plasmas, most of the ion Bernstein wave experiments emphasized the various aspects of plasma heating rather than the aspects of wave coupling and propagation. As a result, the majority of the discussion in this chapter and the succeeding one will focus on the heating results.

Ion Bernstein waves were launched from a stainless steel, center fed, T–shaped, movable loop antenna with the center conductor aligned along the direction of the toroidal magnetic field and surrounded by a double layer, molybdenum coated Faraday shield. The experiments were conducted under the following conditions: rf frequency

$f_0 = 183.6\,\mathrm{MHz}$; plasma minor radius (set by molybdenum limiters) $a = 0.115\,\mathrm{m}$, $0.12\,\mathrm{m}$, or $0.125\,\mathrm{m}$; major radius $R_0 = 0.64\,\mathrm{m}$; hydrogen majority plasma with a deuterium minority $0.1\% \lesssim n_D/(n_{H+D}) \lesssim 20\%$; toroidal magnetic field strength $4.8\,\mathrm{T} \leq B_0 \leq 11\,\mathrm{T}$; line–averaged electron density $0.6 \leq \bar{n}_e \leq 4 \times 10^{20}\,\mathrm{m}^{-3}$; $P_{\mathrm{rf}} \leq 180\,\mathrm{kW}$; plasma current $160\,\mathrm{kA} \leq I_p \leq 290\,\mathrm{kA}$; and $Z_{\mathrm{eff}} \sim 1$–4.

This chapter begins by presenting the wave propagation and absorption results. These results confirm that ion Bernstein wave power was coupled into the plasma and followed the expected dispersion relation. Following this, the antenna–plasma coupling and wave excitation measurements are presented. The radiation resistance shows the strongest dependence on magnetic field and plasma density. Weaker dependences are seen with the injected rf power and antenna orientation. Similarly, the presence of the ion Bernstein wave in the plasma, as measured by CO_2 laser scattering[1], shows its strongest dependence on plasma density and magnetic field. Finally, heating results at three values of the toroidal magnetic field[2] are presented. Ion Bernstein wave power injection at powers $P_{\mathrm{rf}} \lesssim 180\,\mathrm{kW}$ produced both significant ion heating ($\Delta T_i \lesssim 380\,\mathrm{eV}$) and improvements in global particle and central impurity confinement times by a factor of up to 3 at densities $\bar{n}_e \gtrsim 1 \times 10^{20}\,\mathrm{m}^{-3}$. At higher densities ($\bar{n}_e \gtrsim 2 \times 10^{20}\,\mathrm{m}^{-3}$), the heating ceases to be efficient and the particle confinement time is no longer enhanced.

4.2: Ion Bernstein Wave Propagation and Absorption

4.2.1: Wave Propagation

Figure 4.1 (a) shows the perpendicular wave–number spectrum of ion Bernstein waves obtained at $x/a = -0.16$ ($x = R - R_0$) from a shot–to–shot scan of the scattering angle using the CO_2 scattering set–up shown in Fig. 3.2. The dispersion relation obtained from the scattering data is shown in Fig. 4.1 (b). The points in Fig. 4.1 (b) are obtained by scanning the scattering volume horizontally at fixed plasma parameters. The value of $k_\perp$ is obtained from the peak in the measured $k_\perp$ spectrum [see Fig. 4.1 (a)] and ρ_{H} is evaluated from the measured value of T_{H} at the toroidal midplane. The agreement between the theoretical and experimental dispersion relations confirms that the scattered signal originates from ion Bernstein waves near the toroidal midplane. The magnitude of the CO_2 scattered signal at $x = +5.1\,\mathrm{cm}$ exhibits a nearly linear dependence on the rf power as is shown in Fig. 4.2 . This further confirms that ion Bernstein wave power was coupled into the plasma.

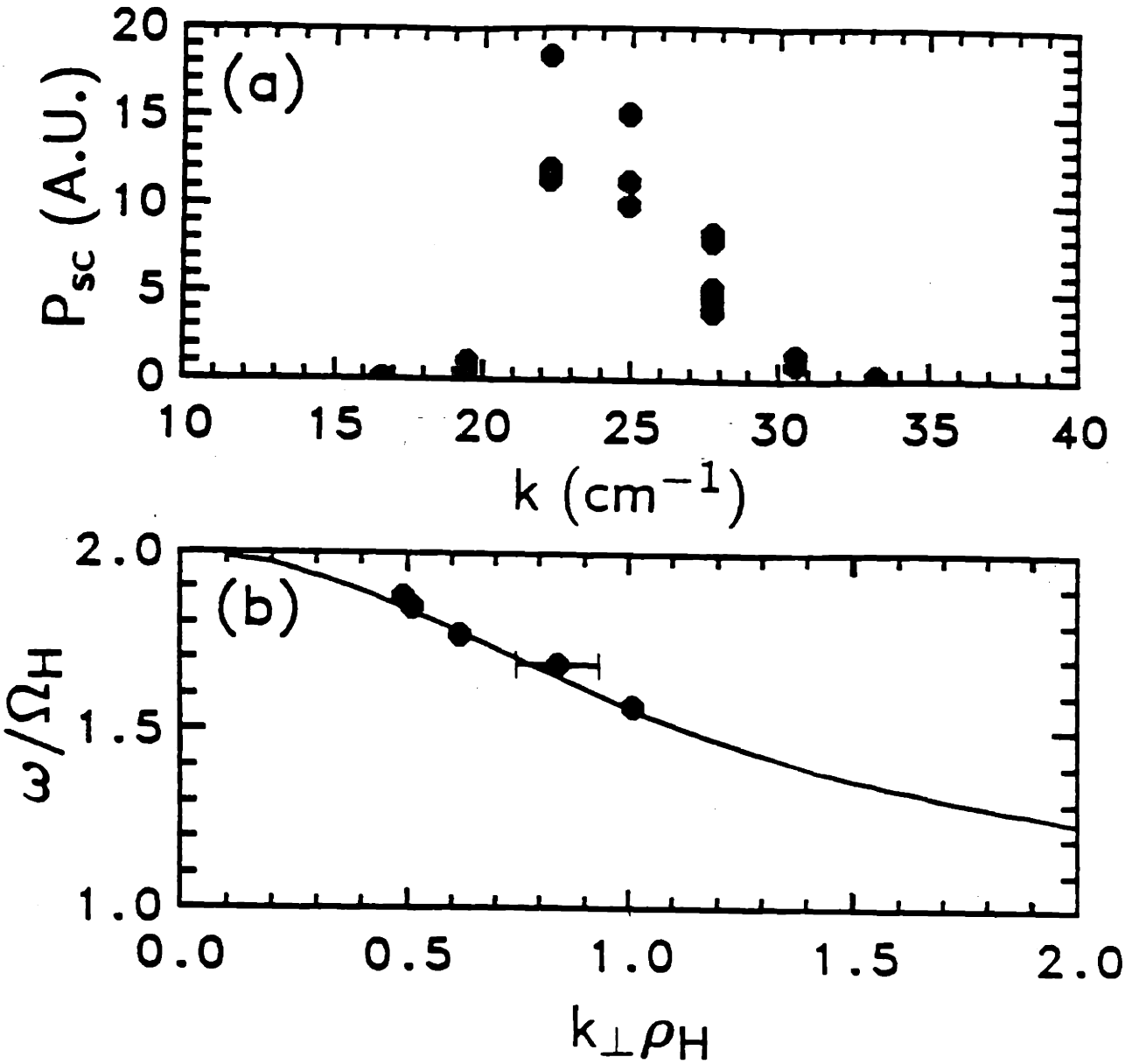

Figure 4.1 —(a) A typical $k_\perp$ spectrum of the ion Bernstein wave. Plasma parameters: Hydrogen, $B = 7.6\,\mathrm{T}$, $I_p = 250\,\mathrm{kA}$, $\bar{n}_e = 2 \times 10^{20}\,\mathrm{m}^{-3}$. (b) Dispersion relation obtained from a spatial scan of the scattering volume. The solid curve represents the theoretical dispersion relation. Plasma parameters: Hydrogen, $B = 7.6\,\mathrm{T}$, $I_p = 290\,\mathrm{kA}$, $\bar{n}_e = 2.3 \times 10^{20}\,\mathrm{m}^{-3}$.

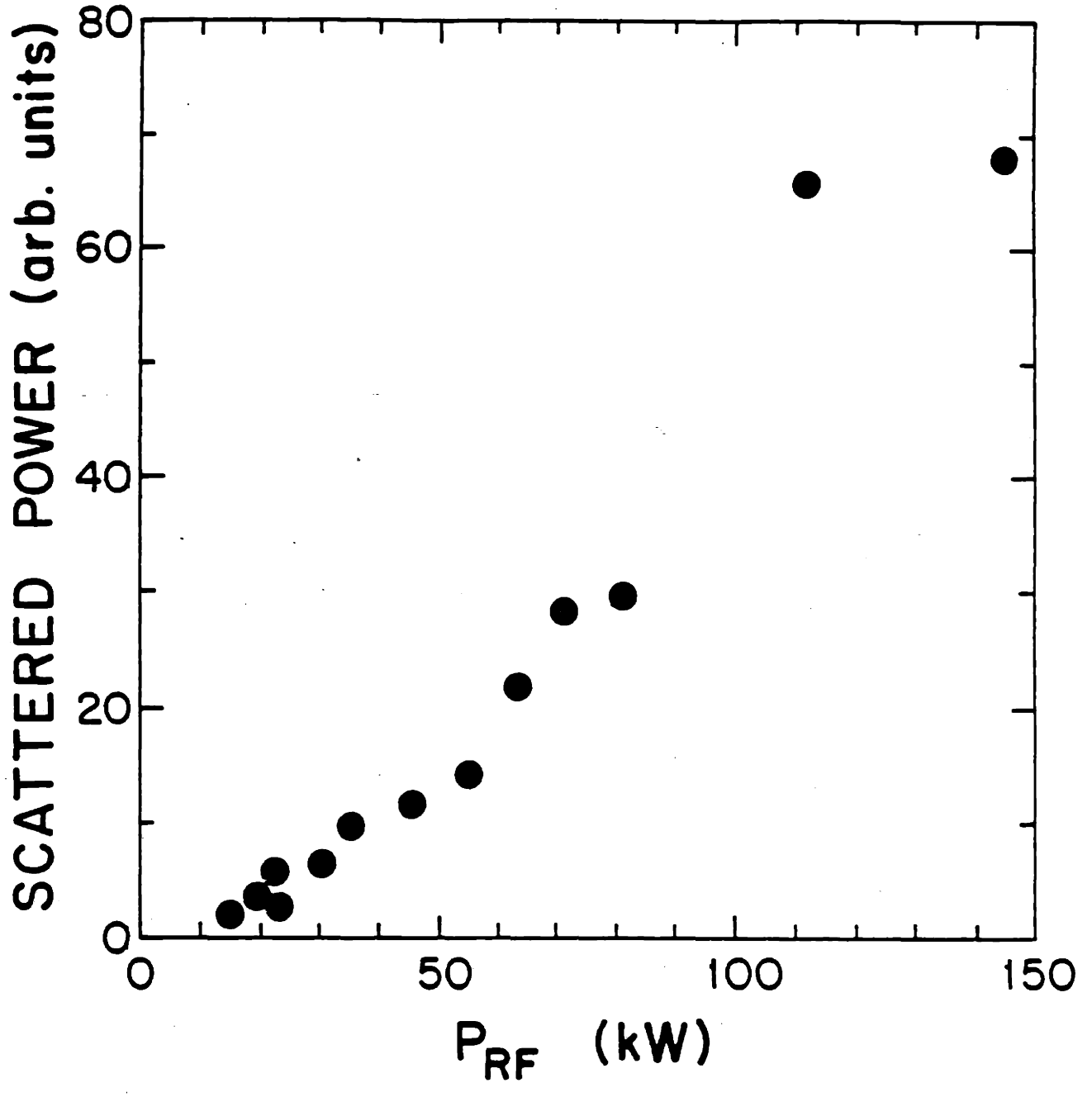

Figure 4.2 —Dependence of CO_2 scattered power on rf injected power at $B_0 =$ 7.6 T. There is a small off–set in the scattered power which has not been included; including this off–set would show zero scattered power for zero rf injected power.

4.2.2: Wave Power Absorption

Absorption of ion Bernstein wave power due to ion cyclotron damping is predicted by linear theory to occur where $\omega = n\omega_{cj}$ (n integer, j ion species). Nonlinear Landau damping may occur where $\omega = \frac{1}{2}(2m+1)\omega_{cj}$ (m integer) and is predicted to dominate linear damping[3] even in the presence of a minority species. The details of ion Bernstein wave power absorption through either mechanism have been given in sections 2.7 and 2.8. Calculated values of the nonlinear threshold power for a single ion species plasma at several central magnetic field values are in the range $P_{\rm th} \sim 10$–$40\,{\rm kW}$ and are given in Ref. 4.

Power absorption of the ion Bernstein wave across the $\omega/\Omega_{\rm H} = 1.5$ layer[1] was studied in a nearly pure hydrogen plasma ($n_{\rm D}/n_e << 0.01$) using CO_2 laser scattering techniques. The radial profile of the scattered power, shown in Fig. 4.3 , exhibits a strong initial radial attenuation near the plasma outer edge. This attenuation, which is observed at all densities, may result from the toroidal spreading of the ion Bernstein wave packet (see Fig. 2.10). Farther into the plasma the scattered power shows a large attenuation across the $\omega/\Omega_{\rm H} = 1.5$ layer. This may be an indication of nonlinear power absorption on the hydrogen or linear absorption on the deuterium.

Power absorption was also investigated at $B \sim 9.3\,{\rm T}$ across the $\omega/\Omega_{\rm D} = 3$ layer located close to the antenna Faraday shield (see Fig. 4.9). The almost complete expected absorption at this location is confirmed by the scattering measurements shown in Fig. 4.4 . The data in Fig. 4.4 was obtained by measuring the scattered power at a fixed scattering location as the magnetic field was increased on a shot–to–shot basis. A large attenuation (by a factor of 40) of the scattered signal from ion Bernstein waves was observed when the $\omega/\Omega_{\rm D} = 3$ layer was placed between the antenna and the scattering volume. Although Fig. 4.4 suggests wave power absorption, the possibility of parametric decay of the ion Bernstein wave at the $\omega/\Omega_{\rm D} = 3$ layer cannot be ruled out[5]. This is the situation where the ion Bernstein wave decays into a lower frequency ion Bernstein wave an an ion quasimode. Since the CO_2 scattering measurement was set up to detect density perturbations only at the pump ion Bernstein wave excitation frequency the lower frequency ion Bernstein wave would be unobservable. Thus, rather than power being absorbed on the ion species through either linear or nonlinear mechanisms at the $\omega/\Omega_{\rm D} = 3$ layer, the wave power may undergo a frequency downshift and continue propagating into the plasma both unimpeded by the $\omega/\Omega_{\rm D} = 3$ layer and undetected by the laser scattering system. At high magnetic fields ($B_0 > 9\,{\rm T}$) such as

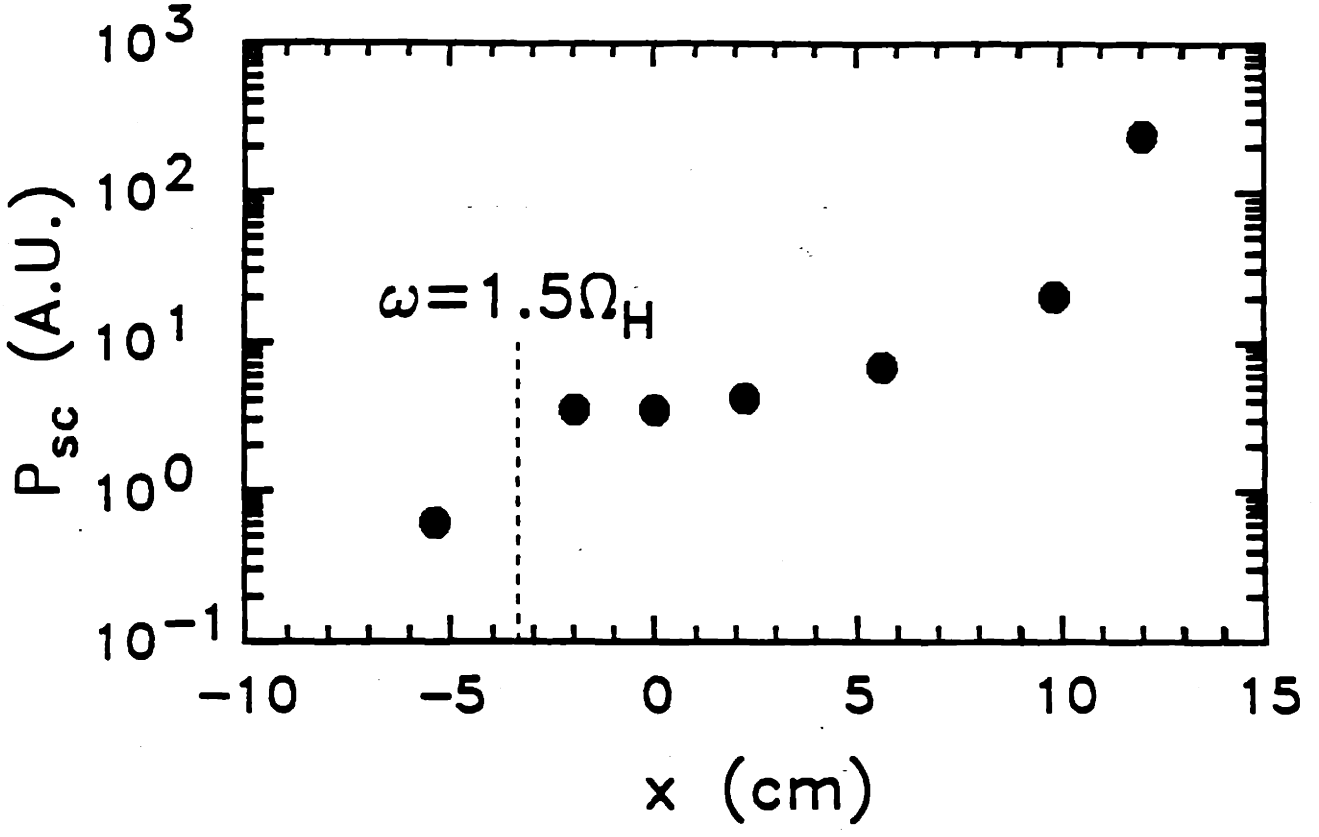

Figure 4.3 —Radial profile of the scattered power. Plasma parameters: Hydrogen, $B_0 = 7.6\,\mathrm{T}$, $I_p = 290\,\mathrm{kA}$, $\bar{n}_e = 0.8 \times 10^{20}\,\mathrm{m}^{-3}$.

this, very broad ($0.98 < f/f_0 < 1.02$) and downshifted frequency spectra were observed confirming the possibility of nonlinear processes.

4.3: Wave Excitation and Antenna–Plasma Coupling

4.3.1: Wave Excitation

Studies of local plasma parameters on wave excitation were made by moving the antenna radially (with respect to the plasma) under fixed plasma parameters. Both the scattered signal from ion Bernstein waves and the ion temperature increase achieved a maximum value when the antenna Faraday shield was located 0.5 cm behind the limiter edge. The density scrape–off length is typically on the order of 0.5 cm. The loading resistance (shown in Fig. 4.5), on the other hand, increased monotonically as the antenna was moved radially closer to the plasma.

4.3.2: Antenna–Plasma Coupling

Antenna–plasma coupling studies were performed with the antenna placed about 0.5 cm behind the limiter edge. Figure 4.6 shows the radiation resistance and scattered signal as a function of magnetic field. A peak in the radiation resistance is observed at about 7.6 T which corresponds to the peak in the scattered CO_2 signal. It is expected that efficient direct launching of ion Bernstein waves should occur when the $\omega/\Omega_H \sim 1.99$ layer is placed just behind the antenna[6]. A nearly field independent background loading of about 1 Ω is observed on either side of the peak. This background may be caused by power dissipation localized near the antenna or by non–resonant excitation of the ion Bernstein wave at a frequency which may be outside the detection range of the CO_2 scattering system.

Figure 4.7 shows the measured value of the radiation resistance and scattered power as a function of line–averaged density. The radiation resistance increases with density until about $\bar{n}_e \simeq 2.8 \times 10^{20}\,\mathrm{m}^{-3}$ and then begins to decrease. The scattered power on the other hand, is maximized at $\bar{n}_e \simeq 1.1 \times 10^{20}\,\mathrm{m}^{-3}$ and decreases to either side of this density. The expected behavior of the scattered power is complicated and is discussed

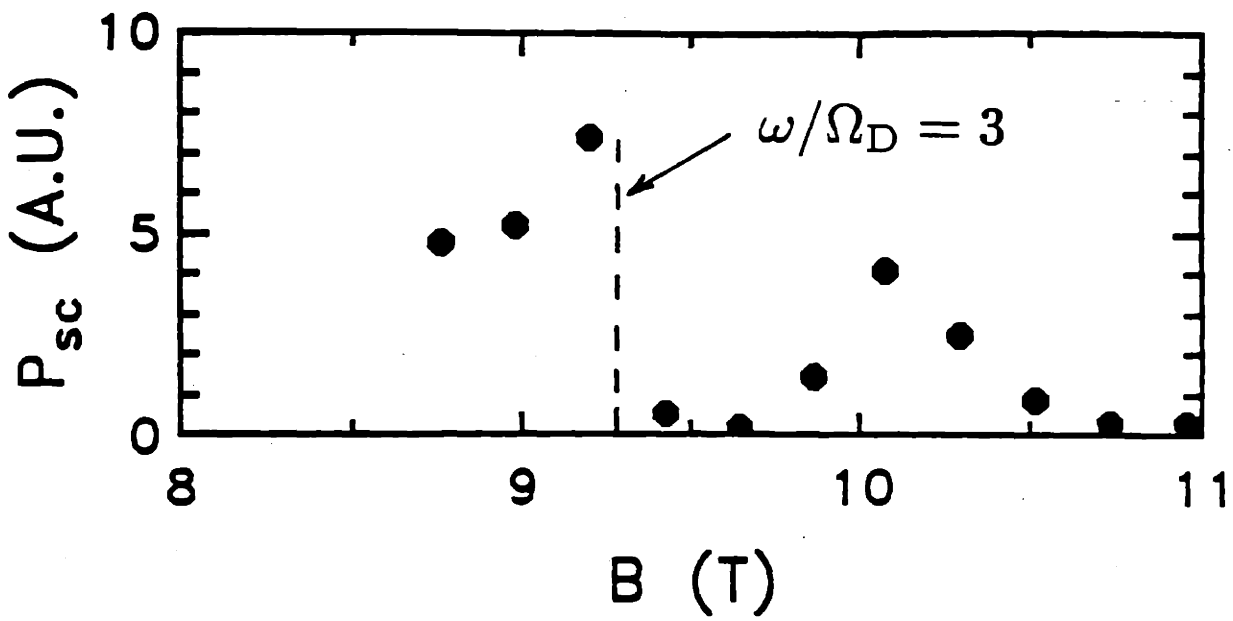

Figure 4.4 —Scattered power at $x/a = +0.85$ as a function of B_0 near 9.3 T showing the strong attenuation of the ion Bernstein wave as it crosses the $\omega/\Omega_D = 3$ layer. Plasma parameters: Hydrogen majority with deuterium minority, $\bar{n}_e = 0.65 \times 10^{20}\,\mathrm{m}^{-3}$.

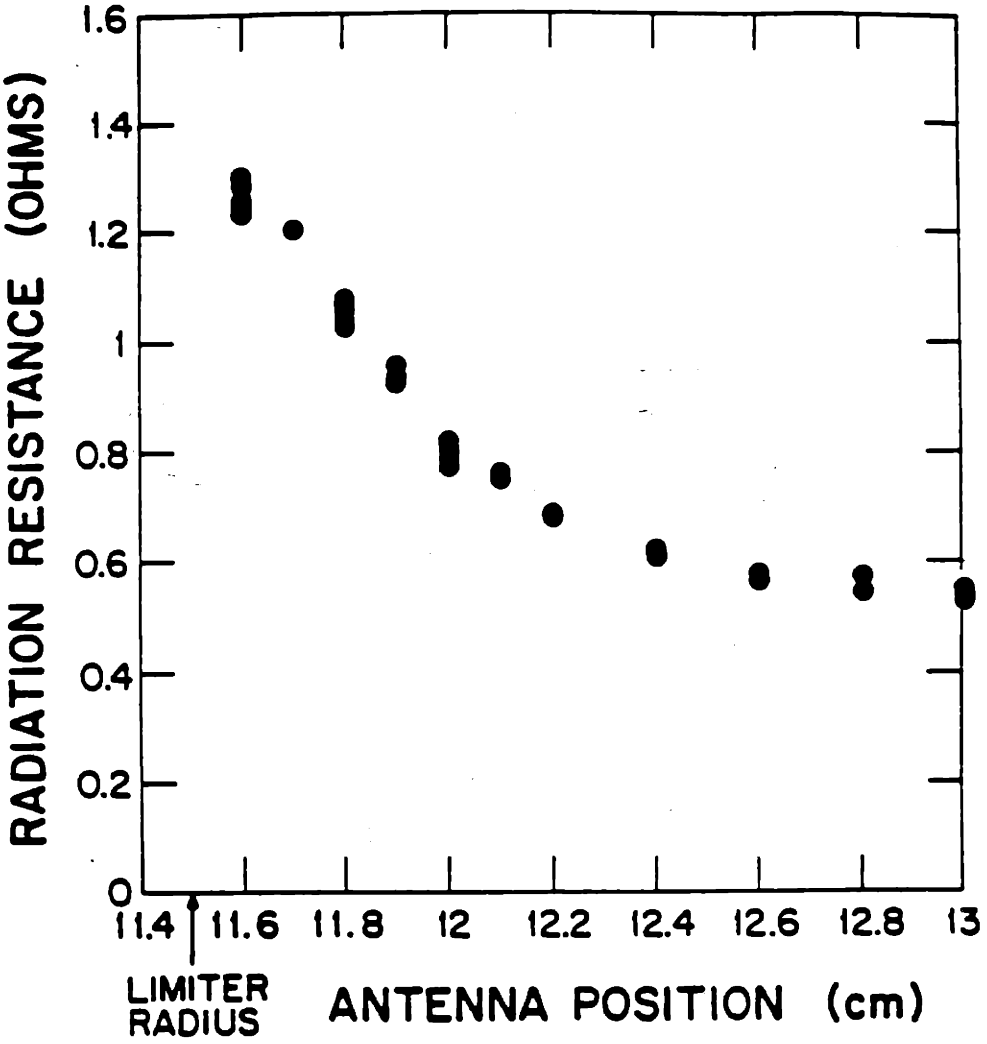

Figure 4.5 —Antenna loading as a function of antenna radial position for $B_0 =$ 7.6 T.

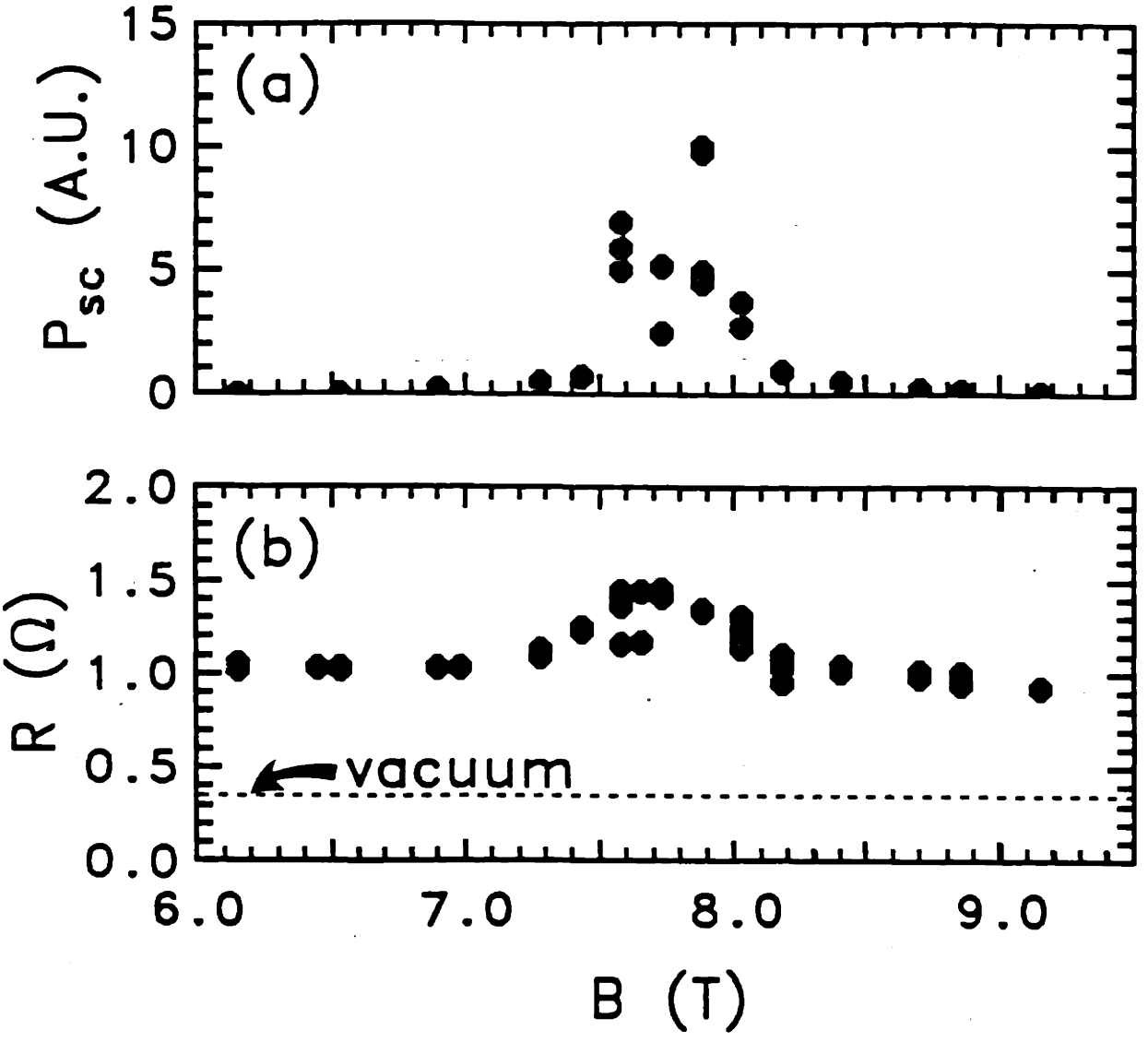

Figure 4.6 —(a) CO_2 scattered power and (b) Loading resistance as a function of magnetic field. Plasma parameters: Hydrogen, $I_p = 290\,\mathrm{kA}$, $\bar{n}_e = 2.3 \times 10^{20}\,\mathrm{m}^{-3}$.

in section 5.3. The departure of the expected behavior from the measured behavior may result from ion Bernstein wave scattering from low–frequency edge density fluctuations (see section 4.4.7) or parametric processes. The density at which the wave excitation frequency is equal to the lower hybrid frequency is about $n_e \simeq 4 \times 10^{17}\,\mathrm{m}^{-3}$. It is thought that the density near the antenna is always somewhat higher than this value.

The antenna loading showed a weak dependence on the rf input power. The overall trend was that the loading decreased ($\sim 20\%$) as the total input power increased from 50 kW to 150 kW. This may also suggest that certain nonlinear effects such as those already mentioned or plasma density modification near the antenna by ponderomotive forces is occurring.

Antenna loading was studied as a function of the orientation of the antenna central conductor with respect to the edge magnetic field. Over a range of $\pm 20°$ no measurable effects on the radiation resistance were observed.

4.4: Heating Experiments

4.4.1: Introduction

Central ion temperature increases ($\Delta T_i/T_i \gtrsim 0.1$) of the Hydrogen majority component were observed on Alcator C during rf power injection for magnetic fields in the range $4.8\,\mathrm{T} \leq B_0 \leq 11\,\mathrm{T}$. Figure 4.8 shows the hydrogen ion temperature increase ($T_{\mathrm{rf}} - T_{\mathrm{Oh}}$) as a function of toroidal magnetic field for all of the ion Bernstein wave experimental data. Although the greatest ion temperature increase was observed at $B_0 = 9.3\,\mathrm{T}$, heating occurred over a broad range of magnetic fields ($2.4 \geq \omega/\Omega_{\mathrm{H}(0)} \geq 1.1$) and was not strongly dependent on having a particular ion cyclotron resonance located near the plasma center. The majority of heating studies were conducted in discharges at $B_0 \simeq 7.6\,\mathrm{T}$, 5.1 T, and 9.3 T, having an axial safety factor value $q(0) \lesssim 1$.

Figure 4.9 shows the location of the hydrogen and deuterium cyclotron harmonics in the poloidal cross section for three magnetic fields. At 7.6 T, rf power absorption is predicted to occur either linearly on deuterium at the $\omega/\Omega_{\mathrm{D}} = 3$ layer, located about 3.4 cm to the high field side of the plasma center ($x/a = -0.3$), via ion cyclotron damping, nonlinearly on hydrogen at the $\omega/\Omega_{\mathrm{H}} = 1.5$ layer (same location) via nonlinear

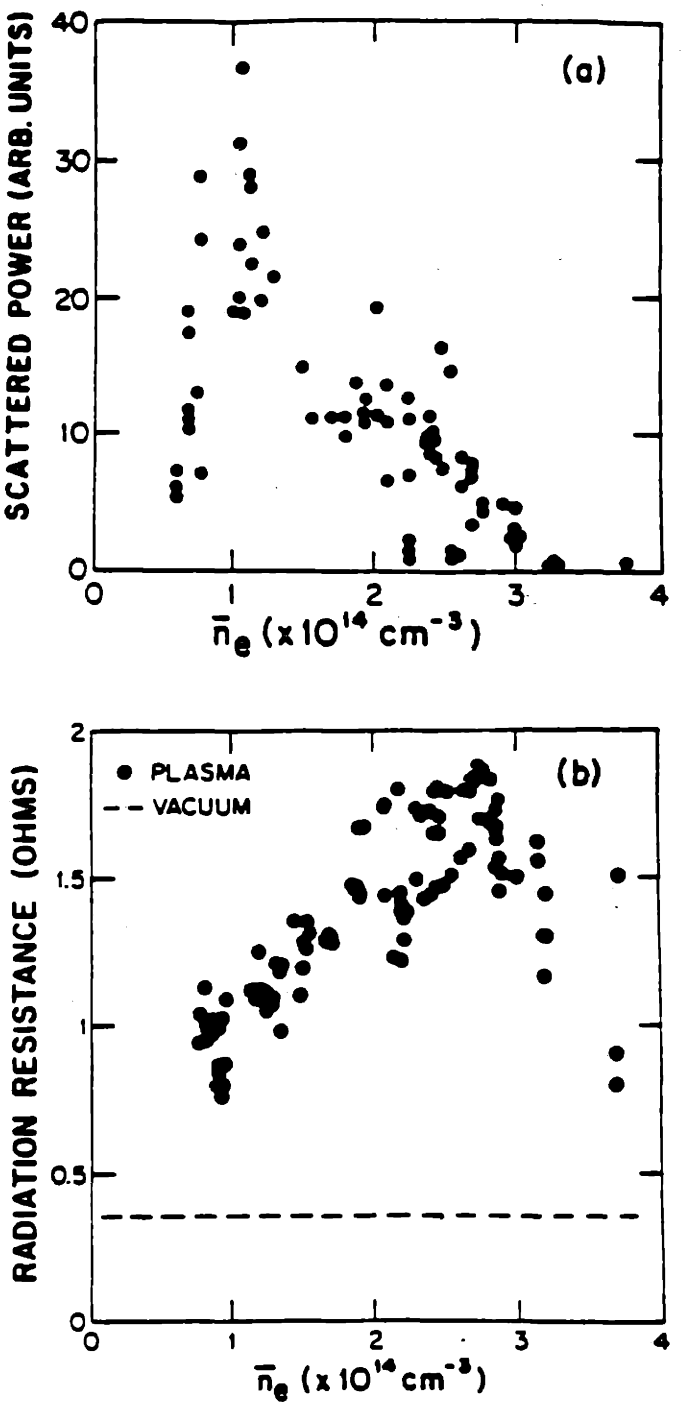

Figure 4.7 —(a) The scattered power observed from ion Bernstein waves at $x/a = +0.4$ as a function of line–averaged density. (b) Loading resistance as a function of line–averaged density. The toroidal field is $B_0 = 7.6\,\mathrm{T}$.

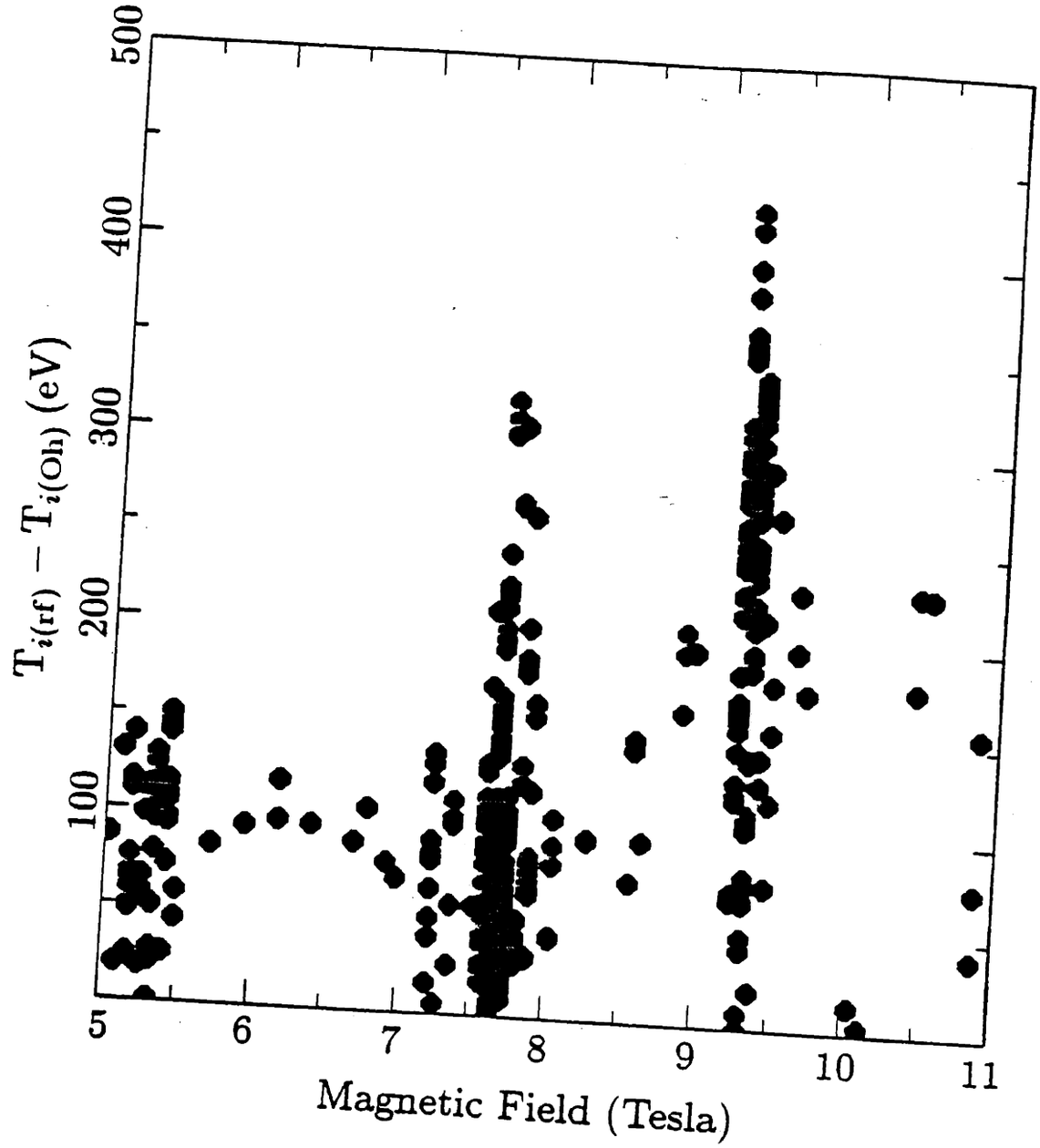

Figure 4.8 —Hydrogen ion temperature increase $T_{rf} - T_{Oh}$ as a function of the toroidal magnetic field.

Landau damping through ion Bernstein wave self–interaction (see section 2.8), or nonlinearly on deuterium near the $\omega/\Omega_H \simeq 1.6$ layer via nonlinear Landau damping through ion Bernstein wave decay (see section 2.8). At 9.3 T, rf power absorption in the plasma interior is predicted to occur nonlinearly on deuterium at the $\omega/\Omega_D = 2.5$ layer located about 4.5 cm to the high field side of the plasma center, via nonlinear Landau damping through self–interaction. At a central field of 5.1 T, rf power absorbtion is predicted to occur linearly via ion cyclotron damping on deuterium at the $\omega/\Omega_D = 5$ layer located 6.8 cm to the low field side of the plasma center, or nonlinearly on hydrogen at the same location ($\omega/\Omega_H = 2.5$ layer) via nonlinear Landau damping through self–interaction.

4.4.2: Heating Results at 7.6 Tesla

At a central magnetic field strength of $B_0 = 7.6\,\mathrm{T}$ and $\bar{n}_e \sim (0.8 - 1) \times 10^{20}\,\mathrm{m}^{-3}$, $n_D/n_{H+D} \sim 10\%$ the central hydrogen temperature increased by an amount $\Delta T_H \approx 200\,\mathrm{eV}$ and the line–averaged electron density increased by $\sim 20\%$ with 100 kW of power injected into the antenna system. A mass–resolving charge exchange neutral analyzer which was scanned radially on a shot–to–shot basis measured the hydrogen and deuterium ion temperature profiles shown in Fig 4.10 which were centrally peaked in both the Ohmic and rf heated portions of the discharge. Figure 4.11 shows the temporal behavior of the plasma parameters during the discharge. The energy distribution for hydrogen showed a thermal spectrum both before and during rf power injection. The deuterium component also exhibited a thermal energy spectrum during rf injection with an effective temperature (obtained from deuterium particle flux at energies $E \geq 4\,\mathrm{keV}$) of approximately 1.3 keV on axis, somewhat hotter than the background heated hydrogen temperature of 0.9 keV. It is possible to estimate that the collisional power transfer from the heated deuterium component to the background hydrogen is $\lesssim 30\,\mathrm{kW}$; however, this estimate is strongly dependent on the fraction of deuterium in the discharge and also on the radial temperature profile and is uncertain to within a factor of 2. Nevertheless, a power of 30 kW transferred from the deuterium into the hydrogen species can produce a temperature increase of $\sim 175\,\mathrm{eV}$ if the plasma confinement during rf injection is assumed to remain the same as in the Ohmic phase.

In principle, the amount of rf power flowing into the hydrogen or deuterium species can be estimated from the rate of increase of the ion temperature at the onset of rf power injection. For the simple situation where only the main species ion temperature increases by ΔT_i in a time Δt†, the power flow into the ions is $P = U_i \Delta T_i/(T_i \Delta t)$

† The time Δt must be small compared to an energy confinement time ($\tau_E \sim 5$–$10\,\mathrm{ms}$) for this estimate to have meaning.

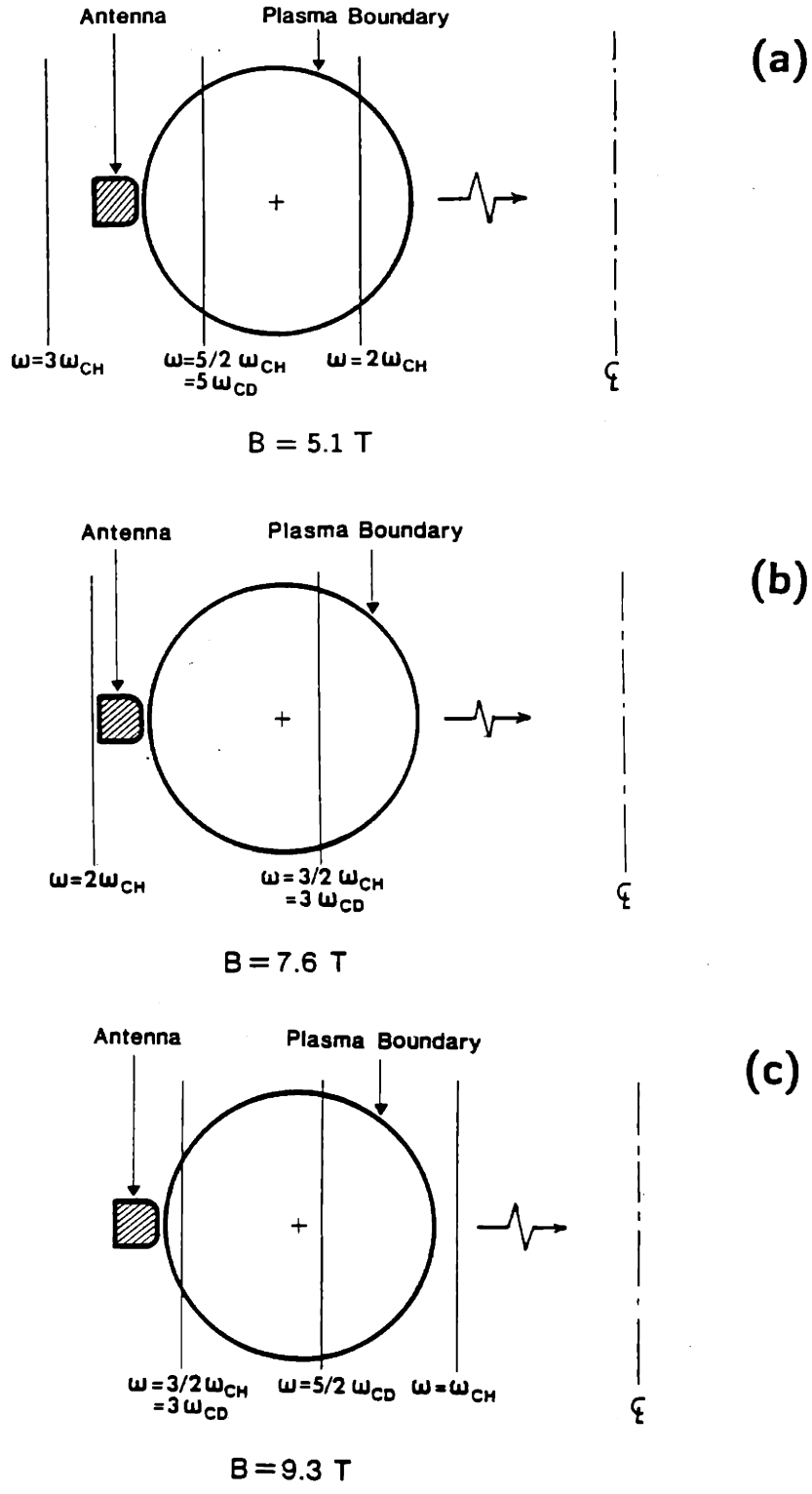

Figure 4.9 —Location of the hydrogen and deuterium integral and odd–half integral cyclotron harmonics in the poloidal cross section for (a) $B_0 = 5.1\,\mathrm{T}$, (b) $B_0 = 7.6\,\mathrm{T}$ and (c) $B_0 = 9.3\,\mathrm{T}$.

where U_i is the total stored ion energy in the Ohmic plasma. When estimated for several of the ion Bernstein wave heated discharges, the calculated value of the power is close to the measured power injected into the antenna system. This estimate is crude for a number of reasons. First, the ion temperature is typically averaged over a 5 ms time period. When averaged over a shorter time period, the temperature is somewhat choppy making it difficult to carry out this type of calculation. Second, the density and temperature profiles are not well known making it difficult to accurately determine the ion stored energy. Third, at the onset of rf power injection, the plasma density typically increases; this also contributes to the increase in ion stored energy. This effect can, in principle, be accounted for by determining the rate of density increase; however, due to experimental uncertainties, this only increases the uncertainty in the overall estimate of the power flow into the ions. Nevertheless, within experimental error, the estimate is within the expected range.

Figure 4.12 shows that the ion temperature increase at $B = 7.6\,\mathrm{T}$ follows an ion heating rate of $2.3\,\mathrm{eV/kW}$ at $\bar{n}_e \lesssim 1 \times 10^{20}\,\mathrm{m}^{-3}$. It is pointed out that this heating rate is calculated by dividing the ion temperature increase by the total rf power entering the antenna system. The actual power which is ultimately coupled into ion Bernstein waves will be somewhat less that this total power due to Ohmic losses in the system. The hydrogen temperature increase appears to show a power threshold of 35 kW at the onset of ion heating which is consistent with the threshold estimated for 63% single pass absorption of the injected rf power[4]. There is also a power threshold of about 30 kW for the high energy deuterium component[7]shown in Fig. 4.13 . The data in Fig. 4.13 shows that the hydrogen and deuterium central temperatures converge at a nonzero value of P_{rf}. The existence of a power threshold for $T_{\mathrm{D}} > T_{\mathrm{H}}$ suggests that a nonlinear heating mechanism is operative on the deuterium species. Two possibilities for this mechanism are nonlinear Landau damping via ion Bernstein wave decay (see section 2.8) near the $\omega/\Omega_{\mathrm{H}} \simeq 1.6$ layer located 0.6 cm to the low field side of the plasma center ($x/a = 0.05$), and nonlinear Landau damping via self–interaction at the $\omega/\Omega_{\mathrm{D}} = 3.5$ layer‡. The power absorbed per pass at the $\omega/\Omega_{\mathrm{D}} = 3.5$ layer via self–interaction is negligible. This has been verified numerically from the equations in section 2.8. Power absorbed via the decay process can amount to a significant fraction of the pump power. The threshold power for 63% power absorption via the decay process in one pass is estimated to be in the range of about 30 kW. Power not depleted

‡ This layer, not shown in Fig. 4.9 (b), lies between the low field plasma edge and the $\omega/\Omega_{\mathrm{D}} = 3$ layer at $x/a = 0.56$.

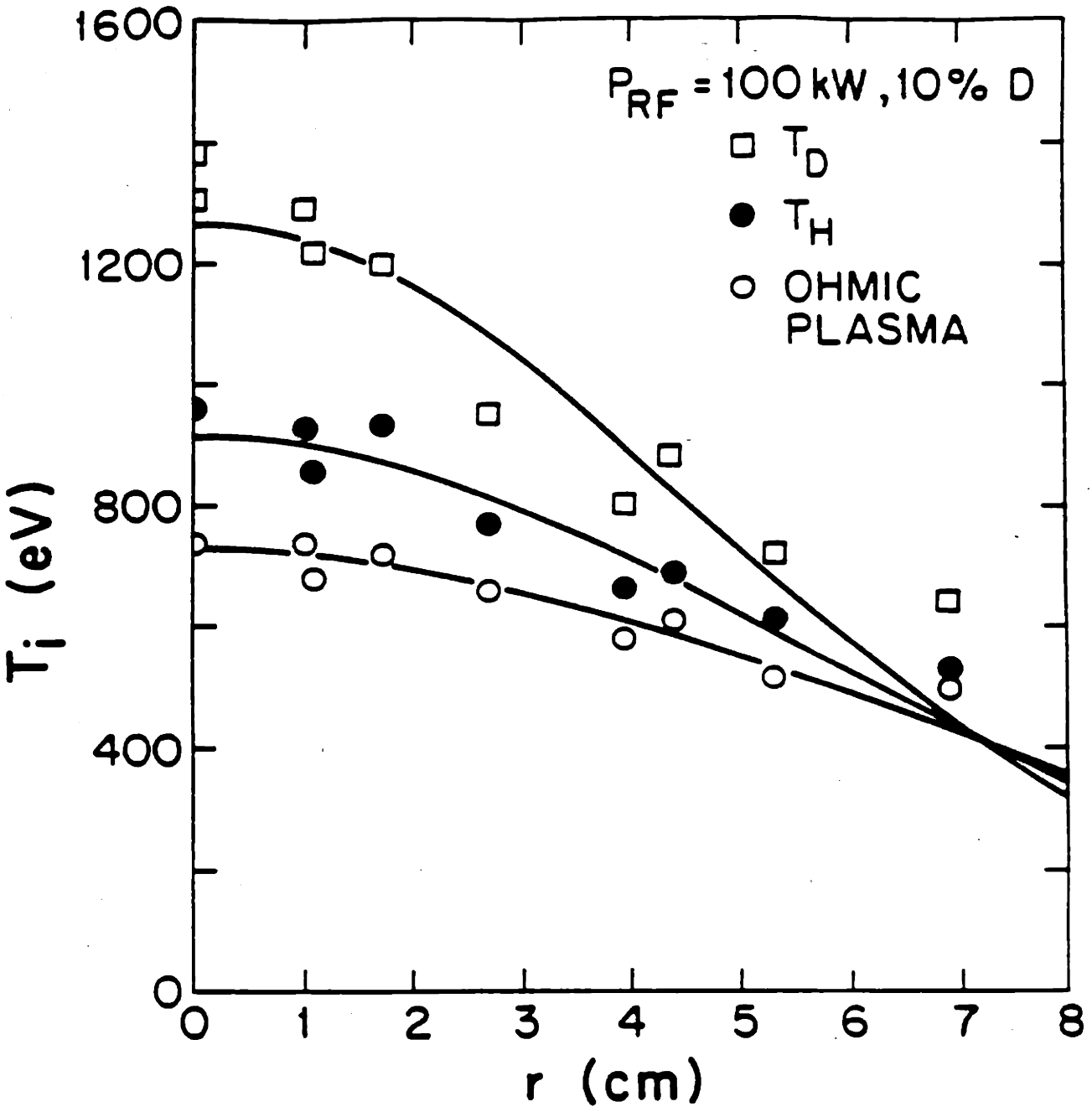

Figure 4.10 —Radial temperature profiles of the hydrogen and deuterium species during the Ohmic and Ohmic plus rf heated portions of the discharge at B_0=7.6 T.

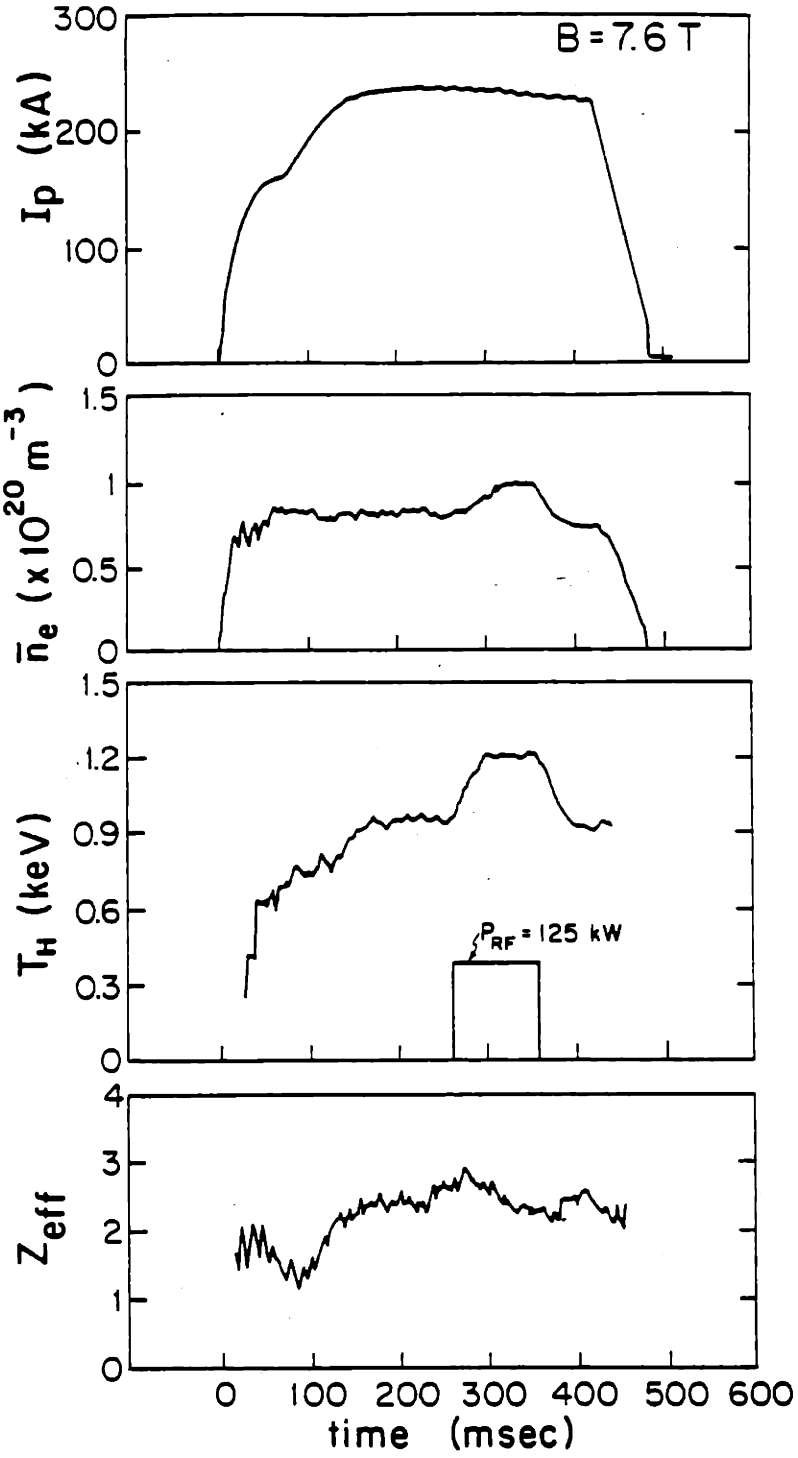

Figure 4.11 —Temporal evolution of the plasma current, line–averaged density, hydrogen ion temperature and Z_{eff} at $B_0 = 7.6\,\text{T}$.

by either of these two mechanisms is damped nonlinearly by hydrogen at the ω/Ω_H=1.5 layer, linearly by deuterium at the $\omega/\Omega_D = 3$ layer, or linearly by electrons through Landau damping.

4.4.3: Heating Results at 5.1 Tesla

At a central magnetic field strength of $B_0 = 5.1\,\mathrm{T}$ the $\omega/\omega_H = 5/2$ ($\omega/\omega_D = 5$) resonance layer is located at $x/a = 0.3$. The temporal evolution of a typical discharge at this field is shown in Fig. 4.14 . The ion temperature increase in this regime shows a heating rate of 2.2 eV/kW, (see Fig. 4.12) similar to the 7.6 T case. The calculated power threshold is $\sim 30\,\mathrm{kW}$, in good agreement with experimental observations (there was no observable heating below this power). At $B_0 = 5.1\,\mathrm{T}$, the temperature increase of the hydrogen majority and deuterium minority ions is thermal ($T_H = T_D$) and is independent of deuterium concentration, suggesting that nonlinear absorption on hydrogen is dominant in this regime.

4.4.4: Heating Results at 9.3 Tesla

The most efficient heating is observed when the magnetic field is increased to high values ($B_0 \gtrsim 9\,\mathrm{T}$). This regime has not been explored in previous experiments and here, the analysis is somewhat more complicated. For example, at a field of $B_0 = 9.3\,\mathrm{T}$ the $\omega/\Omega_D = 5/2$ minority subharmonic resonance layer is located on the high magnetic field side of the plasma axis at $x/a = -0.18$ ($a = 0.12\,\mathrm{m}$). However, the $\omega/\Omega_H = 3/2$ and $\omega/\Omega_D = 3$ layer is at $x/a = 0.85$, approximately 2 cm in front of the antenna (see Fig. 4.9 (c)). Ray tracing and power absorption calculations show that ion Bernstein wave power should be completely absorbed by either the linear or nonlinear mechanism at the plasma edge ($x/a = 0.85$). Using CO_2 laser scattering techniques, a strong attenuation in wave power at frequency f_0 and perpendicular wavelength in the range $40 < k_\perp \leq 140\,\mathrm{cm}^{-1}$ is observed[1] across the $\omega/\Omega_D = 3$ layer (see Fig. 4.4). However, as is shown in Fig. 4.12 , an ion heating rate of 4.1 eV/kW at $\bar{n}_e = 1 \times 10^{20}\,\mathrm{m}^{-3}$ is observed with a very low power threshold ($P_{th} \leq 10\,\mathrm{kW}$ within experimental error). To further complicate matters, the deuterium component has a two temperature energy spectrum with a superthermal component at T_D=2 keV. The radial temperature profile of the deuterium, shown in Fig. 4.15 , is centrally peaked on the plasma axis. The temporal temperature evolution of the hydrogen and deuterium temperatures, shown

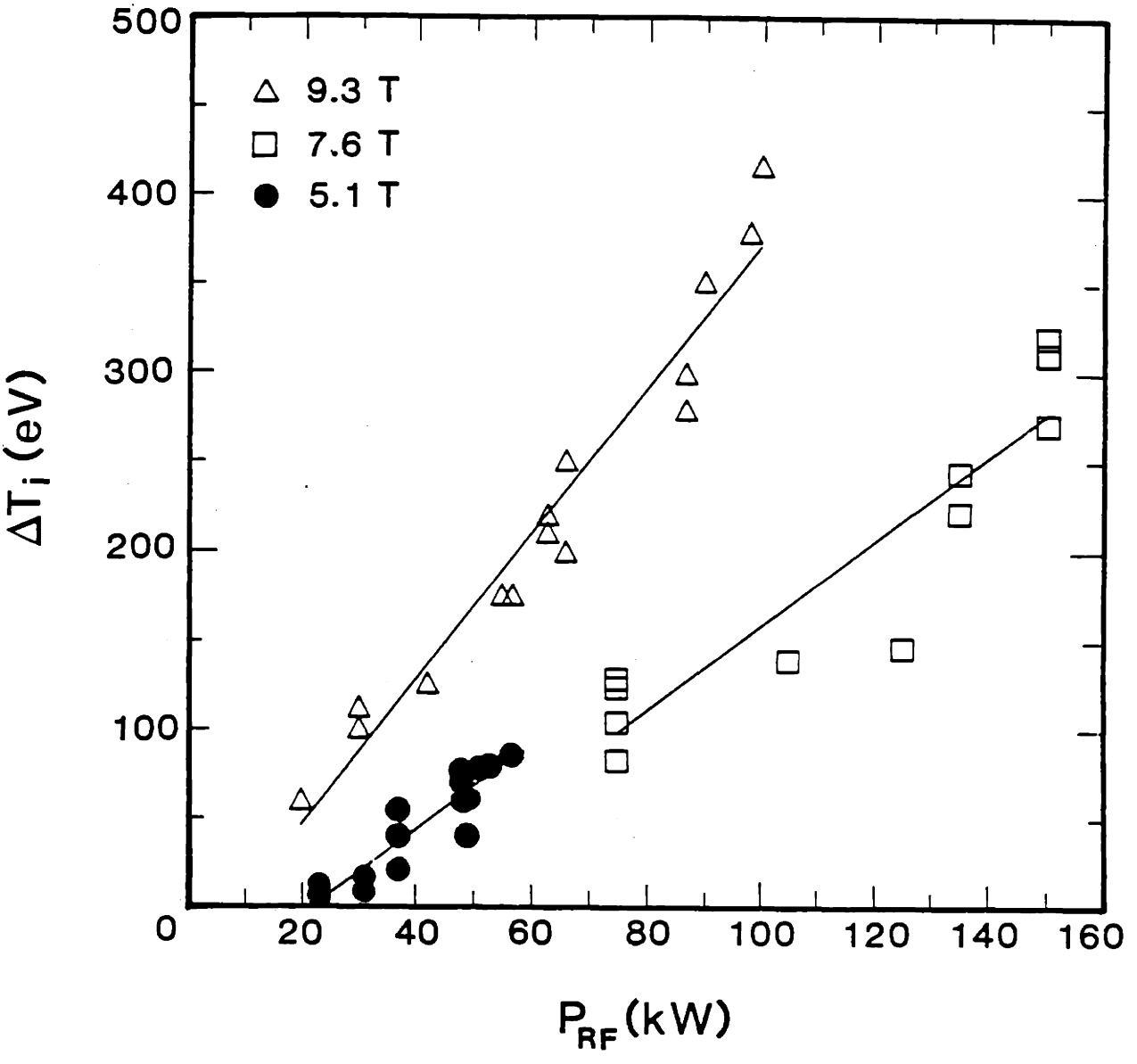

Figure 4.12 —Ion heating ΔT_i as a function of rf power P_{rf} for three magnetic field strengths. Each field indicates that a particular cyclotron resonance is near the plasma center (see Fig. 4.9).

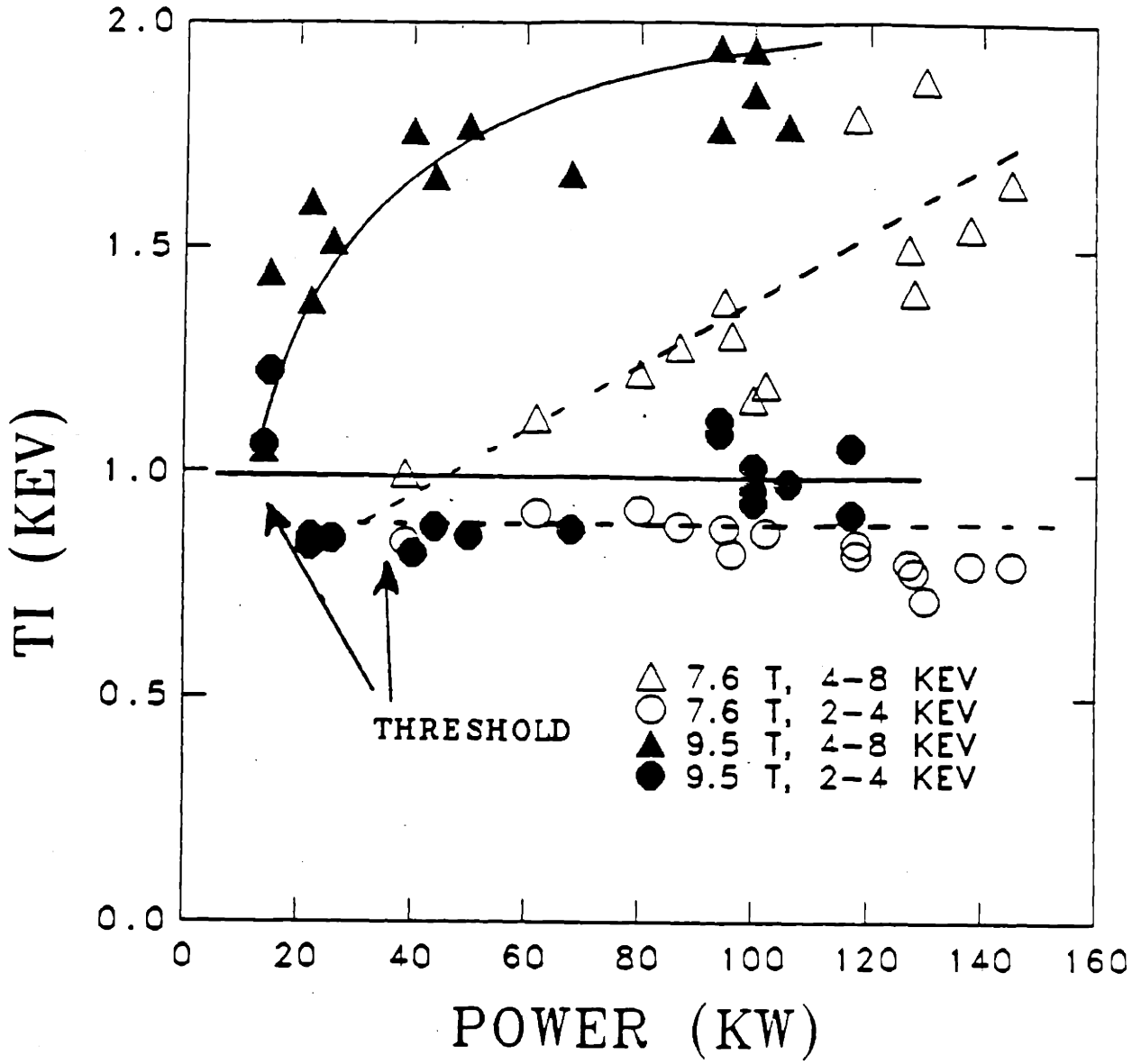

Figure 4.13 —Temperature of the high energy deuterium minority component as a function of rf input power at $B_0 = 7.6\,\mathrm{T}$ and $B_0 = 9.5\,\mathrm{T}$. The threshold power is 30–50 kW at $B_0 = 7.6\,\mathrm{T}$ and 15 kW at $B_0 = 9.5\,\mathrm{T}$. From C. Fiore (Ref. 7).

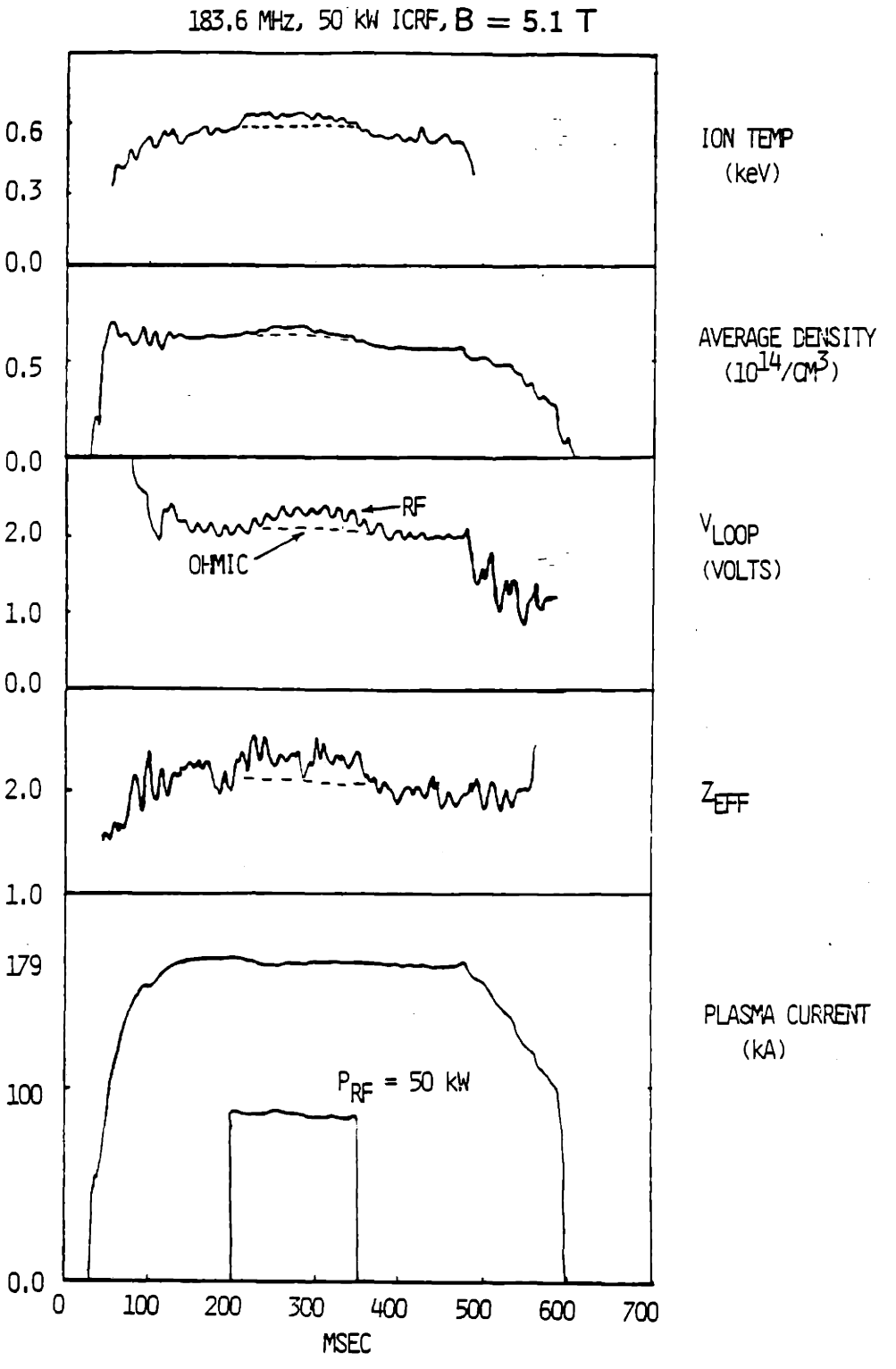

Figure 4.14 —Temporal evolution of the plasma ion temperature, line-averaged density, resistive loop voltage, Z_{eff}, and plasma current at $B_0 = 5.1\,\text{T}$.

in Fig. 4.16 , indicates that the deuterium achieves its maximum temperature before the hydrogen, and both exhibit a slow decay time of about 5 ms after rf power shut–off, indicating central nonlinear rf heating of the deuterium species at the $\omega/\Omega_D = 5/2$ layer. The two temperatures displayed in Fig. 4.16 were obtained on separate but similar discharges. The power flow from deuterium to hydrogen in this case is estimated to be 20–40 kW with large uncertainty.

To explain the energetic deuterium component, at least a fraction of the rf power must penetrate to the plasma interior. One possible mechanism for this is the variation in the toroidal field caused by the toroidal field ripple. The presence of the access port in Alcator C perturbs the toroidal field current causing a toroidal field ripple of about 2–4% near the antenna feed. Consequently, the $\omega/\Omega_D = 3$ layer may be located 2 cm in front of the antenna at the port location but may be positioned behind the Faraday shield at either end of the antenna, away from the port (the port is 4 cm wide and the antenna is 25 cm long). Thus, power from either end of the antenna may freely propagate to the plasma center and heat the deuterium. Another possible mechanism, already mentioned in section 4.2.2, is that the ion Bernstein wave may undergo parametric decay into another ion Bernstein wave of a lower frequency and an ion quasi–mode[5]. The lower frequency ion Bernstein wave could not be detected by the CO_2 scattering system and would not suffer power absorption at the $\omega/\Omega_D = 3$ layer (this layer would be outside of the plasma). The lower frequency ion Bernstein wave could freely propagate into the inner plasma and deposit its power at the $\omega/\Omega_D = 2.5$ layer (which would be located slightly on the low field side of the plasma center for this wave). Nonlinear absorption by the deuterium minority species is possible above a threshold power of ~ 30 kW for $n_D/n_H = 0.02$ (the threshold power is inversely proportional to the deuterium concentration).

4.4.5: Enhancement of Global Particle Confinement

Improvements in τ_p, the global particle confinement time, of up to 3 times its value in the Ohmically heated plasma are often observed for $\bar{n}_e < 2.5 \times 10^{20}\,\mathrm{m}^{-3}$. The global particle confinement time, τ_p, is calculated by dividing the total number of electrons N_e by $S - dN_e/dt$, where S is the source rate of electrons at the plasma edge as inferred from H_α measurements. Figure 4.17 shows a strong dependence of $\tau_{p(\mathrm{rf})}/\tau_{p(\mathrm{Ohmic})}$ on target plasma density with a maximum value of 3.4 at $\bar{n}_e = 0.6 \times 10^{20}\,\mathrm{m}^{-3}$ and decreasing to unity for $\bar{n}_e > 2.5 \times 10^{20}\,\mathrm{m}^{-3}$. Improvements in τ_p are observed over a wide range of toroidal fields $4.8\,\mathrm{T} \leq B \leq 10.4\,\mathrm{T}$; however, the most significant improvement

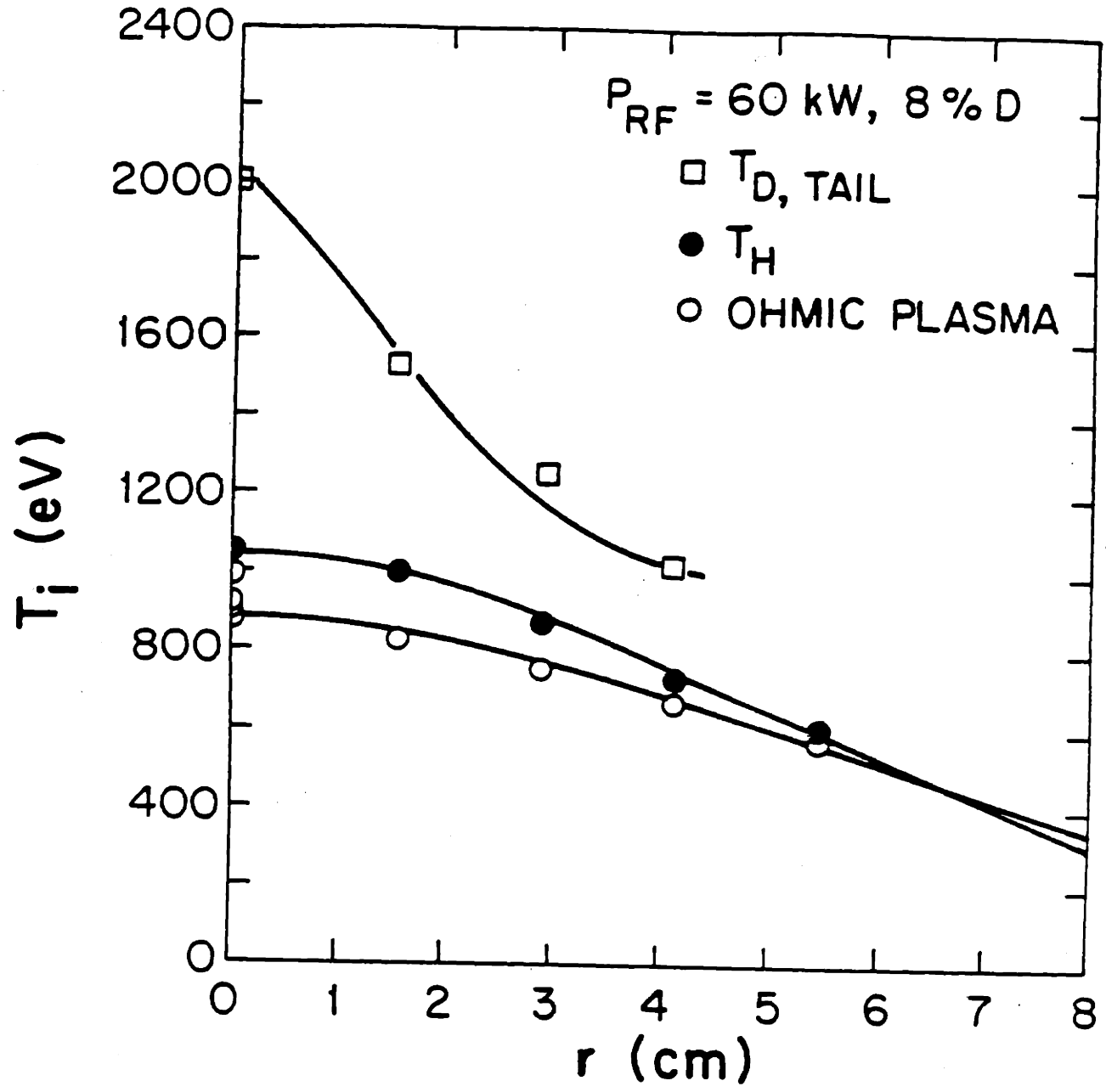

Figure 4.15 —Radial temperature profile of the hydrogen and deuterium components during the Ohmic and rf heated portions of the discharge at $B_0 = 9.3\,\mathrm{T}$.

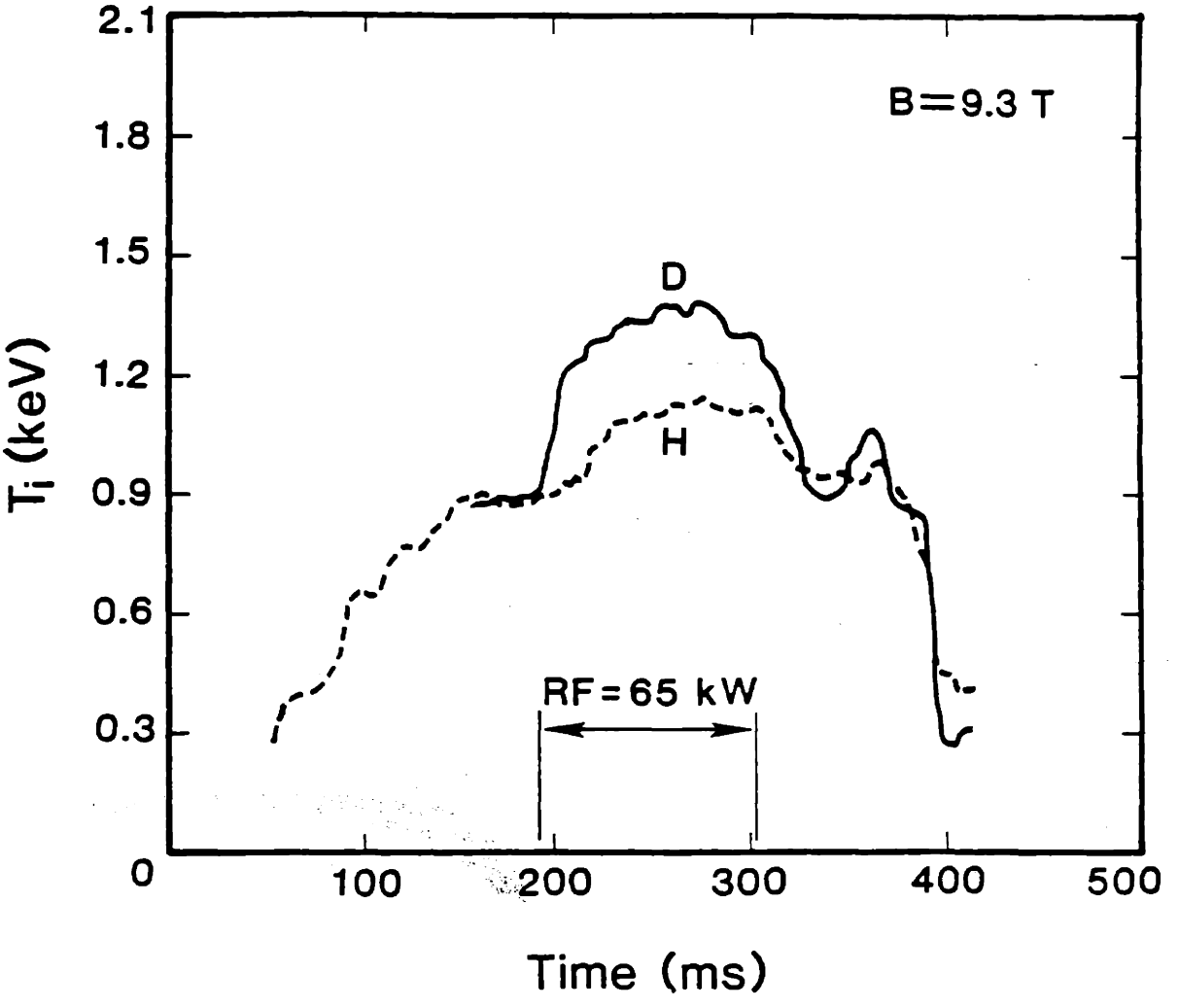

Figure 4.16 —Time history of the bulk hydrogen and superthermal deuterium temperatures during rf power injection at $B_0 = 9.3\,\mathrm{T}$.

in τ_p occurs in the 9.3 T regime where the $\omega/\Omega_D = 3$ resonance layer is located at the plasma edge. Here, the line–averaged electron density typically increases by up to 100% and the source rate S (as determined from H_α measurements) decreases by about 30% during IBW injection. Several non–rf discharges in which the density was increased by gas puffing alone were compared with rf discharges. Figure 4.18 shows a comparison of the line–averaged density and H_α emission for an rf heated discharge and a gas puff discharge at $B_0 = 9.3\,\mathrm{T}$. The H_α measurement was made at the gas feed port, the antenna port, and at a limiter. All three measurements show a decrease in the H_α signal at the onset of rf power. However, in the absence of rf power injection, the H_α intensity shows a fractional increase which is larger than the fractional increase in the density (due to gas puffing), indicating decreasing particle confinement in the absence of rf power injection.

4.4.6: Enhancement of Central Impurity Confinement

Central impurity confinement times were also observed to increase by factors of 2–3 during IBW injection[8]. This was measured by injecting trace amounts of Silicon using the laser blow–off technique[9]. The brightness of He–like Si (an ionization state which exists in the center of these discharges) is observed to decay at a significantly slower rate in rf heated plasmas. Figure 4.19 shows the brightness of silicon emission as a function of time for the Ohmic and rf phase of the discharge. Typical values of τ_{Si} corresponding to before (Ohmic), during, and after ion Bernstein wave injection in the 9.3 T regime are 7, 16–20, and 6 ms. The Z_{eff} is typically constant or decreasing during rf injection in these discharges.

4.4.7: Density Dependence of the Ion Heating Rate

A systematic study of ion heating versus target density was carried out. A strong decrease in the ion heating rate was observed for target plasma densities $\bar{n}_e \gtrsim 1.1 \times 10^{20}\,\mathrm{m}^{-3}$, and as shown in Fig. 4.20 , significant increases in the ion temperature were not seen for target densities $\bar{n}_e > 2.5 \times 10^{20}\,\mathrm{m}^{-3}$ and at rf powers $P_{rf} \lesssim 100\,\mathrm{kW}$ ($4.8\,\mathrm{T} < B_0 < 11\,\mathrm{T}$). The increases in T_i for $\bar{n}_e > 2.5 \times 10^{20}\,\mathrm{m}^{-3}$ are within the experimental error of $\Delta T_i \simeq 0$. In particular, at high densities it was difficult to inject more than $\sim 100\,\mathrm{kW}$ from the antenna (antenna power density $P/A \sim 1\,\mathrm{kW/cm}^2$). The large scatter in the data in Fig. 4.20 appears on a day–to–day basis whereas the

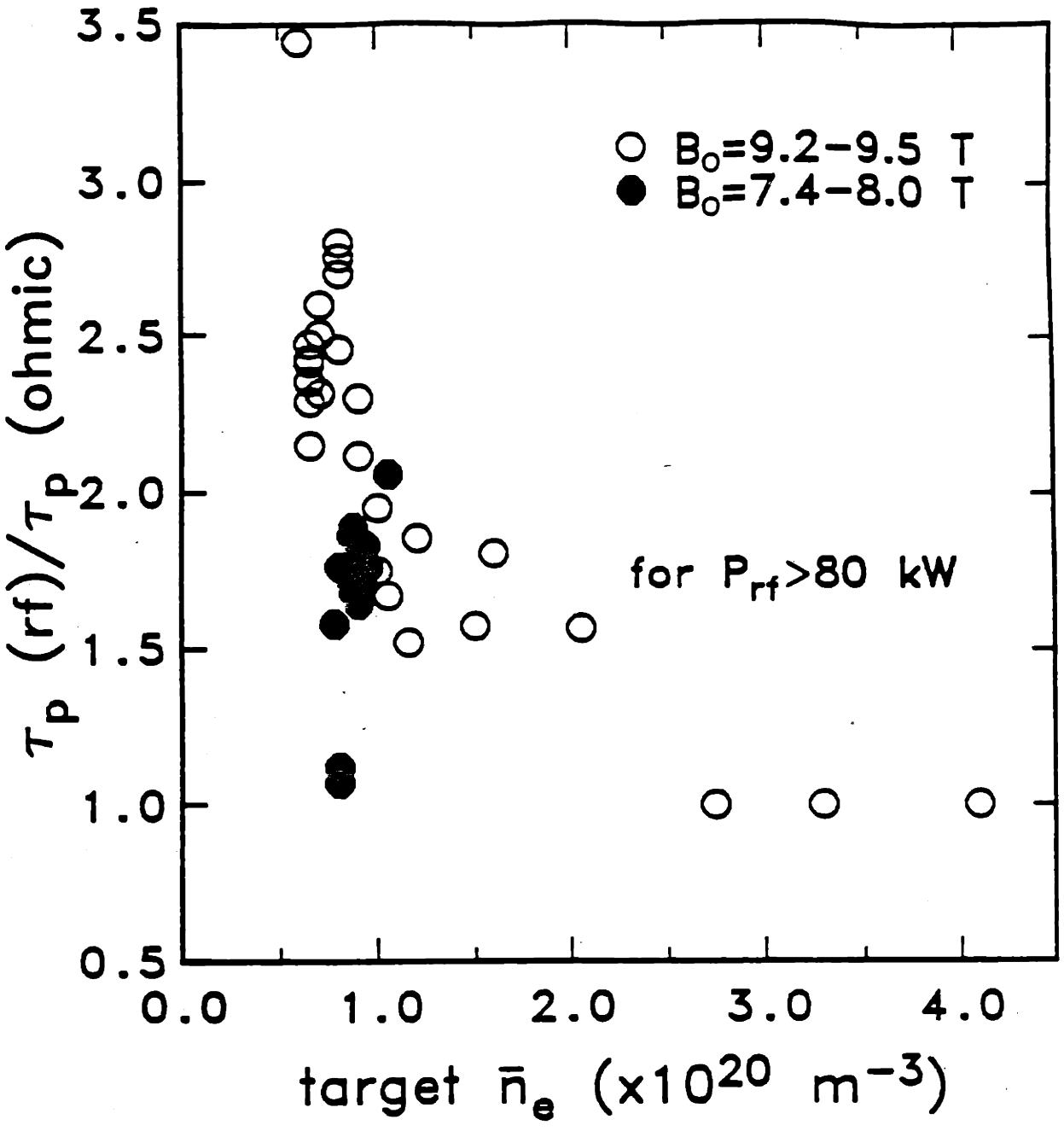

Figure 4.17 —Comparison of particle confinement time for Ohmic and Ohmic plus ion Bernstein wave heated plasma as a function of the line–averaged Ohmic density.

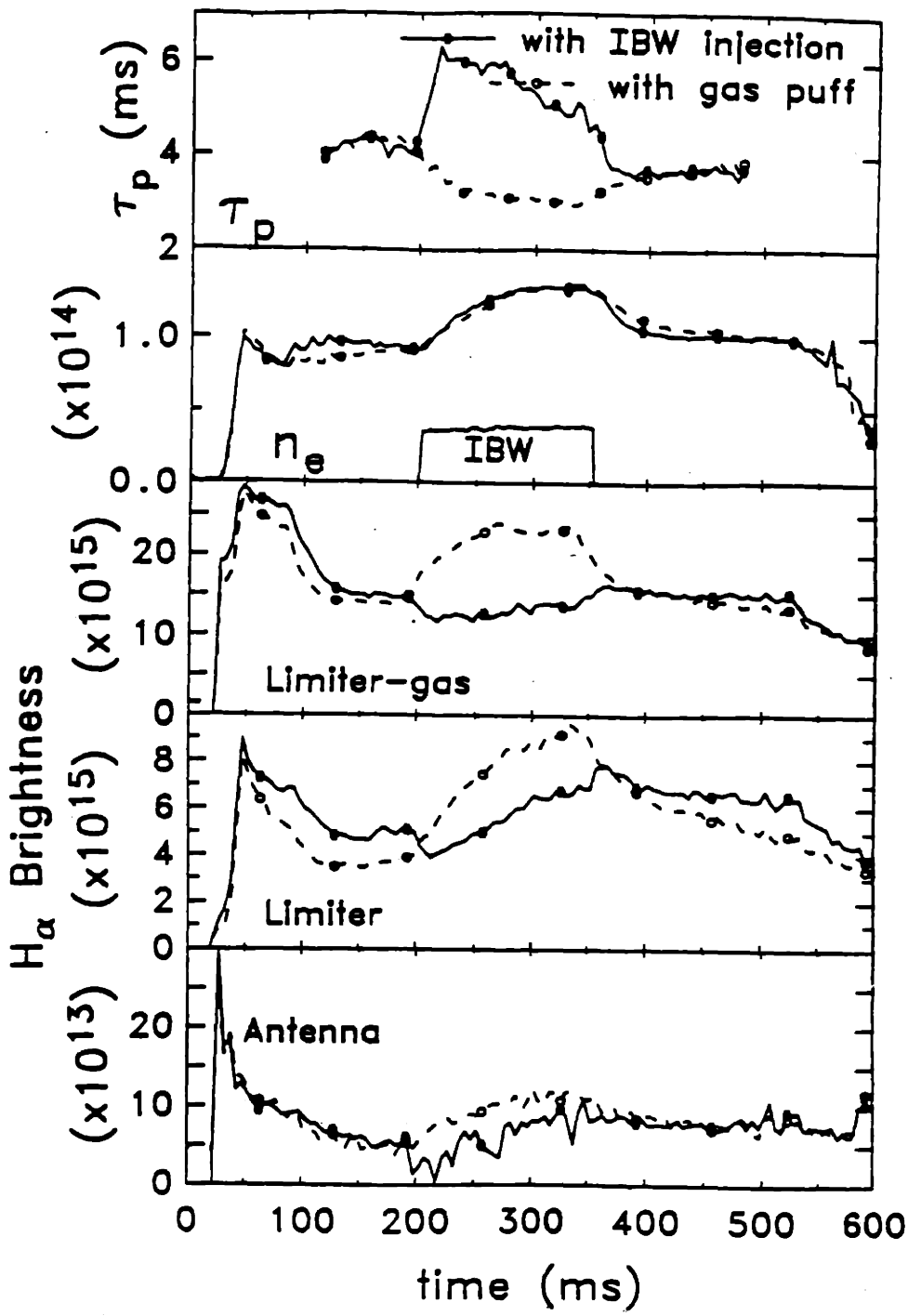

Figure 4.18 —Comparison of H_α emission for a density increase caused by rf power injection or by gas puffing at $B_0 = 9.3\,\mathrm{T}$.

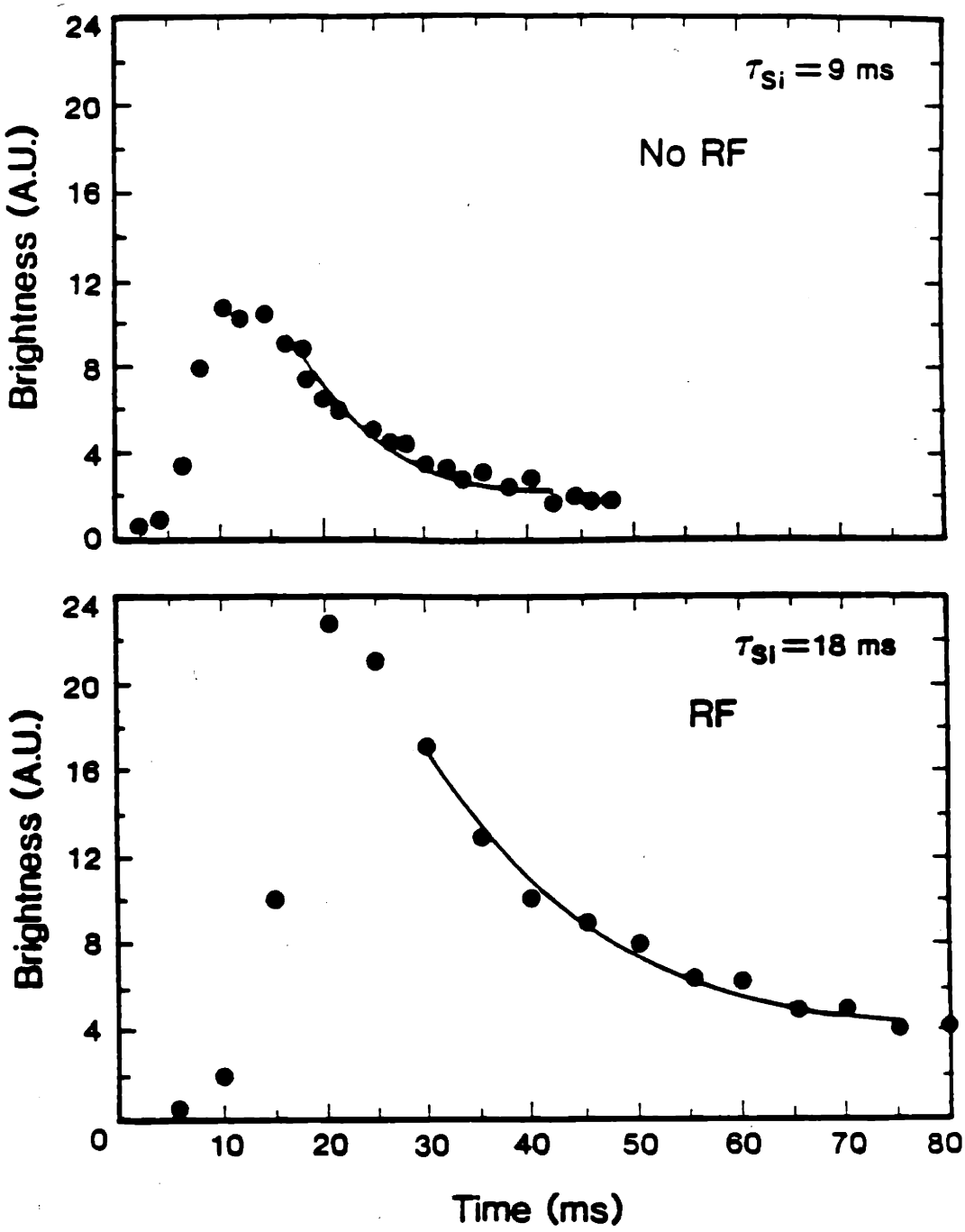

Figure 4.19 —Time dependence of silicon brightness during Ohmic heating and during Ohmic plus ion Bernstein wave heating at $B_0 = 9.3\,\mathrm{T}$.

error bar represents typical scatter within a single day. The large scatter is thought to result from day–to–day variations in the plasma edge conditions which affect the antenna–plasma coupling. It is pointed out that the envelope of the data in Fig. 4.20 is what exhibits the maximum achievable ion heating rate; this envelope exhibits a trend toward decreasing ion heating rate with increasing density. There is a lack of data near $\bar{n}_e \simeq 2 \times 10^{20}\,\mathrm{m}^{-3}$ which may account for the apparent increase in heating rate above this density. It is assumed that more data near this density would only confirm the decreasing trend in the heating rate with density. The envelope also seems to show a decrease in heating rate below $\bar{n}_e \simeq 0.75 \times 10^{20}\,\mathrm{m}^{-3}$. Unfortunately there is not sufficient data below this density to confirm a decreasing trend in the heating rate.

Several mechanisms which have a density dependent effect on the heating rate have been considered to explain the ion heating rate decrease. For example, wave power attenuation due to edge collisions becomes worse as the density is increased. Theoretical estimates of collisional damping indicate that edge absorption is negligible even for an edge density and temperature of $n_e(r = a) \simeq 1 \times 10^{20}\ \mathrm{m}^{-3}$, $T_e \sim T_i \sim 50$ eV, characteristic of high density discharges. The nonlinear power threshold, which increases linearly with increasing plasma density, may account for some of the decrease in heating rate. However, the decrease is more sudden than expected and linear damping of ion Bernstein waves on the deuterium minority should still occur even at high density. Another effect which may partly account for the decrease in the heating rate is that the energy confinement time in these discharges, which is proportional to density at low densities, begins to saturate above $\bar{n}_e \sim 1.5 \times 10^{20}\,\mathrm{m}^{-3}$. This saturation is caused by both increased coupling between the electrons and ions and an increasing anomaly in the ion thermal diffusivity. Thus, the ion energy confinement time degrades as the density is increased and this contributes to the observed decrease in the ion heating rate. The details of the ion confinement will be discussed in the following chapter.

CO_2 scattering results [see Fig. 4.7 (a)] suggest that the decrease in the ion heating rate may partially be attributed to inaccessibility of the ion Bernstein wave to the plasma center due to scattering from low–frequency edge density fluctuations ($\tilde{n}/n \gtrsim 0.3$ at $r/a \simeq 0.9$) as the target density is increased. To investigate the possibility that low–frequency edge density fluctuations may impede the ion Bernstein wave power from propagating into the plasma interior, the CO_2 scattering diagnostic was reconfigured as shown in Fig. 3.3. Low–frequency density fluctuations, integrated up to $5\,\mathrm{cm}^{-1}$ in wave number and up to 400 kHz in frequency, were observed along a chord located at $x/a = +0.83$. Figure 4.21 (b) shows the value of $P_{sc}/\bar{n}_e^2$ [which is proportional to $(\tilde{n}_e/n_e)^2$ for a fixed density profile] plotted as a function of $\bar{n}_e$. The quantity $\tilde{n}_e$ indicates the absolute amplitude of the low–frequency density fluctuation. The absolute magnitude of $\tilde{n}_e/n_e$ could not be determined with accuracy in these measurements; however, based on earlier measurements[10] it is estimated to be in the range of 0.1–0.5

at a density of $\bar{n}_e \simeq 2 \times 10^{20}\,\mathrm{m}^{-3}$. The correlation between figures 4.21 (a) and (b) suggest that edge turbulent scattering may affect the wave accessibility to the plasma center. A detailed calculation to study the turbulent scattering of ion Bernstein waves will be given in Chapter 5.

4.4.8: Energy Confinement in 9.3 Tesla Discharges

Figure 4.22 shows the change in total stored energy, ΔW_t versus the change in total input power, ΔP_t during ion Bernstein wave heating at $B = 9.3$ T. When calculating the total stored energy and input power, the temperature and density profiles are assumed constant in both the rf and Ohmic heated portions of the discharge. All discharges represented in the figure have initial Ohmic energy confinement times, $\tau_{E(\mathrm{Oh})} = 5.6 \pm 0.8\,\mathrm{ms}$, and rf confinement times, $\tau_{E(\mathrm{rf})} = 6.5 \pm 1.2\,\mathrm{ms}$. The incremental energy confinement time, which is defined as $\Delta W_t / \Delta P_t$, has an average value of 15.5 ms, for discharges with very low deuterium concentration and ranges between 3.9 ms and 17.5 ms for discharges with $n_{\mathrm{D}}/n_{\mathrm{H+D}} \leq 20\%$. The improvement in τ_E (with respect to the initial Ohmic confinement time) during rf heating results from the large increase in total plasma energy caused by both strong heating of ions and nearly doubling the plasma density. The Ohmic confinement time at densities similar to those reached during rf injection is $\tau_{E(\mathrm{Oh})} \doteq 8.8 \pm 1.2\,\mathrm{ms}$. At $B = 7.6$ T there are also improvements in τ_E during rf injection (with respect to the initial Ohmic τ_E).

The results obtained at 9.3 T show some remarkable similarities to H–mode type discharges[11]. For example, the energy and particle confinement times improve, the stored energy and line–averaged density increase, and the H_α signal decreases. There are also some marked differences: No clear L–mode phase or delay time to H–mode transition, no measured power or lower density threshold, no separatrix, and no indication of edge localized modes (ELMS). Nevertheless, under similar conditions, typical incremental confinement times during fast wave heating are only 3–5 ms[12], indicating that ion Bernstein wave launching produces H–mode like behavior.

4.4.9: Plasma Edge Conditions at 9.3 Tesla

In order to gain a better understanding of the underlying physics, attempts were made to determine the near edge ion temperature ($r/a \approx 0.9$) as a function of plasma

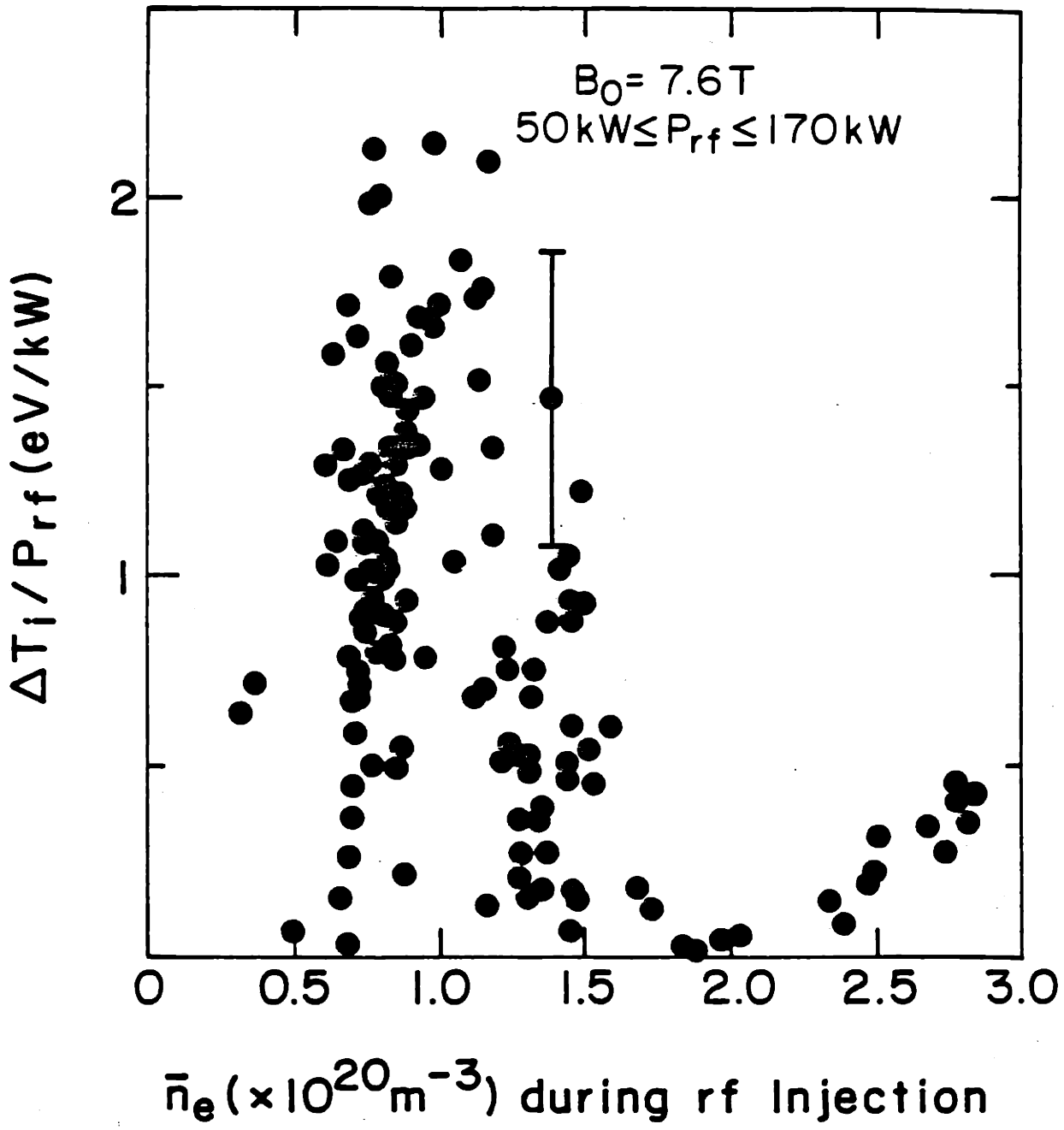

Figure 4.20 —Hydrogen ion heating rate, $\Delta T_i(0)/P_{rf}$ (eV/kW), as a function of the line-averaged density during rf power injection at $B_0 = 7.6$ T.

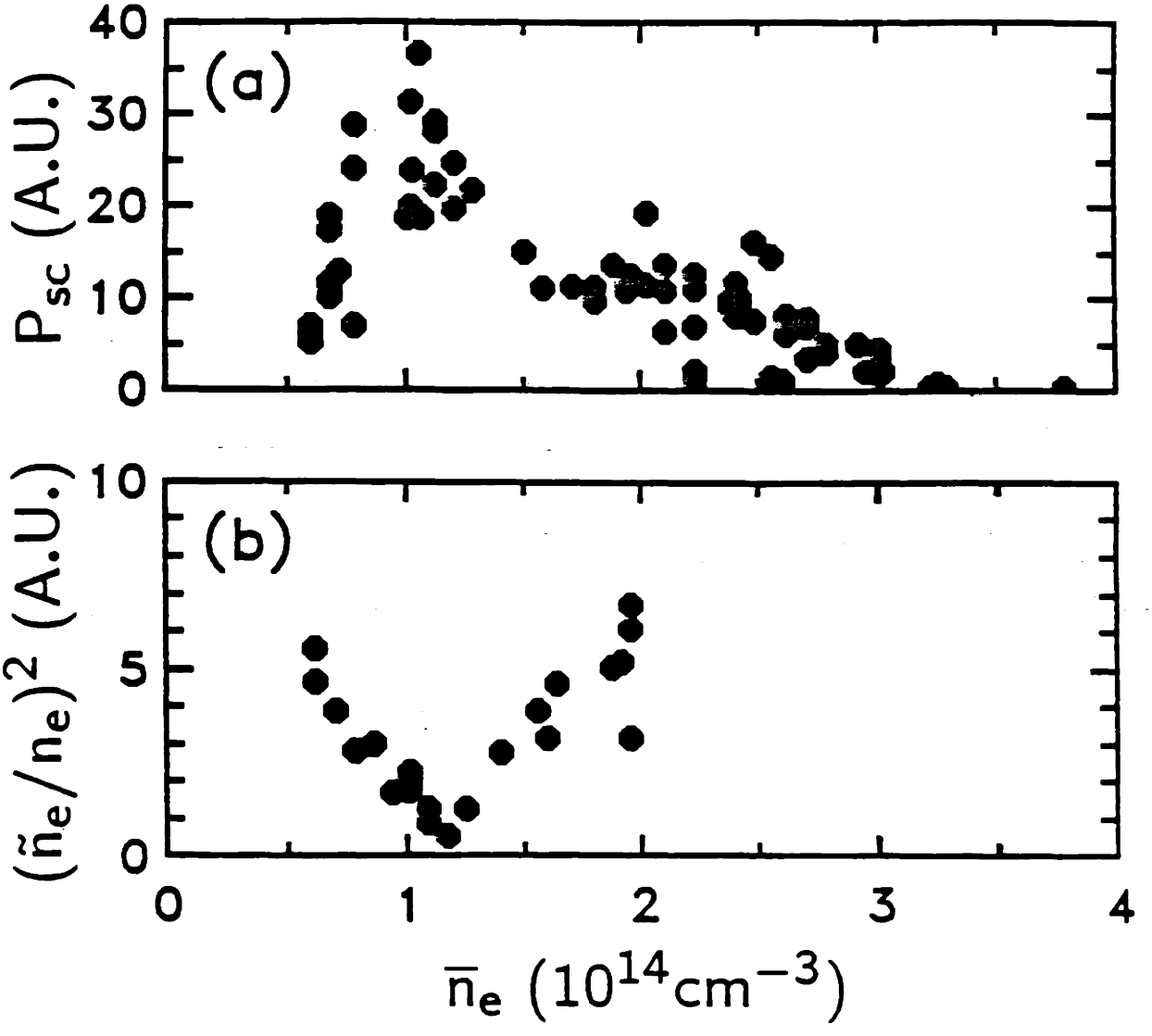

Figure 4.21 —(a) Scattered power from ion Bernstein waves as a function of density. (b) Scattered power from low-frequency edge density fluctuations. Plasma parameters: Hydrogen, $B_0 = 7.6\,\mathrm{T}$, $I_p = 200$–$290\,\mathrm{kA}$.

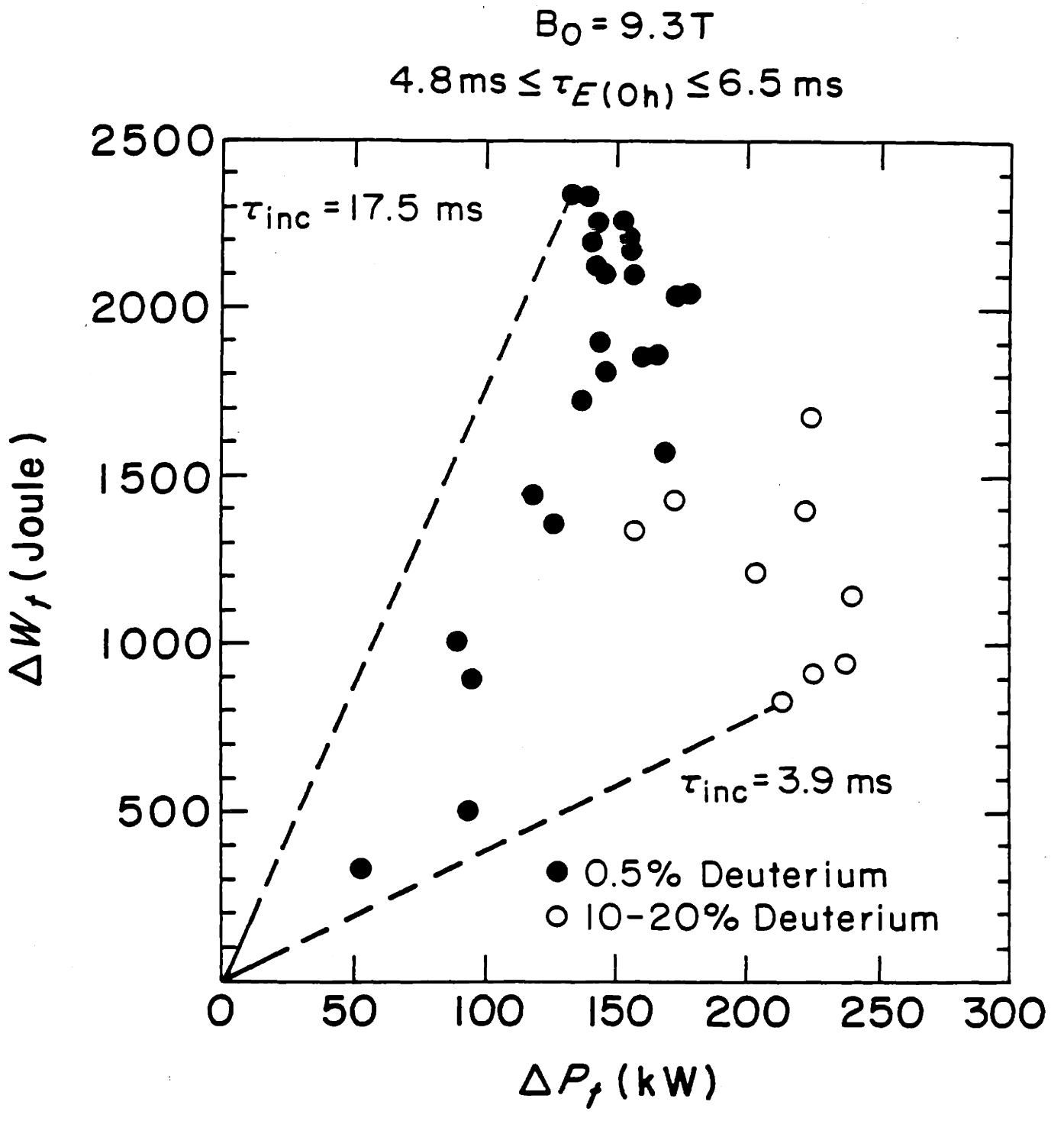

Figure 4.22 —Increase in total plasma thermal energy, ΔW_t, as a function of ΔP_t, the change in total (rf plus Ohmic) input power. The dashed lines show the incremental energy confinement time $\tau_{inc} \equiv \Delta W_t / \Delta P_t$.

density during rf injection. These results were obtained from CO_2 scattering at $B = 9.3\,\mathrm{T}$ by fitting the ion Bernstein wave dispersion relation to the measured value of $k_\perp$[13, 14]. The maximum edge ion temperature occurred at the same density as the minimum in edge density fluctuations and the maximum in particle confinement improvement ($\bar{n}_e \simeq 1 \times 10^{20}\,\mathrm{m}^{-3}$). This is also the same density where the central ion heating is most efficient (see Fig. 4.20). The edge ion temperature at these densities showed an increase with time during the rf pulse (by up to 50%). At higher densities ($\bar{n}_e > 2 \times 10^{20}\,\mathrm{m}^{-3}$) the edge ion temperature was significantly lower. There is a large uncertainty in the actual value of the edge ion temperature which is due to complications caused by the presence of the minority deuterium species and the proximity of the $\omega/\Omega_\mathrm{D} = 3$ layer to the scattering volume. At the lower densities, an edge ion temperature near the estimated upper bound of T_i ($\simeq 300\,\mathrm{eV}$) may yield $\nu_i^* \lesssim 1$ (with large uncertainty), where ν_i^* is the neoclassical ion collisionality parameter[15],

$$\nu_i* \equiv \frac{\sqrt{2}\rho B_0}{B_\mathrm{p} v_{ti} \tau_i \epsilon^{3/2}} \tag{4.4.1}$$

where $v_{ti} \equiv \sqrt{2T_i/m_i}$, B_p is the poloidal magnetic field, and

$$\tau_i^{-1} \equiv \frac{3}{4}\frac{1}{\sqrt{\pi}}\frac{\sqrt{m_i}T_i^{3/2}}{n_i Z_i^4 e^4 \ln\Lambda}. \tag{4.4.2}$$

The nearly collisionless regime for ions ($\nu_i^* \lesssim 1$) may be in agreement with the recent theoretical prediction of Hinton for H–mode type phenomena[16].

Measurements of the OV temperature at $r/a \simeq 1.0$ and $B_0 = 7.6\,\mathrm{T}$ were made using a vacuum ultraviolet spectrometer[17]. The measurements showed an increase in the OV temperature from 75 eV to 95 eV for a density increase from $\bar{n}_e = 0.9 \times 10^{20}\,\mathrm{m}^{-3}$ to $1.5 \times 10^{20}\,\mathrm{m}^{-3}$. At higher Ohmic densities ($\bar{n}_e > 2.2 \times 10^{20}\,\mathrm{m}^{-3}$) no change was observed in the OV temperature from its Ohmic value of 65 eV. Spectroscopic measurements at $B_0 = 9.3\,\mathrm{T}$ are not available.

Edge floating potential measurements in the scrape–off layer $1.05 \leq r/a \leq 1.2$ were also made using a double Langmuir probe and a gridded energy analyzer[18]. Both probes were toroidally separated from the antenna by a limiter and were at different poloidal locations. During rf power injection, the floating potential, measured with respect to the vacuum chamber wall, usually decreased from an initial Ohmic value of $\sim -2\,\mathrm{V}$ to $\sim -10\,\mathrm{V}$ but almost never decreased to less than $\sim -17\,\mathrm{V}$. In the same region $T_e \sim$ 10–30 eV. The variation of the potential inside the limiter edge is not known.

4.5: Conclusions

Laser scattering measurements have confirmed that ion Bernstein wave power was launched into the plasma using a metal loop coupler. The ion Bernstein wave was identified by mapping out the dispersion relation and the scattered power varied linearly with the injected rf power. Wave launching was optimized when the $\omega/\Omega_H = 2$ layer was placed just behind the antenna central conductor. The peak in radiation resistance correlated with this magnetic field value. Wave attenuation, possibly due to power absorption, was observed at the $\omega/\Omega_H = 1.5$ layer at $B_0 = 7.6\,\mathrm{T}$ and $B_0 = 9.3\,\mathrm{T}$. The scattered signal from ion Bernstein waves and the ion heating rate maximized at $\bar{n}_e \simeq 1.1 \times 10^{20}\,\mathrm{m}^{-3}$, whereas the scattered signal from low–frequency edge density fluctuations was minimized at this density. At $P_{rf} < P_{Oh}$ very efficient ion heating ($\bar{n}_e \Delta T_i(0)/P_{rf} \lesssim 45\,\mathrm{eV/kW}10^{19}\,\mathrm{m}^{-3}$) was demonstrated via ion Bernstein wave injection. An improvement in the global particle, and central impurity confinement times (by factors of up to three) accompanied this type of rf heating. The consequence of these results was the attainment of good global energy confinement. The decrease in ion heating rate at higher densities can be explained by a combination of energy confinement saturation, scattering of ion Bernstein waves by edge density fluctuations, and reduced nonlinear absorption with increasing density.

REFERENCES

1. Y. TAKASE, *et al.*, *Phys. Rev. Lett.*, **59**, 1201, (1987).
2. J. D. MOODY, *et al.*, *Phys. Rev. Lett.*, **60**, 298, (1988).
3. M. PORKOLAB, *Phys. Rev. Lett.*, **54**, 434, (1985).
4. M. PORKOLAB, *et al.*, *Plasma Phys. and Contr. Nucl. Fusion Res.* (IAEA 11th Int. Conf., Kyoto, 1986) IAEA–CN–47/F–II–2.
5. M. PORKOLAB, J. D. MOODY, AND C. FIORE, *Bull. Am. Phys. Soc.*, **32**, 1939, (1987).
6. M. BRAMBILLA, in *Application of Radio–Frequency Power to Plasmas–1987*, edited by S. Bernabei and R. W. Motley, AIP Conference Proceedings No. 159 (American Institute of Physics, New York, 1987).
7. C. FIORE, *et al.*in *Application of Radio–Frequency Power to Plasmas–1987*, edited by S. Bernabei and R. W. Motley, AIP Conference Proceedings No. 159 (American Institute of Physics, New York, 1987).
8. H. L. MANNING, J. L. TERRY, *et al.*, *Bull. Am. Phys. Soc.*, **31**, 1587, (1986).
9. E. S. MARMAR, J. L. CECCHI, AND S. A. COHEN, *Rev. Sci. Instrum.*, **46**, 1149, (1975).
10. R. L. WATTERSON, R. E. SLUSHER, AND C. M. SURKO, *Phys. Fluids*, **28**, 2857, (1985).
11. F. WAGNER, G. BECKER, K. BEHERINGER, *et al.*, *Phys. Rev. Lett.*, **49**, 1408, (1982).
12. T. D. SHEPARD, in *Application of Radio–Frequency Power to Plasmas–1987*, edited by S. Bernabei and R. W. Motley, AIP Conference Proceedings No. 159 (American Institute of Physics, New York, 1987).
13. G. A. WURDEN, M. ONO, AND K. L. WONG, *Phys. Rev. A*, **26**, 2297, (1982).
14. H. PARK, P. S. LEE, W. A. PEEBLES, N. C. LUHMANN, JR., *Nucl. Fusion*, **25**, 1399, (1985).
15. F. L. HINTON AND R. D. HAZELTINE, *Rev. Mod. Phys.*, **48**, 239, (1976).
16. F. L. HINTON, *Nucl. Fusion*, **25**, 1457, (1985).
17. R. D. BENJAMIN, *et al.*, *Bull. Am. Phys. Soc.*, **31**, 1157, (1986).
18. A. WAN, MIT Plasma Fusion Center Report PFC/RR–86–13 (1986).

CHAPTER 5

Analyses of the Experimental Results

5.1: Introduction

This chapter presents the detailed analyses performed in order to explain the causes for the observed results in the ion Bernstein wave experiments. In particular, the behavior of the antenna–plasma loading, ion Bernstein wave propagation through edge turbulence, and the plasma response to rf power injection is analyzed in the context of current plasma theories.

Antenna–plasma loading is analyzed in the first part of this chapter by comparing the observed behavior with simulated results from the Brambilla coupling model. Simulations of the antenna loading are performed by varying three plasma parameters; the toroidal field, central density, and edge density. Good agreement is found between the measured and simulated antenna loading over a narrow range of magnetic field values. The simulated loading is found to be strongly dependent on the edge plasma

density. Within the magnetic field range of good agreement, the density dependence of the simulated antenna loading may also agree with the measured dependence.

The remaining part of this chapter presents a detailed study of two density dependent mechanisms which together can explain the decrease in the observed ion heating rate with increasing plasma density. The first mechanism is the scattering of ion Bernstein wave power as it passes through a region of edge plasma turbulence. Observation confirms that the amplitude of the edge turbulence increases with increasing density. The primary effect of this mechanism may be to broaden the power deposition profile. It is shown that a fluctuation amplitude of about $\hat{n}_e \equiv \tilde{n}_e/n_e \sim 0.3$ at $\bar{n}_e = 2\times10^{20}\,\mathrm{m}^{-3}$ is sufficient to broaden the power deposition from being centrally peaked ($0.1 \le \rho/a < 0.3$) to nearly uniform across the plasma cross–section ($0 \le \rho/a \le 1$). The second mechanism is the effect of the density dependence of the ion energy confinement. It is shown that in the Ohmic portion of the ion Bernstein wave discharges, the inferred ion thermal conductivity becomes increasingly anomalous compared to the neoclassical conductivity as the plasma density is increased. This increasing ion thermal conduction anomaly causes the ion energy confinement to degrade with increasing plasma density. The effects of the increasing ion thermal conduction and the broadening of the power deposition profile with density are shown to cause a decrease in the ion heating rate with density corresponding to the measured behavior.

5.2: Antenna–Plasma Coupling

5.2.1: Introduction

Antenna–plasma coupling refers to the ability of an antenna to transmit power into the plasma. If the antenna current and voltage must be extremely high to couple rf power to the plasma ($V_0 >> \sqrt{2Z_0P_{\mathrm{diss}}}$, see Eq. 3.4.25), then the coupling is said to be poor and this is usually marked by a very small value of the radiation resistance ($R_{\mathrm{rad}} << Z_0$ where Z_0 is the antenna characteristic impedance). Coupling to ion Bernstein waves was measured as a function of antenna position and orientation as well as plasma density, central magnetic field, and injected rf power. The strongest dependence of the coupling was observed on the magnetic field, central density and edge density; weaker dependences were observed on the antenna orientation to the edge magnetic field and the injected rf power.

A computer code, developed by M. Brambilla[1] to compute ion Bernstein wave coupling, was used to model and interpret the experimental coupling results from Alcator

C. This code has already been described in section 2.6 and a more detailed description of the code is given by Brambilla in Ref. 2. Only central density, edge density, and magnetic field dependence of the antenna loading were studied here with the Brambilla code. The dependence of the antenna loading on the antenna position predicted by the code is discussed by M. Brambilla in Ref. 2. Section 4.3 presents the observed behavior of the antenna loading on P_{rf}, and antenna orientation. The measurements and code results are comparable in certain plasma regimes; however, there are large discrepancies in other regimes. The disagreement may be caused by nonlinear wave phenomena which can occur near the antenna. These phenomena are not included in the Brambilla model and may cause additional loading which depends in a complicated way on the plasma parameters. These discrepancies between the measurements and theoretical prediction leads one to believe that there is still much which is not yet fully understood about high power ion Bernstein wave antenna–plasma coupling.

The radiation resistance, as defined in section 3.4.4, is given by Eq. 3.4.31 as twice the ratio of the total dissipated power to the square of the maximum current in the antenna. The power dissipation occurs through both Ohmic loss in the transmission line system and radiation loss into the plasma. The Ohmic part of R_{rad} is estimated from the measurements to be $\sim 0.3\,\Omega$ and is independent of plasma parameters. The actual radiation loading, which should be compared with the Brambilla model, is given by the difference between the total loading and the vacuum loading.

This section presents a comparison of the measured antenna–plasma coupling with simulations of the coupling over a range of plasma densities and magnetic fields. The similarities and differences between the measured and simulated values are discussed and some general conclusions are reported.

5.2.2: Simulation Parameters

Simulations of the antenna–plasma coupling were done using the Brambilla code for the plasma parameters listed in Table 5.1. Radiation resistance is calculated for only radiation loading; no Ohmic loading is included. A typical k_z ($k_{||}$) power spectrum is shown in Fig. 5.1 . The coupling is calculated for $k_z \leq 120\,\mathrm{cm}^{-1}$ and $k_y \leq 25\,\mathrm{cm}^{-1}$. The high k_z components can represent an important fraction of power which is coupled into ion Bernstein waves even though this power may eventually Landau damp. An outward radiation condition is imposed at $x/a = -0.25$ ($x = -3$ cm) since this is the approximate location where the power is expected to be absorbed. The density for which the excitation frequency f_0 is equal to the lower hybrid frequency is $n_e \simeq 4 \times 10^{17}\,\mathrm{m}^{-3}$; this is about a factor of 2 below the lowest density assumed possible at the antenna Faraday shield for both the simulations as well as the experiment. As a

result, ion Bernstein waves are directly launched by the antenna and do not undergo a mode transformation process at the lower hybrid layer[3].

5.2.3: Simulation Results

Figure 5.2 shows a series of curves at four different central densities. Each curve connects points with the same ratio of central to edge density and gives the calculated radiation resistance as a function of magnetic field. The curves all exhibit a peak in $R_{\rm rad}$ at a field of 7.25–7.3 T corresponding to $\omega/\Omega_{\rm H} = 1.99$–$1.98$ at the antenna Faraday shield. The data in Fig. 4.6(b) exhibits a peak in $R_{\rm rad}$ when $\omega/\Omega_{\rm H} = 1.9$ at the Faraday shield. The disagreement between the measured and simulated values of the magnetic field which correspond to the peak in $R_{\rm rad}$ can possibly be resolved by considering two effects. First, the toroidal field at the antenna is slightly distorted due to the presence of the access port in the toroidal magnet; however, this distortion is partially compensated giving a field in the vicinity of the port which is about 2–4% lower than expected. To account for the 2–4% lower field, the central field must be about 2–4% higher than expected. Thus, the central field predicted by the Brambilla model for best coupling (7.25 T–7.3 T) is translated into a central field of 7.4 T–7.6 T when the field ripple is taken into consideration. A second effect which may contribute to the discrepancy in the field values is that the Brambilla model assumes that the plasma density within the antenna is zero. As a result, the ion Bernstein waves are, at the earliest, launched from the surface of the Faraday shield (a plasma wave is undefined unless $n_e \neq 0$). It is possible that in reality the waves are launched from within the antenna (from the center conductor for example) where the plasma density is not zero but finite. If this were the case, efficient launching of the ion Bernstein wave (which occurs at $\omega/\Omega_{\rm H} = 1.99$) might occur at a slightly higher field when the $\omega/\Omega_{\rm H} = 1.99$ layer is pushed into the antenna. In this case, the peak in $R_{\rm rad}$, shown in Fig. 5.2 , would actually occur at a higher field (nearly 2% higher if the waves are launched from the central conductor). Combining the effects of the toroidal field ripple and launching the wave from within the antenna can account for the discrepancy in the measured and simulated values of B_0 at the peak in $R_{\rm rad}$. Figure 5.3 shows a comparison of the measured antenna loading (with the 1 Ω background loading subtracted off) with the simulated loading (assuming that the peak is at 7.6 T); the simulated value exhibits a much stronger dependence on the magnetic field than the measured value.

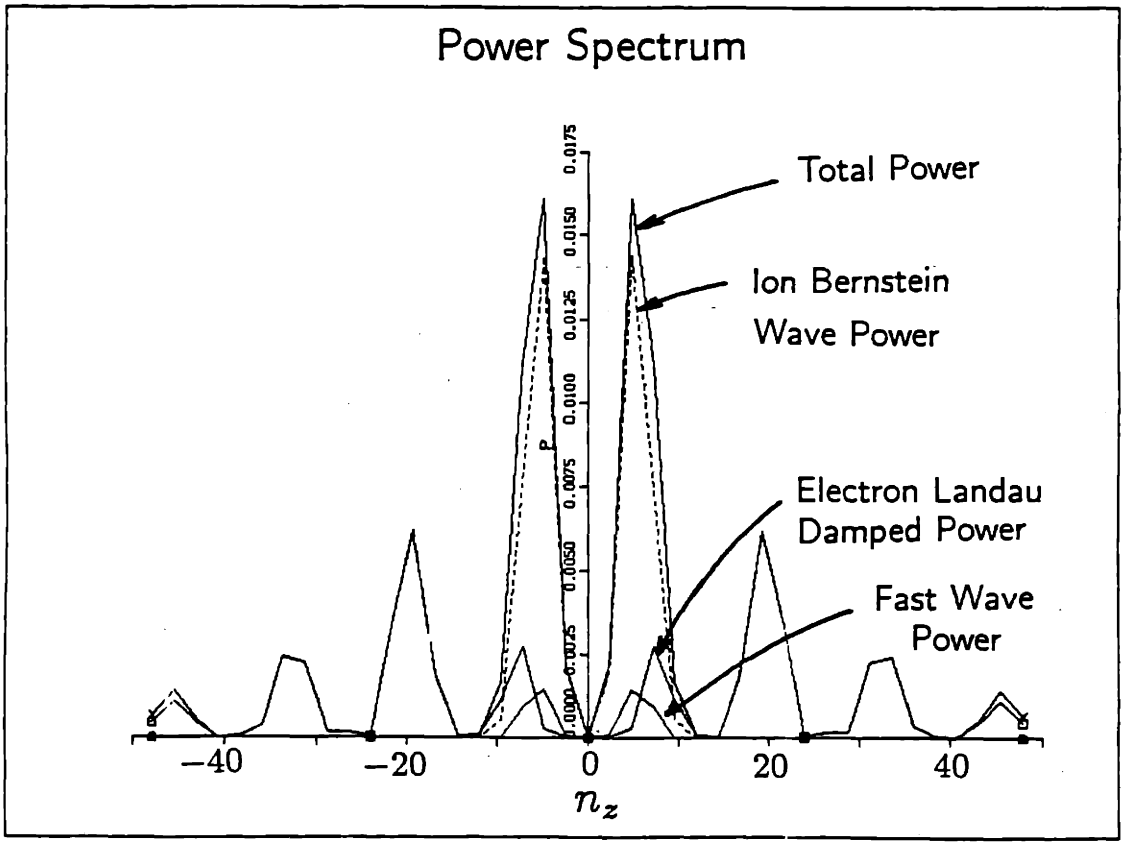

Figure 5.1 —The k_z ($k_\parallel$) power spectrum of the Alcator C ion Bernstein wave antenna calculated from the Brambilla coupling code.

Table 5.1

Simulation Plasma Parameters

Major Radius:	$R_0 = 64\,\text{cm}$
Minor Radius:	$a = 12.5\,\text{cm}$
Vertical Radius:	$b = a = 12.5\,\text{cm}$
Faraday Shield–Plasma:	0.0 cm
Central Conductor–Faraday Shield:	1.3 cm
Central Conductor–Wall:	1.85 cm
Central Conductor Width:	1.4 cm
Antenna Length:	25 cm
$\sqrt{LC}$ Within Antenna:	1.5
Central Density:	$1\text{–}3.5 \times 10^{20}\,\text{m}^{-3}$
Edge Density:	$0.025\text{–}0.35 \times 10^{20}\,\text{m}^{-3}$
Central Electron Temperature:	1.8 keV
Edge Electron Temperature:	0.05 keV
Central Ion Temperature:	1.0 keV
Edge Ion Temperature:	0.05 keV
Magnetic Field:	$B_0 = 7.15\,\text{T}\text{–}7.7\,\text{T}$
Length of Near Field Region:	16 cm
Width of Scrape–off (S.O.) Layer:	0.5 cm
S.O. Density Gradient:	0.5 cm
S.O. Elec. Temp. Gradient:	1.0 cm
S.O. Ion Temp. Gradient:	1.0 cm
Plasma Composition:	90% H with 10% D

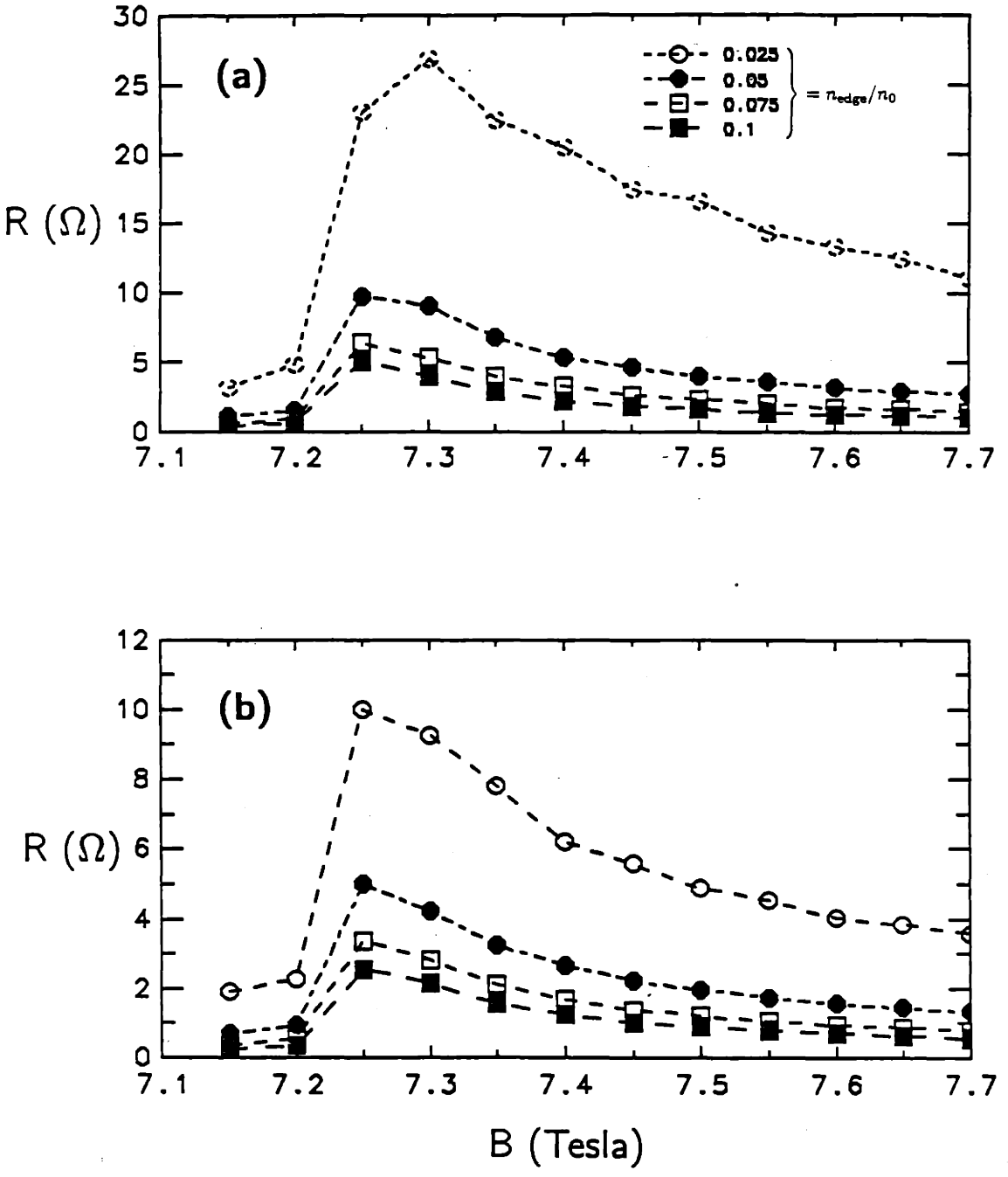

Figure 5.2 —R_{rad} versus B_0 for four central values of the plasma density. (a) $n_0 = 1 \times 10^{20}\,m^{-3}$. (b) $n_0 = 2 \times 10^{20}\,m^{-3}$. (c) $n_0 = 2.5 \times 10^{20}\,m^{-3}$. (d) $n_0 = 3.5 \times 10^{20}\,m^{-3}$.

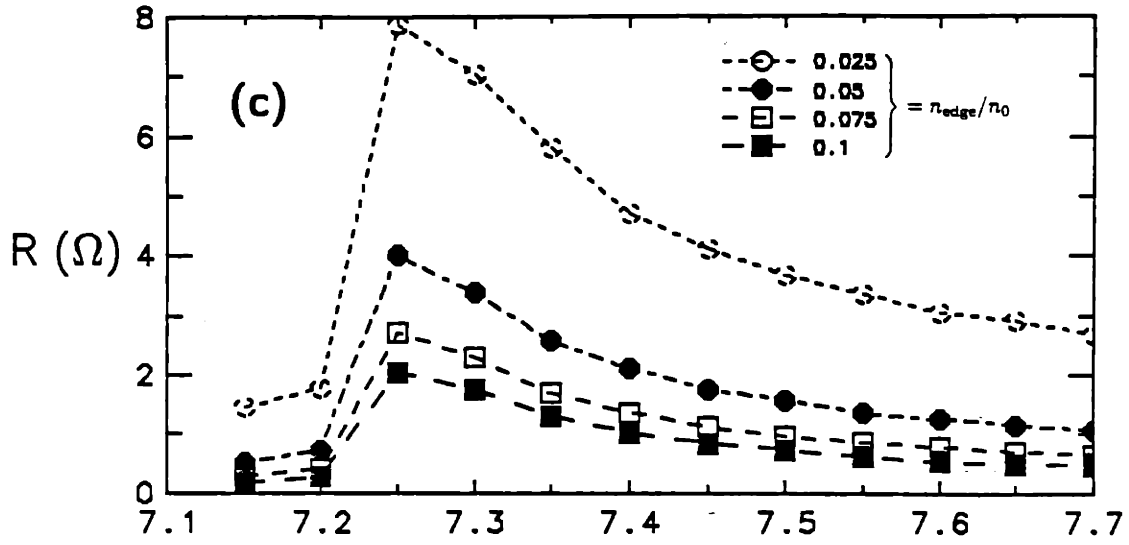
(c)
0.025
0.05
0.075
0.1
$= n_{edge}/n_0$
R (Ω)
0
2
4
6
8
7.1
7.2
7.3
7.4
7.5
7.6
7.7

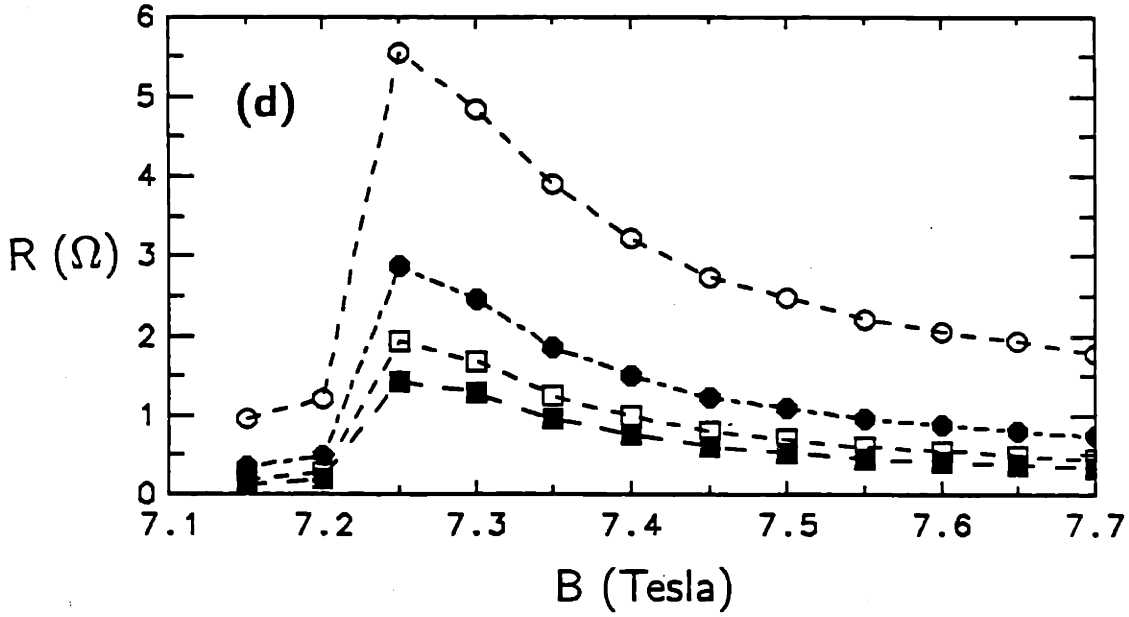
(d)
R (Ω)
0
1
2
3
4
5
6
7.1
7.2
7.3
7.4
7.5
7.6
7.7
B (Tesla)

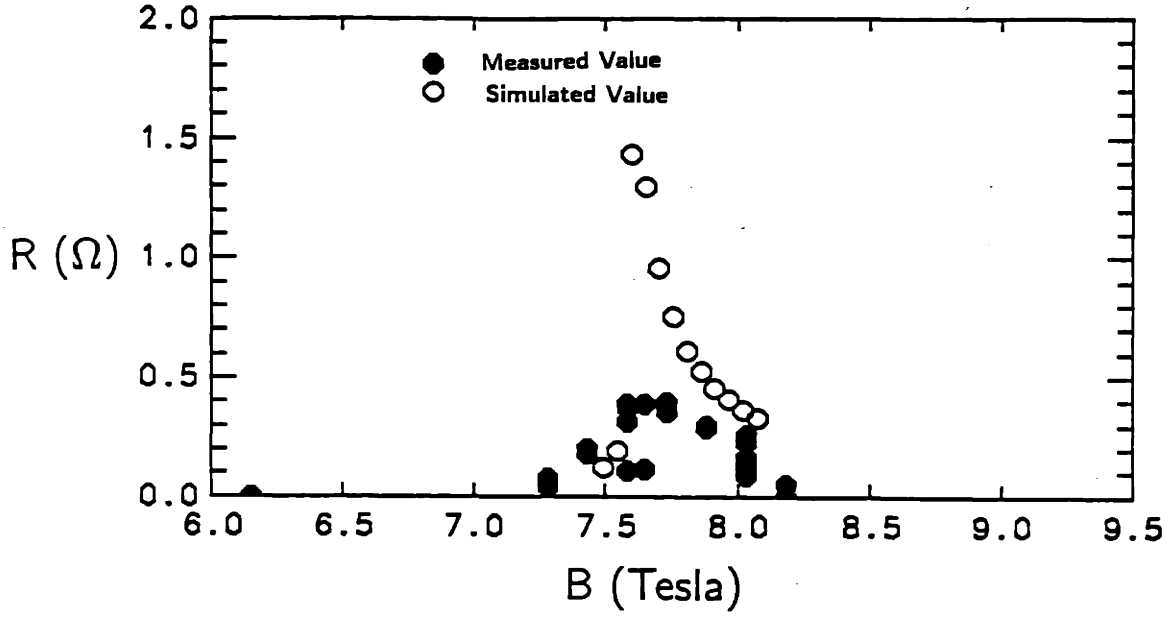

Figure 5.3 —Comparison of R_{rad} versus B_0 for a simulation (corrected for toroidal field ripple) with $n_0 = 3.5 \times 10^{20}\,\mathrm{m}^{-3}$, $n_{edge} = 0.1 n_0$, with the measured value (with the $1\,\Omega$ background subtracted out).

Another observation of the simulated value of R_{rad} is that the width of the simulated peak in Fig. 5.2 is smaller than the measured width. This also may be caused by the toroidal field ripple. The location of the $\omega/\Omega_{\mathrm{H}} = 1.99$ layer intersects the Faraday shield at several toroidal locations due to the toroidal localization of the ripple in the vicinity of the port. Thus, the transition from efficient to inefficient wave launching would be smoothed out over a range of toroidal fields.

The simulated values of R_{rad} for the plasma parameters in Table 5.1 are all somewhat higher than the measured values. An high edge density of $0.6 \times 10^{20}\,\mathrm{m}^{-3}$ and central density of $1 \times 10^{20}\,\mathrm{m}^{-3}$ (not included in Table 5.1 and not shown in Fig. 5.2) give a simulated value of $R_{\mathrm{rad}} \sim 1.3\,\Omega$, nearly the measured value. Outside the magnetic field of efficient coupling† the simulated value of R_{rad} departs by up to an order of magnitude (smaller) than the measured value which exhibits a nearly constant background loading of about $1\,\Omega$. The cause of this background loading may result for example, from nonlinear effects[4, 5, 6] near the antenna. Simulated values of the electric field near the antenna are found to become large enough ($E_x \gtrsim 1\,\mathrm{kV/cm}$), even under efficient coupling conditions, to permit parametric decay of the ion Bernstein wave into another ion Bernstein wave at a slightly downshifted frequency and a low–frequency ion quasimode. This process would create an additional channel for the antenna power to couple to and might increase the antenna loading. Unfortunately, spectral measurements over a wide frequency range are not available to verify the presence of the downshifted ion Bernstein wave or the ion quasimode. Edge collisional absorption may also produce additional loading but a calculation of this shows that it is nearly negligible.

Figure 5.4 shows the simulated fraction of power coupled into the fast ICRF wave as a function of magnetic field. The fraction of power coupled into the ion Bernstein wave is the difference between the fast wave power fraction and unity. At the field value of $\sim$ 7.25 T, Fig. 5.4 shows that the fraction of power coupled into the ion Bernstein wave is maximized and $\lesssim$ 20% of the power flows into the fast wave. At a slightly lower field both the fast wave power fraction increases dramatically (and R_{rad} decreases dramatically). M. Brambilla suggests that this is due to the sudden difficulty of exciting an ion Bernstein wave with a very short wavelength ($\omega/\Omega_{\mathrm{H}} \sim 2.02$ thus $k_\perp \rho_{\mathrm{H}} \gg 1$). The coupling model is not accurate for $k_\perp \rho_{\mathrm{H}} > 1$ but the trend of sudden poor coupling may still be theoretically correct. As the field is increased from $B_0 \sim 7.25\,\mathrm{T}$, Fig. 5.4 shows that the fast wave fraction increases slowly (and R_{rad} decreases slowly). M. Brambilla suggests that this may be due to the gradual increasing difficulty of coupling to a shorter wavelength ion Bernstein wave.

---

† Efficient coupling corresponds to the location where R_{rad} is maximized.

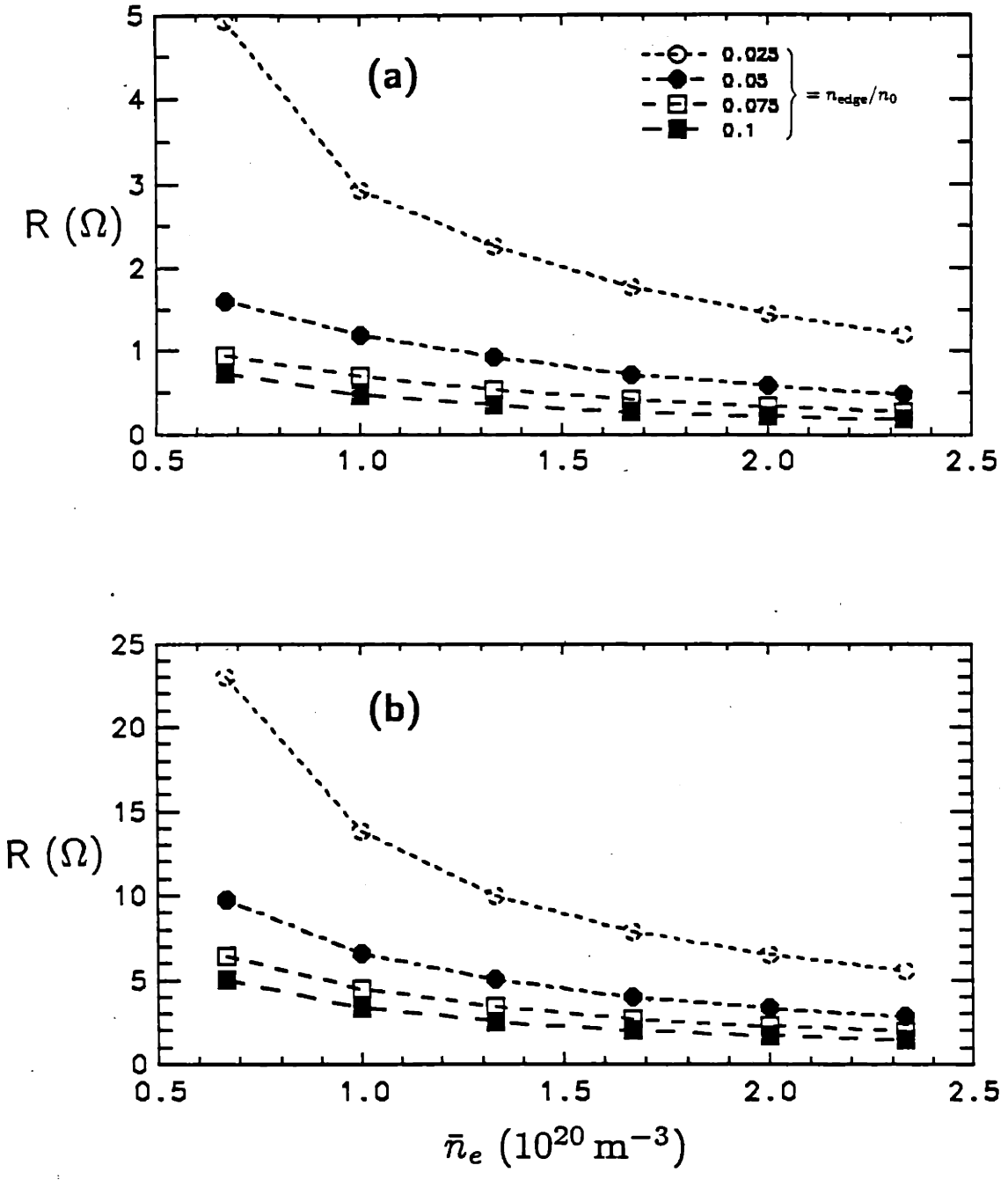

Figure 5.4 —The fraction of power coupled into the fast ICRF wave as predicted by the Brambilla model as a function of the toroidal magnetic field for four central plasma densities. (a) $n_0 = 1 \times 10^{20}\,\mathrm{m}^{-3}$. (b) $n_0 = 2 \times 10^{20}\,\mathrm{m}^{-3}$. (c) $n_0 = 2.5 \times 10^{20}\,\mathrm{m}^{-3}$. (d) $n_0 = 3.5 \times 10^{20}\,\mathrm{m}^{-3}$.

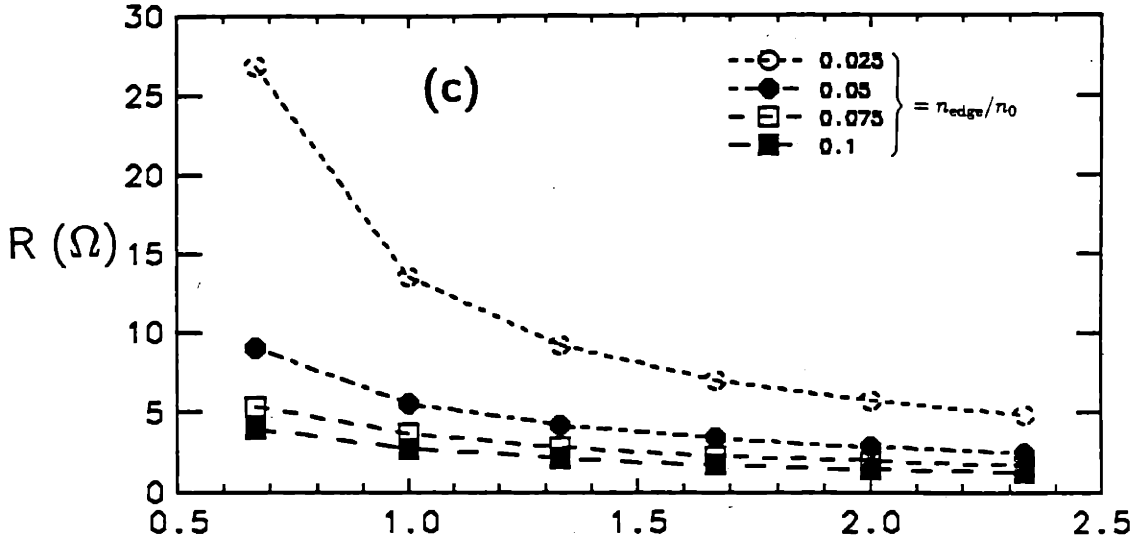
(c)
0.025
0.05
0.075
0.1
$= n_{edge}/n_0$
R (Ω)
30
25
20
15
10
5
0
0.5
1.0
1.5
2.0
2.5

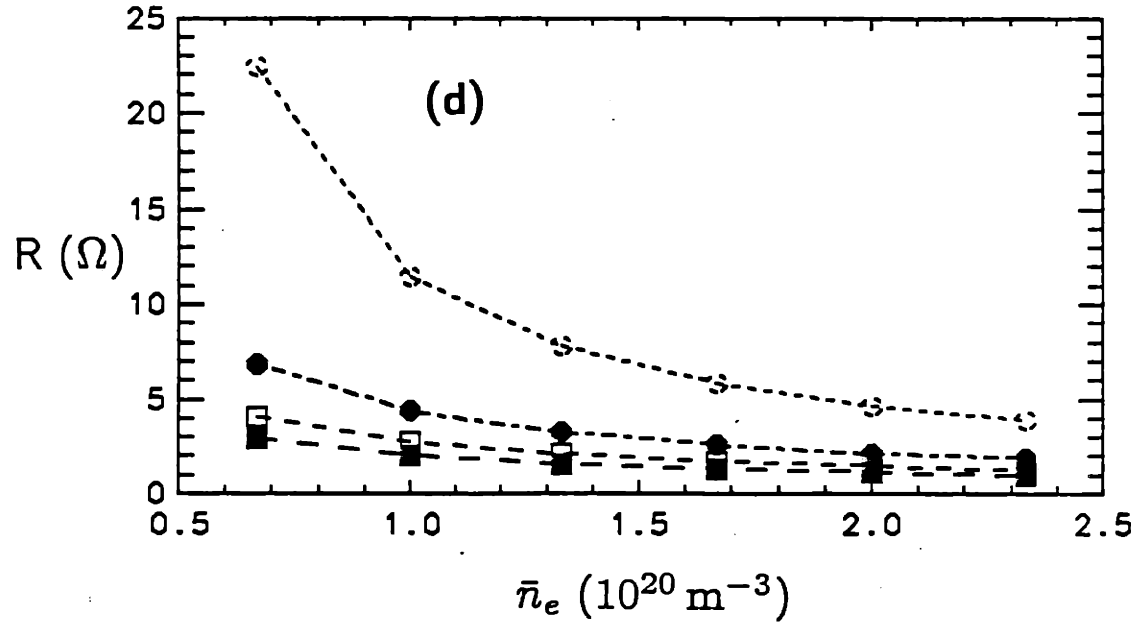
(d)
R (Ω)
25
20
15
10
5
0
0.5
1.0
1.5
2.0
2.5
$\bar{n}_e\ (10^{20}\,\mathrm{m}^{-3})$

5.2.4: Density Dependence of the Antenna Loading

The measured density dependence of $R_{\rm rad}$, shown in Fig. 4.7(b), increases almost linearly with density to a maximum and then decreases. Simulated values of $R_{\rm rad}$ for cases with a constant ratio of edge to central density are shown in Fig. 5.5 . These all exhibit a monotonic decrease with density. The apparent departure of the simulation results from the measured value of $R_{\rm rad}$ may be resolved by considering two effects. First, it may not be realistic to assume that the ratio of the edge to central density remains constant over the range of central densities. If the edge density near the antenna remaines nearly constant or decreases slightly as the central density is increased, the simulated value of $R_{\rm rad}$ would increase with density as does the measured value†. Eventually, the edge density would begin to increase as the central density continued to increase causing the simulated value of $R_{\rm rad}$ to begin decreasing. Thus, the measured density behavior of $R_{\rm rad}$ may be caused mainly by the edge density behavior. Unfortunately, there are no edge density measurements within the vicinity of the antenna to confirm this. Nonlinear processes may once again play a role in determining the density dependence of the antenna loading. It is difficult to accurately determine the expected density dependence of the nonlinear process without working out the details of the nonlinear theory which will not be included in this study.

Near the toroidal field of good coupling ($R_{\rm rad}$ is maximized) the fraction of power coupled into the fast ICRF wave is between 7% and 25%. This fraction shows only weak dependence on the central density; the strongest dependence is on the edge density.

5.2.5: Conclusions

The measured loading to ion Bernstein waves is maximized when the $\omega/\Omega_{\rm H} \simeq 1.90$ layer is placed at the Faraday shield surface. This result is reproduced well by the Brambilla model. The precise value of $R_{\rm rad}$ from the model agrees with the measured value for a high edge density compared to the central density. A large background loading of $\sim 1\,\Omega$ persists at magnetic fields not corresponding to $\omega/\Omega_{\rm H} \simeq 1.90$. This background may result from nonlinear wave processes occurring near the antenna which could introduce additional loading. Near the magnetic field of maximum antenna loading, the fraction of power coupled into the ICRF fast wave is small ($\lesssim 20\%$). The observed density dependence of the loading is reproduced with the model provided the edge density is assumed to remain nearly constant or decrease until the line–averaged

† M. Brambilla has shown that the important parameter in the density dependence of $R_{\rm rad}$ is the value of the edge density rather than the density gradient.

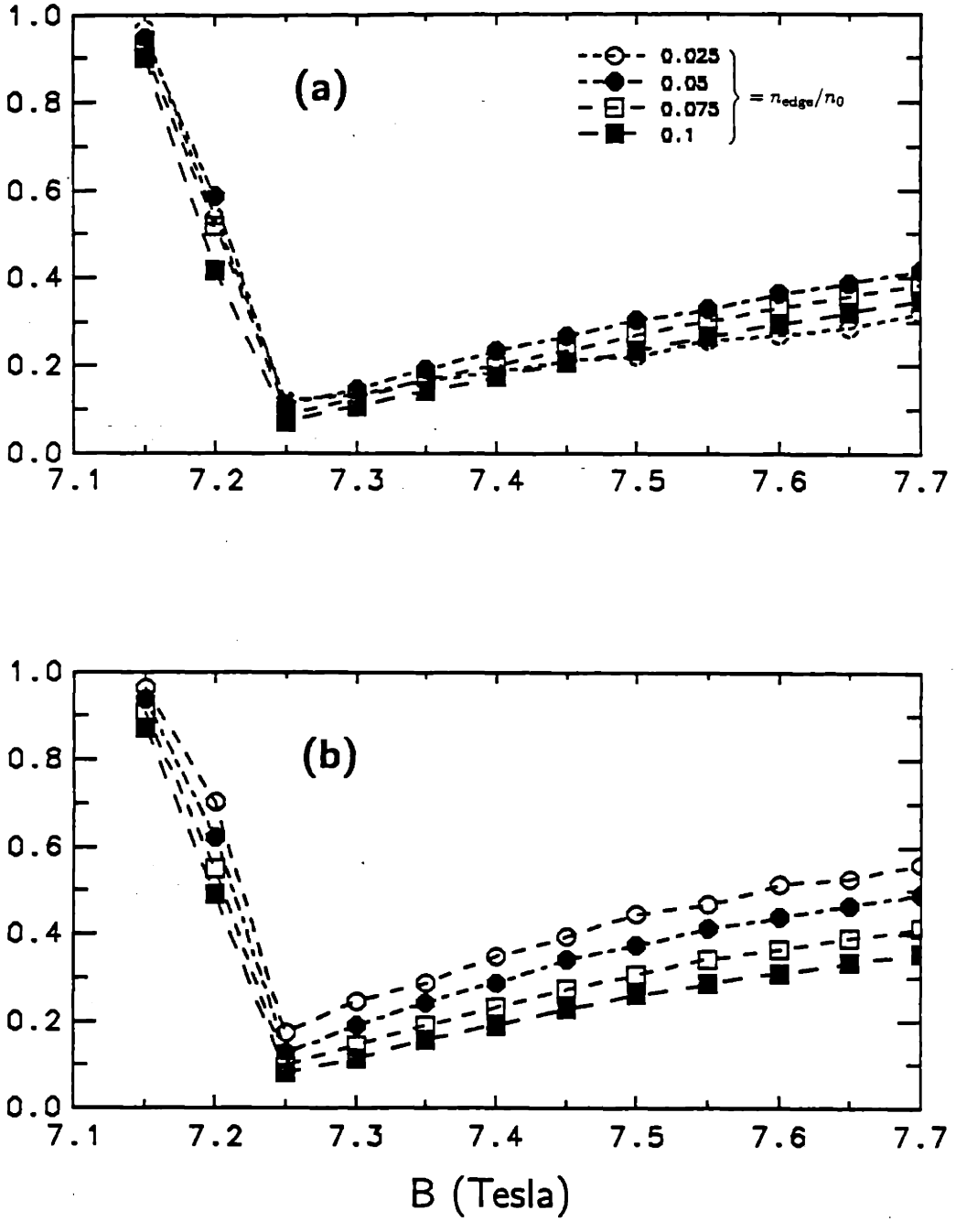

Figure 5.5 —R_{rad} versus plasma density at four toroidal field values. (a) $B_0 = 7.2\,\mathrm{T}$. (b) $B_0 = 7.25\,\mathrm{T}$. (c) $B_0 = 7.3\,\mathrm{T}$. (d) $B_0 = 7.35\,\mathrm{T}$.

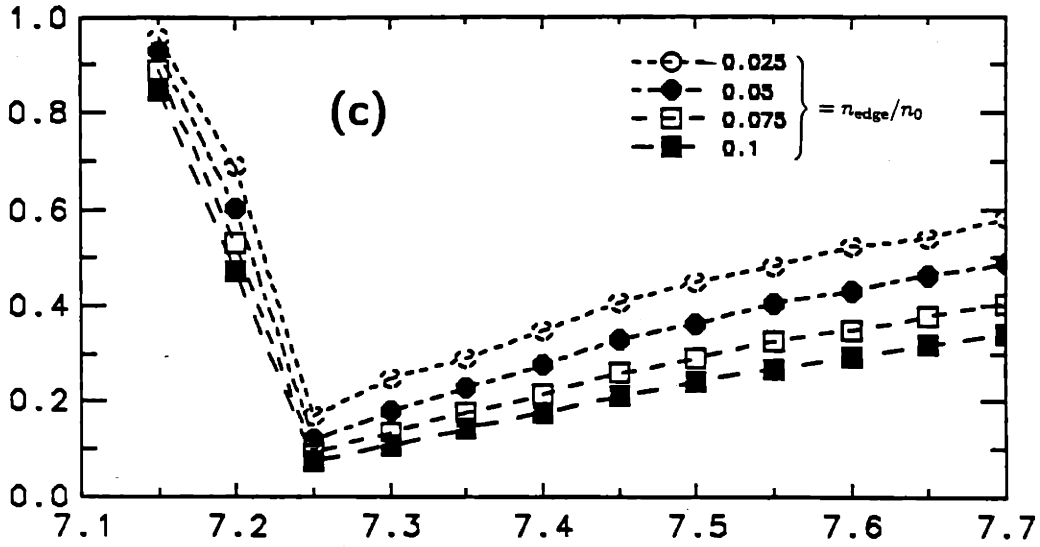
(c)
0.025
0.05
0.075
0.1
$= n_{edge}/n_0$
1.0
0.8
0.6
0.4
0.2
0.0
7.1
7.2
7.3
7.4
7.5
7.6
7.7

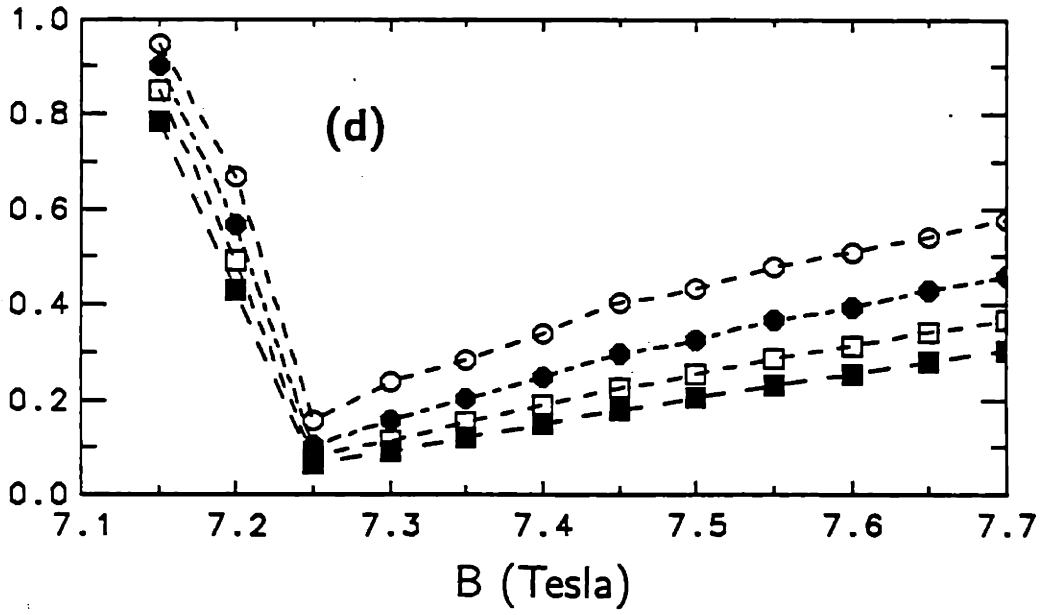
(d)
1.0
0.8
0.6
0.4
0.2
0.0
7.1
7.2
7.3
7.4
7.5
7.6
7.7
B (Tesla)

density increases to $\bar{n}_e \simeq 2.6 \times 10^{20}\,\mathrm{m}^{-3}$; then the edge density must start increasing. A large electric field near the antenna, even in the regime of efficient coupling, is predicted by the Brambilla model. This large field and the slight power dependence of R_{rad} support the possibility of nonlinear effects which might produce loading not included in the Brambilla model.

5.3: Scattering From Density Fluctuations

5.3.1: Introduction

Evidence to suggest that ion Bernstein wave penetration into the plasma may be affected by scattering from edge turbulence[7]is shown in Fig. 5.6 . The edge density fluctuation amplitude [Fig. 5.6 (b)] exhibits a minimum at a line–averaged density of $\bar{n}_e \simeq 1.1 \times 10^{20}\,\mathrm{m}^{-3}$ and increases for both higher and lower densities. This behavior is inversely correlated with the amplitude of the scattered signal from ion Bernstein waves in the plasma center [Fig. 5.6 (a)] and with the hydrogen ion heating rate $\Delta T_i/P_{\mathrm{rf}}$ (Fig. 4.20). Both the ion heating rate and the scattered signal from ion Bernstein waves show a decrease in their value for densities above $\bar{n}_e \gtrsim 1.1 \times 10^{20}\,\mathrm{m}^{-3}$. Below $\bar{n}_e \simeq 1.1 \times 10^{20}\,\mathrm{m}^{-3}$ it is difficult to tell for certain whether the heating rate also decreases. The data at $\bar{n}_e \simeq 0.6 \times 10^{20}\,\mathrm{m}^{-3}$ suggests that the heating rate is down by about a factor of 2; however, more data at lower densities would be necessary in order to confirm this with certainty. The absolute value of $\hat{n}_e^{\dagger}$ could not be measured accurately; however, based on earlier measurements[8]it is estimated to be in the range 0.1–0.5 at $\bar{n}_e = 2 \times 10^{20}\,\mathrm{m}^{-3}$.

In order to investigate the effects of edge density turbulence on ion Bernstein wave propagation, a ray tracing model was developed and used to solve the wave kinetic equation describing ion Bernstein wave scattering from density turbulence. The method used to solve the kinetic equation is described as a Monte Carlo direct sampling simulation[9]. This type of method has been used previously by Bonoli[10]to model the turbulent scattering of lower hybrid waves. Ono[7] has described the theory of turbulent wave scattering for ion Bernstein waves, fast waves, and lower hybrid waves.

---

† Recall that $\hat{n}_e \equiv \tilde{n}_e/n_e$ is the normalized fluctuation amplitude; $\tilde{n}_e$ is the absolute magnitude of the density fluctuation.

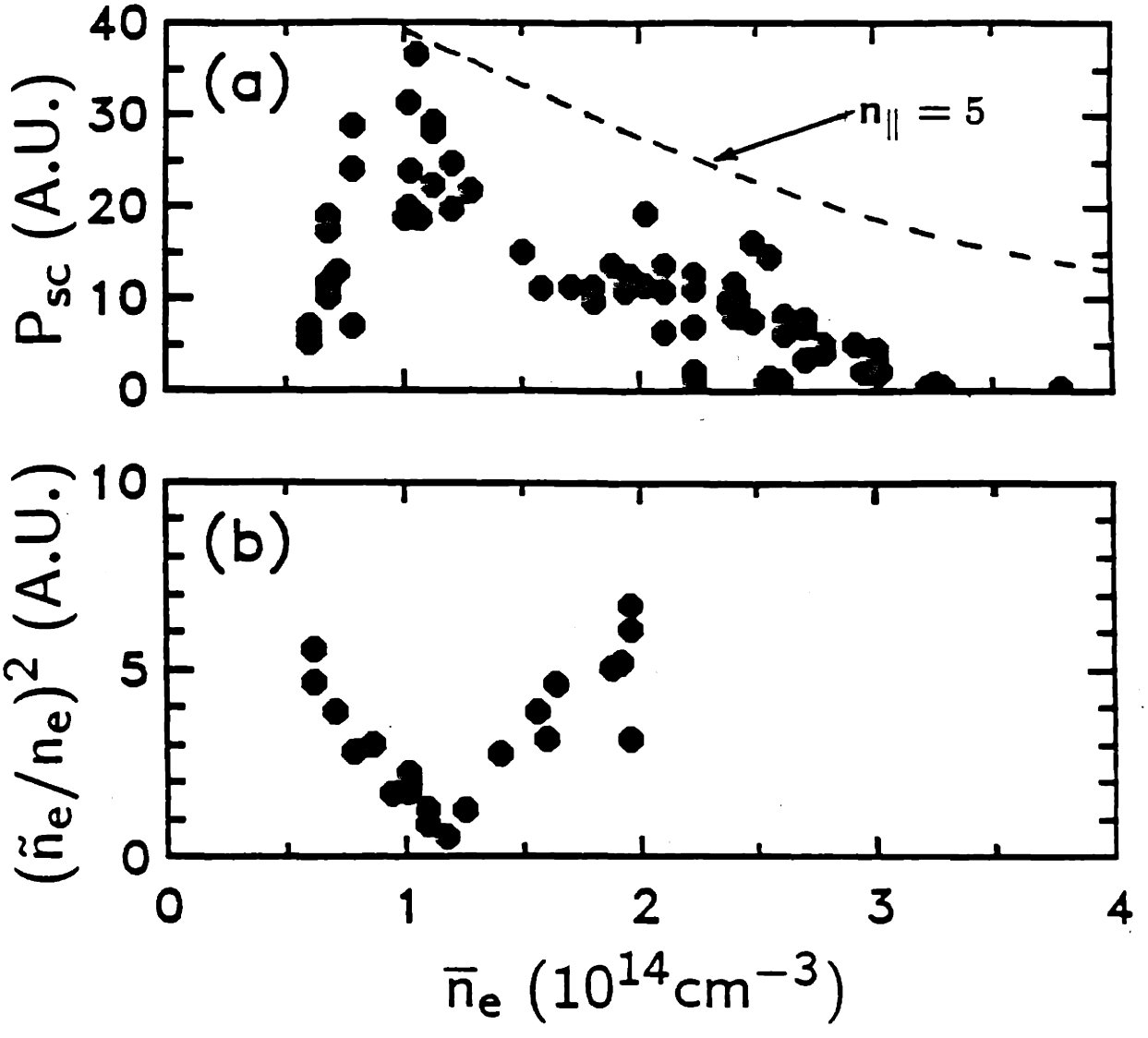

Figure 5.6 —(a) Scattered power from ion Bernstein waves as a function of plasma line–averaged density. The dotted line shows expected value of P_{scat} assuming a large value of $k_{\|}$ ($n_{\|} = 5$). (b) Scattered power from low–frequency edge turbulence as a function of plasma line–averaged density.

This section discusses the details of the scattering process and presents the method used for modeling the effect of plasma turbulence on ion Bernstein wave propagation in Alcator C. The results of this model will be presented and discussed.

5.3.2: Expected Behavior of $\hat{n}_e$

Figure 5.6 (a) shows the scattered power from ion Bernstein waves in the plasma center as a function of density. The scattered power is proportional to the integral of $\tilde{n}_e^2$ over the scattering volume consisting of the region defined by the intersection of the CO_2 laser beam and the plasma. It is important to determine the expected behavior of $\tilde{n}_e^2$ in order to tell how strongly the data in Fig. 5.6 (a) deviates from this.

The normalized electron density fluctuation amplitude $\hat{n}_e$ can be written in terms of the wave electric field amplitude E_x and the dielectric tensor elements. This expression has been given in Ref. 11 as

$$\hat{n}_e \equiv \frac{\tilde{n}_e}{n_e} = i\frac{e}{m_e c\omega}\left[\frac{\omega^2}{\omega_e^2} - i\frac{\omega}{\omega_e}\frac{K_{xy}}{K_{xx} - n_\parallel^2 - n_\perp^2} - \frac{n_\parallel^2}{n_\perp^2 - K_{zz}}\right] n_\perp E_x \qquad (5.3.1)$$

where $\omega_e = |\Omega_e|$. The electric field amplitude $|E_x|$ is related to the wave power P as

$$P = \frac{\omega}{8\pi}\frac{\partial\epsilon}{\partial k_\perp}|E_x|^2 S \qquad (5.3.2)$$

where S is the wave surface area. The precise behavior of $\hat{n}_e$ with density is complicated since it depends on the dominant term(s) in Eq. 5.3.1 and on the electric field. To partly simplify the analysis of Eq. 5.3.1 it is assumed that the antenna is operating under good coupling conditions, *i.e.* the total power coupled into ion Bernstein waves is essentially independent of density. In this case, P in Eq. 5.3.2 is constant with density. In addition, the perpendicular wave vector $k_\perp$ is independent of density (see Eq. 2.4.32). The dielectric constant, ϵ is proportional to the density for the range of densities considered here (see Eq. 2.5.5), thus $\partial\epsilon/\partial k_\perp$ is also proportional to the density. The wave surface area S depends on the extent to which the ion Bernstein waves have spread by the time they reach the scattering volume. The scattering volume extends over the length of the plasma in the poloidal cross section, therefore wave spreading in the poloidal cross section does not affect the integrated scattered power. Wave spreading in the toroidal direction does however affect the integrated scattered power since the scattering volume has finite toroidal extent. Toroidal wave spreading is primarily determined by the value of $n_\parallel$ and weakly by the derivatives of the plasma parameters. This can be seen from Eq. 2.7.19 which shows that the wave spreading

is determined by the group velocity ratios in the ρ, θ, and ϕ direction; these ratios are essentially density independent. The toroidal wave spreading is approximately independent of density provided the profile of the plasma parameters remains nearly constant with density. This is a good assumption. In addition, the $n_{||}$ power spectrum remains relatively constant over the density range considered. It can therefore be concluded that S is essentially independent of density. It is pointed out that the CO_2 laser scattering system can only observe waves with wave vector $\mathbf{k}$ perpendicular to the incident laser $\mathbf{k}_0$; it is possible that the fraction of observable wave power may change with density. This is difficult to determine, but based on numerical simulations of ion Bernstein wave ray trajectories, the effect seems to be negligible. It can be concluded at this point from Eq. 5.3.2 that for constant P, $|E_x|$ is approximately proportional to $n_e^{-1/2}$.

The dominant term in Eq. 5.3.1 for the densities considered here is primarily dependent on the value of $n_{||}$ with a weaker dependence on the plasma density. The first term in Eq. 5.3.1, ω^2/ω_e^2, describes the density perturbation resulting from the E_x wave field. This term is independent of density and is of comparable magnitude to the second term for low densities ($\bar{n}_e \sim 1 \times 10^{20}\,\mathrm{m}^{-3}$). The second term describes the density perturbation resulting from the E_y component (which drives the $E_y \times B_0$ particle drift) and can be approximated as

$$-i\frac{\omega}{\omega_e}\frac{K_{xy}}{K_{xx}-n_{||}^2-n_{\perp}^2} \simeq \frac{\omega}{\omega_e}\frac{D}{n_{\perp}^2} \tag{5.3.3}$$

where D is defined by Eq. 2.4.13. Since $n_{\perp}^2$ is on the same order as K_{zz}, the third term, which gives the density perturbation due to E_z, cannot be approximated. For small $n_{||}$ ($<< 1$), the second term, which increases approximately linearly with density, determines the overall behavior of $\hat{n}_e$. For example, when $n_{||} = 0.1$ the value of $\hat{n}_e^2$ increases by a factor of 20 as the density increases from $\bar{n}_e = 1 \times 10^{20}\,\mathrm{m}^{-3}$ to $4 \times 10^{20}\,\mathrm{m}^{-3}$. In this case, the data in Fig. 5.6 (a) indicates that the observed ion Bernstein wave power is strongly reduced with increasing density compared to the expected value. For large values of $n_{||}$ (> 1), the third term, which decreases with density, determines the behavior of $\hat{n}_e$. The dotted line in Fig. 5.6 (a) shows the overall expected value of $P_{\mathbf{scat}}$ ($\propto \hat{n}_e^2$) for $n_{||} = 5$ normalized to the observed value of $P_{\mathbf{scat}}$ at $\bar{n}_e = 1.1 \times 10^{20}\,\mathrm{m}^{-3}$. The decrease in the expected value of $P_{\mathbf{scat}}$ with density is not quite as strong as the measured decrease. In this case, the data at high density indicates that the ion Bernstein wave power is only weakly reduced from what is expected. The CO_2 laser scattering system preferentially observes ion Bernstein waves with small $n_{||}$ since most of the wave power which enters the scattering volume must propagate nearly perpendicularly to the antenna surface.

5.3.3: Theory of Ion Bernstein Wave Scattering

Ono[7] has previously described the theory of wave–wave interaction between ion Bernstein waves and density turbulence. It is useful to discuss several of the important features of this interaction in preparation for discussing the method used to model the wave scattering from turbulence. The following gives some of the important results of the theory of ion Bernstein wave scattering from Ref. 7.

Since the measured frequency of the density fluctuations is small compared to the ion cyclotron frequency, the frequency shift in the scattered ion Bernstein wave can be neglected. Also, the parallel wave number can be considered to be conserved since $k_{||}$ of the ion Bernstein wave is typically much larger than the average $k_{||}$ of the fluctuation. When this condition is not satisfied, the parallel coupling can be shown to be negligibly small. The main effect, therefore, of the scattering can be well represented simply by a rotation of the ion Bernstein wave vector $\mathbf{k}_\perp$ through an angle β.

The scattering angle β is defined so that $\mathbf{k}_\perp \cdot \mathbf{k}'_\perp = |k_\perp|^2 \cos\beta$ where $\mathbf{k}_\perp$ and $\mathbf{k}'_\perp$ are the incident and scattered perpendicular components of the ion Bernstein wave vector, respectively. The mode coupling equation for this interaction is given as

$$i\left(\frac{\partial\epsilon}{\partial\omega}\right)_{\omega(\mathbf{k})}\frac{\partial E_\perp(\mathbf{k})}{\partial t} = \hat{n}_e(\mathbf{k}-\mathbf{k}')VE_\perp(\mathbf{k}')\exp\left[-i(\omega_{\mathbf{k}}-\omega'_{\mathbf{k}})t\right] \tag{5.3.4}$$

where V is the matrix element which describes the strength of the coupling between the ion Bernstein wave and the fluctuations.

The probability per unit time of scattering $k_\perp$ by an angle between β and $\beta + d\beta$ is given by[7, 10]

$$P(\beta,t) = \frac{2\pi k_\perp}{\partial\omega/\partial k_\perp}\left(\frac{\partial\epsilon}{\partial\omega}\right)^{-2}|V|^2 S_e\left[2k_0\sin\left(\frac{\beta}{2}\right)\right]d\beta. \tag{5.3.5}$$

where S_e represents the functional form of the density fluctuation wave number spectrum. It has been found experimentally[12]that the function S_e is well approximated by the expression

$$S_e(\xi) = \frac{1}{\pi\xi_0}|\hat{n}_e|^2\exp\left[-\frac{\xi^2}{\xi_0^2}\right] \tag{5.3.6}$$

where ξ_0 is the root–mean–square (rms) value of the fluctuation wave number spectrum. A scattering length definition, suggested in Ref. 13, which does not depend on the approximation $\xi_0^2 \ll k_0^2$ is

$$L_s = \left(k_\perp \frac{\partial \epsilon}{\partial k_\perp}\right)^2 \frac{1}{4\pi k_\perp^3} \times \left\{\int_{-\pi}^{\pi} |V|^2 S_e \left[2k_0 \sin\frac{\beta}{2}\right] \sin^2\frac{\beta}{2} d\beta\right\}^{-1}. \tag{5.3.7}$$

This definition gives the perpendicular distance traveled by the lowest nonvanishing eigenfunction of Eq. 5.3.4 (in the random phase approximation) by the time it decays to $\sim$ 63% $(1/e)$ of its initial amplitude. When $\xi_0\rho_i$ is fixed, the scaling of L_s is approximated in Ref. 7 as

$$L_s \propto \sqrt{T_i}/(B_0|\hat{n}_e|^2) \tag{5.3.8}$$

and is independent of the plasma density.

A simple picture of the scattering process follows by considering the effect of a density perturbation (turbulence) on the wave equation (Eq. 2.3.6)

$$\nabla \times \nabla \times \mathbf{E}^{(1)} + \frac{\omega^2}{c^2}\mathbf{K}\cdot\mathbf{E}^{(1)} = -\frac{4\pi i}{\omega}\mathbf{J}^{(1)}_{\mathbf{ext}}. \tag{5.3.9}$$

A normalized density perturbation $\hat{n}$ modifies the plasma contribution to the tensor $\mathbf{K}$ so that

$$\mathbf{K} = (\mathbf{K_0} - \mathbf{I})[1 + \hat{n}] + \mathbf{I} \tag{5.3.10}$$

where $\mathbf{K_0}$ is the unperturbed dielectric tensor ($\mathbf{K_0} - \mathbf{I}$ is proportional to density) and the turbulent density perturbation is assumed to be the same for the ion and electron species. In the absence of external currents, Eq. 5.3.9 can be written as

$$\mathbf{G_0}\cdot\mathbf{E}^{(1)} = -\hat{n}\frac{\omega^2}{c^2}[\mathbf{K_0} - \mathbf{I}]\cdot\mathbf{E}^{(1)}. \tag{5.3.11}$$

The left side of Eq. 5.3.11 is the standard homogeneous wave equation and the right side describes the second order (nonlinear) coupling between the density perturbation $\hat{n}$ and the plasma wave $\mathbf{E}^{(1)}$. Noting the similarity between this equation and the inhomogeneous wave equation (Eq. 2.3.15) leads one to consider the right side of Eq. 5.3.11 as an external current perturbation which does work on the plasma wave. Considered this way, it is easy to see that the right side of Eq. 5.3.11 will influence the wave energy giving rise to a long time scale variation in the wave energy amplitude. Rewritten as an energy equation (kinetic equation) Eq. 5.3.11 gives the time rate of change of wave energy density. The wave energy density in the ion Bernstein wave is depleted, due to turbulent scattering, at a rate which is dependent only on $\hat{n}$; all of the plasma density dependence remains in the wave energy density.

5.3.4: Numerical Procedure

The numerical study of the scattering process proceeds as follows. The Brambilla coupling model is first used to obtain the expected k_y and k_z power spectrum. A typical k_z spectrum (k_y is integrated over) is shown in Fig. 5.1. The power is peaked near $k_z \simeq 0.18\,\mathrm{cm}^{-1}$ (characteristic of the antenna geometry) and has smaller peaks at higher k_z. This spectrum is then divided into 106 regions, each with a corresponding power, k_y (k_θ), and k_z (k_ϕ). The toroidal ray tracing code, described in section 2.7, is next used to advance a ray (representing one region of the power spectrum) in time by Δt. The probability of a scattering event occurring in time Δt where the ion Bernstein wave vector is rotated through any angle $-\pi \leq \beta \leq \pi$ is given by the expression

$$P_{\text{total}} = \Delta t \int_{-\pi}^{\pi} P(\beta, t)\, d\beta. \tag{5.3.12}$$

The value of Δt is selected so that $P_{\text{total}} << 1$. This prohibits multiple scattering events during the time interval Δt. A random number n_p with uniform distribution between 0 and 1 is generated. If $P_{\text{total}} \geq n_p$ the ray is scattered, otherwise the ray is advanced another unit in time by Δt and P_{total} is again calculated and compared with a new random value of n_p. If the ray is to be scattered, a random angle β is generated with the distribution

$$G(\beta) = \frac{P(\beta)}{\int_{-\pi}^{\pi} P(\beta)\, d\beta}. \tag{5.3.13}$$

This is done numerically by generating a random number n_β with uniform distribution between $-\pi \leq n_\beta \leq \pi$. The scattering probability $P(n_\beta)$ is calculated for this number. A second random number n_p is then generated with a uniform distribution between 0 and 1. If $P(n_\beta) \leq n_p$ the random number n_β is accepted as the scattering angle β. If $P(n_\beta) > n_p$, this process is repeated again with two new random numbers n_β and n_p until a random number n_β is selected. Once a scattering angle is determined, the wave vector $k_\perp$ is rotated through this angle. To carry out the rotation on only the perpendicular component of $\mathbf{k}$ it is helpful to rewrite the vector $\mathbf{k} = k_\rho\hat{\rho} + k_\theta\hat{\theta} + k_\phi\hat{\phi}$ in new coordinates as

$$\mathbf{k} = k_\rho\hat{\rho} + k_{\hat{b}\times\hat{\rho}}\hat{b} \times \hat{\rho} + k_\parallel\hat{b} \tag{5.3.14}$$

where $\hat{b}$ is the unit vector in the direction of the total local magnetic field. The perpendicular part of $\mathbf{k}$ is represented by the first two components in Eq. 5.3.14; this part is rotated by the angle β to give $\mathbf{k}'$. The new wave vector $\mathbf{k}'$ is then transformed back to the $\hat{\rho}$, $\hat{\theta}$, and $\hat{\phi}$ coordinate system to resume the ray tracing. The rotation operation can be written compactly as

$$\mathbf{k}' = \mathbf{T}^{-1}\mathbf{R}\mathbf{T}\mathbf{k} \tag{5.3.15}$$

where the operator $\mathbf{T}$ represents a coordinate transformation and $\mathbf{R}$ is a standard rotation operator. Written for each component, this gives

$$k'_\rho = k_\rho \cos\beta - k_\theta b_\phi \sin\beta + k_\phi b_\theta \sin\beta \tag{5.3.16}$$

$$k'_\theta = k_\rho b_\theta \sin\beta + k_\theta(b_\phi^2 \cos\beta + b_\theta^2) + k_\phi b_\theta b_\phi(1 - \cos\beta) \tag{5.3.17}$$

$$k'_\phi = -k_\rho b_\theta \sin\beta + k_\theta b_\theta b_\phi(1 - \cos\beta) + k_\phi(b_\theta^2 \cos\beta + b_\phi^2) \tag{5.3.18}$$

where $b_\theta = B_\theta/|B|$ and $b_\phi = B_\phi/|B|$. The ray tracing calculation is now resumed; the ray is advanced in time by Δt and the probability of scattering is once again calculated.

5.3.5: Power Deposition

Linear power deposition is calculated by Eq. 2.7.22, the power transport equation. This equation is included in the set of ray equations and is numerically integrated along the ray as the ray is traced. The difference in ray power from one time step to the next is equal to the power deposited locally in the plasma in that time step. The radial power deposition profile is calculated numerically by first dividing the minor radius into 50 equal divisions or bins. Each bin represents a *radial shell* centered around the magnetic axis. As each ray is traced, the power absorbed between each time step is stored in the radial bin corresponding to the present location of the ray. This process is repeated for each ray. Once all of the rays are traced, the power deposited in each bin is summed and normalized to the total launched power. The result is the radial power deposition profile.

It is the random selection of scattering angles and the random decision of whether to scatter the ray which makes this particular method a Monte Carlo direct sampling simulation. In principle, as the number of rays traced becomes infinite, the power deposition profile converges to the solution of the wave kinetic equation Eq. 5.3.4. Since this is a statistical method of solving the kinetic equation and the number of rays traced is finite (106), the error in the resulting power deposition is proportional to $N^{-1/2}$ where N is the total number of rays traced. For the cases modeled here the error is about 10%.

The right side of Eq. 2.7.22 (the power transport equation) is for the most part numerically straightforward to calculate. One minor complication arises from the vector dot product of ν and $\mathbf{T}$. The vector ν represents the component of $\mathbf{k}$ in the *poloidal plane* (normalized to $k_\rho^2 + k_\theta^2$) and is expressed in terms of the unit vectors $\hat{\rho}$ and $\hat{\theta}$. The vector $\mathbf{T}$ is expressed in terms of the instantaneous Cartesian coordinate system

of the ray defined by the coordinates

$$\hat{x} = \hat{k}_{\perp} \tag{5.3.19}$$

$$\hat{y} = \hat{z} \times \hat{x} = \hat{b} \times \hat{x} \tag{5.3.20}$$

$$\hat{z} = \hat{k}_{\parallel}. \tag{5.3.21}$$

It is helpful in calculating the product $\nu \cdot \mathbf{T}$ to transform ν to the Cartesian system on the ray. The components of ν in this system (Eqs. 5.3.19–21) are given here as

$$\nu_x = \frac{1}{\Delta}\frac{1}{Kk_{\perp}}\left[k_{\rho}^2 + k_{\theta}\frac{B_z}{B^2}\left(B_z k_{\theta} - B_{\theta}k_{\phi}\right)\right] \tag{5.3.22}$$

$$\nu_y = \frac{1}{\Delta}\frac{1}{Kk_{\perp}}\left[k_{\rho}\frac{1}{|B|}\left(B_z k_{\theta} - B_{\theta}k_{\phi}\right) - k_{\theta}k_{\rho}\frac{B_z}{|B|}\right] \tag{5.3.23}$$

$$\nu_z = \frac{1}{\Delta}\frac{1}{Kk_{\perp}^2}\left[k_{\theta}k_{\rho}^2\frac{B_{\theta}}{|B|} - \frac{k_{\theta}}{|B|}\left(B_z k_{\theta} - B_{\theta}k_{\phi}\right)\left(k_{\phi} - k_z\frac{B_z}{|B|}\right)\right] \tag{5.3.24}$$

where

$$\Delta = \frac{1}{k_{\perp}^2}\left[k_{\rho}^2 + \frac{1}{B^2}\left(B_z k_{\theta} - B_{\theta}k_{\phi}\right)^2\right] \tag{5.3.25}$$

$$K = \left(k_{\rho}^2 + k_{\theta}^2\right). \tag{5.3.26}$$

Finally, it is useful to verify that the kinetic equation is valid throughout the plasma region of interest. This is true provided that the coherence length of the ion Bernstein wave l_{IBW} is greater than the correlation length of the fluctuations $\sim 1/\xi_0$. If this is true, coherent phase effects between individual Fourier turbulent modes can be neglected. This condition is satisfied within a wide margin throughout the plasma.

5.3.6: Numerical Results

Monte Carlo solutions to the kinetic equation were obtained numerically for the following plasma parameters: $0.5 \times 10^{20}\,\mathrm{m}^{-3} \leq \bar{n}_e \leq 2 \times 10^{20}\,\mathrm{m}^{-3}$, $T_i = 900\,\mathrm{eV}$, $T_e = 1800\,\mathrm{eV}$, $I_{\mathrm{p}} = 250\,\mathrm{kA}$, $B_0 = 7.6\,\mathrm{T}$, $n_{\mathrm{D}}/n_e = 0.1$, and $0 \leq \hat{n}_e \leq 0.5$. The density and temperature profiles were parameterized as

$$n(\rho) = n_{\mathrm{edge}} + (n_0 - n_{\mathrm{edge}})\left[1 - \left(\frac{\rho}{a}\right)^2\right]^{\alpha_n} \tag{5.3.27}$$

$$T(\rho) = T_{\mathrm{edge}} + (T_0 - T_{\mathrm{edge}})\left[1 - \left(\frac{\rho}{a}\right)^2\right]^{\alpha_T} \tag{5.3.28}$$

where $\alpha_n = 1.2$, $\alpha_T = 2$, $n_{\rm edge} = 7 \times 10^{18}\,{\rm m}^{-3}$, and $T_{\rm edge} = 40\,{\rm eV}$. The power deposition profile was calculated as a function of plasma density and scattering amplitude. The radial density fluctuation profile is modeled as a Gaussian with a peak at $\rho/a = 0.95$ and has a radial full width at half maximum of 2 cm. Although accurate measurements of the turbulent radial profile were not available in the ion Bernstein wave experiments, the profile characteristics were inferred from earlier measurements[8].

Linear power absorption was calculated for electron Landau damping and ion cyclotron damping on the deuterium species. Nonlinear damping mechanisms were not included in this calculation. Once the power in a single ray was attenuated to less than 1/1000 of the initial power, that ray was assumed completely absorbed and another ray was then traced. Each ray was individually traced for a time t_0 which was long enough so that unimpeded by fluctuations and undamped, a ray could cross the poloidal cross section slightly more than once. Some rays which underwent many scattering events still had a fraction of their initial power undamped after time t_0. This power was discarded and not included in the total radial power deposition. As a result, the total absorbed power was always less than unity but greater than 0.8. In principle, tracing the rays for a longer time would cause the remaining power to become randomly distributed over the radial cross section and wouldn't change the main conclusions of this study.

Rays which scattered into radial locations $\rho > \rho_0$ where ρ_0 is the radial starting position of the ray, were assumed to be absorbed at the plasma edge. Figure 5.7 shows the effect of increasing the scattering amplitude on ion Bernstein wave rays at a plasma central density of $1.5 \times 10^{20}\,{\rm m}^{-3}$. The histograms indicate the absorbed power density.† The large power density at $\rho \sim 2$–3 cm is due to absorption at the $\omega/\Omega_{\rm D} = 3$ layer located at $x = -3.4$ cm. The width of the absorption peak is characteristic of the spread in $k_{||}$ of the rays. The remainder of the absorption results from electron Landau damping and exhibits a minimum near $x \sim 7$ cm. This is the location where rays with the majority of the power encounter a toroidal bounce point ($k_{||} \simeq 0$) and there is very little electron Landau damping here.

As the scattering amplitude is increased, the power reaching the plasma center ($\rho/a \leq 0.5$) is noticeably decreased. This is caused (in this model) by an increasing fraction of power which is both deposited at the plasma edge as well as absorbed on the electrons via electron Landau damping. The power deposited at the plasma edge results from rays which are scattered out of the plasma. The reason for the increased electron Landau damping is two–fold. First, the scattered rays may undergo multiple passes

† The power *density* is the total power deposited in a bin divided by $\rho\Delta\rho/V$ where ρ is the radial location of the bin, $\Delta\rho$ is the width of the bin, and $V = \sum \rho_j \Delta\rho_j$.

through the electron Landau damping region as the direction of their ray trajectory is changed at each scattering event. Second, the value of $k_{\|}$, although not changed by a scattering event, can increase due to toroidal effects as the ray trajectory is altered in a scattering event. M. Brambilla[14] suggests that ion Bernstein wave ray tracing, in general, overestimates the power which is electron Landau damped. This can be shown by comparing a ray tracing calculation with a full wave calculation. Considering this, it is possible that the scattered rays do not undergo increased damping on the electrons but may eventually find their way to the $\omega/\Omega_D = 3$ layer where they damp on the ions (deuterium ions in this model). The primary effect of scattering in this case would be to spread the power reaching the absorption layer over a wider radial region. This effect can be approximated from the numerical results by simply assuming that the calculated radial power density (shown in Fig. 5.7 and 5.7) represents the power deposited into the ions. The total power deposited in the plasma region for $\rho/a \leq 0.5$ is then used as a means of estimating the effect of the wave scattering on ion Bernstein wave propagation. A scattering amplitude of about 30% is sufficient to prevent a large fraction of the ion Bernstein wave power from penetrating to the plasma center. Figure 5.8 shows the effect of increasing the fluctuation amplitude on ion Bernstein wave propagation at a higher central density. The effect is essentially the same; a 30% value of $\hat{n}_e$ is sufficient to prevent much of the power from reaching the plasma center.

Figure 5.9 (a) shows the predicted fraction of power which propagates into the inner 1/2 of the plasma as a function of density; the measured scattering amplitude is shown for comparison in Fig. 5.9 (b). The curve in Fig. 5.9 (a) is obtained as follows. An upper bound of 40% is set for $\hat{n}_e$ which corresponds to the value of 10 in arbritrary units for $\hat{n}_e^2$. This upper bound is selected according to the measurements in Ref. 8. Values of $\hat{n}_e$ corresponding to each density are obtained from the data in Fig. 5.9 (b). Using these values of $\hat{n}_e$, the amount of power reaching the inner 1/2 of the plasma is calculated by solving the kinetic equation using the Monte Carlo method already outlined. The power reaching the plasma region where $\rho/a \leq 0.5$ decreases by about a factor of four when the density increases from $\bar{n}_e = 1 \times 10^{20}\,\mathrm{m}^{-3}$ to $3 \times 10^{20}\,\mathrm{m}^{-3}$. The upper bound of 40% for $\hat{n}_e$ may be too high. If it is assumed to correspond to 10% for example, the power reaching the inner 1/2 of the plasma remains as high as about 60%, even at the highest density.

$$\bar{n}_e = 1.5 \times 10^{20}\,\mathrm{m}^{-3}$$

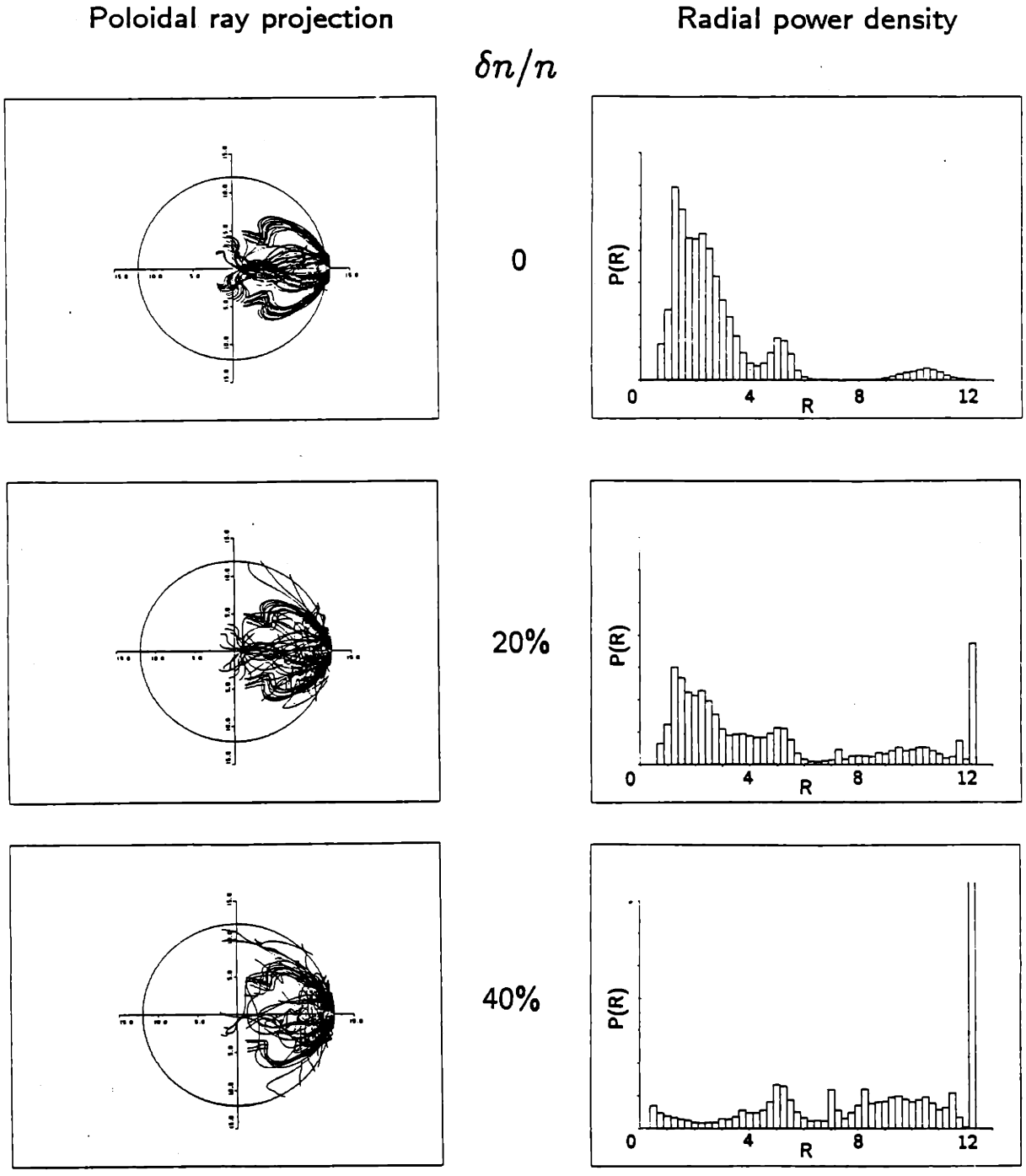

Figure 5.7 —Ion Bernstein wave poloidal ray trajectories and radial power deposition as a function of increasing fluctuation amplitude for a plasma line–averaged density of $1.5 \times 10^{20}\,\mathrm{m}^{-3}$ and $B_0 = 7.6\,\mathrm{T}$. R represents the minor radial position.

$$\bar{n}_e = 2.7 \times 10^{20}\,\mathrm{m}^{-3}$$

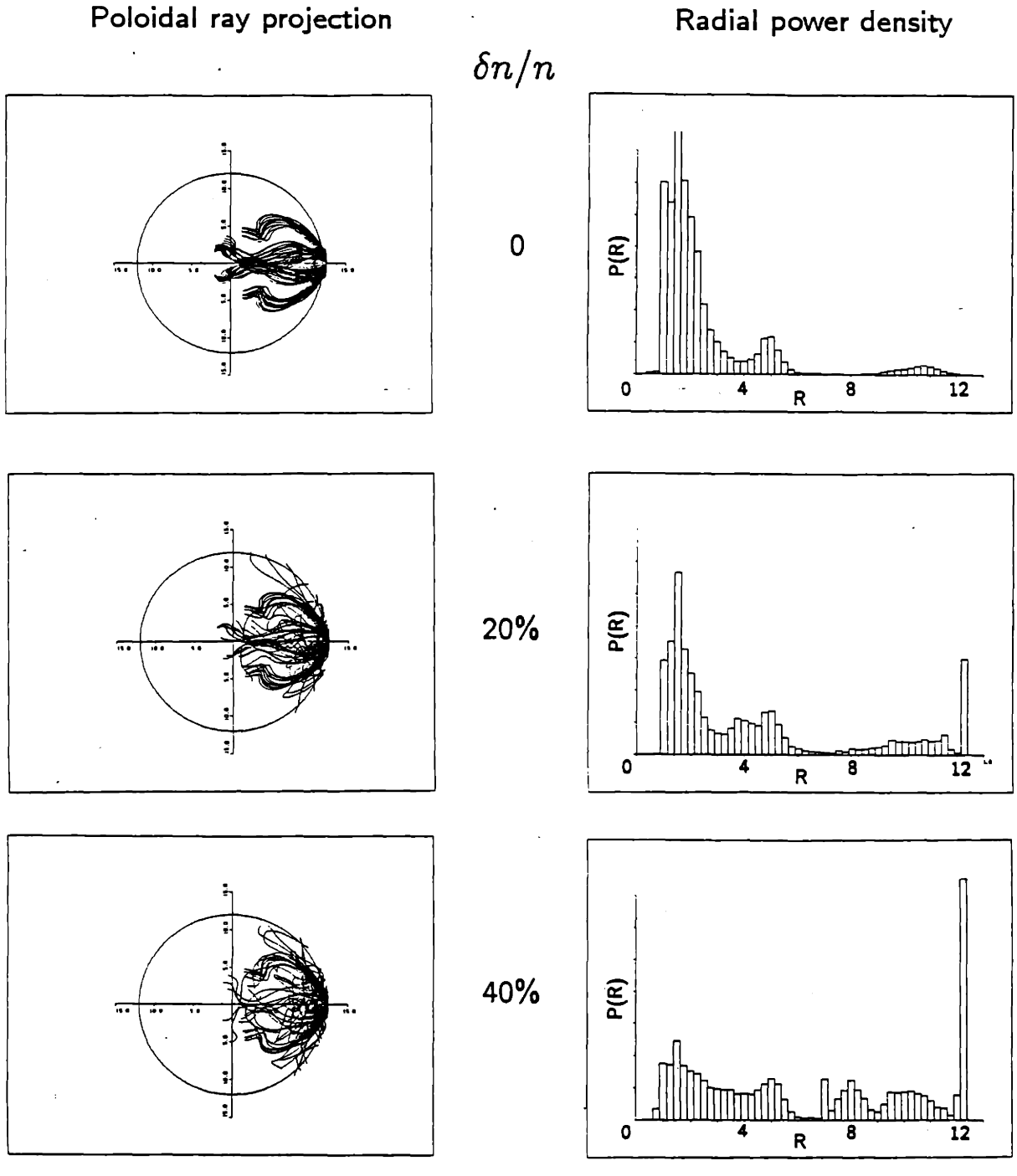

Figure 5.8 —Ion Bernstein wave poloidal ray trajectories and radial power deposition as a function of increasing fluctuation amplitude for a plasma line–averaged density of $2.7 \times 10^{20}\,\mathrm{m}^{-3}$ and $B_0 = 7.6$ T. R represents the minor radial position.

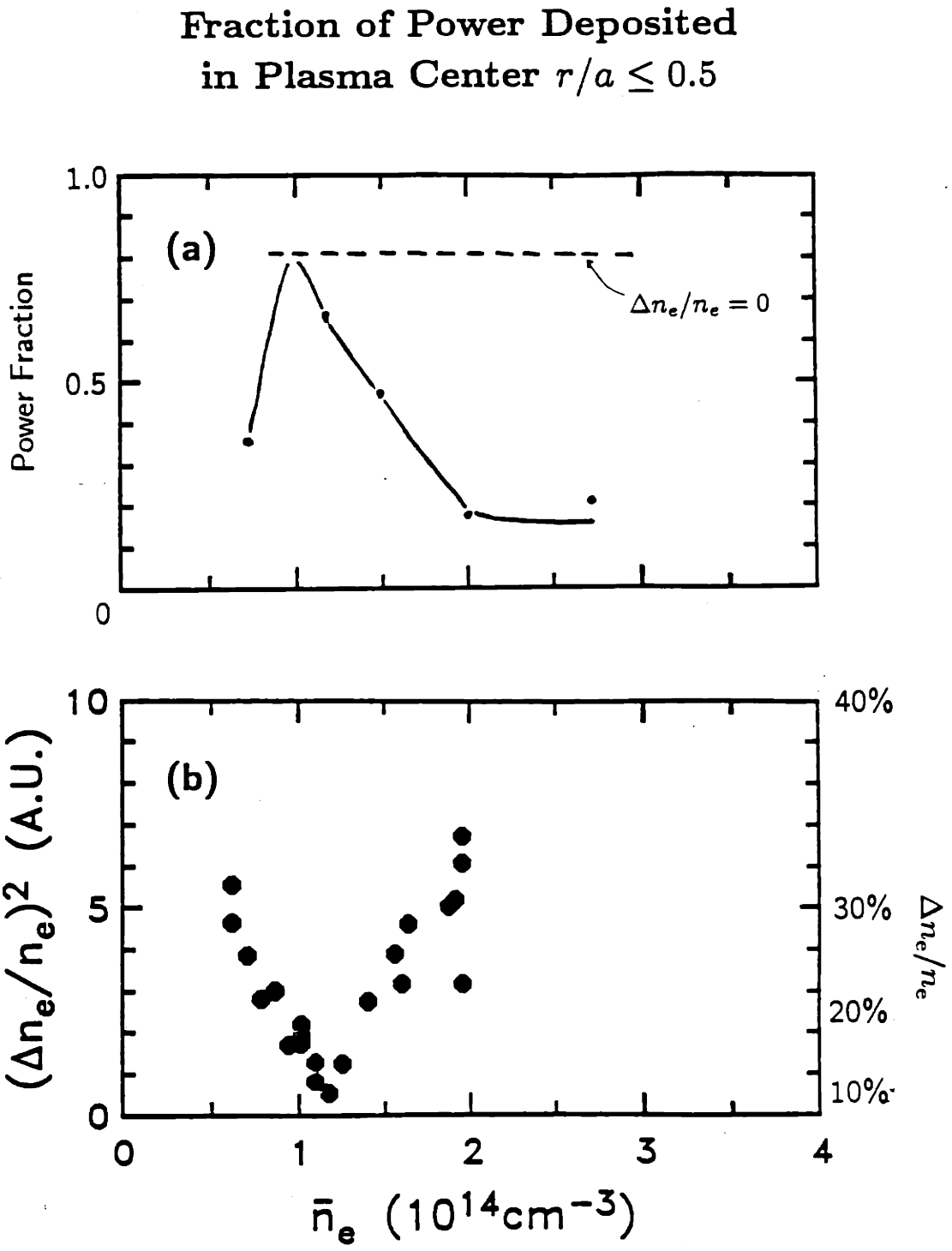

Figure 5.9 —(a) Predicted fraction of ion Bernstein wave power reaching the plasma region $\rho/a \leq 0.5$ as a function of plasma line–averaged density. (b) Measured fluctuation power and corresponding assumed fluctuation amplitude as a function of plasma line–averaged density.

5.3.7: Conclusions

The kinetic equation describing ion Bernstein wave scattering from turbulence has been solved using a Monte Carlo direct sampling simulation. The radial power deposition profile has been calculated as a function of edge density fluctuation amplitude. It is found that the power reaching the plasma center ($\rho/a \leq 0.5$) is only dependent on the normalized fluctuation amplitude and that a value of $\hat{n}_e \simeq 0.3$ is sufficient to significantly reduce the ion Bernstein wave power reaching the central plasma.

An upper bound on the measured value of $\hat{n}_e = 0.4$ at $\bar{n}_e = 3 \times 10^{20}\,\mathrm{m}^{-3}$ gives a decrease of about a factor of four in the wave power which reaches the inner half of the plasma ($\rho/a \leq 0.5$) as the density increases from $\bar{n}_e = 1 \times 10^{20}\,\mathrm{m}^{-3}$ to $\bar{n}_e = 3 \times 10^{20}\,\mathrm{m}^{-3}$. This decrease primarily results from a broadening of the power deposition profile. A lower peak value of $\hat{n}_e$ at $\bar{n}_e = 3 \times 10^{20}\,\mathrm{m}^{-3}$ would produce less broadening of the power deposition profile. The scattering results provide a method for determining the expected rf power deposition profile as a function of plasma density. This profile can now be used to describe the rf ion power source in a particle and energy transport model. This is carried out in the following section.

5.4: Plasma Power Balance Analysis

5.4.1: Introduction

It has been shown previously[15, 16, 17] that at high densities, the global energy confinement time on Alcator departs from the lower density neo–Alcator scaling $\tau_E \propto \bar{n}_e R^{2.04} a^{1.04}$ and becomes saturated. An anomaly in the ion thermal diffusivity χ_i of three to five times greater than the Chang–Hinton neoclassical prediction is sufficient to account for the observed confinement behavior in these high density plasmas. Ion Bernstein wave heating experiments showed that large increases in the ion temperature resulted with low rf powers (compared to the Ohmic power) for relatively low density plasmas ($\bar{n}_e \lesssim 1.1 \times 10^{20}\,\mathrm{m}^{-3}$). In contrast to this, the ion heating rate in higher density plasmas is substantially reduced. To understand the effect of plasma energy confinement on the rf heating rate it is important to analyze the power balance characteristics of the rf heated discharges. This section describes the model used to analyze the plasma power balance and presents the results and interpretation of this analysis when applied to a set of rf heated discharges. Only data at the 7.6 T and 9.3 T magnetic

field regimes is analyzed; the changes in plasma parameters during rf injection at the 5.1 T regime are within experimental error and therefore no conclusions can be drawn from this data.

This section begins by describing the model used for the time dependent transport analyses. The model is then used to analyze the Ohmic portion of a set of discharges in both the 7.6 T and 9.3 T field regimes. The goal of the analysis is to understand the ion behavior. The electron behavior is only monitored due to its necessity in calculating the electron–ion power flow from collisions. The analyses show that in both magnetic field regimes, anomalous ion thermal conduction, relative to the neoclassical value, is required to explain the observed Ohmic ion temperature behavior and this anomaly increases with plasma density. The discharges are then analyzed during rf power injection. The fraction of rf power assumed to be deposited in the plasma is estimated from measured ion temperature profiles to be between 30% and 60% of the total rf power entering the antenna system. The rf power deposition profile is obtained from the scattering results given in section 5.3. The ion temperature behavior during rf power injection at 9.3 T can be explained by assuming that the ion thermal conductivity remains nearly equal to the value in the Ohmic portion of the discharge. The ion temperature behavior at 7.6 T can be explained by assuming that the ion thermal conductivity remains nearly Ohmic–like† but increases slightly at low densities and may decrease some at high densities. These results suggest that at 7.6 T, the ion losses are typically enhanced at low densities at the onset of rf power injection; at high densities, the ion losses may be reduced. At the 9.3 T field regime, ion losses are typically maintained at the onset of rf power injection except at the highest densities. This contrasting behavior between the two field regimes may be caused by the differing power deposition profile in both field cases and by the characteristics of the ion temperature gradient driven instability.

5.4.2: Analysis Technique

Energy and particle transport analysis of the data is carried out using a modified version of the ONETWO[18] transport code. Inputs for this code are the parameterized electron and ion temperature profiles, electron density profile, plasma current, Z_{eff}, and the resistive loop voltage, which are supplied at usually 9 and up to 19 instants of time before and during the time of rf power injection. The ion thermal conductivity is assumed to have the neoclassical form and the code determines an anomalous conduction factor which reproduces the measured central ion temperature.

---

† Ohmic–like ion thermal conduction during rf power injection indicates that the ion thermal conduction anomaly is equal to the Ohmic value at the equivalent rf density.

Since an accurate measurement of the electron density profile was not available from the ion Bernstein wave experimental data, the profile was approximated as a parabola to the power α_n where α_n is adjusted to give the measured ratio of central to line–averaged density. Thus, α_n is given by

$$\frac{\bar{n}_e}{n_{e0}} = \frac{\sqrt{\pi}}{2}\frac{\Gamma(\alpha_n+1)}{\Gamma(\alpha_n+\frac{3}{2})} \tag{5.4.1}$$

where $\Gamma(x)$ is the standard Gamma function. In most of the density interferometer data, only three of the interferometer chords which passed through the small size plasma recorded a signal above the noise level. Abel inverting these chord measurements to obtain a profile provided no better accuracy than the parabolic approximation.

The electron temperature profile was also approximated due to the lack of profile measurements. The T_e profile was assumed to be a parabola to the power α_T. An estimate of the value of α_T can be obtained in terms of the plasma central and edge safety factor $q = \rho B_0/(R_0 B_p)$ as follows. The Ohmic heating electric field E_0 and the value of Z_{eff} are assumed to be uniform across the plasma. The electron temperature profile determines the conductivity and therefore the current profile. Since the conductivity is proportional to $T_e^{3/2}$ the current density can be written as

$$J(\rho) = \sigma_0 \left[\frac{T_e(\rho)}{T_e(0)}\right]^{\frac{3}{2}} E_0 \tag{5.4.2}$$

where σ_0 is evaluated using the central electron temperature. The electron temperature profile is parameterized as

$$T_e(\rho) = T_e(0)\left[1-\left(\frac{\rho}{a}\right)^2\right]^{\alpha_T} \tag{5.4.3}$$

where the edge electron temperature is set to zero for simplicity. Integrating the Ampere equation using the current density in Eq. 5.4.2 gives the poloidal magnetic field as

$$B_p(\rho) = B_p(a)\frac{a}{\rho}\left\{1-\left[1-\left(\frac{\rho}{a}\right)\right]^{\frac{3\alpha_T}{2}+1}\right\} \tag{5.4.4}$$

where the poloidal field at $\rho = a$ is

$$B_p(a) = J_0\frac{2\pi}{a}\left[\frac{3\alpha_T}{2}+1\right]^{-1} \tag{5.4.5}$$

and $J_0 = \sigma_0 E_0$ is the current density on the magnetic axis. The toroidal safety factor has a value on axis ($\rho = 0$) of

$$q(0) = \frac{B_0 a}{R_0 B_p(a)} \left[\frac{3\alpha_T}{2} + 1\right]^{-1} = q(a) \left[\frac{3\alpha_T}{2} + 1\right]^{-1} \tag{5.4.6}$$

giving an expression for α_T as

$$\alpha_T = \frac{2}{3}\left[\frac{q(a)}{q(0)} - 1\right]. \tag{5.4.7}$$

The physical processes included in the power balance analysis are ion and electron heat transport, particle transport, magnetic diffusion, neutral transport, and radiation. The analysis is carried out in 1–D geometry (all quantities are functions only of the space coordinate ρ) assuming concentric flux surfaces. The diffusion equations considered in the transport model are

$$\frac{\partial n_e}{\partial t} + \frac{1}{\rho}\frac{\partial}{\partial \rho}\rho\Gamma_e = S_e \tag{5.4.8}$$

$$\frac{3}{2}\frac{\partial}{\partial t} n_e T_e = \frac{1}{\rho}\frac{\partial}{\partial \rho}\rho\left[n_e \chi_e \frac{\partial T_e}{\partial \rho} - \frac{5}{2} T_e \Gamma_e\right] + P_{\mathrm{Oh}} - P_{ei} - P_{\mathrm{rad}} + \frac{\Gamma_e}{ne}\frac{\partial}{\partial \rho}\sum_{j=\mathrm{ion}} n_j T_i \tag{5.4.9}$$

$$\frac{3}{2}\frac{\partial}{\partial t}\sum_{j=\mathrm{ion}} n_j T_i = \frac{1}{\rho}\frac{\partial}{\partial \rho}\rho\left[\sum_{j=\mathrm{ion}} n_j \chi_i \frac{\partial T_i}{\partial \rho} - \frac{5}{2} T_i \sum_{j=\mathrm{ion}} \Gamma_j\right] + P_{ei} - P_{\mathrm{cx}} - \frac{\Gamma_e}{ne}\frac{\partial}{\partial \rho}\sum_{j=\mathrm{ion}} n_j T_i \tag{5.4.10}$$

$$\frac{1}{c}\frac{\partial B_\theta}{\partial t} = \frac{\partial E}{\partial \rho}. \tag{5.4.11}$$

Here, $\Gamma_{e,i}$ is the electron or ion radial particle flux; S_e is the electron source rate (from all processes); $\chi_{e,i}$ is the electron or ion thermal diffusivity (the thermal conductivity is $\kappa_j = n_j \chi_j$); P_{Oh} is the Ohmic heating power density. The collisional power exchange between the electron and ions, P_{ei}, is given by

$$P_{ei} = \frac{3}{2} n_e \sum_{j=\mathrm{ion}} \nu_{ej}^E (T_e - T_j) \tag{5.4.12}$$

where

$$\nu_{e,j}^{E} = \frac{2m_e}{m_j}\frac{4}{3}\sqrt{\pi}\frac{n_j Z_j^2 e^4 \ln\Lambda}{\sqrt{m_e}T_e^{3/2}}; \tag{5.4.13}$$

P_{rad} is the local radiated power density, and P_{cx} is the charge exchange loss. The last term on the right side of Eqs. 5.4.9–10 represents an additional power exchange between the ions and the electrons[19] and is typically small compared to the other terms.

Boundary conditions for the electron and ion temperature and density are taken from plasma edge and scrape–off measurements. The total plasma current is used as the boundary condition for the magnetic diffusion equation.

A single impurity species is assumed to be present, either oxygen or molybdenum. The electron and ion fluxes are assumed ambipolar and are related as

$$\Gamma_e = \sum_{j=\mathrm{ion}} Z_j \Gamma_j. \tag{5.4.14}$$

The impurity temperature is set equal to the main ion species temperature. The total source rate S_e, in Eq. 5.4.8, is determined with the help of a neutral transport package. An input value for the global particle confinement time τ_p^{in} provides the necessary boundary condition for the source calculation. Radiated power is calculated for bremsstrahlung and line radiation due to the assumed impurity species.

The magnetic diffusion equation is solved assuming classical resistivity and using the total plasma current input $I_p(t)$ as the boundary condition. The value of Z_{eff} is adjusted to match the experimental loop voltage. The resulting value can then be compared with the measured value for consistency. The measured inputs are averaged over any sawtooth effects, thus the calculated values of the transport coefficients include the time averaged effects of sawteeth. For the majority of discharges analyzed, the $q=1$ surface is approximately at the magnetic axis of the plasma [$q(\rho=0) \simeq 1$].

The ion heat transport equation is solved assuming an ion thermal diffusivity of the form

$$\chi_i(\rho,t) = W(t)\chi_i^{\mathrm{neo}}(\rho,t) + D_b f(q) \tag{5.4.15}$$

where $\chi_i^{\mathrm{neo}}(\rho,t)$ is the Chang–Hinton neoclassical diffusivity[20], D_b is the Bohm diffusivity, and

$$f(q) = \begin{cases} 1 - \frac{1}{1+(\frac{1}{q}-1)^2} & q \le 1 \\ 0 & q > 1 \end{cases} \tag{5.4.16}$$

is used to model the time–averaged effect of sawtooth activity. The time dependent anomaly factor $W(t)$ is dynamically adjusted to reproduce the measured central ion temperature and the ion temperature profile is determined by the transport equations.

5.4.3: Anomalous Ion Thermal Conduction

The ion thermal conduction anomaly is essentially an indication of how different the measured ion temperature is than what is expected based on neoclassical theory. Typically, ion power losses are anomalously high causing the measured ion temperature to be lower than expected. To analytically investigate the effect of anomalously low ion temperature on the the neoclassical multiplier W, it is useful to construct an approximate analytic expression for W. This can be obtained by considering the power balance near the magnetic axis. Since the form of the ion thermal conductivity is assumed to be neoclassical and W is adjusted so as to give the central ion temperature, it is the characteristics of the transport near the plasma center which should be considered in determining the value of W. The value of $q(0)$ is assumed to be greater than or equal to unity in this analysis (*i.e.* there are no sawteeth present in the discharge). The neoclassical ion thermal conductivity is given in Ref. 19 as

$$\kappa_i = n_i \chi_i = n_i K_2 \epsilon^{1/2} \frac{\rho_{i\theta}^2}{\tau_i} \tag{5.4.17}$$

where $\rho_{i\theta}^2 = 2m_i T_i c^2/(Z_i^2 e^2 B_p^2)$, τ_i is given by Eq. 4.4.2, $\epsilon = \rho/R_0$, and

$$K_2 = K_2^0 \left\{ \frac{1}{1 + a_2 \nu_{i*}^{1/2} + b_2 \nu_{i*}} + \frac{\epsilon^{3/2}(c_2^2/b_2)\nu_{i*}\epsilon^{3/2}}{1 + c_2 \nu_{i*} \epsilon^{3/2}} \right\}. \tag{5.4.18}$$

The numerical constants in Eq. 5.4.18 are $K_2^0 = 0.66$, $a_2 = 1.03$, $b_2 = 0.31$, and $c_2 = 0.74$. The ion thermal conductivity in the discharges to be considered is essentially in the plateau regime ($1 \ll \nu_{i*} \ll \epsilon^{-3/2}$) for $\rho \leq 0.5\,\mathrm{cm}$ ($a \simeq 12.0\,\mathrm{cm}$). This region near the magnetic axis is not pathological since its size is much larger than an ion Larmor radius at a toroidal magnetic field of 7.6 T ($\rho_{\mathrm{H}} \simeq 0.06\,\mathrm{cm}$). Near the magnetic axis, especially at $\rho = 0$, the limiting value of χ_i^{neo} is written as

$$\chi_i^{\mathrm{neo}}(0) = q \frac{K_2^{(0)}}{b_2} \frac{1}{\sqrt{2} R_0} \frac{v_{ti}^3(0)}{\Omega_{i0}^2} \tag{5.4.19}$$

where Ω_{i0} is the gyrofrequency evaluated using the toroidal field on axis. Since the ion thermal diffusivity is explicitly independent of the collision frequency† , it has no explicit Z_{eff} dependence. Its main dependence is given by $T_j(0)^{3/2}/(Z_j B_0)^2$.

† This is the case where particles which dominate the diffusion have a collision time which is on the order of the time it takes a circulating ion to complete one poloidal orbit. Thus, the collision frequency ν_{ei} can be approximately replaced with $1/\tau_c$ where τ_c is the period for one complete poloidal orbit. This time is only dependent on plasma geometry, magnetic field, plasma current, and ion temperature.

A simple physical argument can be given to explain the basic dependence of the ion thermal diffusivity on the magnetic axis. The diffusion is dominated by circulating particles which undergo a pitch angle scattering after completing half of a poloidal orbit. The approximate deviation of a particle from its flux surface during half of a poloidal orbit is $\delta r = \rho_{i\theta}\epsilon$. In the limit of $\epsilon \ll 1$, $\delta r \sim \sqrt{2}\rho_i = qv_{ti}/\Omega_i$ where Ω_i is the cyclotron frequency for the toroidal field. The time between collisions is approximately $\tau_i \sim \pi R_0 q/v_{ti}$. The fraction of the particles contributing to the diffusion is approximately unity. Constructing a diffusion coefficient from the step size and the step time gives $D \sim qv_{ti}^3/(\pi R_0 \Omega_i^2)$ which is within a factor of order unity of the limiting form (Eq. 5.4.19).

An approximate expression for W can be obtained by writing out the ion power balance at $\rho = 0$ as

$$W \simeq -P_{ei}|_{\rho=0} \Big/ \frac{1}{\rho}\frac{\partial}{\partial \rho}\rho \left[\sum_{j=\text{ion}} n_j \chi_i^{\text{neo}} \frac{\partial Ti}{\partial \rho}\right]_{\rho=0} \tag{5.4.20}$$

where the charge exchange and convective power loss has been neglected‡ and i indicates the main ion species.

The expression for the electron–ion power flow is

$$P_{ei} \propto n_e(0) \sum_{j=\text{ion}} \left(\frac{Z_j}{\mu_j}\right) Z_j n_j(0) \ln \Lambda_{ej} \frac{T_e - T_j}{T_e^{3/2}} \tag{5.4.21}$$

where μ_j is the atomic mass number of the j ion species. The ratio Z_j/μ_j is unity for hydrogen and about 1/2 for the impurity ion. A Z_{eff} different than unity has a minor effect on the behavior of P_{ei}, mainly by adjusting the ion species densities. The hydrogen and impurity densities in a two ion species plasma with an impurity having atomic number Z_I are given by

$$n_{\text{H}} = n_e \left[\frac{Z_I - Z_{\text{eff}}}{Z_I - 1}\right] \tag{5.4.22}$$

$$n_I = n_e \left[\frac{Z_{\text{eff}} - 1}{Z_I(Z_I - 1)}\right]. \tag{5.4.23}$$

If the impurity is molybdenum, for example, $Z_I = 32$ and if $Z_{\text{eff}} = 3$, Eqs. 5.4.22–23 give $n_{\text{H}}/n_e = 0.94$ and $n_I/n_e = 0.002$. Thus, the variation in the hydrogen density

‡ This is justified for the data considered here provided $n_e(0) \gtrsim 1.5 \times 10^{20}\,\text{m}^{-3}$.

over a range of $1 \leq Z_{\rm eff} \leq 3$ is only 6% at most, indicating that the behavior of W is relatively insensitive to the value of $Z_{\rm eff}$. The primary dependence of P_{ei} is given by $n_e(0)n_i(0)(T_e - T_j)/T_e^{3/2}$ where only the main ion species contribution is kept.

The behavior of W can now be simplified to

$$W \propto -\frac{n_e^2 \frac{T_e - T_i}{T_e^{3/2}}}{n_e T_i^{3/2} \frac{\partial^2 T_i}{\partial \rho^2}} \tag{5.4.24}$$

where all quantities are evaluated on the magnetic axis. An estimate of $\partial^2 T_i(0)/\partial\rho^2$ is $T_i(0)/a_s^2$ where a_s is the ion temperature profile scale length. An estimate of P_{ei} can be obtained from Eq. 5.4.20 by setting $T_i = T_i^{\rm neo}$ where $T_i^{\rm neo}$ is the expected ion temperature due to neoclassical transport. In this case, W is unity and

$$P_{ei} = P_{ei}^{\rm neo} \frac{T_e - T_i}{T_e - T_i^{\rm neo}} \propto n_e \frac{1}{a_s^{\rm neo\,2}} T_i^{\rm neo\,5/2} \frac{T_e - T_i}{T_e - T_i^{\rm neo}}. \tag{5.4.25}$$

This gives an overall estimate for W of

$$W \propto \left(\frac{T_i^{\rm neo}}{T_i}\right)^{5/2} \left(\frac{a_s}{a_s^{\rm neo}}\right)^2 \frac{T_e - T_i}{T_e - T_i^{\rm neo}}. \tag{5.4.26}$$

Equation 5.4.26 shows that the value of W can depart from unity through three effects. First, an anomalously low ion temperature gives rise to a lower neoclassical conductive power loss causing the value of W to increase so as to compensate for this. Second, a lower T_i increases the electron–ion power flow. The value of W must increase in response to this so as to carry away the excess power through the ion conduction loss channel. Third, a broader ion temperature profile indicates that $a_s > a_s^{\rm neo}$ and implies a higher ion thermal conduction. Within the approximations considered and assuming that $a_s/a_s^{\rm neo}$ is weakly dependent on the value of W, Eq. 5.4.26 confirms that the value of W is essentially a measure of the anomaly in the central ion temperature.

5.4.4: Ohmic Discharges at 7.6 Tesla

Analysis at the 7.6 T regime was done for 14 discharges which spanned a density range of $0.75 \times 10^{20}\,{\rm m}^{-3} \leq \bar{n}_e \leq 2.8 \times 10^{20}\,{\rm m}^{-3}$. Figure 5.10 shows the inferred value of the ion thermal conduction anomaly in the Ohmically heated portion of these discharges as a function of the line–averaged density. The total plasma current ranges between 230 kA and 290 kA with an Ohmic input power $P_{\rm Oh} = 550 \pm 100\,{\rm kW}$. The value of $Z_{\rm eff}$ is shown in Fig. 5.11 and exhibits the behavior of a decreasing value

with increasing density. The ratio of central to line–averaged density is typically about 1.2–1.4 (corresponding to $\alpha_n \simeq 0.6$) indicating a broad density profile. The ion conduction anomaly is nearly constant at a value close to unity (within the error) for low density discharges but then begins to increase with density. Figure 5.12 shows a plot of the absolute magnitude of the neoclassical ion thermal diffusivity [calculated from the measured values of $n_j(0)$ and $T_j(0)$] on the magnetic axis versus the line–averaged electron density.

Figure 5.13 shows the individual components of the integrated ion power flow at $\rho/a = 0.75$. Each power shown is normalized to the total integrated Ohmic input power at $\rho/a = 0.75$. Most of the power flow important to the description of these discharges appears to take place within $\rho/a = 0.75$. Limiting the analysis to within this region excludes the power flow in the edge region which can be dominated by errors resulting from uncertainties in the boundary values. The power loss through convection is typically about $10\%P_{\rm Oh}$ and remains relatively constant with density. The power loss through charge exchange and ionization is less than $5\%P_{\rm Oh}$ and decreases from a positive value to a negative value with density. The power loss through conduction increases nearly linearly with density and follows the electron–ion power source which also increases with density. The conduction and convection power loss are comparable for $\bar{n}_e \leq 1.5 \times 10^{20}\,\mathrm{m}^{-3}$. In this region, improvements in the particle confinement time can have a significant effect on the overall ion power balance. At higher densities, the particle confinement time is not as important.

5.4.5: Rf Heated Discharges at 7.6 Tesla

The rf power source is modeled in the shape of an annulus with power distributed across the annulus area according to the power deposition profile estimated from the scattering results (see Figs. 5.7 and 5.8). The fluctuation amplitude is assumed to be $\sim 40\%$ at $\bar{n}_e = 3 \times 10^{20}\,\mathrm{m}^{-3}$, consistent with Fig. 5.9 (b). The total rf power which actually flows into the hydrogen comes from both collisional power exchange from the heated deuterium and possibly from direct rf power absorption on the hydrogen. The power flow from the heated deuterium to the hydrogen has been estimated from the data in Fig. 4.10 to be $\sim 30\%P_{\rm rf}$ † . The power deposited directly into the hydrogen

† $P_{\rm rf}$ is used to indicate the total rf power entering the antenna system.

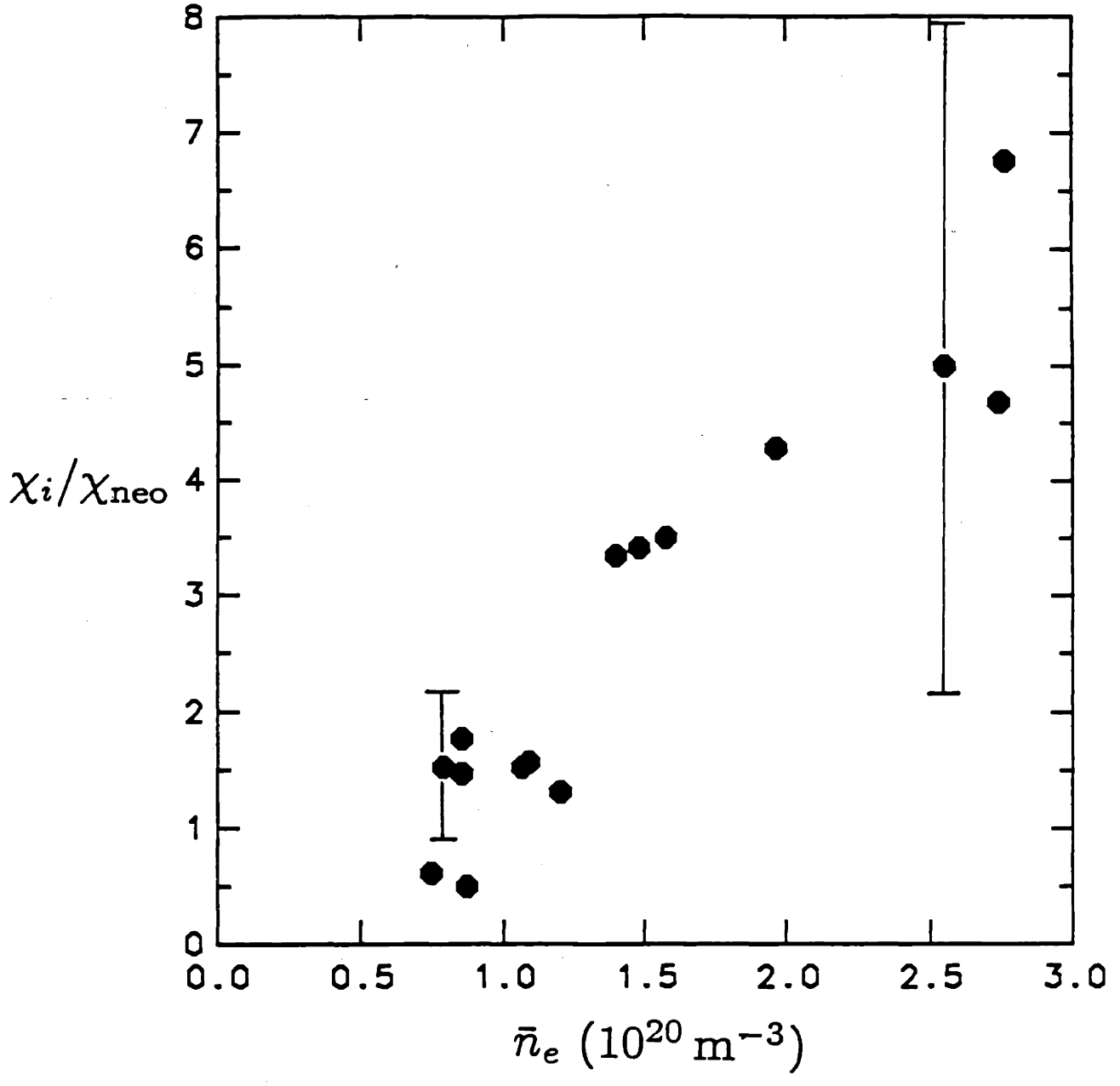

Figure 5.10 —Inferred value of the ion thermal conduction anomaly during Ohmic heating as a function of line-averaged density. $B_0 = 7.6\,\mathrm{T}$.

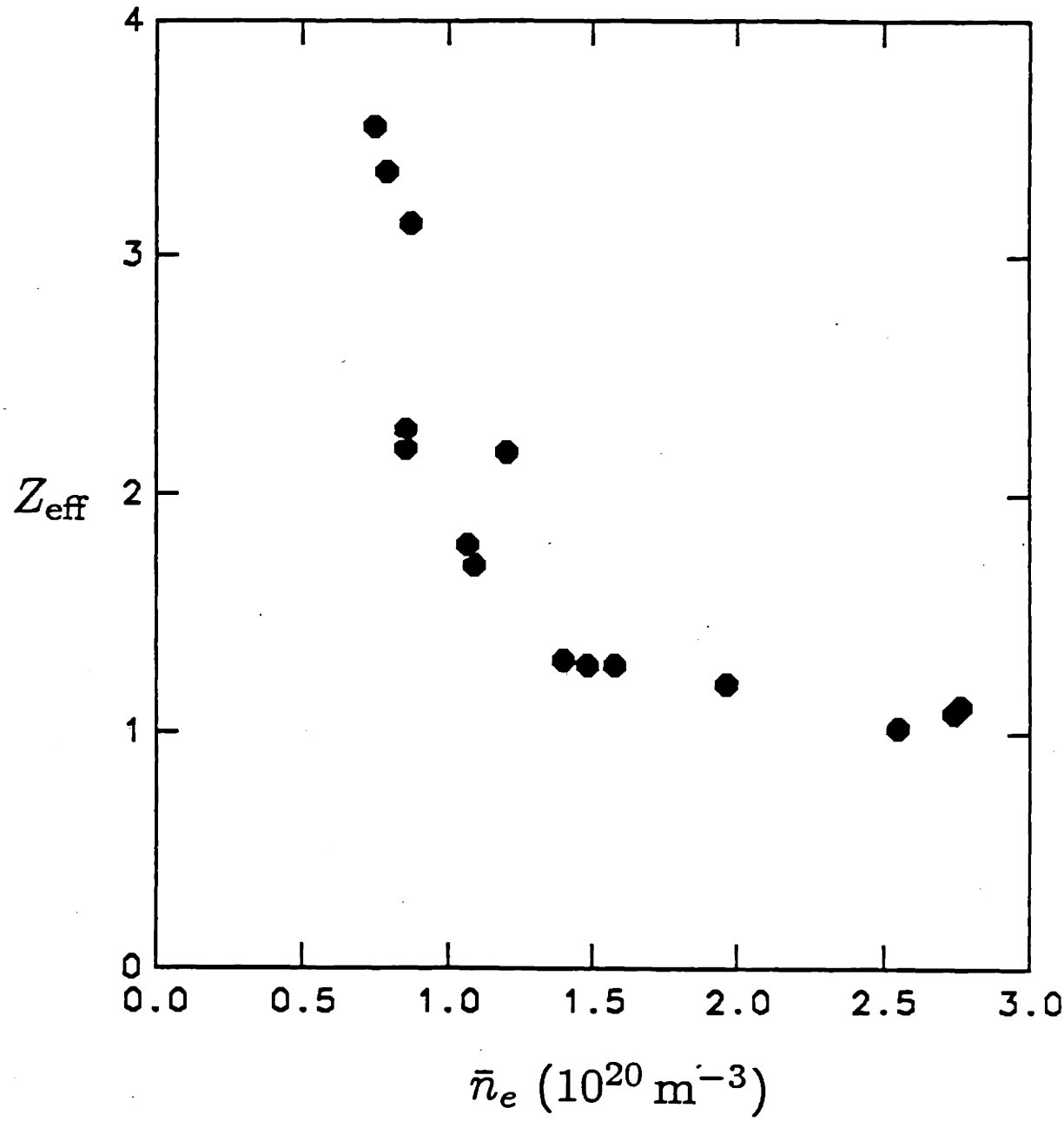

Figure 5.11 —Ohmic Z_{eff} value measured from visible bremsstrahlung as a function of line–averaged density. $B_0 = 7.6$ T.

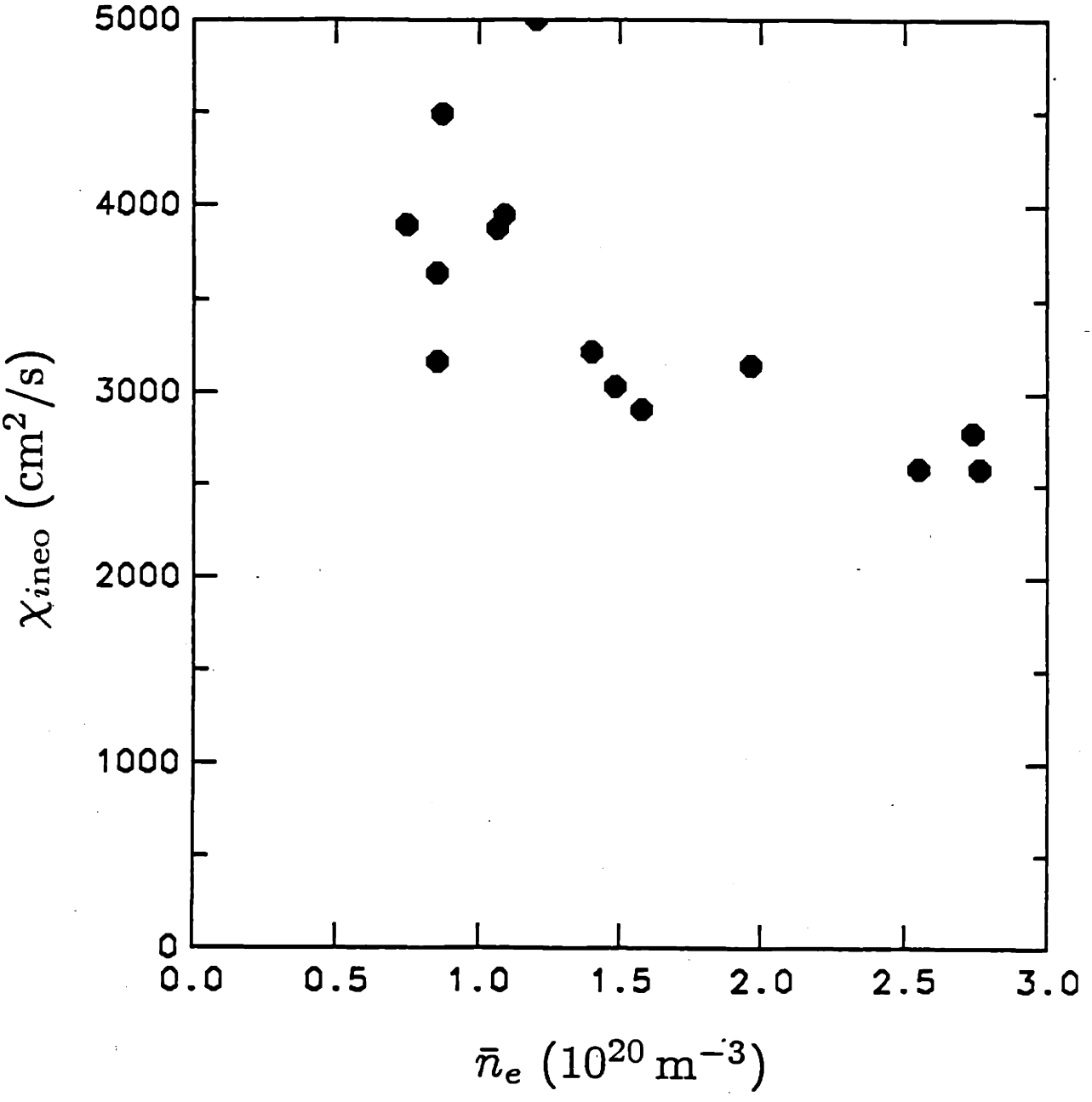

Figure 5.12 —Calculated neoclassical ion thermal diffusivity on the magnetic axis as a function of line-averaged density. $B_0 = 7.6$ T.

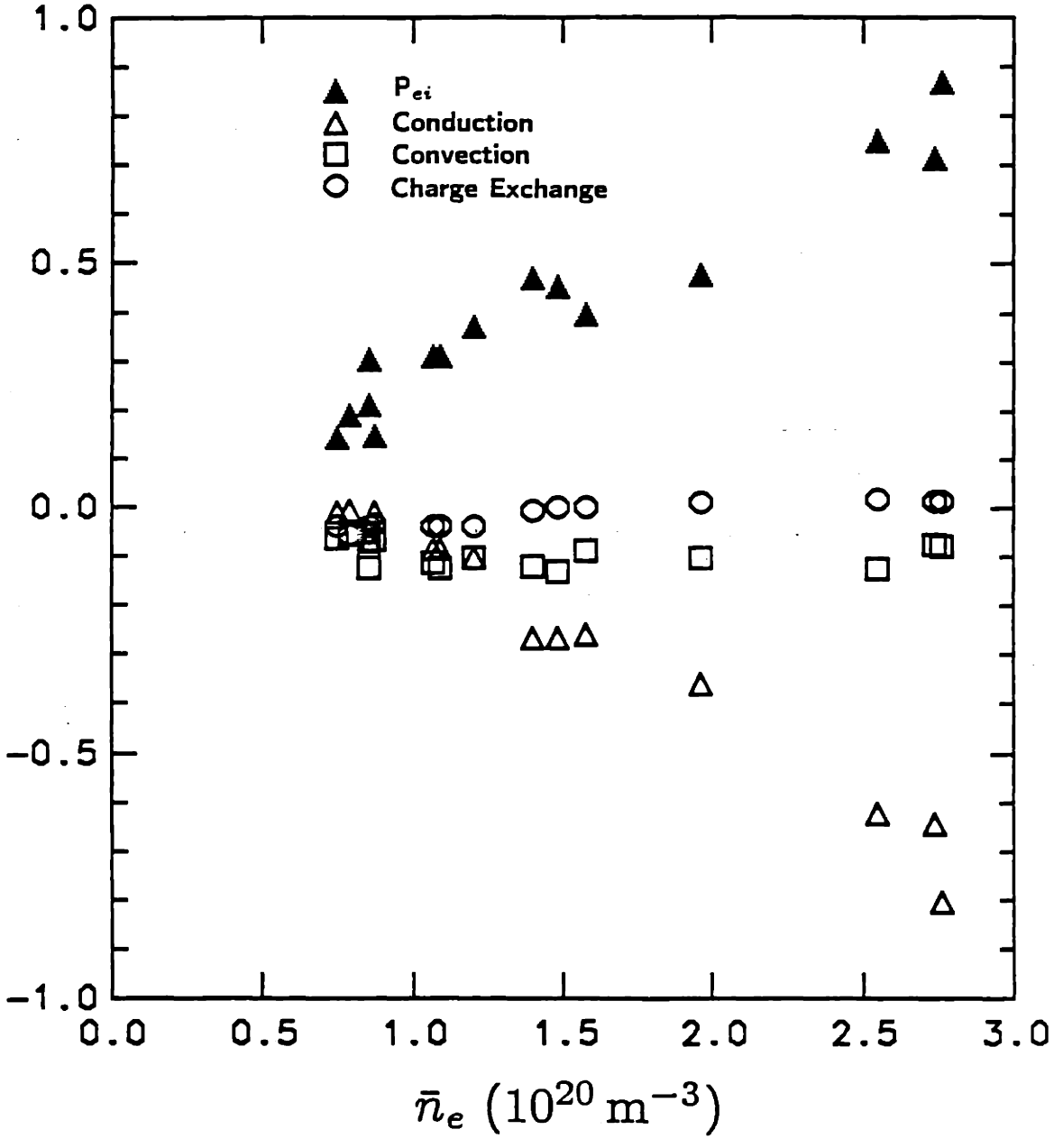

Figure 5.13 —Individual components of the ion power flow during Ohmic heating at $\rho/a = 0.75$ as a function of line-averaged density. $B_0 = 7.6\,\mathrm{T}$.

cannot be obtained from the data and must be estimated from the characteristics of the absorption mechanism. On one hand, if rf power absorption on the deuterium occurs via ion Bernstein wave decay (see section 2.8.4), the quasimode at $\omega = 0.5\Omega_H$, which contains $\sim 30\%P_{rf}$, damps on the deuterium. The lower frequency ion Bernstein wave at $\omega = (1+x)\Omega_H$ ($x \ll 1$), contains $\sim 60\%P_{rf}$ ‡ and damps on the hydrogen. In this case, the total power which flows into the hydrogen is estimated to be $\sim 90\%P_{rf}$. On the other hand, if rf power absorption on the deuterium occurs via linear damping at the $\omega = 3\Omega_D$ layer, the power absorbed directly by the hydrogen via self–interaction near $\omega = 1.5\Omega_H$ can be as low as $\sim 0\%P_{rf}$. In this case, the total power which flows into the hydrogen is $\sim 30\%P_{rf}$. A total power flow into the hydrogen of $60\%P_{rf}$, which lies between both extremes, was used to model the rf portion of the discharges.

Figure 5.14 shows a comparison of the inferred value of the ion thermal conduction anomaly during the Ohmic heated portion of the discharge with the anomaly during the Ohmic and ion Bernstein wave heated portion. The letters label points corresponding to the same discharge. Notice that at low densities, the density during rf power injection is somewhat higher than during the Ohmic heating phase. Assuming that $60\%P_{rf}$ flows into the hydrogen, the ion thermal conduction anomaly can remain nearly Ohmic–like to explain the observed ion temperature behavior. There is a small increase in the ion thermal conduction at low densities (by a factor of ~ 1.5) which is just outside of the error bars. This may indicate that χ_i degrades at the onset of rf power injection at low densities. At higher densities, χ_i appears to improve although the improvement is within the error bars.

There is some uncertainty in both the amplitude of the total power which flows into the hydrogen and in the edge density fluctuation amplitude. The effect of reducing the total power to $30\%P_{rf}$, while keeping the fluctuations the same, is shown in Fig. 5.15 . The figure shows that the ion thermal conductivity can still remain nearly Ohmic–like to explain the ion temperature increase. The slight increase in the ion thermal conductivity at low densities is now $\lesssim 1.5$ times and the decrease at high densities is more significant. This result still suggests that the ion thermal conduction may increase slightly at low densities and decrease at high densities. The effect of reducing the fluctuation amplitude to 0% while keeping the power flowing into the hydrogen at $60\%P_{rf}$ is shown in Fig. 5.16 . The rf power is mainly deposited between $1\,\text{cm} \leq \rho \leq 4\,\text{cm}$ without edge fluctuations. The ion thermal conductivity for this case shows a large increase (2–4 times the Ohmic value) at low densities and is relatively unchanged at high densities. If this power deposition model is correct, then the ion losses are strongly

‡ This fraction of power is estimated from the Manley–Rowe nonlinear energy relations (see Ref. 21).

enhanced at the onset of rf power injection at low densities but are not changed from an already large value at high densities.

Several types of ion temperature simulations were made with the data at $B_0 = 7.6\,\mathrm{T}$. A simulation is carried out by assuming a constant value for the ion thermal conduction anomaly W_{sim} and simulating the central ion temperature behavior. The anomaly used in the simulation is assumed to be Ohmic–like (see Fig. 5.10) at the rf density. In most of the 7.6 T cases the density increase was small ($\lesssim 20\%$) and W_{sim} was nearly equal to the initial Ohmic value. The cases with $W_{\mathrm{Oh}} \lesssim 1$ had the largest density increases and were simulated with $W_{\mathrm{sim}} = 1.5$. Figure 5.17 shows the results of two simulations of $\Delta T_i/P_{\mathrm{rf}}$ compared with the experimentally measured value. The first simulation is made by assuming that no rf power flows into the ions but that the ion temperature increase results only from an improvement in the global particle confinement time so that $\tau_p(\mathrm{rf}) = 1.5\tau_P(\mathrm{Oh})$ (independent of density). The measured behavior of $\tau_p(\mathrm{rf})/\tau_p(\mathrm{Oh})$ (see Fig. 4.17) decreases with density (the maximum value is ~ 2) therefore, this simulation represents an approximate upper bound to the ion heating rate resulting only from a τ_p improvement. Ion heating rate simulations were also done assuming that $\tau_p(\mathrm{rf}) = 2\tau_p(\mathrm{Oh})$; in these cases, the simulated value of $\Delta T_i/P_{\mathrm{rf}}$ was approximately twice that for $\tau_p(\mathrm{rf}) = 1.5\tau_p(\mathrm{Oh})$. The second simulation in Fig. 5.17 is made by assuming that the global particle confinement time improves as in the first simulation and that $60\%P_{\mathrm{rf}}$ is deposited into the main ions in a radial profile given by the scattering results (assuming that $\hat{n}_e = 0.4$ at $\bar{n}_e = 3 \times 10^{20}\,\mathrm{m}^{-3}$). In both simulations, the value of P_{rf} used to calculate the quantity $\Delta T_i/P_{\mathrm{rf}}$ is the total measured rf power entering the antenna system and ΔT_i is the difference in ion temperature between the already described simulation and a *baseline* simulation where $P_{\mathrm{rf}} = 0$, $\tau_p(\mathrm{rf}) = \tau_p(\mathrm{Oh})$, and $W = W_{\mathrm{sim}}$. The simulations confirm that a nonzero source of rf power is required to explain the measured ion temperature behavior provided that the ion thermal conduction doesn't decrease relative to the Ohmic value at the onset of rf power injection.

Ion heating rate simulations of the data at $B_0 = 7.6\,\mathrm{T}$ exhibit two important characteristics. First, both simulations show a strong decrease in the ion heating rate as a function of density. This results solely from the increasing ion thermal conduction anomaly. In the first simulation where $P_{\mathrm{rf}} = 0$, the power loss due to ion conduction quickly becomes the dominant ion loss mechanism as the density increases. As a result, decreasing the convection loss by improving τ_p produces an increasingly smaller effect

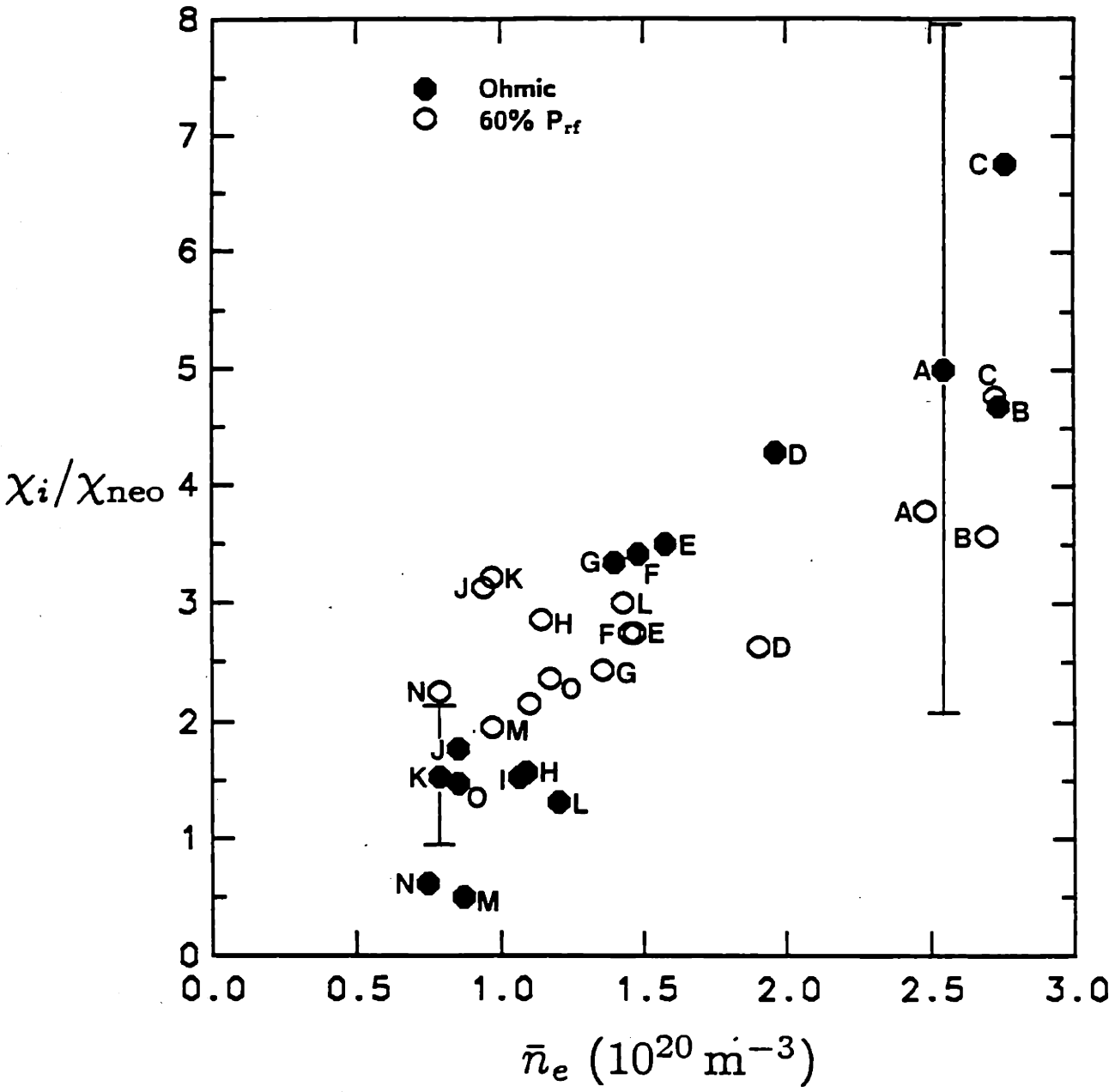

Figure 5.14 —The inferred value of the ion thermal conduction anomaly during Ohmic and ion Bernstein wave heating as a function of line–averaged density assuming that 60%P_{rf} flows into the hydrogen and that the fluctuation amplitude reaches a value of 40% at $\bar{n}_e = 3 \times 10^{20}\,\mathrm{m}^{-3}$. The letter labels indicate data points from the same discharge. $B_0 = 7.6\,\mathrm{T}$.

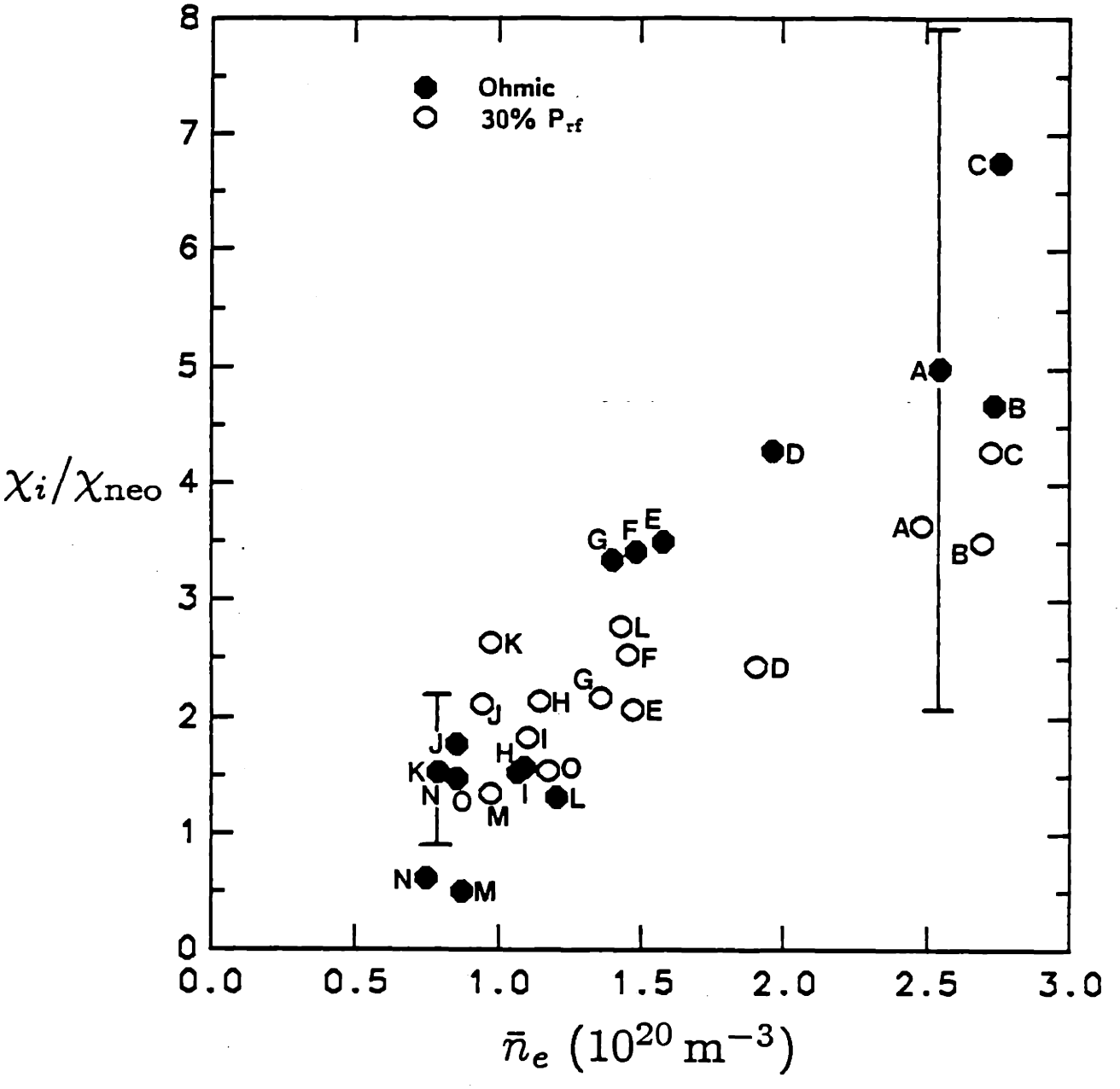

Figure 5.15 —The inferred value of the ion thermal conduction anomaly during Ohmic and ion Bernstein wave heating as a function of line-averaged density assuming that 30%P_{rf} flows into the hydrogen and that the fluctuation amplitude reaches a value of 40% at $\bar{n}_e = 3 \times 10^{20}\,\mathrm{m}^{-3}$. The letter labels indicate data points from the same discharge. $B_0 = 7.6\,\mathrm{T}$.

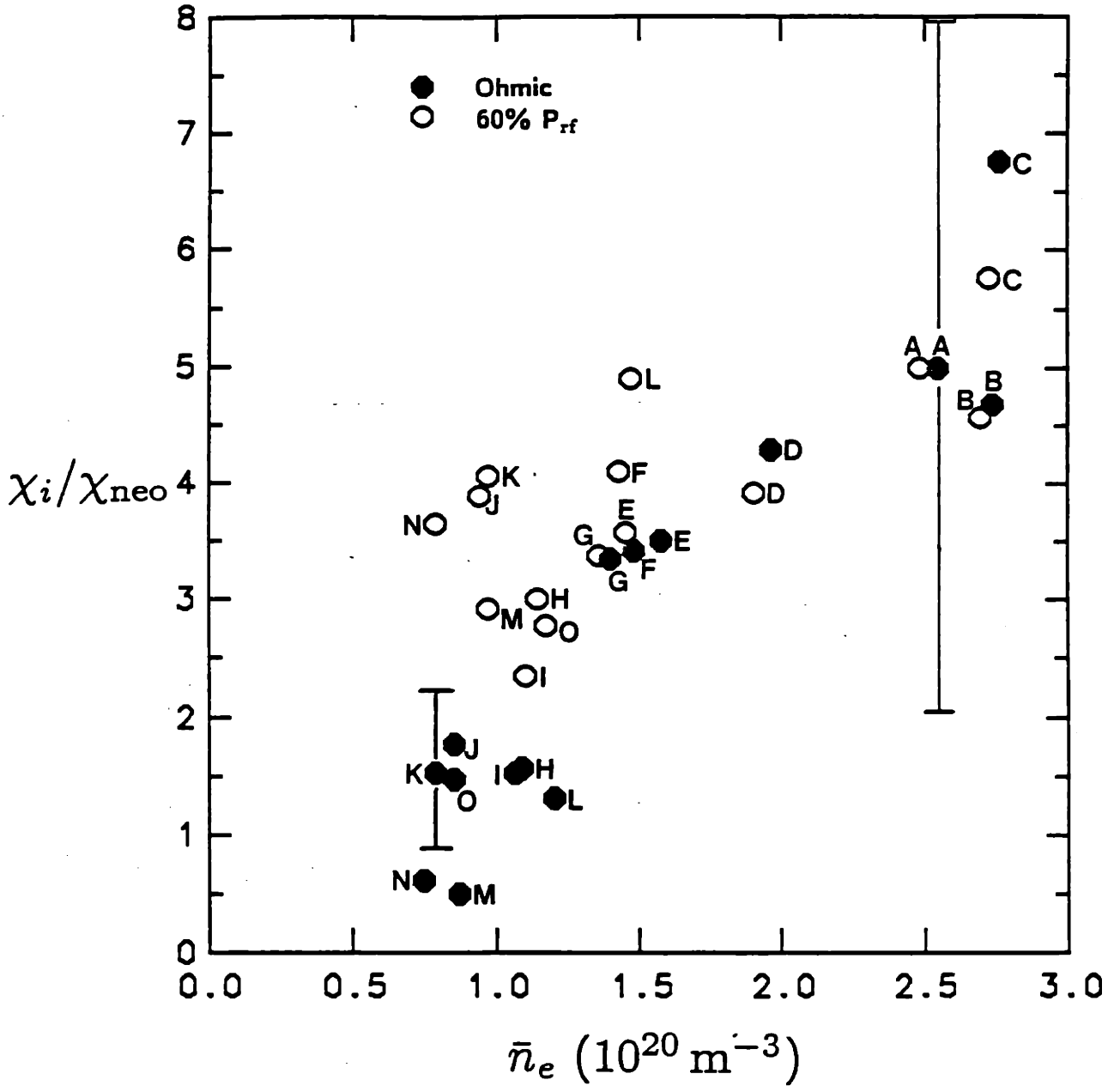

Figure 5.16 —The inferred value of the ion thermal conduction anomaly during Ohmic and ion Bernstein wave heating as a function of line–averaged density assuming that 60%P_{rf} flows into the hydrogen and that the fluctuation amplitude has a value of 0. The letter labels indicate data points from the same discharge. $B_0 = 7.6\,\mathrm{T}$.

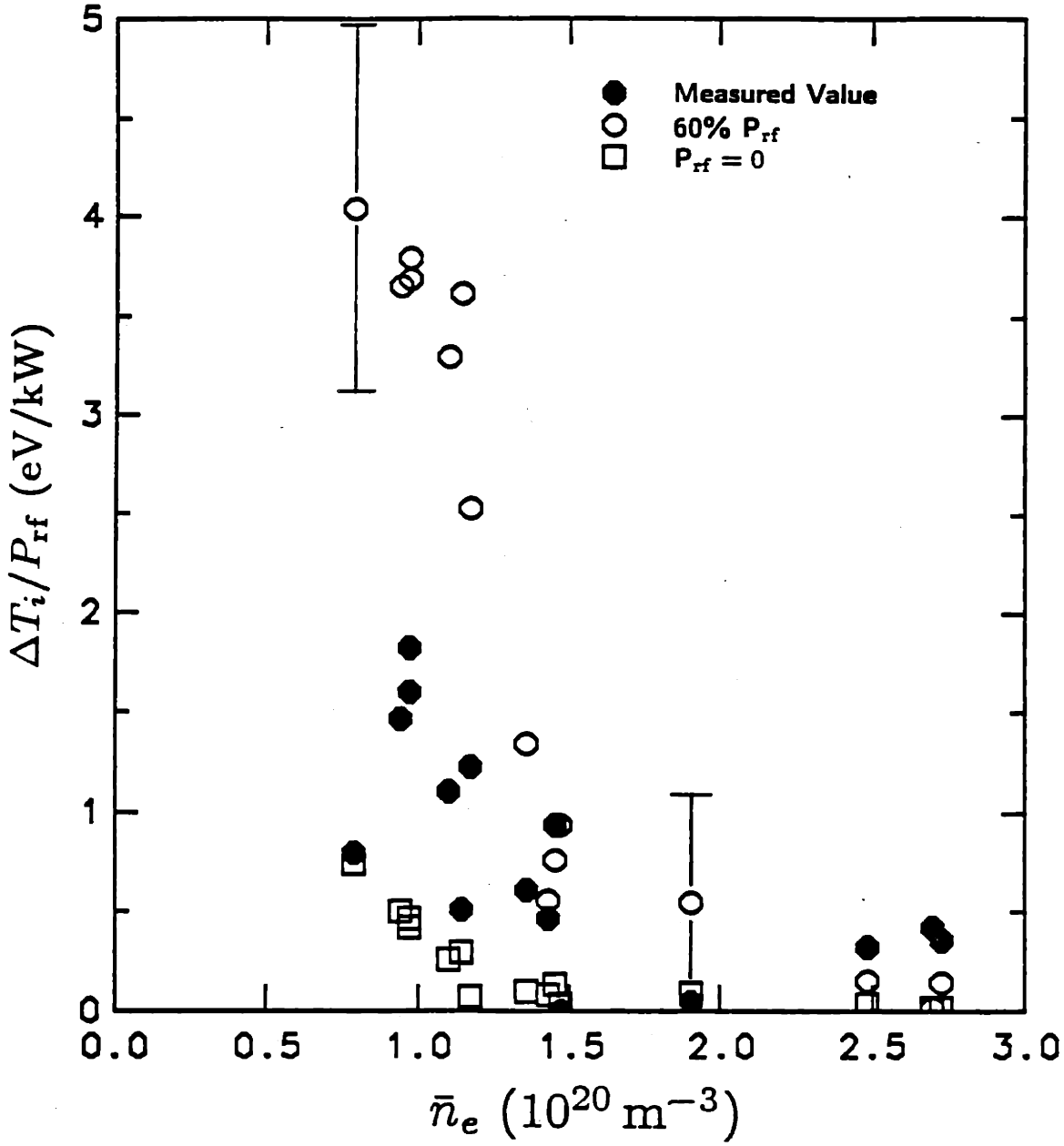

Figure 5.17 —Simulated ion heating rate $\Delta T_i/P_{rf}$ as a function of line–averaged density. In one case, $P_{rf} = 0$ and the ion temperature increase results only from improved particle confinement. In the other case, 60%P_{rf} flows into the hydrogen with a profile given by the scattering results and the ion temperature increase results from both improved particle confinement and rf power absorption. $B_0 =$ 7.6 T.

on the ion power balance. In the second simulation where $60\%P_{rf}$ flows into the hydrogen, the increasing anomalous ion conduction loss reduces the ion energy confinement resulting in less of an ion temperature increase for a given rf input power.

The second characteristic is that the simulated heating rate at low densities (assuming an Ohmic–like ion thermal conduction) is somewhat greater than the measured rate at low densities. However, at higher densities, the simulated heating rate is slightly less than the measured heating rate. The interpretation of these results is that at low densities, rf power injection enhances the ion losses so as to degrade the ion thermal conduction from its Ohmic–like value to a value which is 2–3 times the neoclassical value. The ion thermal conduction at high densities is slightly reduced from its Ohmic–like value at the onset of rf power injection. This interpretation is consistent with the results shown in Fig. 5.14 . Assuming that either the fluctuation amplitude or the total power which flows into the hydrogen is overestimated does not qualitatively change this interpretation. At the onset of rf power injection, the low density discharges still show an increase in the Ohmic–like ion thermal conduction and the high density discharges still show either a slight decrease or no change from the Ohmic–like value.

Summarizing the results at 7.6 T, it is shown that within experimental uncertainty, the inherent ion energy confinement characteristics of these discharges can explain the ion temperature behavior. More specifically, assuming that $60\%P_{rf}$ flows into the hydrogen with a radial profile given by the scattering results, the ion thermal conductivity must increase by ~ 1.5 times the Ohmic value (to 2–3 times the Chang–Hinton neoclassical prediction) at the onset of rf power injection to explain the ion temperature behavior in the low density discharges. At high densities, the Ohmic ion thermal conductivity is already 4–7 times the Chang–Hinton neoclassical value and may decrease slightly at the onset of rf power injection. A lower value of rf power or fluctuation amplitude will produce qualitatively similar results.

5.4.6: Ohmic Discharges at 9.3 Tesla

Analysis at the 9.3 T regime was done for 8 discharges which spanned a density range of $0.8 \times 10^{20}\,\mathrm{m}^{-3} \leq \bar{n}_e \leq 2 \times 10^{20}\,\mathrm{m}^{-3}$. These discharges showed similar behavior as the 7.6 T data; however, there were some marked differences. Figure 5.18 shows the inferred value of the ion thermal conduction anomaly of the Ohmic portion of the discharges as a function of line–averaged density. The Ohmic power is 450 ± 60 kW. This is slightly lower than the 7.6 T data due to a lower plasma current (~ 180 kA) and a slightly lower resistive loop voltage. The density dependence of Z_{eff} is shown in Fig. 5.19 . The ratio of central to line–averaged density is 1.4–1.9 ($\alpha_n \sim 1.6$) indicating a somewhat more peaked density profile than in the 7.6 T discharges. The ion thermal conduction anomaly is small (1–2 times the Chang–Hinton neoclassical prediction) at

low densities and shows an increase at higher densities. The absolute magnitude of the neoclassical ion thermal diffusivity on the magnetic axis in these discharges is somewhat smaller ($2300\,\mathrm{cm}^2/\mathrm{s}$) than in the 7.6 T cases.

The individual components of the ion power flow are shown in Fig 5.20 (a). The power is integrated out to $\rho/a = 0.5$ since most of the power flow in these discharges seems to occur within $\rho/a = 0.5$. This is probably a consequence of the more peaked profiles at higher q. The integrated power at $\rho/a = 0.75$ is shown in Fig. 5.20 (b) for comparison. Convective power loss is typically $< 10\%P_{\mathrm{Oh}}$. Power loss through charge exchange and ionization is less than $5\%P_{\mathrm{Oh}}$. The conductive power loss increases with density and follows the electron–ion power source. Within $\rho/a \leq 0.75$, the convective and conductive power losses are comparable indicating that particle confinement improvements can influence the ion power flow for nearly all of the cases considered.

5.4.7: Rf Heated Discharges at 9.3 Tesla

At this magnetic field, rf power absorption is expected to occur on deuterium and hydrogen at the $\omega = 3\Omega_{\mathrm{D}}$ layer located $\lesssim 2\,\mathrm{cm}$ in front of the antenna and on the deuterium at the $\omega = 2.5\Omega_{\mathrm{D}}$ layer located near to the center of the plasma. Direct power absorption on the hydrogen in the plasma center is not expected. The power flow into the deuterium has been estimated in section 4.4.4 from Fig. 4.15 to be 20 kW–40 kW or $\sim 60\%P_{\mathrm{rf}}$; the primary uncertainty in making this estimate lies in the value of the deuterium concentration. The fraction of power deposited near the plasma edge at the $\omega = 3\Omega_{\mathrm{D}}$ layer cannot be determined from the data but can be estimated from theoretical considerations. If rf power crosses the $\omega = 3\Omega_{\mathrm{D}}$ layer via parametric decay (see section 4.4.4), the lower frequency ion Bernstein wave at $\omega \simeq 2.8\,\Omega_{\mathrm{D}}$ contains (from Fig. 4.15) about $60\%P_{\mathrm{rf}}$. The quasimode at $\omega \simeq 0.2\,\Omega_{\mathrm{D}}$ contains $\sim 5\%P_{\mathrm{rf}}$ (estimated from the Manley–Rowe nonlinear energy relations). The remaining power, $\sim 35\%P_{\mathrm{rf}}$, is assumed to be deposited near the plasma edge at the $\omega = 3\Omega_{\mathrm{D}}$ layer. If rf power crosses the $\omega = 3\Omega_{\mathrm{D}}$ layer due to the toroidal ripple effect on the resonance layer location, the power flow into the deuterium must still be $\sim 60\%P_{\mathrm{rf}}$ and the power deposited at the edge in this case is $\sim 40\%P_{\mathrm{rf}}$. The deuterium exhibits a two temperature energy spectrum and the fraction of deuterium in the superthermal component is estimated to be $\sim 30\%$ of the total deuterium. Power conducted out by the high energy deuterium component is estimated to be negligible due to the low deuterium density. Considering this, a total power flow into the hydrogen from the deuterium of $60\%P_{\mathrm{rf}}$ was chosen to model the rf portion of the discharges.

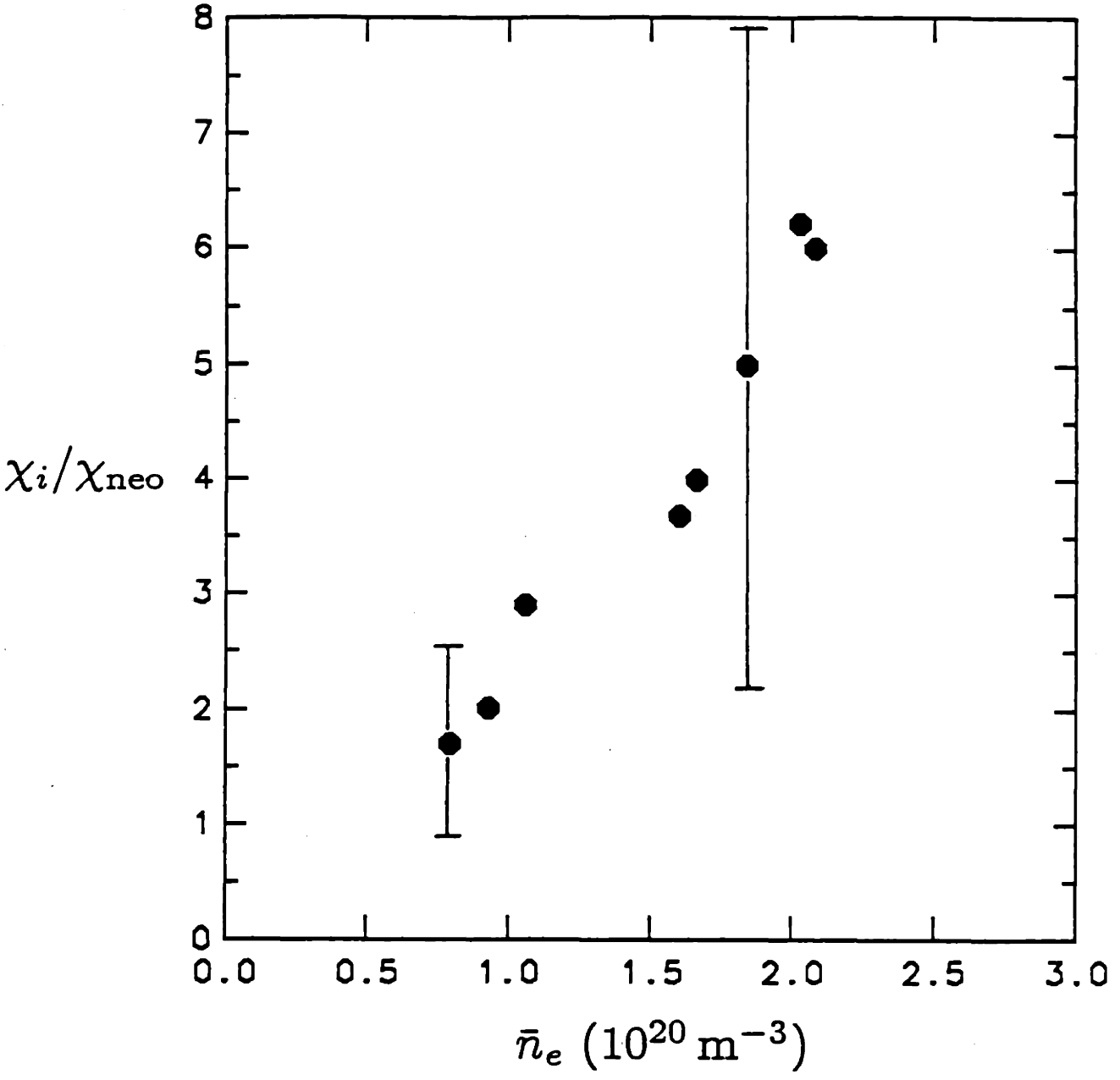

Figure 5.18 —Inferred value of the ion thermal conduction anomaly during Ohmic heating as a function of the line–averaged density. $B_0 = 9.3\,\mathrm{T}$.

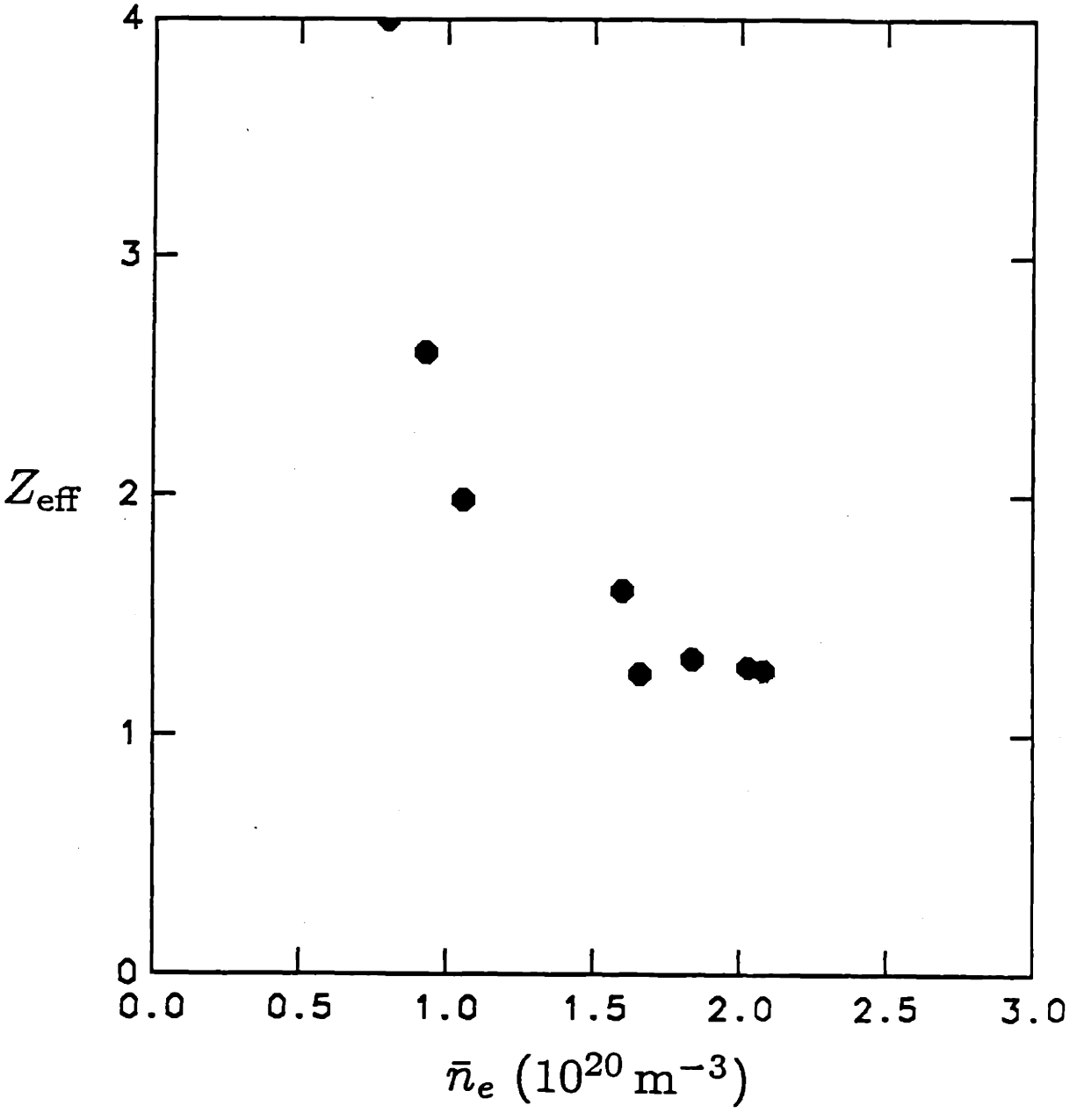

Figure 5.19 —Ohmic Z_{eff} measured by visible bremsstrahlung as a function of the line–averaged density. $B_0 = 9.3\,\text{T}$.

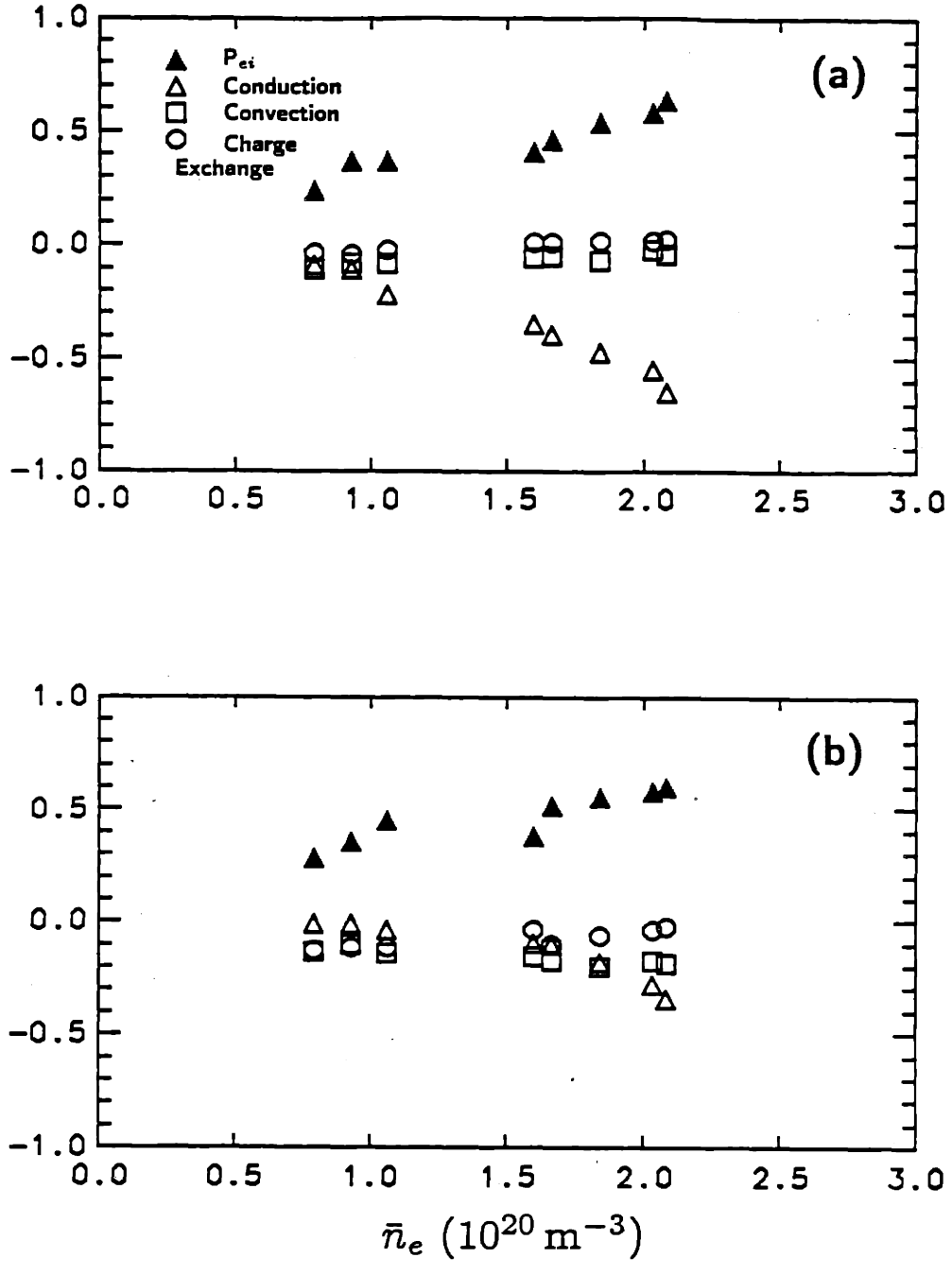

Figure 5.20 —Individual components of the ion power flow as a function of the line–averaged density at radial locations (a) $\rho/a = 0.5$, (b) $\rho/a = 0.75$. $B_0 = 9.3\,\mathrm{T}$.

The rf power source for this regime is also modeled in the shape of an annulus with the power distributed according to the estimated power deposition profile. Once power crosses the $\omega = 3\Omega_D$ layer, ray tracing calculations at this field give a power deposition profile similar to the 7.6 T regime. Edge density fluctuations, measured for $\bar{n}_e > 1 \times 10^{20}\,\mathrm{m}^{-3}$, are observed at 9.3 T; the measurements show a nearly identical behavior as is observed in the 7.6 T regime [see Fig. 5.6 (b)]. The fluctuation amplitude is assumed to be $\sim 40\%$ at $\bar{n}_e = 3 \times 10^{20}\,\mathrm{m}^{-3}$. Figure 5.21 shows a comparison of the inferred value of the ion thermal conduction anomaly during the Ohmic heated portion of the discharge with the anomaly during the Ohmic and ion Bernstein wave heated portion. The data points are plotted at the line–averaged density corresponding to either the Ohmic or the Ohmic and ion Bernstein wave heated portion of the discharge. Within the experimental error, an ion thermal conduction anomaly during rf power injection which is approximately the Ohmic value, is sufficient to explain the ion temperature behavior. This is in contrast to the 7.6 T data at low densities which showed that a small increase in the ion thermal conduction during rf power injection is necessary to account for the ion temperature behavior.

As in the 7.6 T regime, there is some uncertainty in both the amplitude of the total power which flows into the hydrogen and in the edge density fluctuation amplitude. The effect of reducing the total power to $30\%P_{\mathrm{rf}}$, while keeping the fluctuations the same, is shown in Fig. 5.22 . The figure shows that the ion thermal conductivity decreases slightly from the Ohmic value at the onset of rf power injection. This result suggests that the ion losses are reduced in comparison to the initial Ohmic losses at the onset of the rf power. The effect of reducing the fluctuation amplitude to 0% while keeping the power flowing into the hydrogen at $60\%P_{\mathrm{rf}}$ is shown in Fig. 5.23 . In this case, the ion thermal conduction can remain nearly Ohmic–like to explain the ion temperature behavior. In each case, the results at the 9.3 T regime indicate that the ion losses are either reduced or maintained compared to the Ohmic–like losses at the onset of rf power injection.

Figure 5.24 shows the result of an ion temperature simulation where the particle confinement is assumed to improve in accord with the data in Fig 4.17 and $60\%P_{\mathrm{rf}}$ is assumed to flow into the hydrogen with a profile approximated from the scattering results. The ion thermal conduction anomaly is assumed to be Ohmic–like. The particle confinement improvement can explain up to $\sim 50\%$ (at low densities) of the observed ion temperature behavior; however, a nonzero amount of rf power is required to account for the complete ion temperature behavior. A number of the low density discharges (one

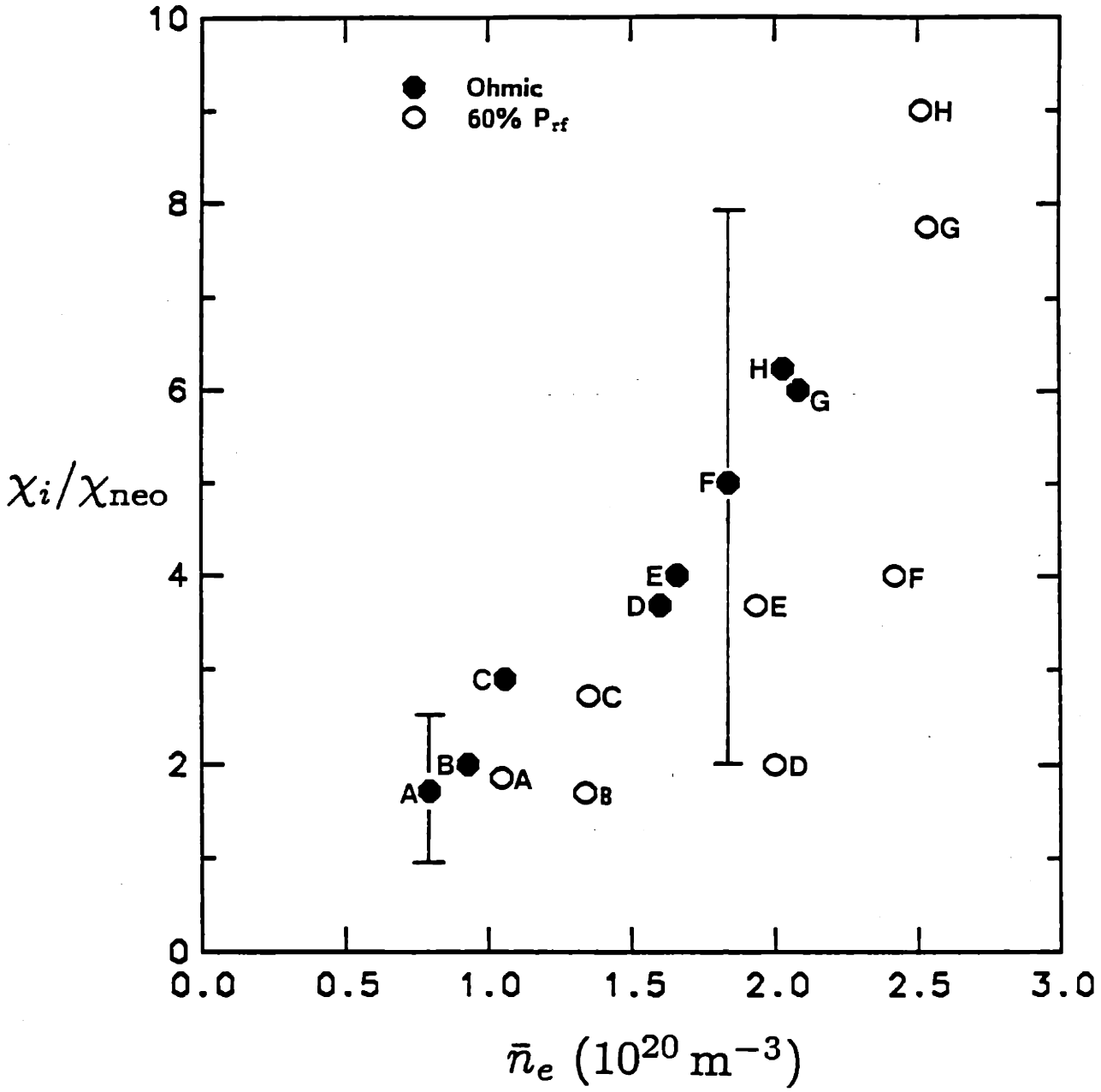

Figure 5.21 —The inferred value of the ion thermal conduction anomaly during Ohmic and ion Bernstein wave heating as a function of line–averaged density assuming that 60%P_{rf} flows into the hydrogen and that the fluctuation amplitude reaches a value of 40% at $\bar{n}_e = 3 \times 10^{20}\,\mathrm{m}^{-3}$. The letter labels indicate data points from the same discharge. $B_0 = 9.3\,\mathrm{T}$.

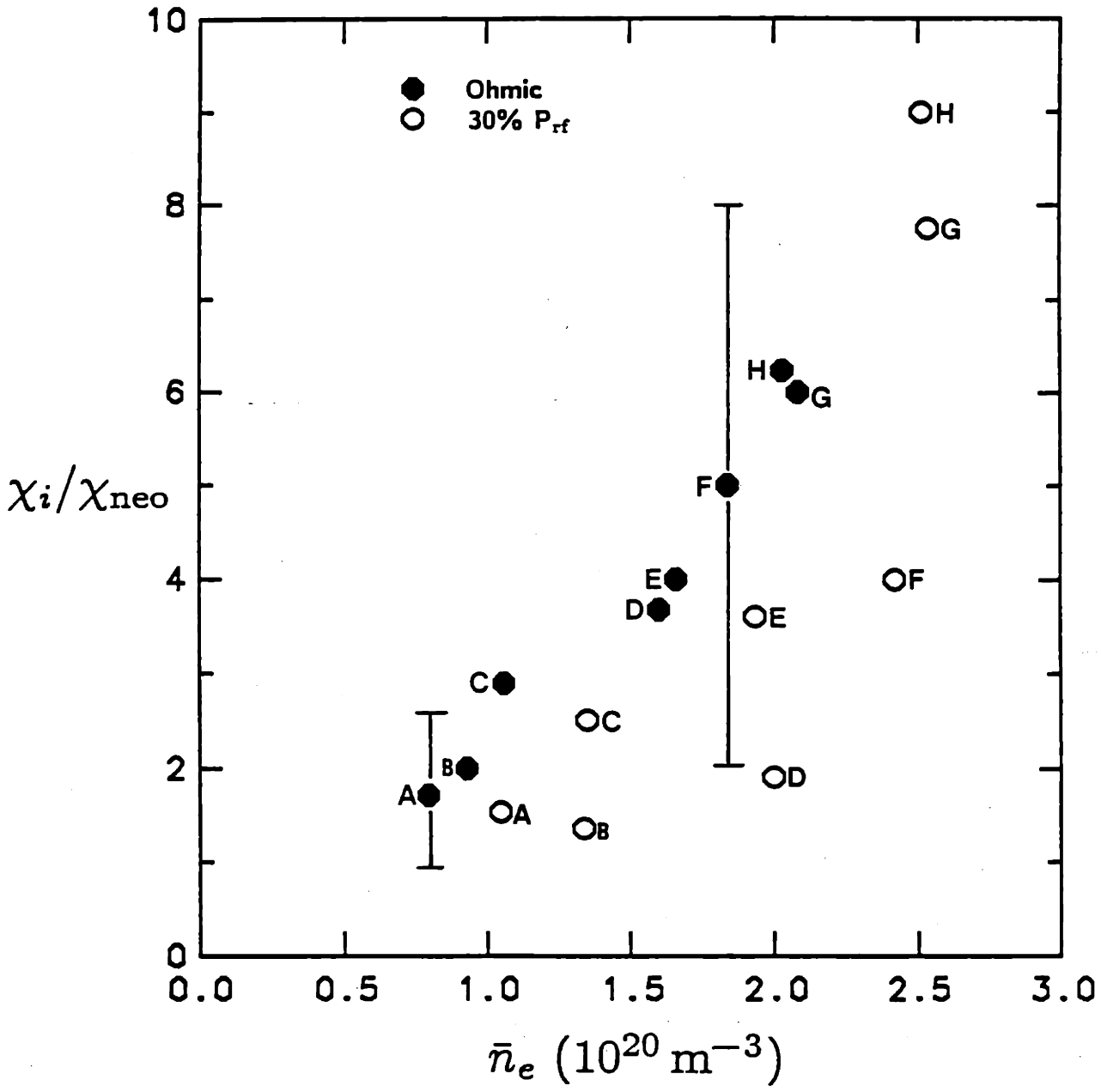

Figure 5.22 —The inferred value of the ion thermal conduction anomaly during Ohmic and ion Bernstein wave heating as a function of line-averaged density assuming that 30%P_{rf} flows into the hydrogen and that the fluctuation amplitude reaches a value of 40% at $\bar{n}_e = 3 \times 10^{20}\,\mathrm{m}^{-3}$. The letter labels indicate data points from the same discharge. $B_0 = 9.3\,\mathrm{T}$.

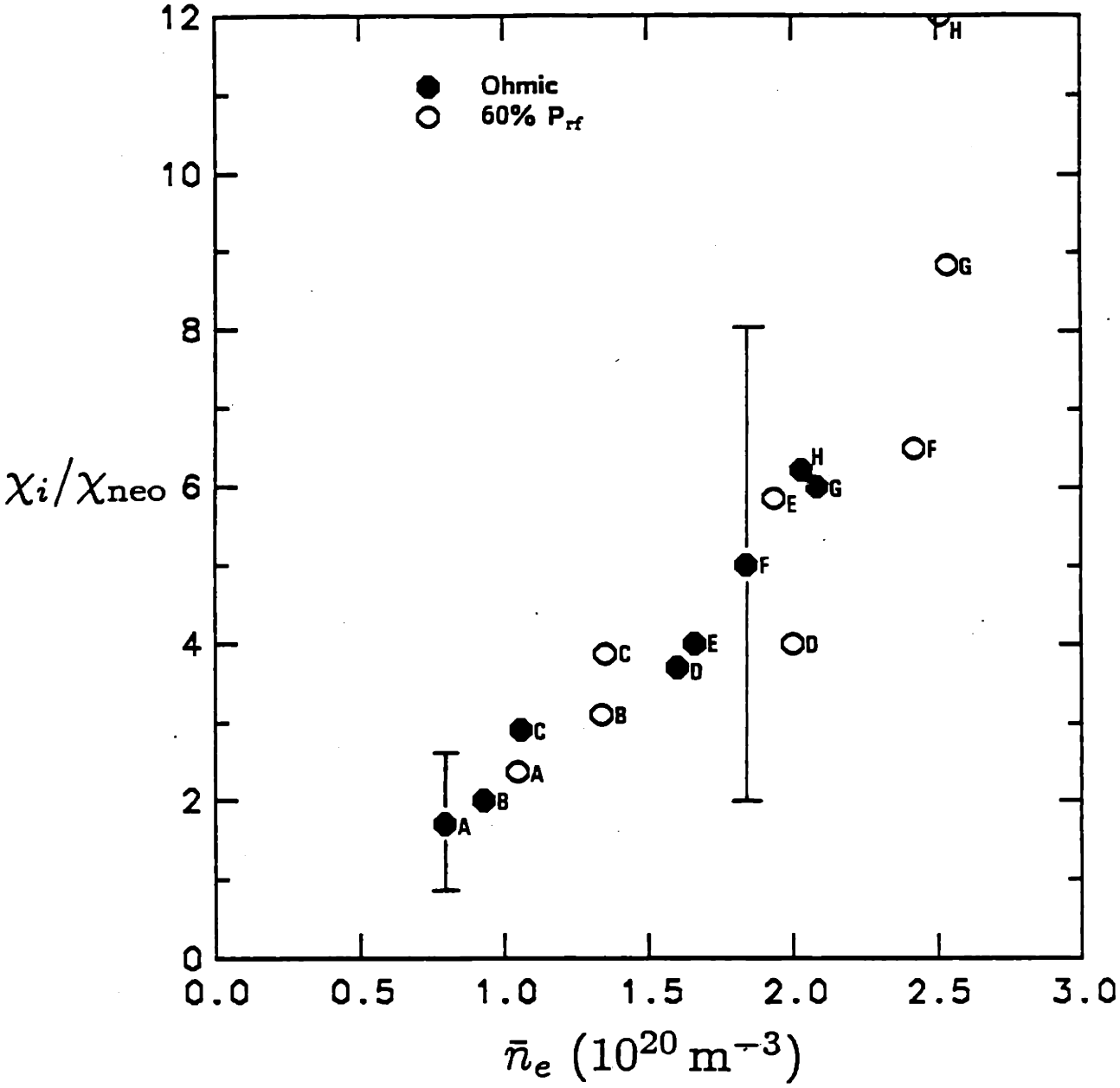

Figure 5.23 —The inferred value of the ion thermal conduction anomaly during Ohmic and ion Bernstein wave heating as a function of line–averaged density assuming that 60%P_{rf} flows into the hydrogen and that the fluctuation amplitude has a value of 0. The letter labels indicate data points from the same discharge. $B_0 = 9.3\,\mathrm{T}$.

is included with the 8 cases analyzed here) with the highest ion heating rate showed a slight peaking of the density profile during rf power injection.

The measured ion heating rate for several of the high density discharges was typically ≤ 0. This resulted because at the onset of rf power injection, the electron temperature decreased markedly. At high densities, since the electrons and ions are strongly coupled, the ion temperature fell below its Ohmic value in response to the electron temperature. The electron temperature behavior resulted from impurity generation at the onset of rf power injection. The rf power is typically $P_{rf} \geq 110\,\mathrm{kW}$ and impurity generation increases with rf power and plasma density.

The ion heating rate simulation at 9.3 T shows a strong decrease as a function of density and is similar in magnitude to the 7.6 T data indicating that the Ohmic ion heating rate of the two magnetic field regimes is nearly identical. The decrease in ion heating rate with density results once again from the increasing ion thermal conduction anomaly. The simulated ion heating rate is typically lower than the measured heating rate. The interpretation of this result is that Ohmic–like ion thermal conduction during rf power injection used in the simulation is too large. This is consistent with the results shown in Figs. 5.21 , 5.22 , and 5.23 . The ion losses are either improved or maintained compared to the Ohmic–like losses at the onset of rf power injection.

Summarizing the results at 9.3 T it is shown that the inherent ion energy confinement characteristics of these discharges can account for the observed ion temperature behavior. Assuming that $60\%P_{rf}$ flows into the hydrogen in a power deposition profile given by the scattering results, an ion thermal conduction during rf power injection, similar to the Ohmic value, is sufficient to explain the observed ion temperature behavior. Uncertainties in the total power flowing into the hydrogen and in the edge density fluctuation amplitude do not qualitatively alter this conclusion.

5.4.8: Sensitivity of Results

Uncertainties in the experimental parameters can alter the results of the power balance analyses. To determine the effects of the uncertainties, several test discharges were constructed by varying the measured quantities of actual discharges within the limits of experimental error. The primary sources of error are in the electron central temperature and profile, electron central density and profile, and the absolute value of the particle confinement time τ_p. The error in the T_e central value is estimated to be about 10%[15]. The error in central electron density from the Thompson scattering system is estimated to be about 15%, the error in the calculated profile is taken to be 15%. The error in the absolute magnitude of τ_p is roughly estimated to be about 50%.

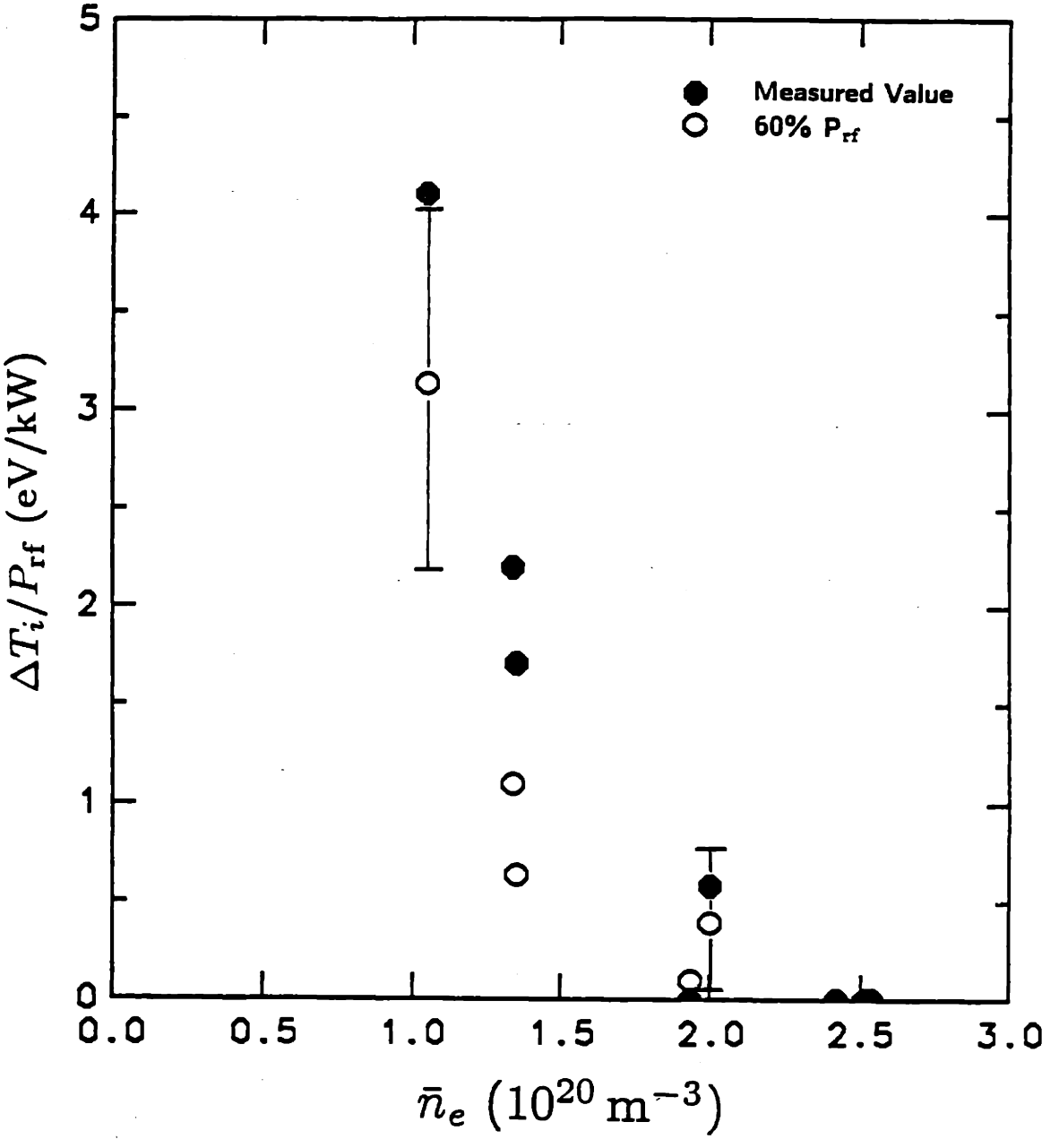

Figure 5.24 —Simulated ion heating rate $\Delta T_i/P_{rf}$ as a function of line–averaged density assuming an Ohmic–like ion thermal conductivity and that 60%P_{rf} flows into the hydrogen with a profile given by the scattering results. The ion temperature increase results from both improved particle confinement and rf power absorption. $B_0 = 9.3\,\mathrm{T}$.

The resulting variation in the inferred ion thermal conductivity and the simulated ion heating rate is shown by the error bars. The uncertainty in χ_i/χ_i^{neo} is small at low densities and large at high densities. At low densities, the electrons and ions are not well coupled since the difference in their temperatures is large. A 10%–15% change in the electron temperature and density does not produce a large effect on the ions. This situation is different at high densities where the electron and ion temperatures are much closer together and the value of P_{ei}, which mainly influences the value of W, is very sensitive to variations in T_e. Within the experimental error it can still be concluded that the ion thermal conduction anomaly in these discharges increases with density.

5.4.9: Discussion

Previous authors[15, 16, 22, 23] have indicated the presence of anomalous ion thermal conduction on Alcator C and have shown that the anomaly increases with plasma current. In addition, experiments on other tokamaks suggest the existence of anomalously high ion losses. The results of the analyses of the ion Bernstein wave data show that the anomaly also increases with increasing plasma density.

It has been suggested that the cause of the anomalous ion thermal conduction may arise from ∇T_i–driven ion drift instabilities (*e.g.* the ion mixing mode or η_i mode). This instability has been discussed by a number of authors[24, 25, 26, 27, 28, 29, 30] and arises from ion drift modes which tend to mix hot and cold ion populations. The mode becomes unstable when η_i exceeds a critical value η_{crit} where

$$\eta_i \equiv \frac{d(\ln T_i)}{d(\ln n_i)}. \tag{5.4.27}$$

and $\eta_{crit} \sim 1.5$. The mode tends to be excited by both a broad ion density profile and a narrow ion temperature profile. Measurements of the propagation velocity of the edge density fluctuations in a 16 cm Alcator C plasma[8] indicate that at low densities ($\bar{n}_e < 1.5 \times 10^{20}\,\mathrm{m}^{-3}$) the direction of wave propagation is in the electron diamagnetic direction. Above this density ($\bar{n}_e > 1.5$–$2 \times 10^{20}\,\mathrm{m}^{-3}$) the direction of propagation changes to the ion diamagnetic direction. The minimum value of $\tilde{n}_e^2$ in Fig. 4.21(b) may represent the transition in propagation direction of the density fluctuations. The fluctuations at higher densities possibly result from ion drift waves in the plasma and their presence may indicate that the ion–mixing mode is operative giving rise to the observed anomalous ion losses.

The measured ion temperature and density profiles contain significant errors and unfortunately cannot be used to estimate a meaningful value of η_i. Nevertheless, previous estimates[15] indicate that $0.8 \leq \eta_i(a/2) \leq 1.7$ for gas fueled discharges. It is interesting to estimate an upper bound for χ_i due to the enhanced transport from ion temperature gradient driven modes. One estimate for the ion thermal diffusivity has been given in Ref. 23 as

$$\chi_i \approx T^2 \left(\frac{\rho_i}{r_T}\right)\left(\frac{qR}{r_T}\right) D_b F(r) \tag{5.4.28}$$

where $r_T^{-1} = d(\ln T_i)/d\rho$, $D_b = cT_i/eB$, ρ_i is the ion gyro–radius, $2\pi Rq$ is the relevant connection length, T is of order unity, and $F(r)$ is a function which represents the spatial dependence of the amplitude. Estimating this near $\rho/a \sim 0.5$ for either magnetic field regime for $F \sim 1$ gives a value for χ_i which is 20–100 times larger than the neoclassical value. This result additionally confirms the possibility of enhanced transport due to ion temperature gradient driven modes.

The behavior of the rf heated discharges at 7.6 T and 9.3 T may be understood in terms of the rf power deposition profile and the characteristics of the ion temperature gradient driven instability. For example, at low densities in the 7.6 T regime, rf power deposition is peaked near the plasma center (1 cm $\leq \rho \leq$ 4 cm). This may cause the ion temperature profile to peak in the center, increasing the value of η_i, and leading to an enhancement of the ion losses. At higher density, the power deposition profile becomes spread over the plasma cross–section. This may cause the ion temperature profile to increase in a more uniform way causing the value of η_i to remain nearly constant or possibly decrease. The ion thermal conduction then remains nearly constant or decreases in response. At the 9.3 T regime, rf power deposition occurs both at the plasma edge (at the $\omega = 3\Omega_D$ layer) and near the center of the plasma. Power deposited at the plasma edge may broaden the ion temperature profile causing the value of η_i to decrease independently of the central power deposition profile. The ion thermal conduction then decreases or maintains an Ohmic–like value at the onset of rf power injection.

The different behavior of the rf heated discharges at 7.6 T and 9.3 T may indicate the importance of favorably modifying the ion temperature profile with the rf power. The 9.3 T regime provides a natural way of doing this with the $\omega = 3\Omega_D$ layer located just in front of the antenna. Although the ion heating is best at this high field regime, it is only good at low densities. At high densities, the electron temperature drops markedly at the onset of rf power injection causing the ion temperature to drop from its Ohmic value. This behavior is attributed to increased impurity injection at high densities. The 7.6 T regime also exhibits decreases in the electron temperature at the onset of rf power

injection at high densities, but the decrease is not as large as in the 9.3 T regime. The presence of the $\omega = 3\Omega_D$ layer therefore, may be helpful at low densities for modifying the ion temperature profile but may be detrimental at high densities by causing a large impurity production. Another source of impurity production is the edge electron heating due to the quasi–mode (as a result of parametric decay in front of the antenna in the 9.3 T case) which would cause enhanced sputtering near the edge[5, 6, 31].

5.4.10: Global Energy Confinement

Figure 5.25 shows the global energy confinement time during the Ohmic heating phase and the Ohmic plus ion Bernstein wave heating phase for both field regimes. Although numerous discharges showed a global energy confinement time during rf power injection which was greater than the initial Ohmic value, the global energy confinement time during rf power injection was always less than the confinement time of an equivalent Ohmic discharge (at the same density) for both field regimes. The cause of this is due to increased radiation loss from impurities. This is especially apparent in the 9.3 T data which shows large electron temperature decreases (particularly at higher densities) at the onset of rf power injection. The electron temperature also decreases in the 7.6 T data; however, the decrease is not as significant as in the 9.3 T data. As a result, the global energy confinement time during rf power injection is somewhat lower ($\tau_E \sim$ 8–10 ms) at 9.3 T than at 7.6 T ($\tau_E \leq 15$ ms).

5.4.11: Conclusions

Analyses of Ohmic discharges at 7.6 T and 9.3 T have indicated the presence of anomalous ion thermal conduction which increases with plasma density. This anomalous ion thermal conduction may be due to increased transport arising from η_i modes. The ion temperature behavior at 7.6 T can be explained by assuming that $\sim 60\% P_{rf}$ is deposited into the hydrogen in a profile given by the scattering results. At low densities, the rf power deposition profile, which is peaked near the plasma center, may cause the ion temperature profile to peak. This may increase the value of η_i causing the ion thermal conductivity to increase above the Ohmic–like value. At higher densities, the power deposition profile is broadened as a result of the edge fluctuations causing the value of η_i to remain equal to the Ohmic value or possibly decrease. The result is that the ion thermal conduction remains nearly the same as the Ohmic value or decreases slightly. The ion temperature behavior at 9.3 T can be accounted for by assuming that $60\% P_{rf}$ is absorbed by the hydrogen in a profile given by the scattering, and that the

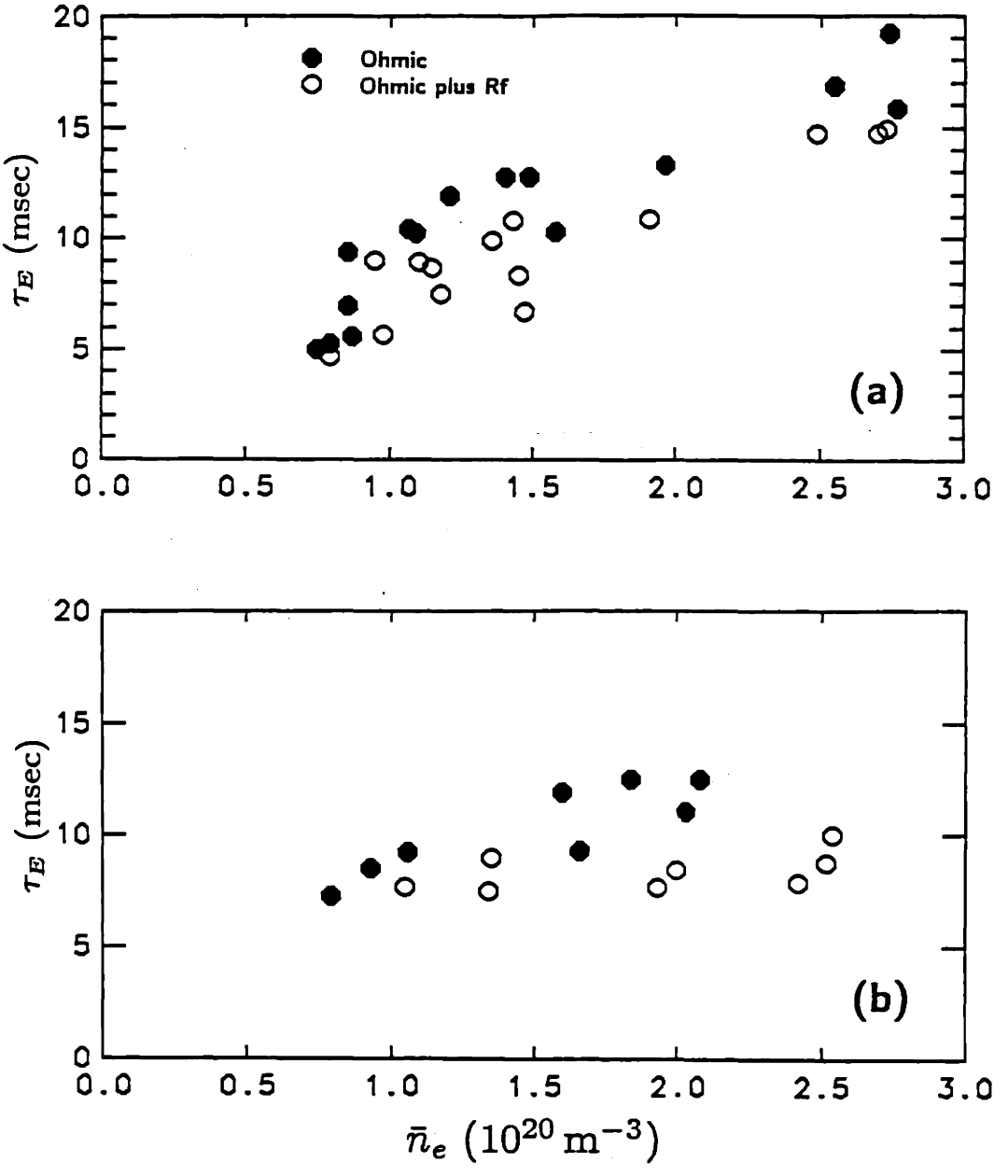

Figure 5.25 —Experimental global energy confinement time during the Ohmic and Ohmic plus ion Bernstein wave heated portions of the discharge as a function of line-averaged density. (a) $B_0 = 7.6\,\mathrm{T}$. (b) $B_0 = 9.3\,\mathrm{T}$.

ion thermal conductivity remains nearly equal to the Ohmic value. Power deposition near the plasma edge at the $\omega = 3\Omega_D$ layer may broaden the ion temperature profile causing the value of η_i to decrease or remain constant. The ion thermal conduction then remains constant or decreases in response. The decrease in the ion heating rate with increasing density in both magnetic field regimes is essentially accounted for by the increasing anomaly in the ion thermal conductivity as a function of plasma density. Uncertainties in the total power flow into the hydrogen and in the fluctuation amplitude do not qualitatively alter these conclusions. Unfortunately, due to a lack of accurate ion density and temperature profile measurements, more definitive statements regarding η_i modes cannot be made.

REFERENCES

1. M. BRAMBILLA, 7th Topical Conf. on Rf Plasma Heating, Kissimmee, FL, (1987).
2. M. BRAMBILLA, Max–Planck Institut für Plasmaphysik Report IPP 5/15, April 1987.
3. M. ONO, Ion Bernstein Wave Heating, Theory and Experiment, in Proc. Course and Workshop on Applications of rf Waves to Tokamak Plasmas, Varenna 1985.
4. F. SKIFF, M. ONO, AND K. L. WONG, *Phys. Fluids*, **27**, 1051, (1984).
5. M. PORKOLAB, J. D. MOODY, AND C. FIORE, *Bull. Am. Phys. Soc.*, **32**, 1939, (1987).
6. R. VAN NIEUWENHOVE, G. VAN OOST, J.–M. NOTERDAEME, M. BRAMBILLA, J. GERNHARDT, AND M. PORKOLAB, Max–Planck Institut für Plasmaphysik Report IPP III/129, January 1988.
7. M. ONO, *Phys. Fluids*, **25**, 990, (1982).
8. R. L. WATTERSON, R. E. SLUSHER, AND C. M. SURKO, *Phys. Fluids*, **28**, 2857, (1985).
9. JEROME SPANIER AND ELY M. GELBARD, *Monte Carlo Principles and Neutron Transport Problems*, (Addison–Wesley Publishing Company, Reading, Massachusetts, 1969).
10. P. T. BONOLI AND E. OTT, *Phys. Fluids*, **25**, 359, (1982).
11. Y. TAKASE *et al.*, *Phys. Rev. Lett.*, **59**, 1201, (1987).
12. R. E. SLUSHER AND C. M. SURKO, *Phys. Rev. Lett.*, **37**, 1747, (1976).
13. E. OTT, *Phys. Fluids*, **22**, 1732, (1979).
14. M. BRAMBILLA, Private communication, (1987).
15. S. WOLFE, *et al.*, *Nucl. Fusion*, **26**, 329, (1986).
16. R. R. PARKER, *et al.*, *Nucl. Fusion*, **25**, 1127, (1985).
17. B. D. BLACKWELL, *et al.*, in Plasma Physics and Controlled Nuclear Fusion Research 1982 (Proc. 9th Int. Conf. Baltimore, 1982), **2**, IAEA, Vienna (1983) 27.
18. W. W. PFEIFFER, R. H. DAVIDSON, R. L. MILLER: A Computer Code for Modelling Plasma Transport in Tokamaks, Gulf General Atomic, Inc., San Diego, CA, Rep., GA–A16178 (1980).
19. F. L. HINTON AND R. D. HAZELTINE, *Rev. Mod. Phys.*, **48**, 239, (1976).

20. C. S. CHANG AND F. L. HINTON, *Phys. Fluids*, **29**, 3314, (1986).

21. J. M. MANLEY AND H. E. ROWE, *Proc. IRE*, **44**, 904, (1956).

22. B. COPPI, Invited Paper 3A, Annual Controlled Fusion Theory Conference, Lake Tahoe, NV (1984).

23. B. COPPI, S. COWLEY, P. DETRAGIACHE, R. KULSRUD, F. PEGORARO, AND W. M. TANG, in Plasma Physics and Controlled Nuclear Fusion Research 1984, **2**, IAEA, Vienna (1984), 93.

24. M. PORKOLAB, *Physics Letters*, **22**, 427, (1966).

25. B. COPPI, M. N. ROSENBLUTH, AND R. Z. SAGDEEV, *Phys. Fluids*, **10**, 582, (1967).

26. M. PORKOLAB, *Nucl. Fusion*, **8**, 29, (1968).

27. T. ANTONSEN, B. COPPI, AND R. ENGLADE, *Nucl. Fusion*, **19**, 641, (1979).

28. G. S. LEE, P. H. DIAMOND, in Sherwood Annual Controlled Fusion Theory Conference (Proc. Mtg. Madison, WI, 1985), (1985) paper 1S24.

29. R. ENGLADE, B. COPPI, S. MIGLIUOLO, in Sherwood Annual Controlled Fusion Theory Conference (Proc. Mtg. Madison, WI, 1985), (1985) paper 2Q20.

30. G. S. LEE AND P. H. DIAMOND, *Phys. Fluids*, **29**, 3291, (1986).

31. M. PORKOLAB, Presented at the ICRF–Edge Physics Workshop, Boulder Colorado, 31 March, 1988. (To be published.)

CHAPTER 6

Conclusions

6.1: Summary

The previous chapters presented the experimental study of ion Bernstein waves in the Alcator C tokamak and attempted to explain through detailed analyses the causes for the experimentally observed results. In particular, the antenna–plasma loading, wave propagation and power absorption, and the plasma response to ion Bernstein wave power injection were analyzed within the context of current plasma theories. Also, the characteristics of the ion Bernstein wave were discussed.

The ion Bernstein mode was shown to be essentially a sound–like plasma wave which oscillates at a frequency near the ion cyclotron frequency or its harmonics. The majority of the wave energy is in the ion kinetic motion. The wave length perpendicular to the background magnetic field is on the same order of magnitude as the ion Larmor gyro–radius. The wave can undergo strong linear damping at integral ion cyclotron harmonics. Two nonlinear power absorption mechanisms are mentioned. First, nonlinear Landau damping via ion Bernstein wave self–interaction gives rise to power absorption at odd–half integral ion cyclotron harmonics. This may be important at

several magnetic field regimes studied in the experiment. Second, nonlinear Landau damping on deuterium via ion Bernstein wave decay is considered. In this process, the ion Bernstein wave decays into another ion Bernstein wave at a downshifted frequency and an ion quasimode at $\omega/\Omega_{\rm H} = 0.5$ ($\omega/\Omega_{\rm D} = 1$). The ion quasimode is resonant with the fundamental ion cyclotron frequency of the deuterium species. This process is shown to be important at the 7.6 T regime.

Antenna–plasma loading measurements were made as a function of plasma density, magnetic field, and rf power. The antenna loading exhibited a maximum of 1.5 Ω when the hydrogen second harmonic layer was placed just to the low field side of the antenna. Outside of this magnetic field, the antenna loading was nearly constant at $\sim 1\,\Omega$. The antenna loading increased with density until $\bar{n}_e \simeq 2.6 \times 10^{20}\,{\rm m}^{-3}$; beyond this density, the antenna loading decreased. The loading also showed a $\sim 20\%$ decrease in value as the rf power was increased from 50 kW to 150 kW.

A CO_2 laser scattering diagnostic system was used to study ion Bernstein wave propagation and absorption in Alcator C. The ion Bernstein wave perpendicular wave vector was mapped out as a function of minor radius and showed good agreement with the theoretical dispersion curve. The amplitude of the scattered signal was nearly linearly dependent on the rf power. Power absorption was investigated across the $\omega/\Omega_{\rm D} = 3$ layer at both the 7.6 T and 9.3 T field regimes. The CO_2 scattered signal showed a strong attenuation across this layer suggesting ion Bernstein wave power absorption.

Ion Bernstein wave heating experiments were carried out in plasmas within the density range $0.6 \times 10^{20}\,{\rm m}^{-3} \leq \bar{n}_e \leq 4 \times 10^{20}\,{\rm m}^{-3}$ and magnetic fields within the range $4.8\,{\rm T} \leq B_0 \leq 11\,{\rm T}$. Central ion temperature increases of $\Delta T_i/T_i \gtrsim 0.1$ and density increases of $\Delta n/n < 1$ were observed during rf power injection of up to 180 kW. Although the greatest ion heating was observed at a central magnetic field of 9.3 T, heating occurred over a broad range of magnetic fields ($2.4 \geq \omega/\Omega_{cH(0)} \geq 1.1$) and did not show a strong dependence on having a particular ion cyclotron resonance located near the plasma center. The density increase was usually accompanied by an improvement in the global particle confinement time relative to the Ohmic value and the ion temperature increase appeared to show rf power thresholds which were dependent on the magnetic field and agreed with the theoretical predictions within experimental error. Near densities of $\bar{n}_e \lesssim 1.1 \times 10^{20}\,{\rm m}^{-3}$ rf power injection typically produced an ion heating rate of $\Delta T_i/P_{\rm rf} \sim 2$–$4.5\,{\rm eV/kW}$. At higher densities, $\bar{n}_e > 1.5 \times 10^{20}\,{\rm m}^{-3}$, the ion heating rate decreased to 0.5 eV/kW.

6.2: Results of Analyses

6.2.1: Power Absorption Mechanisms

The variety of possible rf power absorption mechanisms introduce a significant complication in determining the operative absorption mechanism at each magnetic field regime. A strong indication of nonlinear power absorption is the presence of a measured power threshold for $\Delta T_H \neq 0$. A power threshold is observed at both the 7.6 T and 5.1 T regimes and may be present at the 9.3 T regime. In all three cases, central ion heating is observed. In both the 7.6 T and 9.3 T regimes, there is clear experimental evidence that the deuterium minority is heated by the rf power. The 35 kW rf power threshold for $\Delta T_D \neq 0$ at 7.6 T may indicate that the deuterium heating is nonlinear. This threshold suggests the possibility of ion Bernstein wave decay where the quasimode is resonant with the deuterium first cyclotron harmonic. The remaining power, not absorbed by this nonlinear mechanism on the deuterium, is predicted to undergo nonlinear absorption on the hydrogen. Finally, any remaining power not absorbed by either nonlinear process should be absorbed linearly by the deuterium. The estimated theoretical power threshold for either nonlinear mechanism is in good agreement with the measured threshold further supporting the possibility that power absorption occurs through nonlinear mechanisms at 7.6 T.

The measured power threshold at 9.3 T is small (≤ 10 kW) compared to the theoretically estimated value of ~ 30 kW. It is pointed out, especially in this field regime, that the ion temperature behavior is influenced both by particle confinement improvements (up to a factor of 3 from the Ohmic value) as well as rf power absorption. This complicates the determination of the rf power absorption threshold. In this field regime, absorption of rf power at the $\omega/\Omega_D = 2.5$ layer is predicted to be the only central absorption mechanism at this field. However, the $\omega/\Omega_D = 3$ layer, located at the plasma edge in front of the antenna, is estimated to cause complete power absorption by either linear or nonlinear mechanisms. To explain the central deuterium heating, at least a fraction of the rf power must penetrate to the plasma interior. Two mechanisms are suggested which may explain this. Variation of the edge magnetic field due to the toroidal field ripple may push the $\omega/\Omega_D = 3$ layer behind the antenna center conductor (away from the vicinity of the toroidal access port) allowing some rf power to propagate into the central plasma from either end of the antenna. Also, ion Bernstein wave parametric decay to a slightly downshifted (in frequency) ion Bernstein wave would cause the $\omega/\Omega_D = 3$ layer to be shifted outside of the vacuum vessel for the decay wave. It is pointed out that the plasma current is $\sim$ 180 kA and is not enough in itself to

significantly affect the location of the $\omega/\Omega_D = 3$ layer; however, it contributes slightly to pushing the layer further toward the plasma edge.

Power absorption is expected to occur nonlinearly on the hydrogen ion species at the 5.1 T regime. The presence of a power threshold of $\sim$25 kW confirms that nonlinear power absorption is operative. The theoretically estimated threshold is $\sim$ 30 kW, in good agreement with the measured value.

6.2.2: Antenna Loading

The antenna loading measurements are compared with the results of an antenna–plasma coupling model developed by M. Brambilla. This model, which is based entirely upon linear plasma wave theory, predicts the observed dependence of the radiation resistance on magnetic field over a small range of fields where the $\omega/\Omega_H = 2$ layer is positioned just behind the antenna. The large observed background loading, not predicted by the model, may result from nonlinear wave processes occurring near the antenna which could add additional loading. Near the field of maximum antenna loading, the model predicts that a small $\sim$ 15% fraction of power is coupled into the ICRF fast wave. The observed density dependence of the loading is reproduced well by the model provided the edge density is assumed to remain nearly constant or decrease until the line–averaged density increases to $\bar{n}_e \simeq 2.6 \times 10^{20}\,\mathrm{m}^{-3}$; then the edge density must begin to increase beyond this density. Certain parametric processes may occur near the antenna surface where the predicted electric field energy density is large compared to the plasma thermal energy density. This large electric field and the weak dependence of R_{rad} on rf power support the possibility of nonlinear effects which might produce loading not included in the Brambilla model.

6.2.3: Ion Heating

The primary analyses of the ion heating centered around the density dependence of the ion heating rate. Several density dependent mechanisms were considered which together can account for the decrease in the ion heating rate with density. However, the effect of edge collisional power absorption, which increases with density, was indicated to be negligible. The nonlinear power threshold increases linearly with density; however, this cannot explain the ion heating rate decrease with density at 7.6 T. Linear power absorption on the deuterium should still be operative independent of density.

CO_2 laser scattering measurements show that low–frequency edge turbulence increases with density. The turbulence can scatter the ion Bernstein wave power which would broaden the radial power deposition profile. Scattering of the ion Bernstein wave rays from edge turbulent fluctuations was modeled at 7.6 T using a Monte Carlo

direct sampling simulation. It was found that in the absence of fluctuations, the power deposition is peaked near the plasma center and approximately 80% of the injected rf power reaches the plasma inside $\rho/a \leq 0.5$. A fluctuation amplitude of $\hat{n}_e = 0.3$ is sufficient to reduce this power to $\sim 20\%$ and spread the power deposition profile across the entire poloidal cross–section. Unfortunately, the absolute value of $\hat{n}_e$ could not be accurately determined from the experimental data. Nevertheless, using previous results from earlier measurements of the fluctuation level from Alcator C, the scattering model provided a way to calculate the power deposition profile. This profile was then used in an energy and particle transport code.

The effect of ion energy confinement on the ion temperature behavior was also analyzed. It was found that the Ohmic discharges at both the 7.6 T and 9.3 T regimes exhibit an increasing anomalous ion thermal conduction relative to the Chang–Hinton neoclassical prediction with increasing density. This increasing anomaly may be caused by increased transport resulting from η_i modes. It was shown that the ion temperature behavior at the 9.3 T regime can be accounted for by assuming that $60\%P_{\rm rf}$ flows into the hydrogen in a profile given by the scattering results, and that the value of the ion thermal conduction remains nearly the same as the Ohmic value. The ion temperature behavior at 7.6 T can potentially be explained by assuming that $60\%P_{\rm rf}$ is absorbed by the hydrogen in a profile given by the scattering results. In addition, it is necessary to assume that the ion thermal conduction increases by a factor of ~ 2 at low densities and remains constant or decreases at high densities compared to the Ohmic value. Uncertainties in the total absorbed rf power and in the fluctuation amplitude do not qualitatively alter these results.

The difference in the behavior between the two field regimes was suggested to result from the differing power deposition profiles in both regimes as well as the characteristics of the η_i mode. At low densities, the power deposition profile is peaked near the plasma center at 7.6 T. This may cause a peaking of the ion temperature profile, increasing the value of η_i, and increasing the ion thermal transport. At higher densities, the power deposition profile broadens. This may cause the value of η_i to remain unchanged or slightly decrease, causing the ion thermal transport to remain constant or decrease some. The power deposition profile at 9.3 T has a peak near the plasma edge at all densities; within the plasma, the power deposition profile is peaked at low densities and broad at high densities. The power deposition at the plasma edge may result in a broader ion temperature profile at all densities, maintaining or even reducing the value of η_i, which then causes the ion thermal conduction to remain nearly constant or slightly decrease. There is no accurate ion temperature or density profile data to support these claims; however, the effect of the rf power deposition profile on the anomalous Ohmic ion thermal conduction suggests that the anomalous ion thermal

conduction is determined by the ion temperature profile, a characteristic of the η_i mode.

The results of the power balance analyses are significant since they suggest that the ion heating behavior in this experiment is mainly a result of the plasma ion energy confinement. The properties of the ion Bernstein wave coupling structure and the wave characteristics do not seem to be strongly influential in affecting the ion heating behavior. The results of this experiment suggest that for future ion heating schemes on high density devices such as Alcator C (*i.e.*, C-Mod and CIT), one must consider the inherent ion energy confinement characteristics of the plasma when interpreting the experimental results.

6.3: Suggestions for Future Work

Numerous suggestions can be drawn from this experiment regarding future ion Bernstein wave experiments. For example, there is still much that can be learned concerning high power ion Bernstein wave antenna–plasma coupling. It would be useful to study the wave frequency spectrum near the antenna as a function of magnetic field, plasma density, and rf power. This could confirm the presence of parametric processes and establish their dependences on plasma parameters. Measurements of plasma density, temperature, and rf electric field in the vicinity of the antenna would also aid the study of antenna–plasma coupling.

Accurate measurements of the amplitude and radial profile of the low–frequency edge turbulence is crucial for determining the accessibility of ion Bernstein wave power to the plasma center. The ion Bernstein wave, due to its short wavelength, is very susceptible to scattering from low–frequency edge density fluctuations. It was shown earlier that a fluctuation amplitude of $\hat{n}_e = 0.3$ is sufficient to reduce the power reaching the plasma center by a factor of four in these experiments. Experimentally, the absolute amplitude of $\hat{n}_e$ could not be determined and therefore it was not possible to estimate quantitatively the power accessible to the plasma interior and its spatial distribution. Knowledge of $\hat{n}_e$ and its affect on wave power accessibility is important for deciding the feasibility of plasma heating via the ion Bernstein wave in future high density, compact devices.

Finally, future ion Bernstein wave experiments may benefit by combining rf power injection with pellet injection. Fueling the Alcator C plasma by pellet injection has been shown to reduce the initial Ohmic ion thermal conduction by a factor of 3–5, bringing it to a value nearly equal to the Chang–Hinton neoclassical prediction. The ion heating

rate from ion Bernstein wave power injection is shown to be greatly reduced at high densities due to the large anomalous ion thermal conductivity. Pellet injection could possibly reduce this large anomaly and may lead to a substantially higher ion heating rate even at high densities when combined with ion Bernstein wave power injection.